

Estimation of forest structure parameters in  
Mexico by integration of remote sensing  
and forest inventory data

**Dissertation**

(kumulativ)

zur Erlangung des akademischen Grades doctor rerum naturalium

(Dr. rer. nat.)

vorgelegt dem Rat der Chemisch-Geowissenschaftlichen Fakultät der  
Friedrich-Schiller-Universität Jena

von M. Sc. Mikhail Urbazaev

geboren am 21.02.1987 in Ulan-Ude, Russland

Gutachter:

1. Prof. Dr. Christiane Schmullius
2. PD Dr. Christian Thiel
3. Prof. Dr. Tuomas Häme

Tag der Verteidigung: 21.08.2019





*“To see the trees we need to get closer, whereas to see the forest we  
need to step back”*

(nach Liberman & Trope 2008: “The Psychology of Transcending the Here and Now “)



# Content

<b>CONTENT .....</b>	<b>VII</b>
<b>FIGURES .....</b>	<b>XI</b>
<b>TABLES.....</b>	<b>XVII</b>
<b>ABBREVIATIONS.....</b>	<b>XIX</b>
<b>ABSTRACT.....</b>	<b>XXIII</b>
<b>ZUSAMMENFASSUNG .....</b>	<b>XXVII</b>
<b>CHAPTER 1.....</b>	<b>1</b>
1 Introduction.....	1
1.1 Global carbon cycle and forest ecosystems.....	2
1.1.1 Climate change.....	3
1.1.2 Role of forests in climate change mitigation .....	5
1.1.3 Forest monitoring with in situ measurements.....	7
1.1.4 Importance of accurate carbon stock maps .....	11
1.2 Remote sensing of forest structure.....	14
1.2.1 Passive optical imagery for forest structure mapping .....	14
1.2.2 Synthetic Aperture Radar for forest structure mapping .....	17
1.2.3 LiDAR for forest structure mapping .....	26
1.2.4 Multi-sensor combination for forest structure mapping .....	30
1.2.5 Statistical models for forest structure mapping.....	32
1.3 Study area.....	36
1.4 Research objectives.....	39
<b>CHAPTER 2.....</b>	<b>41</b>

2	Improved Multi-Sensor Satellite-Based Aboveground Biomass Estimation by Selecting Temporally Stable Forest Inventory Plots Using NDVI Time Series.....	41
	Abstract.....	42
	2.1 Introduction .....	43
	2.2 Materials and Methods.....	47
	2.2.1 Study area.....	47
	2.2.2 Earth Observation Data .....	48
	2.2.3 INFyS Data.....	50
	2.2.4 Processing steps .....	51
	2.3 Results.....	55
	2.4 Discussion.....	60
	2.5 Conclusions.....	63
	<b>CHAPTER 3.....</b>	<b>65</b>
3	Estimation of forest aboveground biomass and uncertainties by integration of field measurements, airborne LiDAR, and SAR and optical satellite data in Mexico .....	65
	Abstract.....	66
	3.1 Background .....	67
	3.2 Methods.....	70
	3.2.1 Study area and field data.....	70
	3.2.2 Remote sensing data .....	71
	3.2.3 AGB modelling and uncertainty analysis .....	73
	3.2.4 Validation of mean forest AGB maps at different scales.....	78
	3.3 Results.....	80
	3.3.1 Estimation of AGB and uncertainties along the LiDAR strips .....	80
	3.3.2 Estimation of AGB and uncertainties at national scale with NFI- AGB as calibration data.....	82
	3.3.3 Estimation of AGB and uncertainties at national scale with LiDAR-AGB as calibration data .....	85
	3.3.4 Validation of forest AGB maps at different scales .....	90
	3.4 Discussion.....	93
	3.5 Conclusion.....	96
	<b>CHAPTER 4.....</b>	<b>99</b>
4	Potential of Multi-Temporal ALOS-2 PALSAR-2 ScanSAR Data for Vegetation Height Estimation in Tropical Forests of Mexico.....	99
	Abstract.....	100
	4.1 Introduction .....	101



*Content*

4.2	Material and Methods.....	104
4.2.1	Study area .....	104
4.2.2	Remote Sensing Data .....	106
4.2.3	Splitting Methods of Reference Data .....	107
4.2.4	Estimation of Vegetation Height from SAR Data.....	109
4.3	Results .....	111
4.3.1	Estimation of Vegetation Height from SAR Data.....	111
4.3.2	Impact of Number of L-Band Observations on Model’s Predictive Performance.....	115
4.3.3	Impact of Number of Samples on Model Prediction Performance .....	116
4.4	Discussion and Summary .....	118
4.5	Conclusion.....	120
	<b>CHAPTER 5.....</b>	<b>123</b>
5	Synthesis.....	123
5.1	Comparison with the existing national AGB maps .....	124
5.2	Summary.....	130
5.3	Outlook .....	133
	<b>REFERENCES .....</b>	<b>137</b>
	<b>MANUSCRIPT OVERVIEW.....</b>	<b>157</b>
	<b>STATEMENT OF AUTHORSHIP .....</b>	<b>163</b>



# Figures

Figure 1-1: Simplified schema of the global carbon cycle. Black numbers and arrows indicate carbon stock and fluxes estimated prior to the Industrial Era, circa 1750. Red numbers and arrows represent annual “anthropogenic” fluxes averaged over the 2000-2009 time period. Carbon stocks are in PgC; carbon fluxes are in PgC yr <sup>-1</sup> (Ciais et al. 2013) .....	3
Figure 1-2: Multiple indicators of a changing global climate system (Ciais et al. 2013).....	5
Figure 1-3: Propagation of errors in estimating the AGB from field measurements (Chave et al. 2004) .....	9
Figure 1-4: Relationships between field-measured DBH and aboveground dry biomass according to different allometric equations in tropical forests (Baccini et al. 2012).....	10
Figure 1-5: Illustration of complex sum of individual scatterer within a resolution cell (after Raney 1996) .....	19
Figure 1-6: Influence of topography in radar image (Lillesand et al. 2008).....	20
Figure 1-7: Scattering mechanism over forested areas: 1) backscatter from the crown (volume scattering), 2) direct backscatter from the trunks, 3) direct backscatter from the ground (single bounce), 4) crown-ground backscatter, and 5) trunk-ground backscatter (double bounce) (Leckie and Ranson 1996).....	21
Figure 1-8: An illuminated area by LiDAR and different number of returns depending on land cover (pulses A and B) (Jensen 2009) .....	27

Figure 1-9: Differences in recording of return signal between the full waveform and discrete return LiDAR systems (Lefsky et al. 2002b) .....28

Figure 1-10: Schematic representation of (a) linear parametric model and (b) non-parametric model (b) (James et al. 2015) .....34

Figure 1-11: (a) Land use and vegetation map of Mexico from the Mexican National Institute for Statistics and Geography (INEGI) Series IV (INEGI 2010). (b) Elevation in meters above sea level from the SRTM DEM.....37

Figure 2-1: Study areas. Forest type information provided by the Instituto Nacional de Estadística y Geografía (INEGI) landcover map series IV. ....48

Figure 2-2: AGB distribution over Campeche (left) and Comillas (right) study areas before (dark grey bars) and after BFAST-filtering (light grey).....51

Figure 2-3: Flow chart of the data processing and analysis steps.....52

Figure 2-4: Google Earth imagery from 2005 and 2011 over a field plot (red polygon) showing an example of abrupt changes (above) and corresponding BFAST plot (below) with NDVI values ( $Y_t$ ), and seasonal ( $St$ ), trend ( $Tt$ ) and noise ( $et$ ) components.....55

Figure 2-5:  $R^2$ , RMSE and bias between estimated and observed AGB using different reference data and predictor variables over Campeche (a) and Comillas (b) study areas. P: FBD and FBD PALSAR backscatter; M: PALSAR mosaic backscatter; CC: PALSAR interferometric coherence; TC: Landsat Tree Cover .....57

Figure 2-6: Comparisons of observed and predicted AGB estimates based on original (left) and BFAST-filtered (right) NFI data in Campeche study area. Dotted line is the 1:1 line.....58

Figure 2-7: Comparisons of observed and predicted AGB estimates based on original (left) and BFAST-filtered (right) NFI data in Comillas study area. Dotted line is the 1:1 line.....59

Figure 3-1: Land use and vegetation map of Mexico from the Mexican National Institute for Statistics and Geography (INEGI) Series IV (INEGI 2010) .....70

## Figures

Figure 3-2: INFyS sampling plot design for a) temperate and b) tropical forests.....	71
Figure 3-3: Flow chart of the data processing and analysis steps. Blue: first modelling scenario based on NFI data; red: second modelling scenario based on two-stage up-scaling method.....	74
Figure 3-4: Filtering steps of reference data (both NFI and LiDAR) for calibration of satellite imagery and validation of the AGB maps. ....	79
Figure 3-5: a) Linear regression between reference (INFyS) and predicted (LiDAR) AGB. The dotted line is the 1:1 line. b) CI 95 of LiDAR-estimated AGB increases with increasing reference AGB. c) The highest uncertainties of LiDAR-estimated AGB at low AGB range decreases with higher reference AGB.....	80
Figure 3-6: a) Histogram of field-estimated AGB used for calibration of LiDAR metrics; b) histogram of LiDAR-estimated AGB; c) histogram of uncertainties in LiDAR-estimated AGB .....	81
Figure 3-7: National forest AGB map based on NFI-estimated AGB, satellite imagery, Cubist machine learning algorithm, and Monte Carlo analyses.....	83
Figure 3-8: Estimated uncertainties (incl. error in field data and model prediction error) based on NFI-estimated AGB, satellite imagery, Cubist machine learning algorithm, and Monte Carlo analyses .....	84
Figure 3-9: a) Histogram of field-estimated AGB used for calibration of satellite imagery; b) histogram of estimated national forest AGB calibrated with field-AGB; c) histogram of uncertainties in AGB map calibrated with field-AGB.....	85
Figure 3-10: National forest AGB map based on LiDAR-estimated AGB, satellite imagery, Cubist machine learning algorithm, and Monte Carlo analyses.....	86
Figure 3-11: Estimated uncertainties (incl. error in field data, model prediction errors: NFI to LiDAR and LiDAR to satellite imagery) based on all LiDAR estimated AGB, satellite imagery, Cubist machine learning algorithm, and Monte Carlo analyses.....	87

Figure 3-12: National forest AGB map based on LiDAR-estimated AGB (with uncertainties <50%), satellite imagery, Cubist machine learning algorithm, and Monte Carlo analyses.....88

Figure 3-13: Estimated uncertainties (incl. error in field data, model prediction errors: NFI to LiDAR and LiDAR to satellite imagery) based on LiDAR-estimated AGB (with uncertainties <50%), satellite imagery, Cubist machine learning algorithm, and Monte Carlo analyses .....89

Figure 3-14: a) Histogram of estimated national forest AGB calibrated with all LiDAR-AGB pixels; b) histogram of estimated national forest AGB calibrated with LiDAR-AGB pixels with uncertainties <50%; c) histogram of uncertainties in AGB map calibrated with all LiDAR-AGB pixels; d) histogram of uncertainties in AGB map calibrated with LiDAR-AGB pixels with uncertainties <50%. .....90

Figure 3-15: Validation at pixel scale: field-estimated AGB plotted against a) NFI-calibrated AGB map, b) AGB map calibrated with all LiDAR-AGB pixels, c) AGB map calibrated with LiDAR-AGB\_50%. Dotted line is the 1:1 line. Blue to red colours indicate low to high point density, respectively. ....91

Figure 3-16: Validation at hexagon scale: field-estimated forest area weighted AGB plotted against a) NFI calibrated AGB map, b) AGB map calibrated with all LiDAR-AGB pixels, c) AGB map calibrated with LiDAR AGB\_50%. Dotted line is the 1:1 line. ....91

Figure 3-17: Validation at state scale: NFI- and LiDAR-calibrated AGB maps plotted against field-estimated forest area weighted AGB. Every point represents mean forest area weighted AGB for each federal state. Dotted line is the 1:1 line. ....92

Figure 3-18: Absolute difference between the NFI- and LiDAR-calibrated AGB map (based on all LiDAR-pixels). Zoom sections a) and b) illustrate different spatial patterns for dense tropical forests. ....94

Figure 4-1: Study area. Land use and vegetation map of Mexico from the Mexican National Institute for Statistics and Geography (INEGI) Series IV (INEGI 2010) with the available airborne LiDAR strips..... 105

*Figures*

Figure 4-2: Mean monthly air temperature (circles on the left-hand side) and total monthly precipitation (bars on the right-hand side) for three Mexican federal states for the years 2013–2017. Error bars represent monthly standard deviations.....105

Figure 4-3: Location of training and validation data using the “spatial sampling” approach of the LiDAR metric p100. Black stripes represent model training data; red stripes represent validation data. ....108

Figure 4-4: Histograms of LiDAR-based vegetation height data used for training and test using (a) “stratified random sampling” (i.e., based on value intervals while ignoring spatial location) and (b) “spatial sampling” (i.e., based on spatial location).....109

Figure 4-5: Acquisition dates of the ScanSAR mosaics with corresponding monthly precipitation for the three federal states from (SMN 2018).....110

Figure 4-6: ScanSAR (above) and FBD (bottom)-based vegetation height estimates plotted against LiDAR p100 metric. The training and test data were split using “stratified random sampling” (left) and “spatial sampling” (right). ScanSAR mosaics (24 scenes) show higher retrieval accuracy compared to FBD mosaics (3 scenes) due to a larger number of SAR images. The “stratified random sampling” approach shows higher goodness-of-fit statistics compared to the “spatial sampling” approach due to spatial autocorrelation between training and test data.....112

Figure 4-7: Vegetation height estimates based on ScanSAR (A) and FBD (B) mosaics using the “spatial sampling” approach. The difference map (C) between the two products depicts disagreements in areas with low (northern part) and tall trees (central and southern parts). The height values over the two red transects (A-B profile and C-D profile) are shown in Figure 4-8. White gaps in the ScanSAR-based vegetation height map resulted from the gaps in the ScanSAR backscatter mosaics.....113

Figure 4-8: Transects of the vegetation height of the three products over areas with small (upper profile) and tall trees (bottom profile). The upper image shows vegetation height for the transect A-B

in the northern part of the peninsula (Figure 4-7), while the bottom image shows vegetation height for the transect C-D in the central part of the peninsula (Figure 4-7). The FBD-based map overestimated height in areas with small vegetation and underestimated in areas with tall vegetation more noticeably compared to the ScanSAR-based map. For visualisation reasons, every 5 pixels from north to south was averaged..... 114

Figure 4-9: Impact of number of scenes on model prediction performance using “stratified random sampling” (left) and “spatial sampling” (right) for multi temporal Qeegan speckle-filtered data (“mtf”, white boxplots) and unfiltered ScanSAR data (“orig”, dark-grey boxplot)..... 116

Figure 4-10: Impact of sample quantity on model prediction performance using “stratified random sampling” (dark-grey boxplot) and “spatial sampling” (white boxplot). With an increasing number of training samples, the model performance increases continuously for “stratified random sampling” and saturates for “spatial sampling”. 1% of training data corresponds to 1000 1-ha samples..... 117

Figure 5-1: Distribution of the Mexican national forest AGB according to the six remote sensing based maps (Table 5-1) and the INFyS estimates. Non-forested areas were masked out using Landat Tree Cover product (Hansen et al. 2013) with a threshold of 10%. ..... 126

Figure 5-2: Comparison between the Mexican national AGB maps. The maps in the diagonals show single AGB maps at pixel spacing of 1 km. The maps outside the diagonal represent absolute AGB difference between the products. To calculate the absolute difference, a map in the row is the minuend and a map in the column is the subtrahend (e.g., Saatchi-Avitabile difference map represents Saatchi AGB minus Avitabile AGB). In the scatterplots between the single AGB maps the columns indicate the X-axes and the rows are the Y-axes. Non-forested areas were masked out using Landat Tree Cover product (Hansen et al. 2013) with a threshold of 10%. ..... 129



# Tables

Table 2-1: Earth observation data used in this study.....	49
Table 3-1: Remote sensing products used for AGB estimation at national scale.....	73
Table 4-1: Dataset used in the study .....	107
Table 5-1: Summary of Materials and Methods used for AGB estimation.....	124



# Abbreviations

ACD	Aboveground Carbon Density
AGB	Aboveground Biomass
AGC	Aboveground Carbon
ALOS	Advanced Land Observing Satellite
AMSR-E	Advanced Microwave Scanning Radiometer Earth Observing System
AVHRR	Advanced Very High Resolution Radiometer
AVNIR	Advanced Visible and Near Infrared Radiometer
BA	Basal Area
BFAS	Breaks for Additive Seasonal and Trends
C	Carbon
CH <sub>4</sub>	Methane
CO <sub>2</sub>	Carbon Dioxide
CART	Classification and Regression Trees
CI	Confidence Interval
CONAFOR	Comision Nacional Forestal
DBH	Diameter at Breast Height
DEM	Digital Elevation Model
DLR	German Aerospace Center
DOI	Digital Object Identifier
DR	Discrete Return
DUE	Data User Element
ENL	Equivalent Number of Looks
EnMAP	Environmental Mapping and Analysis Programme
ESA	European Space Agency
ETM+	Enhanced Thematic Mapper
FAO	Food and Agriculture Organization
FAPAR	Fraction of Absorbed Photosynthetically Active Radiation
FBD	Fine Beam Dual polarization
FBS	Fine Beam Single polarization

FIA	Forest Inventory and Analysis National Program
FLEX	Fluorescence Explorer
FRA	Forest Resources Assessment
FORMIND	Forest Model Individual-based
FW	Full Waveform
GEDI	Global Ecosystem Dynamics Investigation
GLAS	Geoscience Laser Altimeter System
G-LiHT	Goddard's LiDAR, Hyperspectral & Thermal Imager
GPP	Gross Primary Production
GSV	Growing Stock Volume
ICESat	Ice, Cloud and Land Elevation Satellite
INEGI	Instituto Nacional de Estadística y Geografía
INFyS	Inventario Nacional Forestal y de Suelos
InSAR	Interferometric SAR
IWCM	Interferometric Water Cloud Model
JAXA	Japan Aerospace Exploration Agency
LiDAR	Light Detection and Ranging
MCH	Mean Canopy Height
MODIS	Moderate Resolution Imaging Spectroradiometer
MOLI	Multi-footprint Observation Lidar and Imager
MS	Multi-Sensor
N <sub>2</sub> O	Nitrous Oxide
NASA	National Aeronautics and Space Administration
NDVI	Normalized Differenced Vegetation Index
NFI	National Forest Inventory
NISAR	NASA-ISRO Synthetic Aperture Radar
PALSAR	Phased Array type L-band Synthetic Aperture Radar
PolSAR	Polarimetric SAR
PolInSAR	Polarimetric Interferometric SAR
R <sup>2</sup>	coefficient of determination
RADAR	RAdio Detection And Ranging
REDD+	Reducing Emissions from Deforestation and Forest Degradation and enhancement of forest carbon stocks in developing countries
RF	Random Forests
RMSE	Root Mean Square Error
RSE	Relative Squared Error
RSS	Residual Sum of Squares
SAOCOM	Satelite Argentino de Observacion COm Microondas
SAR	Synthetic Aperture Radar
ScanSAR	Scanning Synthetic Aperture Radar
SLC	Single Look Complex
SMN	Servicio Meteorologico Nacional

## *Abbreviations*

SPOT	Satellite Pour l'Observation de la Terre
SR	Surface Reflectance
SRTM	Shuttle Radar Topography Mission
SWIR	Short Wave Infrared
TC	Tree Cover
TM	Thematic Mapper
TomoSAR	Tomographic SAR
UNFCCC	United Nation Framework Convention on Climate Change
VCF	Vegetation Continuous Fields
VHR	Very High Resolution
WCM	Water Cloud Model
WD	Wood Density



# Abstract

Covering one third of the land surface, global forests provide important ecosystem services for environment and society. Forests strongly affect the global climate system by influencing the energy, carbon and hydrological cycles. Forests are important for climate change mitigation by capturing a huge amount of atmospheric CO<sub>2</sub> that is comparable to the ocean carbon sink. Forests impact the water balance and protect the soil against erosion, avalanches and floods. Tropical forests play an important role for biodiversity, accommodating 50% of all animals and plant species. Therefore, preserving and enhancing global forests is an important step to react to climate change.

Being the main storage of aboveground terrestrial carbon, knowledge about the distribution, magnitude and dynamics of global forests improves our understanding of the global carbon cycle and their feedbacks with the global climate system. In situ measurements of forest structure parameters are limited in space and time. With rapid advances in information technology forest parameters can be estimated using remote sensing techniques. In particular, in tropical forests remote sensing data provide spatially consistent information for areas that are difficult to access. Accurate information on the forest carbon stocks supports the projection of future climate change through modelling. Spatially explicit estimates of forest carbon stocks assists policymakers by providing consistent baseline data over large areas to develop and monitor climate policies. Besides the science and policymakers communities, these data are of interest for industry due to their cost efficient way to map and monitor forest resources.

This work provides insights about the current opportunities and limitations associated with the use of remote sensing data to map forest structure at local, regional and national scales in Mexico. In particular, the impacts of multi-sensor and multi-temporal remote sensing data on retrieval accuracies of forest structure

parameters (i.e., aboveground biomass (AGB) and vegetation height) were examined. Moreover, the influence of the quality, amount and spatial distribution of reference data on model's predictive performance was investigated. To address these questions, remote sensing data acquired from optical and L-band Synthetic Aperture Radar (SAR) sensors were integrated with national forest inventory as well as with airborne Light Detection and Ranging (LiDAR) data by applying various modelling scenarios.

The results indicate that the multi-sensor combination of remote sensing data improves the retrieval accuracy of AGB by providing additional explanatory information. Furthermore, it was shown that outdated forest inventory plots can be detected automatically using Normalized Difference Vegetation Index (NDVI) time series and a change detection algorithm. By filtering out these outdated reference data, AGB could be estimated more accurately.

For forest AGB mapping at large scale, very high resolution (VHR) remote sensing data (optical or LiDAR at ~1 m) can be utilized as reference data to reduce the field data collection effort. VHR remote sensing data is an extremely valuable sampling tool for repetitive reference data acquisitions over large areas. Moreover, these data can provide measurements from areas that are difficult to access. However, it is important that errors contained in the VHR-based reference data are characterized in order to prevent propagation of errors in the wall-to-wall map. We showed that ignoring the field to VHR errors leads to high uncertainties (up to 150%) in the final classification result. The NFI- and LiDAR-calibrated national AGB maps feature similar goodness-of-fit statistics ( $R^2$  and RMSE) compared with an independent validation dataset as the two already published Mexican AGB maps. Furthermore, both produced maps show similar AGB statistics at federal state and at national level as national forest inventory data.

An increasing number of spatial predictors and training samples improves model's predictive performance of vegetation height. Using multi-temporal L-band SAR data it was possible to reduce over- and underestimation in sparse and dense forests, respectively. The prediction performance saturates, however, at a specific level (i.e., at 12 dual-polarised L-band backscatter measurements and at around 20% of all training samples), when no relevant extra information can be gained from the additional images and training samples.

The main limitation for the estimation of forest parameters in Mexico is the hilly terrain of the country. Local topography affects sampling of field data and hence, their quality, quantity and distribution. On the other side topography impacts the



signal scattered (or reflected) back to the sensors (SAR, optical and LiDAR). This limitation can be partly reduced by using high quality digital elevation models (DEM) and advanced terrain correction methods. A further issue in the forest AGB mapping in Mexico is the signal saturation and underestimation in high biomass ( $>100 \text{ tha}^{-1}$ ), even dense forests cover only a small part of the country. The limitation due to saturation effect can be partly solved by multi-temporal combination of SAR data.

Although satellite-based maps of forest structure parameters contain errors, in contrast to field data, they come with the advantage to better represent the relative distribution of forest parameters over large areas. Beside the spatial coverage, remote sensing offers unique opportunities for a repetitive mapping of forest parameters and thus, to assess their temporal dynamics. Bearing in mind new L-band missions in the near future (SAOCOM, NISAR, ALOS-4, potentially Tandem-L), the development of new algorithms based on dense time series of L-band backscatter are of high importance to map forest dynamics. An increasing number of optical, radar and LiDAR sensors in space and in the air (e.g., unmanned aerial vehicle), open opportunities to map forest parameters on an unprecedented spatial and temporal resolution with increased accuracies. These spatially explicit estimates on forest structure are of great interest for science, policy and industry and provide consistent baseline information for large scale monitoring.



# Zusammenfassung

Die globalen Wälder decken ein Drittel der Landfläche ab und bieten wichtige Ökosystemleistungen für Umwelt und Gesellschaft. Wälder wirken sich stark auf das globale Klimasystem aus, indem sie die Energie-, Kohlenstoff- und Wasserkreisläufe beeinflussen. Wälder sind wichtig für die Abschwächung des Klimawandels durch die Aufnahme von großen Mengen an CO<sub>2</sub> aus der Atmosphäre. Diese Mengen sind mit der Kohlenstoffsенke in den Ozeanen vergleichbar. Wälder beeinflussen den Wasserhaushalt, schützen den Boden vor Erosion, Lawinen und Überschwemmungen. Tropische Wälder spielen eine wichtige Rolle für die Biodiversität und beherbergen 50% aller Tiere und Pflanzenarten. Daher ist der Erhalt und die Förderung der globalen Waldfläche ein wichtiger Schritt, um dem Klimawandel entgegenzuwirken.

Die globalen Wälder sind Hauptspeicher von oberirdischem Kohlenstoff auf der Erde. Das Wissen über die Verteilung, das Ausmaß und die Dynamik globaler Wälder verbessert somit unser Verständnis des globalen Kohlenstoffkreislaufs und seiner Rückkopplungen mit dem globalen Klimasystem. In situ Messungen von Waldstrukturparametern sind räumlich und zeitlich begrenzt. Mit der rasanten Entwicklung in der Informationstechnologie können Waldparameter unter Verwendung von Fernerkundungstechniken abgeschätzt werden. Insbesondere in tropischen Wäldern liefern Fernerkundungsdaten räumlich konsistente Informationen für schwer zugängliche Gebiete. Akkurate Informationen über die Kohlenstoffbestände in Wäldern unterstützen die Modellierung des zukünftigen Klimas. Räumlich explizite Schätzungen der Kohlenstoffbestände in Wäldern unterstützen die politischen Entscheidungsträger durch Bereitstellung von konsistenten Basisinformationen über große Gebiete, um die klimarelevanten Programme zu entwickeln und zu überwachen. Neben der Wissenschaft und Politik

sind diese Daten auch für die Industrie von Interesse, da sie kostengünstige Methoden zur Kartierung und Überwachung von Waldressourcen darstellen.

Diese Arbeit liefert Einblicke in die aktuellen Möglichkeiten und Einschränkungen der Verwendung von Fernerkundungsdaten zur Kartierung der Waldstruktur auf lokaler, regionaler und nationaler Ebene in Mexiko. Insbesondere wurden die Auswirkungen von multisensorischen und multitemporalen Fernerkundungsdaten auf die Kartierungsgenauigkeit von Waldstrukturparametern (d.h., oberirdische Biomasse (AGB) und Vegetationshöhe) untersucht. Darüber hinaus wurde der Einfluss von Qualität, Anzahl und räumlicher Verteilung von Referenzdaten auf die Modellierungsgenauigkeit untersucht. Um diese Fragen zu beantworten, wurden optische und L-Band *Synthetic Aperture Radar* (SAR) Fernerkundungsdaten zusammen mit nationalen Waldinventurdaten sowie flugzeuggestützten *Light Detection and Ranging* (LiDAR) Daten unter Verwendung von verschiedene Modellierungsszenarien integriert.

Die Ergebnisse zeigen, dass die Multisensorkombination von Fernerkundungsdaten die Modellierungsgenauigkeit von AGB verbessert. Dies lässt sich durch die zusätzlichen Informationen von optischen und SAR-Sensoren erklären. Außerdem es wurde gezeigt, dass veraltete Waldinventurdaten mithilfe von Zeitreihen des *Normalized Difference Vegetation Index* (NDVI) automatisch detektiert werden können. Durch das Entfernen dieser veralteten Referenzdaten kann AGB genauer modelliert werden.

Für die Erfassung von Waldbiomasse über große Gebiete, können sehr hoch aufgelösten Fernerkundungsdaten (VHR) (optisch oder LiDAR von ~1 m) als Referenzdaten verwendet werden, um den Erfassungsaufwand von in situ Daten zu reduzieren. VHR-Fernerkundungsdaten stellen ein sehr wichtiges Werkzeug zur wiederholten Stichprobenentnahme von Referenzdaten über große Flächen dar. Weiterhin können diese Daten Referenzwerte aus schwer zugänglichen Gebieten liefern. Es ist jedoch wichtig, dass Fehler, die in den VHR-basierten Referenzdaten enthalten sind, charakterisiert werden, um die Fortpflanzung von Fehlern in der finalen Karte zu verhindern. Wir haben gezeigt, dass das Ignorieren von Fehlern, die sich von Feld in VHR-Daten fortpflanzen, zu hohen Unsicherheiten (bis zu 150%) in dem finalen Klassifizierungsergebnis führt. Die NFI- und LiDAR-kalibrierten nationalen AGB-Karten weisen im Vergleich zu unabhängigen Validierungsdatensätzen ähnliche statistische Modellgüte ( $R^2$  und RMSE) auf, wie die bereits veröffentlichten AGB-Karten in Mexiko. Weiterhin, zeigen die beiden

erstellten Karten eine ähnliche AGB-Statistik auf Landes- und Nationalebene wie die nationalen Waldinventurdaten.

Durch eine zunehmende Anzahl räumlicher Prädiktoren und Trainingsdaten verbessert sich die Modellierungsgenauigkeit für die Vegetationshöhe. Mit Hilfe von multitemporalen L-Band SAR-Daten konnten Über- und Unterschätzung in lichten bzw. dichten Wäldern reduziert werden. Die Kartierungsgenauigkeit sättigt jedoch auf einem bestimmten Niveau (d.h., bei 12 doppelt polarisierten L-Band Rückstreuintensitäten und bei etwa 20% aller Trainingsdaten), da aus den zusätzlichen Aufnahmen und Trainingsdaten keine weiteren relevanten Informationen gewonnen werden können.

Eine der wichtigsten Einschränkungen für die Abschätzung der Waldparameter in Mexiko ist das hügelige Gelände des Landes. Die lokale Topographie erschwert zum einen die Probenentnahme von Felddaten, d.h., die Qualität, Quantität und Verteilung von Felddaten kann beeinträchtigt werden. Andererseits beeinflusst die Topographie das Signal, das zurück zu Sensoren (SAR, optisch und LiDAR) gestreut (oder reflektiert) wird. Diese Auswirkung kann teilweise durch die Verwendung hochwertiger digitaler Höhenmodelle (DEM) und fortgeschrittener Methoden zur radiometrischen Geländekorrektur reduziert werden. Ein weiteres Problem der Waldbiomassekartierung in Mexiko stellt die Signalsättigung und Unterschätzung hoher Biomasse ( $> 100 \text{ t ha}^{-1}$ ) dar, selbst wenn die dichte Wälder nur einen kleinen Teil des Landes bedecken. Diese Unterschätzung kann zum Teil durch die Kombination multitemporalen SAR-Daten verringert werden.

Obwohl satellitenbasierte Karten von Waldstrukturparametern auch Fehler enthalten, weisen sie, im Gegensatz zu Felddaten, den Vorteil auf, die relative Verteilung der Waldparameter über große Flächen besser darzustellen. Neben der räumlichen Abdeckung bietet die Fernerkundung einzigartige Möglichkeiten die wiederholte Kartierung von Waldparametern und damit die Abschätzung ihrer zeitlichen Dynamik. Unter Berücksichtigung neuer L-Band-Missionen in naher Zukunft (SAOCOM, NISAR, ALOS-4, möglicherweise Tandem-L) ist die Entwicklung neuer Algorithmen, die auf dichten Zeitreihen der L-Band Rückstreuungsintensitäten basieren, für die Kartierung der Walddynamik von großer Bedeutung. Eine zunehmende Anzahl von optischen, Radar- und LiDAR-Sensoren im Weltraum und in der Luft (z. B. unbemanntes Luftfahrzeug) eröffnet die Möglichkeit, Waldparameter auf einer beispiellosen räumlichen und zeitlichen Skala mit hoher Genauigkeit zu kartieren. Diese räumlich expliziten Abschätzungen der Waldstruktur sind für Wissenschaft, Politik und Industrie von großem Interesse und liefern konsistente Basisdaten für das Monitoring über große Gebiete.



# Chapter 1

## **Introduction**

*Global carbon cycle and forest ecosystems*

*Remote sensing of forest structure*

*Study area*

*Research objectives and questions*

## 1.1 Global carbon cycle and forest ecosystems

The global carbon cycle is a biogeochemical cycle, which describes the exchanges of carbon (C) between the atmosphere, ocean and land. For a fundamental understanding of the global carbon cycle accurate estimates of C stocks in the three main pools (atmospheric, oceanic and terrestrial) and C fluxes between the pools are needed. In contrast to the oceanic and atmospheric carbon reservoirs, the terrestrial pool represents the most uncertain term in the global carbon balance (Houghton et al. 2009). Terrestrial and oceanic carbon reservoirs can act as carbon sinks (net uptake from the atmosphere) or sources (net emissions to the atmosphere).

The atmospheric C increase by ca.  $4.1 \pm 0.1 \text{ PgC yr}^{-1}$  (Pan et al. 2011) and the net uptake by oceans of ca.  $2.3 \pm 0.4 \text{ PgC yr}^{-1}$  (Pan et al. 2011) are relatively well known. In contrast, the land sink is more uncertain (Figure 1-1) and is usually calculated as the residual of anthropogenic emissions, the net land-use change flux and the sum of atmospheric and oceanic uptake. Furthermore, the location of the terrestrial sink is rather uncertain (Pan et al. 2011), i.e., the relative contributions of different forest ecosystems to the sink (Mitchard 2018). Based on millions of forest inventory data combined with statistical models, Pan et al. (2011) estimated carbon sources and sinks in boreal, temperate and tropical global forests for the time frame between 1990 and 2007. Global intact forests annually removed  $2.41 \pm 0.42 \text{ PgC yr}^{-1}$  from the atmosphere between 1990 and 2007, which is the same order of magnitude as the C-uptake by oceans. The tropical intact forests showed the highest C uptake rates of around  $1.19 \pm 0.41 \text{ PgC yr}^{-1}$  compared to  $0.5 \pm 0.08 \text{ PgC yr}^{-1}$  and  $0.72 \pm 0.08 \text{ PgC yr}^{-1}$  in boreal and temperate forests, respectively (Pan et al. 2011). In addition to the global intact forests, tropical regrowth forests absorb around  $1.64 \pm 0.52 \text{ PgC yr}^{-1}$  (Pan et al. 2011).

The main anthropogenic source of carbon into the atmosphere are the emissions from the use of fossil fuels and cement production (ranging from  $7.6 \pm 0.4 \text{ PgC yr}^{-1}$  (Pan et al. 2011) to  $7.8 \pm 0.6 \text{ PgC yr}^{-1}$  (Ciais et al. 2013) for the time frame between 2000 and 2009, causing around 85-90% of total annual human-induced carbon emissions) (Figure 1-1). Around 8-15% of total annual human-induced carbon emissions are from land-use change (e.g., tropical deforestation or forest degradation) (Houghton et al. 2015). Land-use change emission estimates range between 0.5 and  $3.5 \text{ PgC yr}^{-1}$  (Mitchard 2018). This wide range is primarily caused



by different methods used (i.e., forest inventory plots, atmospheric inversions, modelling) and a wide uncertainty of each method (Mitchard 2018).

Increasing CO<sub>2</sub> concentrations in the atmosphere since the last 50-60 years hamper the transmission of long-wave radiation from the Earth surface back to space and thus trap heat in the atmosphere and warm the Earth. In the next subsection the so called “greenhouse effect” will be described together with its consequences.

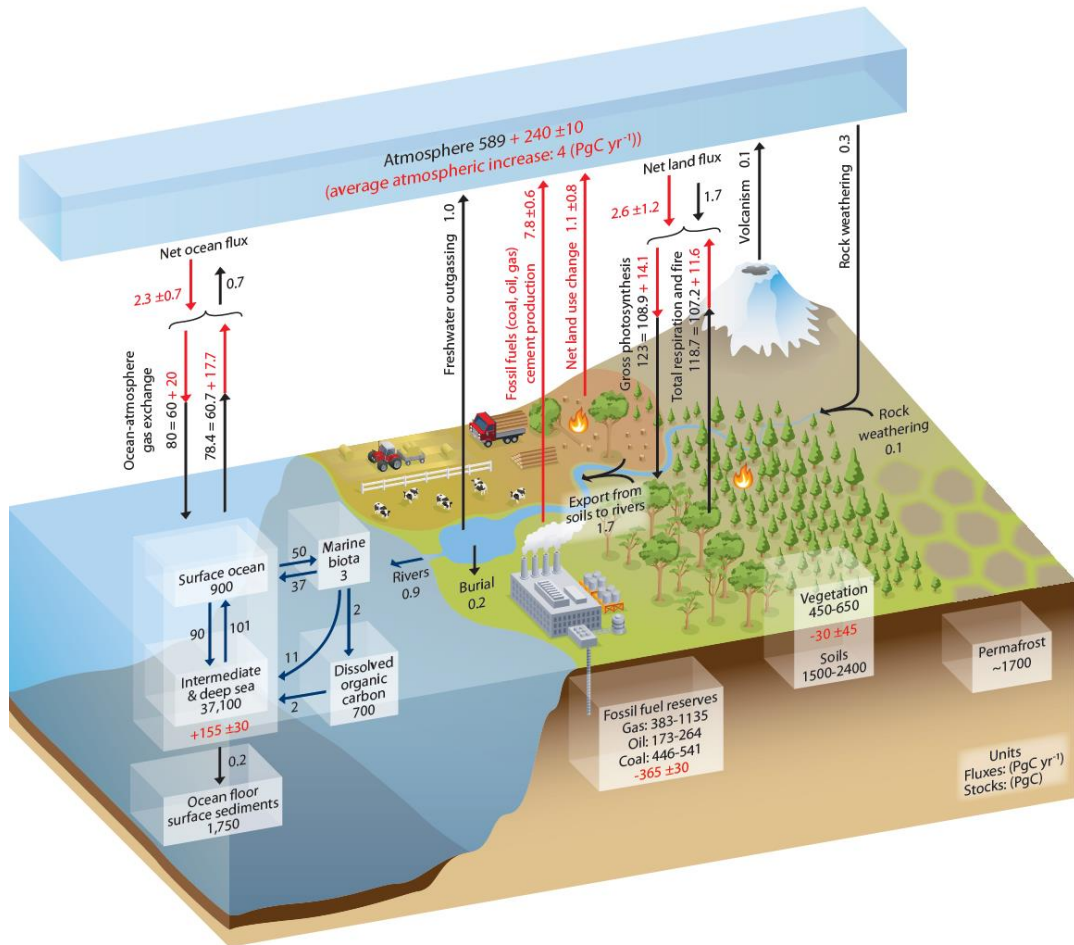


**Figure 1-1:** Simplified schema of the global carbon cycle. Black numbers and arrows indicate carbon stock and fluxes estimated prior to the Industrial Era, circa 1750. Red numbers and arrows represent annual “anthropogenic” fluxes averaged over the 2000-2009 time period. Carbon stocks are in PgC; carbon fluxes are in PgC yr<sup>-1</sup> (Ciais et al. 2013)

### 1.1.1 Climate change

The greenhouse effect is a natural process when water vapor, carbon dioxide (CO<sub>2</sub>), methane (CH<sub>4</sub>), nitrous oxide (N<sub>2</sub>O) and other gases absorb long-wave radiation emitted from the Earth surface and re-emit it partly back downwards

(towards the Earth surface) and thus, trap heat in the atmosphere and warm the Earth, creating ideal conditions for living organisms.

In the Earth's history, atmospheric CO<sub>2</sub> has reached several times 10-fold higher concentrations than today (i.e., greater than 3000 ppmv) (Chapin III et al. 2002). On the other side, atmospheric CO<sub>2</sub> concentrations have also been below 300 ppmv, partly in years of reduced volcanism (Pagani et al. 1999; Pearson and Palmer 2000). However, since the industrial time the intensive use of fossil fuels and land-use changes (i.e., deforestation and conversion to agricultural areas) lead to higher carbon emissions into the atmosphere, which strengthen the natural greenhouse effects. Based on high-resolution ice-core records, atmospheric CO<sub>2</sub> concentration has increased more rapidly during the past century than at any other time during the previous 20,000 years and probably the last 400,000 years (Petit et al. 1999).

As the result of enhancing atmospheric CO<sub>2</sub>, the Earth is warming and the climate is changing, which also leads to a continuously increasing number of climate-driven extreme events (i.e., flooding, droughts, wildfires, storms) (Reichstein et al. 2013). Changes in temperature, moisture and radiation (Figure 1-2) impact vegetation carbon uptake (e.g., photosynthesis) and release (e.g., respiration, mortality) (Chapin III et al. 2002). Elevated atmospheric CO<sub>2</sub> fosters photosynthesis, an effect called CO<sub>2</sub> fertilization (Sitch et al. 2008). However, since the plant growth is also water and nutrient limited, the overall effect of CO<sub>2</sub> fertilization on terrestrial carbon storage is probably smaller than that of reforestation (Chapin III et al. 2002). On the other side, increasing air temperatures boost respiration rates by plants and soils (Chapin III et al. 2002). Moreover, warming and droughts convert tropical peat forests to a net source of carbon (Hooijer et al. 2010; Page et al. 2011). An increased number of fires caused by climate change leads to forest degradation with direct C-emissions into the atmosphere (Mitchard 2018). Overall, changes in temperature and precipitation (Figure 1-2) together with an increasing number of extreme events will most probably convert global forests from a carbon sink to a large carbon source (Mitchard 2018). For instance, during warm and dry years (e.g., El Niño years in Indonesia) tropical forests become a net carbon source (Bonan 2008; Mitchard 2018).

At the same time, global forests influence climate and play a crucial role in mitigating climate change by their uptake of a huge amount of atmospheric CO<sub>2</sub> that is comparable to the carbon sink in global oceans (Pan et al. 2011). Therefore, preserving and enhancing global forest carbon stocks is an important step to react to

climate change. In the next subsection the role of global forests in climate change mitigation is discussed in detail.

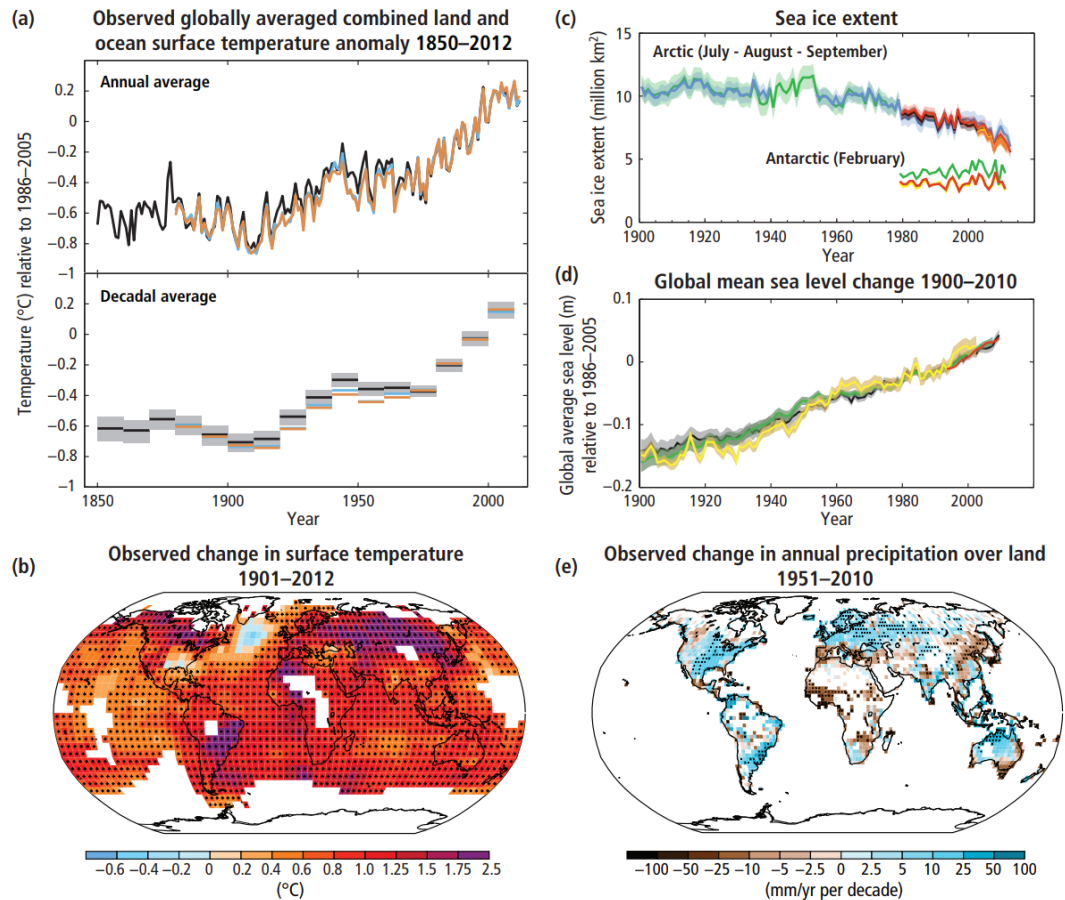


**Figure 1-2:** Multiple indicators of a changing global climate system (Ciais et al. 2013)

### 1.1.2 Role of forests in climate change mitigation

Covering 30% of the land surface (Bonan 2008), global forests strongly affect the global climate system by influencing the energy, carbon and hydrological cycles. Forests impact climate through biogeophysical processes (i.e., evapotranspiration and albedo), whereby evapotranspiration leads to cooling effects by increased cloud formation and precipitation in forest ecosystems. In contrast, the lower albedo of forests compared to e.g., snow-covered areas, pasture or sand, causes higher absorption of solar radiation leading to surface warming. Moreover, forests influence climate through biogeochemical processes (carbon cycle) through photosynthesis and respiration. Finally, forests as a main storage of aboveground terrestrial carbon, have an impact on climate through biogeographical processes (e.g., land use (change), vegetation dynamics and disturbances) (Bonan 2008). Ignoring the direct (i.e., land-use change) and indirect (i.e., climate change-driven) anthropogenic

impact on forests, at the global scale forests mitigate warming through evaporative cooling and carbon sequestration, these effects are however regionally different. For instance, tropical reforestation is likely to dampen global warming, while forest expansion in boreal areas amplifies global warming due to decreasing albedo (Bonan 2008).

Through photosynthesis global forests capture around  $123 \pm 8$  PgC yearly from the atmosphere (i.e., gross primary production) (Beer et al. 2010), but also release almost as high amounts back to the atmosphere due to plant and microbial respiration and decomposition (Mitchard 2018). The global vegetation stores around 450-650 PgC (Ciais et al. 2013) (Figure 1-1), which is more than half of the total carbon held in the atmosphere ( $\sim 829$  PgC) (Ciais et al. 2013). Although soils are the main terrestrial carbon storage (i.e., two to three times more carbon in soil than in forest biomass), the carbon in soil is physically and chemically protected (except peatlands) and contributes little to sources and sinks from land-use changes (Houghton 2005; Houghton et al. 2009). In contrast, carbon stored in forests is exposed to natural (storms, fires, pests) and anthropogenic (clear-cutting, selective logging) disturbances and thus, can be easier released to the atmosphere (Houghton et al. 2009). Moreover, large-scale deforestation does not only lead to the release of carbon stored in forest biomass, but it creates also warmer and drier local climates in deforested areas, e.g. pastures (Bonan 2008). Additionally, combustion of biomass alters atmospheric chemistry and aerosols (Bonan 2008).

Tropical intact and regrowth forests, being nowadays the most efficient carbon-capture method (Mitchard 2018), removed annually ca. 2.83 PgC from the atmosphere between 1990 and 2007, and thus account for around 70% of the global forest sink ( $4.05 \pm 0.67$  PgC yr<sup>-1</sup>) (Pan et al. 2011). The C-emissions due to land-use change range between 0.5 to 3.5 PgC yr<sup>-1</sup> depending on different methods (i.e., forest inventory plots, atmospheric inversions, modelling). Pan et al. (2011) estimated net (subtracting C uptake by regrowth forests) land-use change C-emissions to be  $1.3 \pm 0.7$  PgC yr<sup>-1</sup> for the years from 1990 to 2007 using forest inventory data combined with statistical models. Ciais et al. (2013) estimated C-emissions due to land-use change of about  $1.1 \pm 0.8$  PgC yr<sup>-1</sup>. One highly uncertain term in forest carbon fluxes are CO<sub>2</sub>-emissions from forest degradation. Since forest degradation, defined as a reduction of carbon stocks within forests without land-cover change (i.e., forest remains forest), occurs at small scales (e.g., selective logging), CO<sub>2</sub>-emissions from forest degradation are difficult to assess and usually underestimated (Baccini et al. 2017; Pearson et al. 2017). Using time series of pan-tropical aboveground carbon

density maps between 2003 and 2014, Baccini et al. (2017) estimated C-emissions from forest degradation to be 68.9% of total carbon losses from deforestation and forest degradation ( $861.7 \pm 80 \text{ TgC yr}^{-1}$ ). Pearson et al. (2017) estimated contribution of forest degradation to total carbon losses to be 25% for tropical countries, whereas in 28 of 74 countries the C-emissions from forest degradation exceeded those from deforestation.

Although a key element to stabilize atmospheric CO<sub>2</sub> is reducing emissions due to fossil fuel burning (Van der Werf et al. 2009), which account for around 85-90% of total anthropogenic CO<sub>2</sub>-emissions (Ciais et al. 2013; Pan et al. 2011), forest conservation and enhancement of forest carbon stocks could create a large land sink and probably help to keep the global temperature increase below 2°C (Mitchard 2018). A study of Houghton et al. (2015) indicated that stopping tropical deforestation and forest degradation and enhancing carbon stocks could generate a terrestrial C-sink of 5 PgC yr<sup>-1</sup> and thus, might offset C-emissions from fossil fuels to a large extent. This potential C-sink (5 PgC yr<sup>-1</sup>) of tropical forests consists of around 1 PgC yr<sup>-1</sup> otherwise emitted due to deforestation and forest degradation (in some studies this estimate is twice that amount), C-uptake by secondary forests of around 3 PgC yr<sup>-1</sup>, and finally, reforestation activities removing another 1 PgC yr<sup>-1</sup> from the atmosphere (Houghton et al. 2015). Moreover, vegetated areas in temperate zones (forests, agriculture, grassland and wetlands) could capture additional carbon from the atmosphere through sustainable management strategies. Sustainable management strategies are also of particular importance to reduce C-emissions from permafrost thawing in arctic and boreal zones (Houghton et al. 2015).

Forests are not only important for climate change mitigation due to their sequestration of atmospheric CO<sub>2</sub>, forests also provide important ecosystem services for both environment and society. For instance, forests impact the water balance, protect the soil against erosion, avalanches and floods. Furthermore, tropical forests plays an important role for biodiversity, accommodating 50% of all animals and plant species.

### **1.1.3 Forest monitoring with in situ measurements**

The status of forests and their temporal dynamics can be assessed and monitored by measuring and estimating different tree structure parameters (e.g., tree height, tree canopy cover, stem volume and aboveground biomass (AGB)). Tree biomass can be measured directly using a destructive method, i.e., tree harvesting, oven drying and weighing of all tree compartments. Although this method is direct and

most accurate, it is also most time and cost consuming, destructive and not applicable for monitoring. Alternatively, mathematical (allometric) equations can be developed based on allometric relationships between tree parameters that can be easily measured in situ (e.g., tree height and tree diameter at breast height) and weighed dried biomass. Thus, using allometric equations, the biomass of single trees can be estimated. Usually, biomass allometric equations are based on information about trunk diameter, tree height, wood specific gravity and forest type (e.g., dry, moist or wet) (Chave et al. 2005). In boreal and temperate forests, where a small number of tree species dominates, species-specific allometric equations for AGB estimation can be applied. In contrast, in tropical forests, where as many as 300 different tree species within a 1 ha plot can occur, species-specific allometric equations are difficult to apply, so that generalized allometric equations for mixed tropical vegetation have been developed. For instance, Brown (1997) developed generalized allometric equations for tropical areas based on an analysis of 371 harvested trees with a diameter at breast height (DBH) ranging from 5 to 148 cm from all three tropical regions (i.e., South America, Africa and Asia). The allometric equations were generated for three forest types: dry (<1500 mm rain/year), moist (1500-4000 mm rain/year) and wet (>4000 mm rain/year). However, these rainfall regimes should be applied to lowland conditions only. The developed equations describe the relationships between DBH and basal area (BA) and AGB (Brown 1997). The use of allometric equations that are based only on one forest parameter (e.g., DBH or BA) simplifies the estimation of AGB and is the only option in regions where measurement of tree height is difficult in closed-canopy forests. However, including wood specific gravity and tree height leads to an important improvement for AGB estimation models, as reported in Chave et al. (2005) and Feldpausch et al. (2012). Chave et al. (2005) analysed a large dataset of 2,410 trees (DBH ≥ 5 cm) directly harvested since the 1950s in 27 study sites across the tropics ranging from dry woodlands to very humid closed-canopy forests, from highly seasonal to aseasonal climates, lowland to high-elevation forests, and secondary to old-growth forests, to develop generalized equations for tropical areas. In this study, the authors determined the importance of the tree parameters for the AGB estimation. The most important predictive variables, in decreasing order of significance, are tree trunk diameter, wood specific gravity, total height, and forest type (Chave et al. 2005).

Since allometric models are applied to estimate biomass, these estimates include errors of different origins. The errors in field-estimated AGB can have four types of

sources (Figure 1-3): (1) measurement error; (2) error due to the choice of an allometric model relating AGB to other measured variables; (3) sampling uncertainty related to the size of the study plot; (4) representativeness of a network of small plots across a vast forest landscape (Chave et al. 2004). These four types of errors add up and need to be quantified to provide estimates of biomass with corresponding uncertainties, which are useful for further analyses (e.g., carbon accounting and reporting, calibration of remote sensing data etc.). It is recommendable to establish large sample plots (e.g., greater than 0.25 - 0.5 ha) (Chave et al. 2004; Houghton 2005), since (1) tree-level errors average out in large plots (Chave et al. 2004), (2) a small plot can either include or not include a large tree, which can lead either to over- or underestimation of biomass (Houghton 2005). Furthermore, the AGB of large trees should be estimated especially carefully, if their diameter is bigger than the range of tree diameters for which the allometric equations were developed (Chave et al. 2004). The errors in field estimated biomass are larger in the tropical forests than in boreal and temperate forests, due to a much smaller number of inventory plots, larger spatial variability and greater number of tree species (Clark et al. 2001).

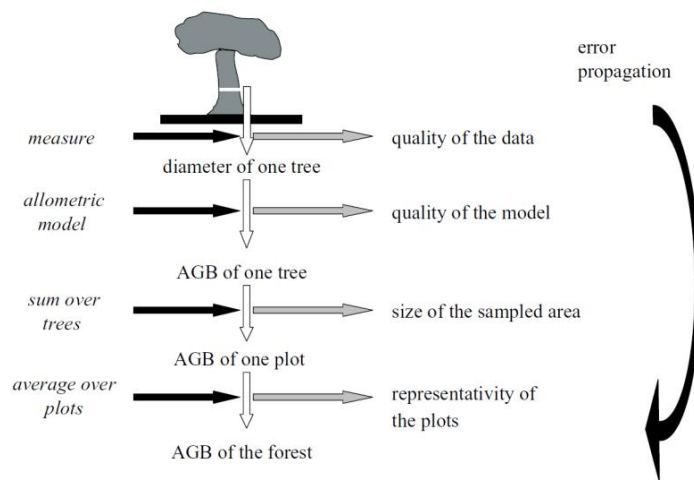


**Figure 1-3:** Propagation of errors in estimating the AGB from field measurements (Chave et al. 2004)

The most important source of error is related to the choice of the allometric model (Chave et al. 2004). Figure 1-4 illustrates the variance of AGB estimates using different allometric equations for tropical areas (Baccini et al. 2012). For instance, a single tree in wet forests with a DBH of 60 cm can have a biomass ranging between 2.5 Mg (“Chave (2005)-Wet-Forest” equation) and 10 Mg (“Higuchi-Wet” equation) depending on the applied allometric equation.

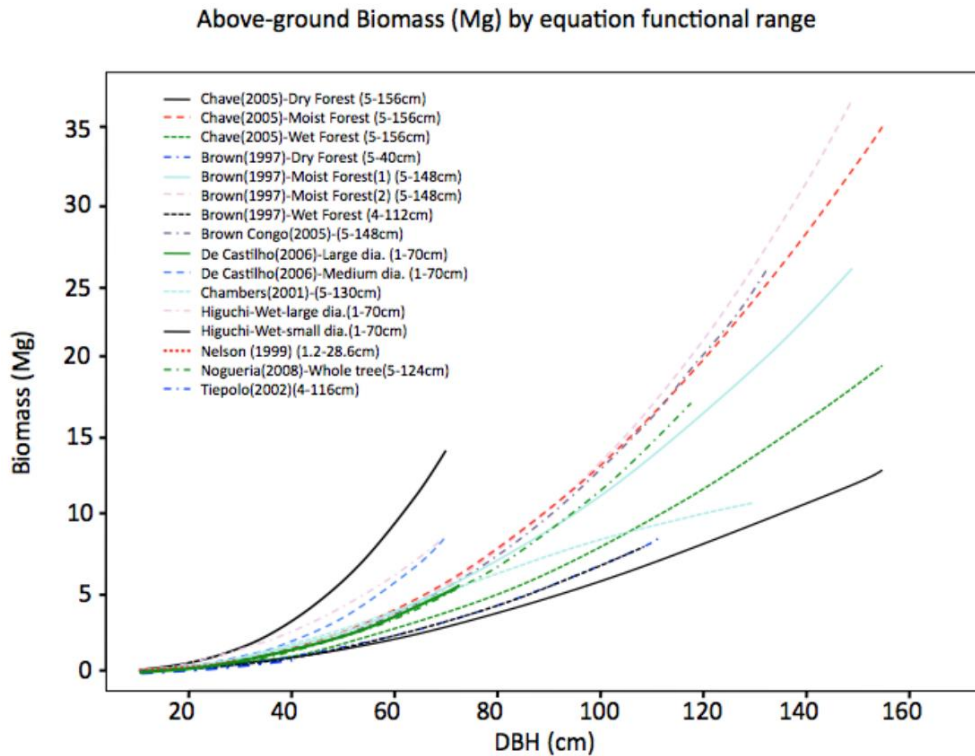


**Figure 1-4:** Relationships between field-measured DBH and aboveground dry biomass according to different allometric equations in tropical forests (Baccini et al. 2012)

Changes in forest carbon stocks (e.g., due to forest degradation or regrowth) can be assessed in the field by revisiting such inventory plots, e.g., every five years. Since only a limited number of plots can be established, these estimates are restricted in time and space with some areas completely undersampled (e.g., due to geographical and political reasons). Furthermore, the capacity of a tropical country to measure their forest and carbon dynamics varies from country to country. For instance, 14 African countries have reported the same annual change in forest area every year from 1990 to 2015 to the Food and Agriculture Organization (FAO) (FAO 2015; Mitchard 2018), while other datasets (based on remote sensing data) have detected significant changes in rates of loss over time (Achard et al. 2014).

Nevertheless, high quality in situ data are the crucial component to assess carbon stocks and fluxes at local, regional and global scales. To provide wall-to-wall estimates of carbon stocks using remote sensing, in situ data are needed to understand the physics of a remote sensing signal, to calibrate this signal and to assess the accuracy of the generated map. Moreover, in situ data can contain much more information than AGB (i.e., tree species, mortality, litter fall, root dynamics, belowground biomass), which are needed for other ecological studies (e.g., soil



science). In addition, permanent forest plots provide a baseline information for scientists and policymakers to understand forest dynamics (Feldpausch et al. 2012).

#### **1.1.4 Importance of accurate carbon stock maps**

Measurements and estimation of forest structure parameters in the field are associated with high costs (e.g., labour intensive and time consuming). Field data are restricted to point measurements and can cover only a small part of heterogeneous tropical forests. This leads to a limited and possibly biased information on forest carbon stocks (Houghton et al. 2009), since average values (from in situ measurements) can be significantly different from spatially explicit estimates (from satellite measurements). Therefore, our knowledge about the distribution, magnitude and dynamics of global forest carbon stocks is poor (Houghton et al. 2009; Mitchard 2018). Recent advances in remote sensing techniques have enabled the derivation of forest parameters from space. In particular in tropical forests, where only limited and unevenly distributed field data are available, remote sensing data are an important source of information, providing spatially consistent biomass estimates for areas that are difficult to access.

Spatially explicit and detailed estimates of forest carbon stocks will improve our understanding of the global carbon cycle by providing accurate information on the distribution and dynamics of the terrestrial carbon pools and their feedbacks with the global climate system (Houghton 2005; Houghton et al. 2009). Such data support the projection of future climate change through modelling (Le Quéré et al. 2017), e.g., more accurate modelling of interactions between tropical forests and climate fluctuations and disturbance events (Mitchard 2018). In addition to the science community, spatially explicit estimates of forest carbon stocks support policymakers by providing consistent baseline data over large areas to develop and monitor climate policies. Accurate carbon stock maps can then be used for reporting carbon emissions to the United Nations Framework Convention on Climate Change (UNFCCC) (e.g., in the Reducing Emissions from Deforestation and Forest Degradation (REDD+) programme) at fine spatial scale. Although satellite-based maps of forest structure parameters also contain errors, in contrast to field data, they come with the advantage that they better represent the relative distribution of forest parameters over large areas. Therefore, satellite-based products can be used for forest stratification analyses, i.e., to improve sampling strategies of field data by reducing cost and increasing representativeness of them. Furthermore, remote sensing based maps can support land use planning by identifying and prioritizing specific areas, e.g., for biodiversity conservations (Hese et al. 2005) or where changes

in land use would minimize carbon emissions (Houghton et al. 2009). Besides the science and policymakers communities, these data are of interest for industry as well due to their cost efficient way (in time and space) to map and monitor forest resources.

Although the assessment of aboveground biomass provides a very important baseline information for understanding the global carbon cycle, monitoring the change in carbon stocks is even more important for carbon science (Houghton et al. 2009). The changes of forest carbon stocks result from three main processes: (1) short term changes due to land use and management change (e.g., conversion of forested to an agricultural area); (2) short term changes due to natural disturbances (e.g., insect outbreak, storm damage, forest fire); (3) long term changes driven by interannual variability (e.g., temperature, precipitation, droughts) that affect rates of photosynthesis, growth, respiration etc. (Houghton et al. 2009). Field and eddy flux measurements in general can capture the third process (i.e., long-term changes) only, since they are limited in space. Short-term changes at fine scale, such as deforestation and forest degradation, or the impact of droughts and fire, usually cannot be covered by field measurements (including eddy flux measurements) (Mitchard 2018). The sum of these small-scale changes largely contributes to the total uncertainty of net sources and sinks of terrestrial carbon stocks (Houghton et al. 2009), which is the largest source of uncertainty in the global carbon budget (Section 1.1). For instance, Baccini et al. (2017) used time series of satellite-based aboveground carbon stock maps and reported that degradation and disturbance account for 69% of total carbon losses in the entire tropics, and for 70%, 81%, 46% of total carbon losses across tropical America, Africa, and Asia, respectively. These results indicated that tropical forests might even be a net carbon source (emitting  $0.425 \text{ PgC yr}^{-1}$ ), where carbon losses exceed carbon gains (Baccini et al. 2017).

Satellite observations are able to monitor long term vegetation trends (De Jong et al. 2013; Forkel et al. 2013) as well as short term changes such as deforestation (Hansen et al. 2013) and disturbances (Curtis et al. 2018; Hermosilla et al. 2015). However, the remote sensing signal over forests results from complex interactions between the electromagnetic wave, object geometry and local environmental conditions. To better understand the remote sensing signal and thus, to generate more accurate models based on it, field observations are required. Therefore, an integration of high quality field data with remote sensing data can generate more accurate assessments of aboveground carbon stocks and dynamics than either approach alone (Goetz and Dubayah 2011). In situ data are needed to assess the

accuracy of the satellite-based product. For instance, an uncertainty of 50% for carbon stock estimates translates to an uncertainty of about 80% for carbon flux estimates (Houghton 2005). In the next Section, the mechanisms of remote sensing technologies and their potential to assess forest structure parameters are presented.

## 1.2 Remote sensing of forest structure

Remote sensing methods offer a unique opportunity to generate spatially continuous maps over large areas that are partly not accessible. Remote sensing instruments measure electromagnetic radiation reflected from an object and use this information to characterize the Earth's surface. Remote sensing sensors can be divided into passive and active instruments. Passive instruments measure reflected electromagnetic radiation by the Earth and thus, can be used during the day-time only. In contrast, the active sensors send energy out and measure reflected (backscattered) energy received at the sensor. The received energy at the sensor can be measured at different portion of electromagnetic spectrum (from visible light to microwaves). Therefore, instruments can be further subdivided regarding the measured part of electromagnetic spectrum, e.g., optical and radar sensors.

In following subsections the description of functionality of optical (passive visible and infrared spectrums), radar (active microwaves) and LiDAR (active near-infrared spectrum) sensors in relation to vegetation monitoring is introduced. Further a synergetic usage of the sensors is discussed, since each sensor measures different properties of a target. Finally, statistical models that relates remote sensing measurements to in situ observations are presented.

### 1.2.1 Passive optical imagery for forest structure mapping

Passive optical remote sensing sensors (e.g., Landsat, MODIS, Sentinel-2, etc.) measure electromagnetic radiation reflected by the Earth in visible, near- and middle-infrared parts of electromagnetic spectrum between 0.4  $\mu\text{m}$  and 2.5  $\mu\text{m}$  (Jensen 2007). Different surfaces (e.g., sand, vegetation, water) possess specific spectral characteristics (i.e. spectral signature) allowing to use this information for classification purposes. Vegetation has low reflectance in the visible electromagnetic spectrum due to chlorophyll absorption, a high reflectance in the near-infrared region (Gates et al. 1965) as well as drops in reflectance in middle-infrared due to leaf water absorption (Jensen 2007). Spectral signatures of vegetation vary according to vegetation type (e.g., grassland, agriculture, forest), growth stage, leaf type, etc. Using this specific spectral signature, it is therefore possible to derive information on vegetation type, health and moisture content.

Optical data have been widely investigated to find relationships between optical reflectance of Earth's surface and vegetation parameters (e.g., canopy cover, AGB,

LAI). In general, optical data are partly appropriate for AGB estimation in global forests. The spectral signature of vegetation depends on vegetation density as reflectance decreases in visible and in near- and middle-infrared channels with an increasing crown cover (Wulder and Franklin 2003). Vegetation density relates to AGB and saturates at high biomass values (Huete et al. 1997; Huete et al. 2002). The channels most correlated with vegetation density are near- and middle-infrared channels (e.g., Landsat channel 4, 5 and 7) (Avitabile et al. 2012; Foody et al. 2001; Steininger 2000). Since the optical datasets represent two dimensions of the land surface and less relate to vertical vegetation structure, they possess limitations in the AGB estimation. The main disadvantages in using of optical data for AGB estimation are a high cloud cover rate over tropics, strong dependence on environmental, seasonal and acquisition conditions (e.g., solar zenith angle) as well as signal saturation over dense forests (Avitabile et al. 2012). To solve the problem due to cloud cover, the optical data at coarse spatial resolution (e.g., >500 m (MODIS-like)) with a high temporal repetition rate can be used. However, the use of these types of sensors restricts to provide high spatial details. Since the relationships between spectral reflectance and vegetation structure parameters vary from site to site, development of the site-specific method for AGB mapping is required. Non-parametric classifiers (e.g., artificial neural network, Random Forest) were identified to be able to describe non-linear relationship between spectral information and AGB estimates (Avitabile et al. 2012; Foody et al. 2001). For instance, Foody et al. (2001) compared AGB mapping performance using 230 vegetation indices calculated from Landsat TM imagery and three types of neural networks over Bornean tropical rain forests. The results show that each of the three investigated neural networks exhibits a higher correlation to AGB as each of the 230 vegetation indices, indicating restrictions of vegetation indices for AGB modeling. A reason for this is that vegetation indices are mostly based on two or three spectral channels, while the neural networks use all six Landsat spectral wavebands.

In the 90s and early 2000s usually only single optical imagery was used to map forest structure parameters, due to restricted data access. As a result, the relationships between spectral reflectance of individual bands and forest structure parameters were highly variable and instable due to influence of environmental conditions (e.g., rain event) and phenological state. For instance, Steininger (2000) found strong correlation between the middle-infrared Landsat TM channel and AGB in Brazilian secondary forests with a correlation coefficient between 0.71 and 0.85. In contrast, no correlation was observed in the Bolivian secondary forests between Landsat TM channels and AGB (R ranging between 0.03 and 0.4). Significant

differences in the results between the two study areas are probably caused by a low solar zenith angle during the data acquisition over Bolivia. Another reason could be a difference in the development of regrowth canopy structure between the two areas, so that a relationship between canopy infrared reflectance and stand variables (e.g., AGB) is not valid for regrowth areas in the Bolivian study site (Steininger 2000).

Open data policy of optical Earth observation satellites (e.g., Landsat and MODIS) has revolutionised the use of these data for scientific investigations, enabling to gain their full value (Wulder et al. 2012). A 100-fold increase of Landsat data use from 2001 (25,000 images) to 2010 (2.5 million images) (Wulder et al. 2012) together with advanced computational power lead to a rapid increase in the development of new algorithms. Time series of optical data can be used to generate annual cloud-free spectral reflectance and vegetation indices (e.g., maximum, minimum, mean annual NDVI) that is less impacted by environmental conditions, providing more robust results over large areas. Furthermore, with advanced time series analysis (e.g., Kennedy et al. 2010) every Landsat pixel can be tracked through time (e.g., disturbance, regrowth) that can help to reconstruct forests carbon dynamics (Pflugmacher et al. 2012). Moreover, more open data (e.g., from Sentinel-2) - additionally to the existing programs - foster development of multi-sensor fusion techniques to increase the number of cloud-free observations and to monitor forests at different phenological stages.

Hyperspectral optical data (e.g., >50 spectral channels) can be applied to map tree species as well as biochemical status of the forests, which can further improve the sensitivity to forest structure (Koch 2010). However, since hyperspectral sensors are usually operated from an aerial platform, they are restricted to a small study site. In the near future, the launch of spaceborne hyperspectral sensors (DLR EnMAP, ESA FLEX) will provide new insights for forest structure mapping at large scale with hyperspectral information. Similar to hyperspectral data, very high spatial resolution imagery (~1 m spatial resolution) (e.g., WorldView) possess strong correlation to canopy cover and vegetation density (single trees and gaps between them can be identified), however, they are also limited in spatial coverage.

The main advantages of optical data for forest structure mapping are: a) free data at high and moderate spatial resolutions (e.g., Landsats, Sentinel-2, MODIS), b) long time series (back to 70s-80s with Landsats and AVHRR), c) sensitivity to photosynthetic active vegetation and time series of the corresponding products (NDVI, fAPAR, GPP). The recent large-scale studies for AGB estimation that are based on optical sensors (Saatchi et al. 2011; Baccini et al. 2012; Matasci et al.

2018b) used a fusion of time-series of Landsat or MODIS data with airborne and spaceborne LiDAR. The potential of multi-sensoral combination for forest structure mapping is discussed in Section 1.2.4.

### **1.2.2 Synthetic Aperture Radar for forest structure mapping**

Alternatively to the optical remote sensing, so called **RA**dio **D**etection **A**nd **R**anging (RADAR) sensors, which operate in microwave domain with a spectral range between 1 mm and 1 m, can be used to obtain information about forest structure. Due to longer wavelengths, microwaves have the capability to penetrate into vegetation, and thus to probe the three-dimensional vegetation structure. Furthermore, microwaves are particularly useful for weather independent applications, since long electromagnetic waves can penetrate clouds.

Active radars transmit a microwave signal, illuminate a target and measure the return energy. The received backscattered signal can be recorded in form of magnitude and phase measurements. The magnitude measurement (backscatter intensity) describes the strength of the return signal and is determined by the geometrical and electrical properties of the reflective material, as well as by the frequency, polarisation and angle of incidence of the emitted wave (Raney 1996). Electrical properties of a reflective material can be measured with dielectric constant, ability of a material to conduct electrical energy. Dielectric constant is mostly determined by moisture content and is high for wet and low for dry surfaces, respectively. For instance, wet soils (high dielectric constant) conduct and scatter back more electrical energy (i.e., high backscatter) than dry soils, which absorb more energy and scatter back a lower amount of energy (i.e., low backscatter). Furthermore, moisture content determines penetration depth of the incident microwaves. Generally, penetration depth of a microwave is in order of the size of emitted wave, however, in extremely dry soils a microwave can penetrate several meters (Jensen 2007). Seen from imaging radar surface roughness is connected to the wavelengths and incidence angle of the emitted wave. Surface appears “smoother” for microwaves with increasing wavelengths and increasing incidence angle (Jensen 2007). The interaction of the emitted wave with the objects on the ground is determined by their size and shape. For instance, short microwaves (3-5 cm) interact primarily with objects in order of the size of the wavelength (i.e., with objects equal or greater than 3 5 cm: tree leaves and small branches). Since long microwaves (20-70 cm) are sensitive to large objects (e.g., tree trunk) and can penetrate deeper into the forests than short waves, they are more suitable for forestry applications (e.g., mapping of forest cover and forest structure) (Le Toan et al. 1992; Saatchi et al.

2011b). The polarisation of the microwave also affects the backscatter mechanisms of vegetated areas. The interaction of vertically polarised waves is generally higher for objects with vertically oriented elements (branches, trunks) and horizontally polarised waves with horizontally oriented objects (leaves, twigs) (Leckie and Ranson 1996). The cross-polarised (HV or VH) waves are more sensitive to volume scattering (e.g., as occurring within woody canopies) and less affected by surface properties (e.g., soil moisture) as opposed to co-polarised (HH or VV) waves (Le Toan et al. 1992; Rauste et al. 1994; Saatchi and Moghaddam 2000).

A radar phase describes the oscillation of electromagnetic waves and measures the phase angle of returned signal. By comparing two radar phases acquired from slightly different positions over the same area, the phase difference can be calculated, with which the elevation of the target can be determined, a remote sensing technique that is called SAR interferometry. Ideally, two radar imagery should be acquired simultaneously in order to eliminate the temporal decorrelation between them. Strong temporal decorrelation caused by changes on the surface between the acquisitions (e.g., moisture conditions, location and orientation of a target) can reduce the quality of an interferogram and the corresponding elevation product. Furthermore, from an interferogram an interferometric coherence can be calculated that describes the correlation between the two complex radar imagery with values ranging between 0 (no correlation) and 1 (strong correlation). Since different land cover classes exhibit various degree of “stability” between two acquisitions, interferometric coherence can be used for classification of the Earth surface (Grey and Luckman 2003; Luckman et al. 2000; Wagner et al. 2003). For instance, urban areas do not change as fast as vegetated areas over time and thus, possess a higher coherence value. Similarly, with an increasing vegetation density forested areas become more variable (caused due to slightly changing position and orientation of branches) and interferometric coherence decreases. Therefore, interferometric coherence is sensitive to vegetation density and can be used for AGB estimation (e.g., Askne and Santoro 2005; Wagner et al. 2003).

Since the wavelength of the emitted signal is usually much smaller than the resolution cell, many scatterers within this cell are present. In Figure 1-5 each arrow represents backscattered signal of individual scatterer within a resolution cell. The total backscattered signal of a resolution cell originates from the vector addition of the individual scatterers with changing magnitude and phase. Even if individual scatterers would have the same magnitude, they will possess different phase due to slightly different distance to sensor. For this reason the backscattered signals from



neighbouring cells appear brighter or darker, resulting in a noise like effect called speckle. In most applications, speckle is considered as a disturbing noise, since the changes in backscatter measurements are caused not by surface variability.

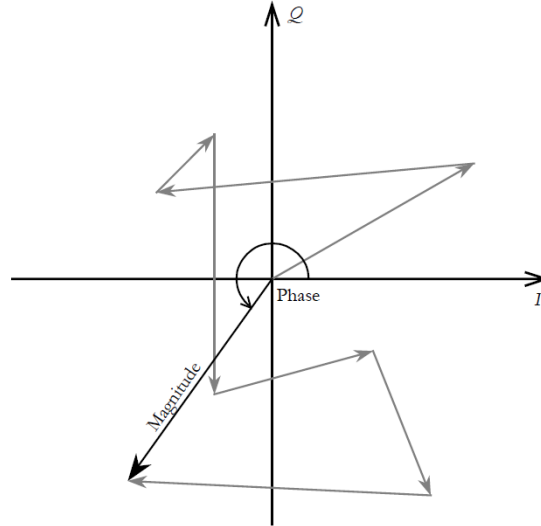


**Figure 1-5:** Illustration of complex sum of individual scatterer within a resolution cell (after Raney 1996)

To reduce speckle, either spatial (from the neighbouring cells) or temporal (from the time series) information can be used. Classical speckle filters (e.g., Lee, Frost) apply a moving window approach and calculate local statistics to homogenise a single cell according to its neighbours. This type of speckle filters are fast, easy to use, they are implemented in common remote sensing software (e.g., ENVI, Erdas, SNAP etc.), and do not require multi-temporal imagery. However, since a moving window approach is applied, the spatial details are reduced. Nowadays, with availability of dense SAR time series, multi-temporal speckle filters are being developed (e.g., Cremer et al. 2018; Lê et al. 2014). This type of speckle filters use temporal information and thus, spatial details are fully preserved. Alternatively, a combination of spatial and temporal information can be used to reduce the speckle effect (e.g., Quegan and Yu 2001).

Since radar sensors are side-looking systems, a SAR imagery possess specific geometrical properties. From near (close to nadir) to far range increases the incidence angle, so that objects far from the nadir appear more distorted and are in the so called slant-range geometry. Using depression angle (angle between the line of sight from the radar to a target and the horizontal plane at the radar) slant-range geometry can be converted into ground-range geometry. However, in the presence of topography the transformation from the slant- to ground-geometry is not straightforward, since the return from a high object (e.g., mountain peak) is time

sooner as from the foot of a mountain. This effect is called foreshortening, when the slope appears shorter than in reality. The higher the object and the greater the depression angle (or smaller the incidence angle), the greater is foreshortening (Jensen 2007). In extreme case the backscattered energy from the peak of mountain can overlay the return from the base of mountain and the position of the peak is displaced toward the sensor (layover effect) (Figure 1-6). Additionally to foreshortening and layover, a further effect called radar shadow can occur in mountainous or urban areas. In this case, areas behind high objects are not illuminated by the sensor and thus, no energy is scattered back. Using information on surface topography (e.g., digital elevation model) it is possible to correct geometry and backscattering coefficients caused by foreshortening, while distortions caused by layover and radar shadow are not possible to correct (Jensen 2007).

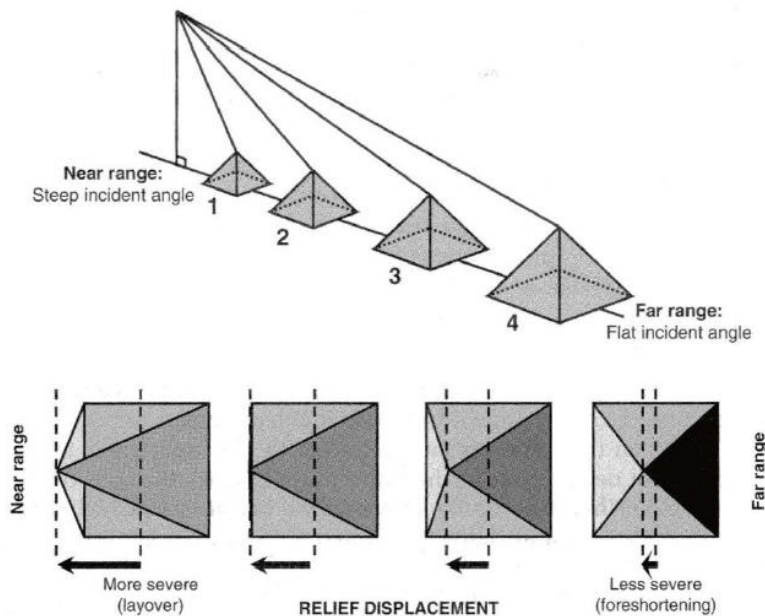


**Figure 1-6:** Influence of topography in radar image (Lillesand et al. 2008)

Generally, there are three main scattering mechanism when using radar imagery: 1) single bounce (or specular reflection), 2) double bounce, and 3) volume scattering. In case of single bounce the most energy sent reflects away from the sensor and only a minor part is scattered back (i.e., low backscatter). Double bounce appears when a signal hits two smooth areas that are perpendicular to each other (e.g., road and building) and send a strong backscatter to the sensor. When a signal penetrates a three-dimensional body (e.g., vegetation, ice), a radar signal is scattered back in multiple directions and some part is returned back to the sensor. Based on these dominant scattering mechanism the Earth surface can be classified into water, bare

soils (both single bounce), urban areas (double bounce) and vegetated areas (dominant volume scattering). Over vegetated areas all three scattering mechanism can occur. For instance, an L-band signal can penetrate the forest canopy and interact with the ground (single bounce), the signal can be reflected from the ground to the trunk and back to the sensor (also other way around) (double bounce), and finally, the signal can interact with tree elements within the crown (volume scattering) (Figure 1-7).

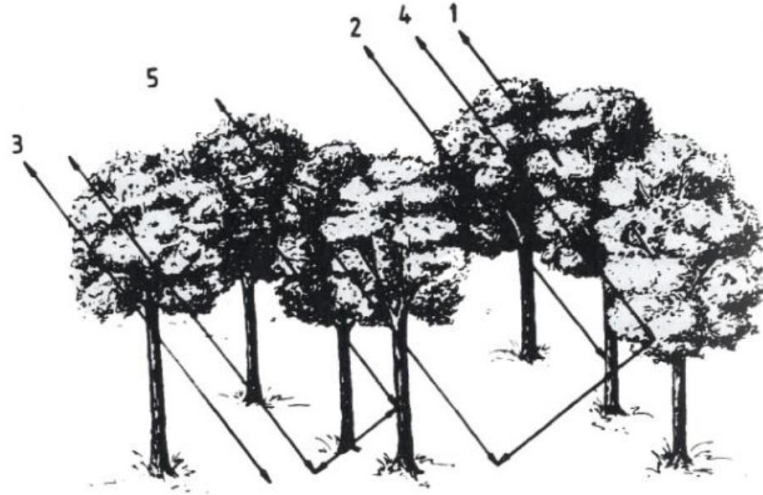


**Figure 1-7:** Scattering mechanism over forested areas: 1) backscatter from the crown (volume scattering), 2) direct backscatter from the trunks, 3) direct backscatter from the ground (single bounce), 4) crown-ground backscatter, and 5) trunk-ground backscatter (double bounce) (Leckie and Ranson 1996)

Over vegetated areas with increasing vegetation density (i.e., biomass) enhances also backscattered intensity. However, depending on radar frequency, polarisation of the emitted wave, environmental conditions (freezing, thawing, rain, drought, etc.), and biome-specific forest characteristics (i.e., coniferous and deciduous forests over boreal, temperate, tropical zone), the backscattered intensity saturates at different biomass levels, i.e., it is not further possible to discriminate biomass classes (Imhoff 1995; Le Toan et al. 1992). Usually short microwaves (X- and C-band) do not penetrate the tree crown and the wave interacts with small tree parts (leaves, twigs) (Le Toan et al. 1992). For this reason, backscattering coefficients acquired at these frequencies can be used to estimate biomass at low range (up to  $\sim 50 \text{ t ha}^{-1}$ ) (Imhoff 1995; Lucas et al. 2006) and are useful for vegetation parameter estimation in open forests and woodlands (Lucas et al. 2006; Mathieu et al. 2013). Longer wavelengths (e.g., L- or P-band) usually do penetrate the tree crown and interact with big tree compartments (branches and trunk), where most of the total biomass is stored. The saturation level of L- and P-band backscattering coefficients occurs at around 100

and  $200 \text{ t ha}^{-1}$  (Dobson et al. 1992; Saatchi et al. 2007), respectively. In some studies (e.g., Joshi et al. 2017; Mermoz et al. 2015; Yu and Saatchi 2016) a decrease of L-band backscattered intensity with increasing biomass has been reported. The reason for this could be signal attenuation, i.e., the returned intensity attenuates and decreases proportionally with increasing canopy opacity (Mermoz et al. 2015). Furthermore, with increasing biomass radar signal decreases probably due to a reduced trunk-ground double bounce scattering (Joshi et al. 2017). It has been also reported that biomass saturation level is affected by polarisation (Dobson et al. 1992; Le Toan et al. 1992). Since cross-polarised waves (HV or VH) are more sensitive to volume scattering (Rauste et al. 1994; Watanabe et al. 2006) and less affected by surface properties (soil moisture and roughness) (Saatchi and Moghaddam 2000; Saatchi et al. 2007) as opposed to co-polarised waves (HH or VV), the cross-polarised SAR imagery show a stronger sensitivity to forest biomass with a greater saturation level (Dobson et al. 1992; Saatchi et al. 2007).

Moreover, weather conditions (e.g., freezing, thawing, rain, drought) impact the potential of SAR imagery to estimate forest structure parameters. The best weather conditions for stem volume estimation over Northern-Hemisphere boreal forests using L-band intensity have been reported to be under dry unfrozen weather (summer period) (Rauste 2005; Santoro et al. 2006). During the frozen conditions Santoro et al. (2006) noticed signal saturation and low sensitivity of L-band intensity to stem volume. This can be caused by increased radar backscatter from the snow on the trees and on the ground (with ice layers inside), which is almost as high as backscatter from the tree canopy (Rauste 2005; Santoro et al. 2006). Over semi-arid forests, woodlands and savannahs SAR data acquired during the dry season showed higher correlation to the vegetation structure metrics than data acquired during the wet season (Lucas et al. 2010; Mathieu et al. 2013; Naidoo et al. 2015; Urbazaev et al. 2015). During the dry season there is almost no rainfall in these regions (semi-arid forests and savannahs), thus, moisture in the soil and on the vegetation is at its minimum resulting in a reduced impact of moisture on the radar backscatter. Similarly, in the tropical dry forests with a pronounced seasonality, SAR data from the dry season possess stronger sensitivity to forest structure parameters (Bouvet et al. 2018; Lucas et al. 2010).

Finally, forest structure influences relationships between backscattered intensity and AGB. Yu and Saatchi (2016) used spaceborne LiDAR-based AGB estimates collected over 11 forest biomes to investigate its correlation to the L-band backscatter intensity. Depending on the forest structure different saturation levels

were determined for L-band data. For instance, L-band intensity saturates at  $\sim 80 \text{ t ha}^{-1}$  over fresh water swamp forests, while over homogeneous boreal and temperate needleleaf forests the saturation level occurs first at  $\sim 250 \text{ t ha}^{-1}$  (Yu and Saatchi 2016). It is concluded that L-band intensity at HV polarisation can be used to estimate AGB up to  $100 \text{ t ha}^{-1}$  over all eleven forest types (Yu and Saatchi 2016).

Saturation effect can be partly solved by reducing the impact of environmental conditions on backscatter, so that the signal is primarily driven by vegetation structure. For this, multi- or hyper-temporal combination of SAR data is applied, e.g., by calculating multi-temporal statistics (mean, percentiles of backscatter) or by weighted averaging of stem volume estimates (Cartus et al. 2012b; Santoro et al. 2011). With multi-temporal SAR data forest structure parameters can be estimated more accurately and robust as with single SAR imagery (Antropov et al. 2017; Cartus et al. 2012b; Kurvonen et al. 1999; Rauste 2005; Santoro et al. 2011; Urbazaev et al. 2015). For instance, Santoro et al. (2011) combined C-band time series and reported no saturation to a stem volume up to  $300 \text{ m}^3\text{ha}^{-1}$  (i.e.,  $\sim 150 \text{ t ha}^{-1}$  AGB). Multi-frequency SAR data can potentially improve modelling accuracies of forest structure parameters, since short and long microwaves interact with different tree compartments (Englhart et al. 2011). Over dense tropical forests in Central Kalimantan, Indonesia, Englhart et al. (2011) reported an improved AGB retrieval accuracy by combining X- and L-band backscattering coefficients compared to the results that are based on L-band only ( $R^2$  of 0.789 for combined results vs.  $R^2$  of 0.706 for L-band based only). Multi-temporal X-band backscatters modelled AGB more accurately at low range than multi-temporal L-band backscatters (Englhart et al. 2011). In South African savannahs Naidoo et al. (2015) examined the potential of multi-frequency combination of dry season X-, C- and L-band backscatters for vegetation structure mapping (woody cover, AGB). Although the best retrieval performance was achieved using all three frequencies ( $R^2$  of 0.83 and relative RMSE of 29.18% for AGB estimation), L-band dataset alone produced marginally lower goodness-of-fit statistics ( $R^2$  of 0.78 and relative RMSE of 32.9%). The authors reported that inclusion of the data at short wavelength (X- and C-band) did not improve mapping accuracies of the shrubby layer as it was expected (Naidoo et al. 2015).

Supplementary information on forest structure (number of stems, stem size, understory) can further improve AGB modelling with radar backscatter (Joshi et al. 2017). The impact of forest structure on radar backscatter can be modelled and analysed using e.g., a simulated forest (e.g., FORMIND) (Cazcarra-Bes et al. 2017; Köhler and Huth 1998). However, even if it will be possible to extract “pure”

backscatter determined by vegetation, there are technical restrictions of radar signal to estimate biomass at high levels ( $>200 \text{ t ha}^{-1}$ ), e.g., signal attenuation in dense forest. Understanding radar signal behaviour at specific frequency, polarisation and forest structure, can partly extent saturation level of radar signal for estimation of forest parameters.

Besides the backscatter analysis, advanced SAR techniques, such as Polarimetry (PolSAR), Interferometry (InSAR), Polarimetric Interferometry (PolInSAR) and Tomography (TomoSAR) have been applied for forestry applications. PolSAR uses polarimetric information acquired at different polarisation to decompose the signal into main scattering mechanism and apply this decomposed information for land cover classification (Cloude and Pottier 1997) and biomass modelling (Antropov et al. 2017; Chowdhury et al. 2014). As already mentioned, InSAR utilizes at least two phases to calculate phase difference and estimate elevation with corresponding object height. PolInSAR combines both techniques (polarimetry and interferometry) to detect volume phase scattering height that is closely related to top of canopy. For TomoSAR multi-baseline SAR data (i.e., acquired from different positions) are required to delineate SAR tomogram. In contrast to InSAR or PolInSAR, where 2.5D information (top and bottom height) is estimated, SAR tomogram can be used to reconstruct 3D structure of an area. It has been shown in many studies that with InSAR (Askne et al. 2013; Askne et al. 2017; Solberg et al. 2013), PolInSAR (Hajnsek et al. 2009) and TomoSAR (Dinh Ho Tong et al. 2014) vegetation height can be mapped accurately, which can be further converted to volume or biomass. Interferometric coherence for AGB mapping was mostly used in boreal forests under stable environmental conditions (e.g., under long frozen periods) (e.g., Askne and Santoro 2005) and less investigated in (sub-) tropical regions, due to a low repetition rates (e.g., 46 days for ALOS PALSAR), which increase temporal decorrelation in heterogeneous (sub-) tropical areas. The main restriction to apply all of these advanced techniques is limited data access. Currently, there are only one spaceborne system that can be used for single-pass InSAR (TanDEM-X) and thus, for large scale mapping. Single-pass interferometry based on TanDEM-X data is further limited due to data policy, including restricted data access for scientific use. PolInSAR and TomoSAR systems are currently operated from an airplane only and thus, limited in time and space. For the first time these two advanced SAR techniques together with P-band SAR backscatter will be applied from space with an ESA mission, BIOMASS, which is being developed to assess global carbon stocks (Le Toan et al. 2011).

From previous studies a number of recommendations for AGB retrieval using SAR backscatter can be summarized as follows:

1. In general, cross-polarised backscatter (i.e., HV or VH) is more sensitive to vegetation structure than co-polarised backscatter (i.e., HH or VV), due to a higher volume scattering from vegetation canopy and a lower impact of surface properties (e.g., soil moisture and roughness). However, the sensitivity of co- and cross-polarised backscatter to vegetation parameters varies across study areas and depends on vegetation structure.
2. SAR backscatter acquired at high incidence angle ( $>45^\circ$ ) showed a higher saturation level and thus, better appropriate for AGB estimation than that acquired at low incidence angle. One of the main reasons is that data acquired at high incidence angle have a higher dynamic range (i.e., contrast between non-vegetated and dense vegetated areas). However, the impact of incidence angle is reduced for the data at low frequencies (Lucas et al. 2006).
3. Topography affects strongly SAR signal. AGB retrieval accuracies in flat areas are much higher than in areas with steep slopes ( $>15^\circ$ ) (Cartus et al. 2014). Therefore, the use of high quality DEM (e.g., TanDEM-X DEM or LiDAR DEM) at high spatial resolution can potentially improve topographic normalisation of the SAR data and thus, the AGB retrieval accuracy.
4. Multi-temporal SAR data improve the retrieval accuracies, as the impact of environmental conditions on the data is reduced (e.g., Kurvonen et al. 1999; Santoro et al. 2011).
5. In (semi-) tropical regions SAR backscatter acquired during dry season show stronger correlation to forest parameters, due to a reduced impact of moisture on radar signal. Further, an interpretation of operational products on soil moisture and/or vegetation water content (e.g., derived from AMSR-E) is recommended before the data ordering (Lucas et al. 2010).
6. Since SAR backscatter acquired at different frequencies reflects different scattering mechanisms from the vegetation, a combination of data at high and low frequencies can enhance the retrieval accuracy. Furthermore, data at different frequencies can be used for AGB modeling at certain biomass intervals, e.g., high frequency data for low biomass range, and low frequency data for middle-high biomass range (Englhart et al. 2011).
7. Tanase et al. (2014a) compared parametric and non-parametric models for AGB estimation with SAR backscatter and concluded that at different AGB intervals, parametric and non-parametric models showed various retrieval accuracy, suggesting that a combination of model types can improve overall accuracy.

8. Saatchi et al. (2011b) reported that for calibration of SAR data, field plots should be established at a minimum plot size of 0.25 ha, since the smaller plots are affected by large trees and thus possessed a high variability. The same recommendations were done by Chave et al. (2004) and Zolkos et al. (2013) to establish field plots with a minimum size of 0.2 ha.
9. Saatchi et al. (2011b) showed that adding of vegetation height information in the AGB model improves the retrieval accuracy significantly. Vegetation height can be obtained e.g., from LiDAR or InSAR data.
10. Polarimetric decompositions do not seem to improve estimation accuracy, and showed the similar or lower sensitivity to AGB than cross-polarised backscatter (e.g., Neumann et al. 2012; Tanase et al. 2014b).
11. The advanced SAR techniques such as PolInSAR and TomoSAR showed very accurate results to tree height estimation and thus to AGB (e.g., Dinh Ho Tong et al. 2014; Hajnsek et al. 2009), but limited in time and space as operated from an aerial platform.

### 1.2.3 LiDAR for forest structure mapping

Three-dimensional vegetation structure can be detected by Light Detection and Ranging (LiDAR) sensors. LiDAR is an active system that sends a pulse of light and measures returned energy. Knowing the precise travel time of the signal, the distance to targets can be calculated (Lim et al. 2003). LiDAR for terrestrial applications usually operates in near-infrared range between 900 and 1064 nm of electromagnetic spectrum and are capable to penetrate tree canopy (Lefsky et al. 2002b) allowing derivation of vegetation structure, understory and bare-ground information. A LiDAR system illuminates an area (called instantaneous laser footprint) by sending a laser pulse, which can generate one or many returns depending on the Earth Surface characteristics (bare-ground or vegetated area) (Figure 1-8). Laser footprint can vary in size between centimetres for an airborne sensor to several meters for a spaceborne instrument (e.g., 70 m ICESat GLAS instrument).



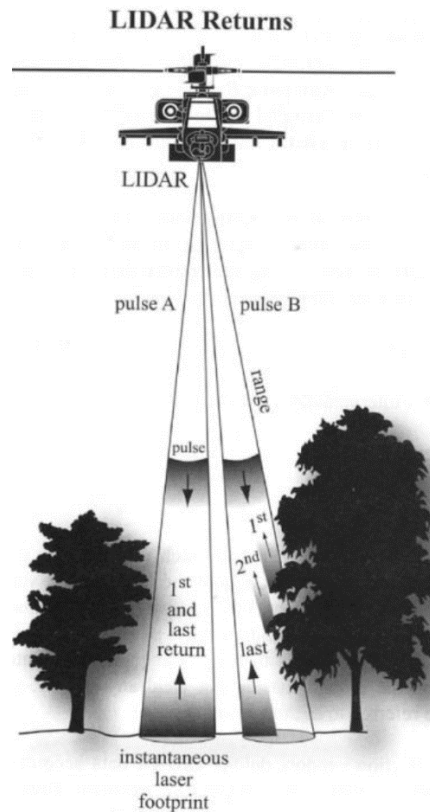


**Figure 1-8:** An illuminated area by LiDAR and different number of returns depending on land cover (pulses A and B) (Jensen 2009)

LiDAR systems can be categorized as “discrete return” (DR) and “full waveform” (FW) systems (Lefsky et al. 2002b; Lim et al. 2003). The difference between these two systems is the way the reflected energy is recorded. While DR LiDAR records returns from the major peaks, FW systems measure the time-varying intensity of each pulse (Lefsky et al. 2002b) (Figure 1-9). A FW LiDAR therefore measures a vertical structure over an illuminated area. The footprint size of FW LiDAR ranges between 8 to 70 m (Lim et al. 2003) and contains information on multiple forest elements (trees, shrubs etc.). Since a DR LiDAR possesses a small footprint (less than a meter) (Lim et al. 2003) many returns can occur within a cell of 1x1 m. Therefore, vertical target distribution can be simulated from these multiple returns (Lefsky et al. 2002b).

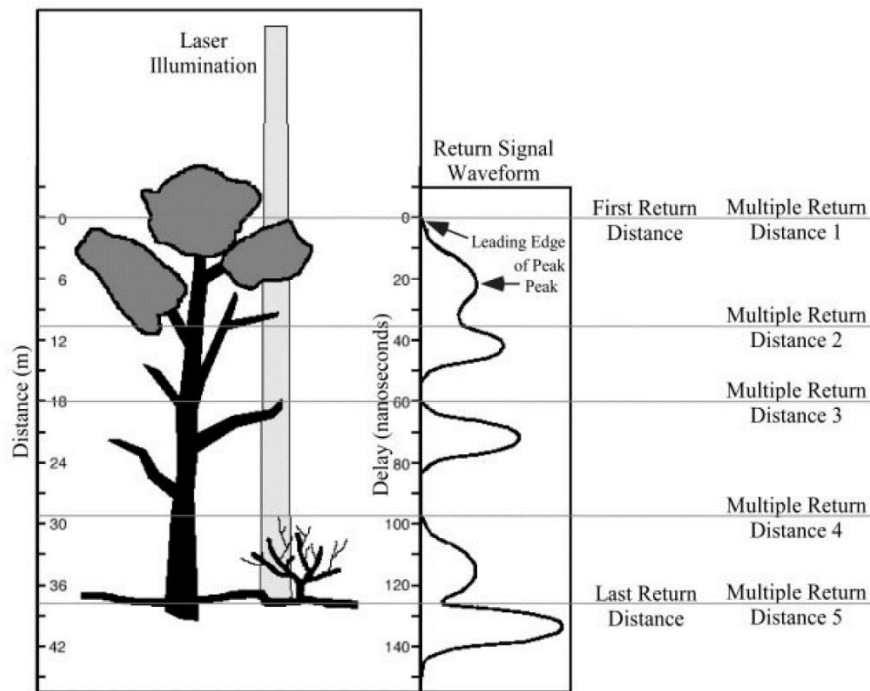


**Figure 1-9:** Differences in recording of return signal between the full waveform and discrete return LiDAR systems (Lefsky et al. 2002b)

LiDAR is able to measure some vegetation structure parameters directly (e.g., vegetation height, density), but not the tree volume and biomass. The latter can be estimated via statistical modelling with AGB estimates derived from field measurements. Alternatively, height-to-biomass allometry can be developed to convert LiDAR-height to biomass. For instance, Asner et al. (2012) developed an universal equation to estimate aboveground carbon density (ACD) from the LiDAR mean canopy height (MCH) over four tropical regions (Panama, Peru, Madagascar, and Hawaii). The idea to develop an universal model for tropical forest is based on generalized pan-tropical equations after Chave et al. (2005). Asner et al. (2012) substituted the tree height derived from field measurements with the LiDAR MCH and combined together with the plot specific basal area (BA) and wood density (WD) parameters. If plot specific BA and WD are applied, the universal model explained 95% of the variation in ACD across all 482 field plots with an  $R^2$  of 0.95 and RMSE of  $12.6 \text{ MgC ha}^{-1}$  between LiDAR predicted and field based ACD. Using regional specific BA and WD together with LiDAR MCH predicted and observed ACD have an  $R^2$  of 0.80 and RMSE of  $27.6 \text{ MgC ha}^{-1}$ .

Since vegetation height and density metrics correlate strongly with biomass, LiDAR-metrics can be used for accurate biomass mapping. Zolkos et al. (2013) compared more than 70 studies for AGB estimation, which were based on LiDAR

and synergetic (i.e., multi-sensor) approaches and carried out across the world. The authors concluded that LiDAR-based AGB models are significantly more accurate than those based on radar or optical data. Multi-sensor approaches are more variable than LiDAR-only models and they do not always enhance AGB retrieval accuracy. The use of imaging sensors is, however, required to provide “wall-to-wall” products over large areas. In contrast to radar and optical approaches, only LiDAR and multi-sensor based models may satisfy “Monitoring, Reporting and Verification” (MRV) guidelines (Herold and Skutsch 2011) with Root Square Error within  $20 \text{ Mg ha}^{-1}$  or 20% of field estimates. Accuracies of LiDAR based AGB models are dependent on the type of LiDAR system (airborne discrete return (DR), full waveform (FW), spaceborne (GLAS)), forest type (boreal, temperate, tropical), and field inventory plot size. The accuracies achieved by different LiDAR and multi-sensor (MS) models were similar with mean  $R^2$  of 0.80, 0.78, 0.76 and 0.70 for FW, MS, DR and GLAS, respectively. In contrast, mean  $R^2$  for radar and optical data based models were significantly lower with 0.50 and 0.59, respectively. The best model performance was achieved in tropical forests (mean RSE=20.7%), while in temperate deciduous and boreal forests (mean RSE=31.0% and RSE=34.3%, respectively) the errors were higher. Finally, model performance is affected by the field plot size. RSE decreases rapidly with increasing of plot size. The relationship between model error and plot size is asymptotic and saturates at  $\sim 0.2 \text{ ha}$ , i.e. the plot size for LiDAR model calibration should be at least 0.2 ha (Zolkos et al. 2013).

LiDAR can provide very accurate information on vertical distribution of canopy elements (Goetz and Dubayah 2011) and thus, can be used for AGB modelling without signal saturation (Lefsky et al. 2005). The main limitation of the LiDAR is a restricted spatial coverage, since LiDARs are samplers and not imagers. Although airborne LiDAR systems are capable to generate a continuous scan of the Earth, they are limited in space and time. Spaceborne LiDARs collect samples of the Earth, e.g., NASA’s ICESat GLAS sampled the Earth approximately every 170 m (distance between single laser footprints). At local scale airborne LiDAR are able to measure forest dynamics (e.g., Dubayah et al. 2010). At continental or intercontinental scales airborne and spaceborne LiDAR can serve as training data for optical and/or radar imagery (Section 1.2.4). LiDAR-based AGB estimates can provide a larger number of training data, which is necessary for a large scale mapping (continental or intercontinental scale). Furthermore, in contrast to forest inventory data, LiDAR can help to reflect local spatial variability and thus to establish robust statistical models. LiDAR possess, however, some further limitations, e.g., it is difficult to separate first and last return over hilly terrain or dense understory (Goetz &

Dubayah 2011). Lasers still have some penetration (especially during leaf-off conditions) and may reflect not the highest vegetation point (Dubayah et al. 2010). Similar to passive optical remote sensing data, LiDAR is hindered by clouds (Lefsky et al. 2002b). Therefore, one important step in using LiDAR-AGB as reference data is error characterisation by up scaling of field data. For instance, Saarela et al. (2016) and Holm et al. (2017) showed that ignoring field to LiDAR error can underestimate uncertainty in the final satellite based AGB map by a factor of three or higher.

In addition to topography and forest carbon stocks mapping, LiDAR provides unique data for a number of ecological applications (e.g., characterisation of biodiversity and habitat, understory structure and dynamic) (Goetz & Dubayah 2011). New spaceborne LiDAR missions (e.g., NASA’s Global Ecosystem Dynamics Investigation (GEDI) and ICESat-2, JAXA’s MOLI), partly are specifically designed for vegetation monitoring, will provide unique multi-temporal datasets on vertical vegetation structure over undersampled dense tropical forests. These datasets alone can provide statistics (mean, total AGB) over an area of interest using sampling theories (e.g., design- or model-based interference (Gregoire 1998; Ståhl et al. 2016)). However, to provide wall-to-wall estimates of a variable of interest a fusion with satellite imagery is necessary (Section 1.2.4).

#### 1.2.4 Multi-sensor combination for forest structure mapping

Since optical, LiDAR and SAR data reflect different characteristics of a vegetated area (e.g., spectral and vertical properties of vegetation), a synergetic combination of these datasets can be used to describe horizontal and vertical vegetation structure and thus, to enhance vegetation parameter estimation (e.g., tree height, crown density, AGB). Limitations of each data type, e.g., impact of moisture and topography on SAR data, cloud cover and seasonal effects on optical imagery, and sampling mode of LiDAR, can be minimized when using these data synergetically (Goetz et al. 2009). Moreover, different sensor type features their advantages. For instance, optical sensors are sensitive to photosynthetically active vegetation and possess long and continuous time series of imageries (back to 70s-80s). SAR has the ability to penetrate tree crown and is sensitive to woody vegetation. Thus, SAR can be effectively used to separate woody and herbaceous layers (e.g., Naidoo et al. 2016). LiDAR provides accurate measurements of tree height, tree crown and vegetation density without signal saturation (Lefsky et al. 2002b).

Since LiDAR can provide very accurate estimates of biomass (Zolkos et al. 2013) and height (Simard et al. 2011), these data can be used as training data for large scale mapping. Using a combination of spaceborne LiDAR and optical imagery it was possible to estimate AGB for the entire tropical region (Baccini et al. 2012; Saatchi et al. 2011a). Baccini et al. (2008 and 2012) reported a sensitivity of a short wave infrared (SWIR) spectral band to texture and shadows, which are related to stand age structure and thus to AGB of dense tropical forests. Without spaceborne LiDAR (i.e., with field data only) it would not be possible to train adequately machine learning algorithms, which require a large amount of training data. Furthermore, using time series of optical data (Landsat and MODIS) together with LiDAR data it was possible to track forest dynamics over time in boreal forests of Canada (Matasci et al. 2018) as well as over the entire tropical region (Baccini et al. 2017).

TanDEM-X scattering phase height is closely related to the canopy height due to the low penetration depth of X-band signal as well as due to the quasi simultaneous acquisition from two different positions allowing to apply single-pass InSAR. In application preparation phase of the spaceborne GEDI LiDAR data, Qi and Dubayah (2016) investigated the potential of the fusion of TanDEM-X data with simulated GEDI LiDAR to provide wall-to-wall estimates of vegetation height under varying terrain conditions. Although TanDEM-X features strong capability to estimate vegetation height (Askne et al. 2013; Solberg et al. 2013), inclusion of topographic information such as from spaceborne LiDAR, improves modelling accuracies, especially over hilly terrain than using TanDEM-X alone (Qi and Dubayah 2016).

Optical and SAR signals are determined by different vegetation characteristics. While optical data are sensitive to foliar properties and canopy gap structure (Avitabile et al. 2012), SAR signal interacts primarily with woody tree compartments (i.e., trunk, branches and twigs). Therefore, a fusion of SAR and optical data provide more complementary information of forests, which can potentially improve retrieval accuracies of forest parameters. For instance, over homogeneous even-aged forest plantations in Chile Cartus et al. (2012a) estimated canopy height and growing stock volume using L-band SAR (backscatter intensity and interferometric coherence) and optical Landsat data. Single sensor models (i.e., PALSAR-only and Landsat-only) achieved similar retrieval accuracies, while a synergetic combination of PALSAR and Landsat data produced consistently higher accuracies for three test sites in Chile. Over tropical forests in central Laos investigated Hame et al. (2013b) performance of L-band SAR backscatter and

optical data (acquired from ALOS AVNIR) in single-sensor and combined approaches to estimate AGB. The results showed similar prediction performance of single SAR- and optical-based models as well as in a combined manner (Hame et al. 2013b). Bearing in mind data collection efforts and local site conditions, the use of data from one sensor (either SAR or optical) can be sufficient to provide reliable estimates of vegetation structure parameters at local scale. For instance, SAR data have been proven to be more appropriate for vegetation parameter estimation in a savannah landscape (Naidoo et al. 2016), mostly due to difficulties to separate herbaceous and woody vegetation with optical imagery (Lucas et al. 2006). Combination of L-band backscatter with Landsat surface reflectance improves prediction performance marginally (Naidoo et al. 2016).

Overall, for large scale mapping a combination of SAR and optical data would enhance prediction performance by compensating limitations of one sensor type for specific local conditions (e.g., hilly terrain areas in case of SAR data, areas permanently covered by clouds in case of optical data). For forest structure mapping at local scale, however, single sensor data (either SAR or optical) might be used that reflect the best site specific conditions (e.g., savannahs). LiDAR data are generally used to increase the amount of reference data that better describe spatial variability of heterogeneous forests as field data (Baccini et al. 2008; Baccini et al. 2012; Englhart et al. 2011; Saatchi et al. 2011a). For a spatially continuous mapping a fusion of LiDAR with optical and/or SAR imager is required. Nowadays with increasing number of optical, radar and LiDAR sensors in space and in the air (e.g., unmanned aerial vehicle), opportunities emerge to map biomass on an unprecedented spatial and time scales with a high retrieval accuracy.

### 1.2.5 Statistical models for forest structure mapping

To relate a signal measured by a remote sensing sensor (optical, radar, LiDAR) to a target variable (i.e., biomass, height etc.) and to do a prediction based on this relationship, different types of statistical models can be applied. For forest parameter estimation simple parametric regression models (e.g., linear regression, multiple linear regression), physically-based models (e.g., Water Cloud Model (WCM)), and machine and deep learning algorithms (e.g., Random Forests, Support Vector Machine) have been applied.

Assuming there is a relationship between  $\mathbf{X}$  (predictor, i.e., remote sensing measurement) and  $\mathbf{Y}$  (response, i.e., target variable), a very straightforward approach to predict a response  $\mathbf{Y}$  is to use a simple linear regression in the form

$Y=a+b*X$ , where  $a$  (intercept) and  $b$  (slope) are unknown model coefficients. The model coefficients  $a$  and  $b$  can be estimated, where samples of  $Y$  and  $X$  are known using e.g., least squares approach. Least squares criterion selects  $a$  and  $b$  to minimise the residual sum of squares (RSS) (James et al. 2015), i.e., data points from  $Y$  and  $X$  values are located as close as possible to the regression line. This procedure can be called model fitting or training. The simple linear regression can be extended to multiple linear regression by applying a number of predictors and can be written in the form  $Y=a+b_1*X_1+b_2*X_2+...+b_n*X_n$ . The model coefficients ( $a, b_1...b_n$ ) are determined empirically as well with the sample data. Since the relationships between remote sensing measurements and forest parameters are usually not linear, a linear regression with logarithmic transformation can be used, e.g., in the form of  $Y=a+b*\log(X)$ . The linear regressions are flexible, well understood, and serves as basis for many advanced statistical approaches that represent generalisations and extensions of linear regression (James et al. 2015).

An extension of linear regressions are the physically-based models that have been developed specifically to describe a SAR signal as a function of complex signal interaction within a vegetated area, e.g., Water Cloud Model (WCM) (Attema and Ulaby 1978) and Interferometric Water Cloud Model (IWCM) (Askne et al. 1997). These models try to describe total SAR signal over forests (backscatter intensity or interferometric coherence) as a sum of ground scattering through canopy gaps, ground scattering attenuated by the crown and scattering from vegetation layer (Askne et al. 1997). Total forest backscatter can be expressed as a function of stem volume or biomass in the form of  $\sigma_{for}=\sigma_{gr}e^{-\beta V} + \sigma_{veg}(1-e^{-\beta V})$ .  $\sigma_{for}$  represents backscatter intensity over forest,  $\sigma_{gr}$  and  $\sigma_{veg}$  are backscatter intensities of the forest floor and vegetation layer, respectively,  $\beta$  is related to dielectric and forest structure properties (Santoro et al. 2011). The unknown model coefficients ( $\sigma_{gr}$ ,  $\sigma_{veg}$  and  $\beta$ ) can be estimated empirically with sample data, e.g., using a least squares approach similar as for linear regression. For large scale applications, however, empirical estimation of the model coefficients is not feasible as sample data are rare and might not reflect spatial variations of SAR backscatter caused by forest structure and environmental conditions (Santoro et al. 2011). Therefore, Santoro et al. (2011) estimated the model coefficients  $\sigma_{gr}$  and  $\sigma_{veg}$  by means of globally available MODIS tree cover map (Hansen et al. 2003), where  $\sigma_{gr}$  and  $\sigma_{veg}$  represent backscatter intensities of unvegetated land surfaces and dense forests, respectively. These parameters are estimated by applying different windows sizes and tree cover thresholds (Santoro et al. 2011). Empirical estimation of the parameter  $\beta$  showed that this coefficient varies in average between 0.004 and 0.008 ha m<sup>-3</sup> and impacts

Growing Stock Volume (GSV) estimates by less than 10% regardless of the study area (Santoro et al. 2011). Therefore, using a set of  $\sigma_{gr}$ ,  $\sigma_{veg}$  and  $\beta$  values it was possible to estimate GSV without model fitting, i.e., without training data. The authors further applied temporal (i.e., multi-temporal weighting of single scenes estimation) and spatial aggregation to reduce impacts caused by spatial variations and environmental conditions on GSV estimation (Santoro et al. 2011). So far, this algorithm (called BIOMASAR) has been applied on C-band SAR time series and generated accurate estimates of GSV at low spatial resolution (1 km) over entire Northern Hemisphere boreal forests. With new spaceborne L- and P-band SAR systems available in the near future, adaption of the BIOMASAR algorithm to these data would be very promising, considering higher sensitivity of low frequency SAR to forest structure.

Alternatively to the parametric type of statistical models, non-parametric models, such as machine and deep learning algorithms, can be applied to derive vegetation structure parameters from remote sensing data. These types of models make no prior assumption on the shape of data distribution and can therefore, describe complex non-linear relationships (James et al. 2015) (Figure 1-10). However, a very large amount of training data (far more than typically needed for parametric models) are required to obtain an accurate model (James et al. 2015). Furthermore, non-parametric models are prone to overfitting (Figure 1-10), i.e., the model is tuned too much to the sample data and can fail to do a prediction of unknown observations.

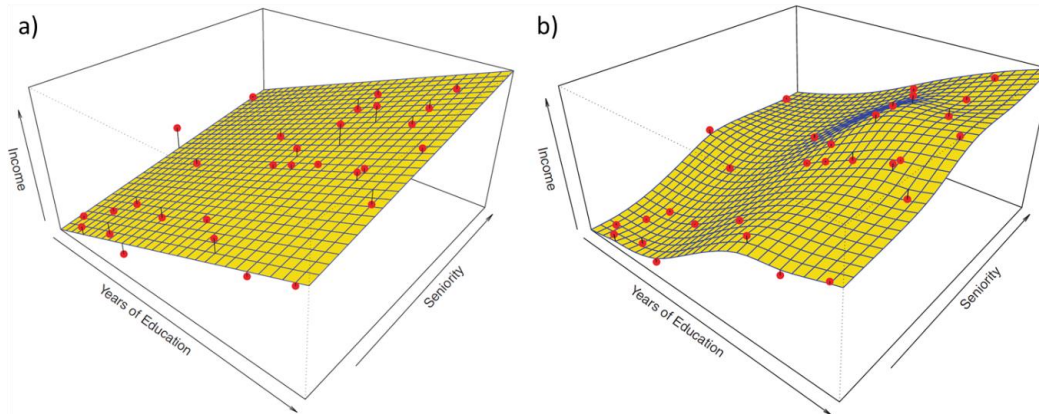


**Figure 1-10:** Schematic representation of (a) linear parametric model and (b) non-parametric model (b) (James et al. 2015)

One of the most popular machine learning algorithms for estimation of forest structure parameters is the Random Forests (RF) algorithm (Breiman 2001). The RF by Breiman (2001) is built on the Classification and Regression Trees (CART) algorithm (Breiman et al. 1984). In contrast to CART many regression trees are



generated in RF instead of one, which generally produce more accurate results (Baccini et al. 2008). This machine learning algorithm generates an ensemble of regression trees with a random selection of predictors at each node as well as with a random subset of samples for each tree to prevent overfitting. In order to calculate a single estimate, the predictions of each regression tree are averaged (Breiman 2001). The RF is a computationally efficient and a robust non-parametric model, which was successfully applied to map vegetation structure metrics (e.g., AGB, tree height) with high retrieval accuracy at large spatial scales (e.g., Avitabile et al., 2012; Baccini et al. 2008; Cartus et al., 2012a). Alternatively to RFs, hybrid tree-based approach Cubist showed among the best modelling predictive performance (Moisen et al. 2006; Walker et al. 2007). Cubist combines rule-based regression with linear multivariate models (Quinlan 1993). Based on the training data a collection of rules is defined. A rule represents a path through a decision tree, for each rule a multivariate linear regression is used to calculate a predicted value. The final prediction is calculated by combining linear models at each node of the trees; therefore, it is smoothed compared to a single linear model.

In summary, parametric linear regressions possess following advantages: they are simple (easy to understand and interpret results), computationally fast, and they do not require a large amount of sample data. On the other side, parametric models are constrained, i.e., not flexible, they are more suitable for simple linear relationships and less for complex functions (Brownlee 2016). In contrast, non-parametric statistical models are flexible, i.e., able to fit complex relationships, and accordingly, possess high modelling performance. The advantages of non-parametric models are at the same time their disadvantages, for instance, they are computationally intensive, they require a large amount of training data, and they are prone to overfitting (Brownlee 2016). Moreover, non-parametric models usually represent black-box models that are difficult to understand. Tanase et al. (2014a) compared parametric and non-parametric models for AGB estimation and concluded that at different AGB intervals, parametric and non-parametric models showed various retrieval accuracies, suggesting that a combination of model types can improve overall accuracy.

### **1.3 Study area**

The study area of this work is the United Mexican States (hereafter Mexico), a sub-tropical country with an area of approx. 2 million km<sup>2</sup> (5.5 times larger than Germany). Forest in Mexico is defined as an area with a minimum size of 1 ha, where vegetation cover is higher than 10% and vegetation height is greater than 2 m (CONAFOR 2010). According to this definition approximately one-third of the country is covered by forests (ca. 65 million ha) (FAO 2015). Mexico has been selected as a study area for several reasons. Mexican forests represent a wide variety of forest types ranging from temperate coniferous and deciduous forests to cloud forests and mangroves to woodlands (savannah-like environments) and to tropical humid and dry forests under different topographic conditions (flat terrain in the Yucatan peninsula, hilly terrain in other parts of Mexico) (Figure 1-11). Furthermore, availability of reference data is one of the crucial issues to estimate various forest parameters with remote sensing. Mexico is one of the REDD countries with a dense nationwide publicly available network of forest inventory data (CONAFOR 2012) (Figure 1-11a). Additionally to the dense network of field data, there exist free available airborne LiDAR data collected by NASA over the major Mexican's forest types (Cook et al. 2013) (Figure 1-11a). The results of this study can be potentially transferred to similar environments.

Study area

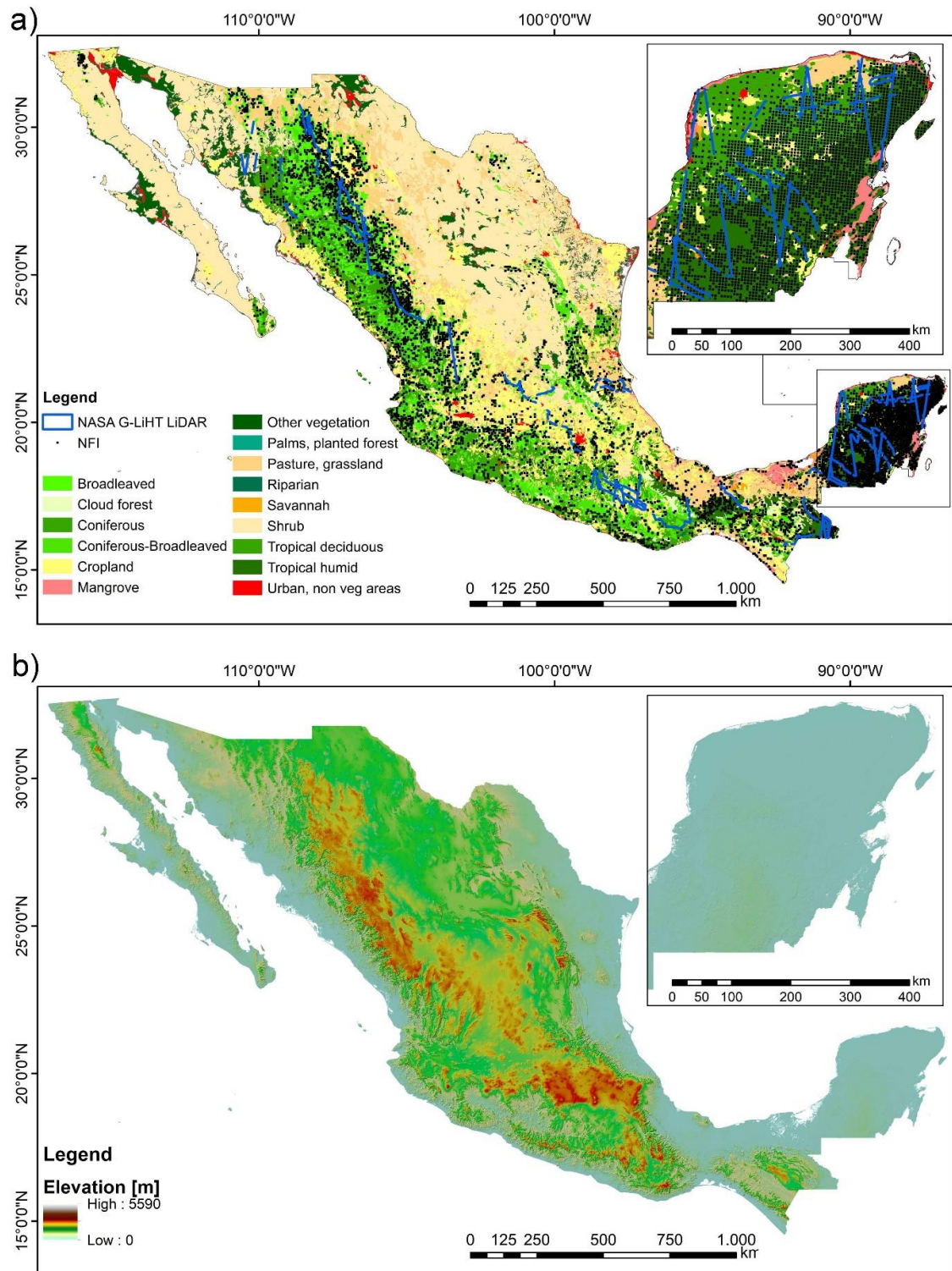


**Figure 1-11:** (a) Land use and vegetation map of Mexico from the Mexican National Institute for Statistics and Geography (INEGI) Series IV (INEGI 2010). (b) Elevation in meters above sea level from the SRTM DEM

Forest biomass in Mexico is estimated using national forest inventory data (Spanish acronym INFyS (*Inventario Nacional Forestal y de Suelos*)) conducted by

the National Forestry Commission of Mexico (Spanish acronym CONAFOR (*Comisión Nacional Forestal*)). These inventory-based estimates are used for reporting to the FAO and REDD+ programme. The first national forest inventory programme was accomplished between 1961 and 1985 (CONAFOR 2012). Since 2004 CONAFOR has established a systematic nationwide network of forest inventory plots (Figure 1-11), which are re-measured every five years. In the national forest inventory programme conducted between 2004 and 2009 more than 26,000 plots were sampled (CONAFOR 2012). A single circular sampling plot has a radius of 56.42 m covering an area of 1 ha and comprises four sub-plots with an area of 400 m<sup>2</sup> (0.04 ha) (Figure 3-2). The plot design of INFyS data is similar to the United States Forest Service Forest Inventory and Analysis program (FIA) (Bechtold and Patterson 2005). From the central sub-plot three further sub-plots at an azimuth of 0°, 120° and 240° were defined. The plots are sampled over the whole country using rectangular grid with a distance between single plots varying from 5 km (in tropical and temperate forests) to 20 km (in arid regions). Within each sub-plot, different forest structure parameters (e.g., diameter at breast height, tree height, etc.) were measured. AGB was calculated for each sub-plot using 339 species and genus-specific allometric models and wood densities (CONAFOR 2016) and then extrapolated to 1 ha. If more than one allometric model was available, the one with highest R<sup>2</sup> or with the closest regional relevance was used. Due to the lack of allometries, especially in the tropical areas, also pan-tropical generalized models (Chave et al. 2005) were used. Beside the forest structure parameters further variables, such as species composition, disturbance impacts, leaf area index are collected in the field.

Additionally to the NFI-based forest biomass estimates, there exist two remote sensing based products on national forest biomass (Cartus et al. 2014; Rodriguez-Veiga et al. 2016). Comparison of these products with the results of this study and the corresponding discussion is presented in the Section 5.

## **1.4 Research objectives**

The general objectives of this thesis are to determine the capabilities and limitations of remote sensing data (SAR, optical and LiDAR data) to estimate forest structure parameters (e.g., AGB and vegetation height) over sub-tropical forests of Mexico. According to the general objective of the thesis, following specific research objectives were defined:

1. Potentials to improve AGB estimation over tropical dry and humid forests by combining SAR and optical data and by automatic selection of temporally stable forest inventory plots using NDVI time series (Section 2).

To address this research objective a different number of remote sensing data, e.g., L-band SAR backscatter intensities, interferometric coherences, Landsat-based tree cover information and SRTM Digital Elevation Model were used to assess AGB modelling performance under different scenarios (i.e., single-sensor based and multi-sensor combination). Since reference data used for model training and for results validation can contain outdated information (caused by deforestation or fire), these outdated data can lead to a reduction of model prediction performance. It was investigated whether filtering of reference data using automatic change detection algorithm can improve AGB model prediction performance.

2. Integration of SAR, optical, airborne LiDAR and forest inventory data to estimate AGB and corresponding uncertainties at national scale (Section 3).

In this study, two modelling scenarios for AGB estimation using different sets of reference data were assessed. In the first modelling scenario forest inventory data were used as reference data, while in the second modelling scenario LiDAR-based AGB served as training data. Errors were estimated in the field data and propagated to the LiDAR-based AGB and to the final national satellite-based AGB maps. From the error propagation analysis corresponding uncertainty layers for NFI- and LiDAR-calibrated AGB maps were generated.

3. Potential of multi-temporal combination of L-band time series data to improve vegetation height estimation over tropical dry and humid forests (Section 4).

For this research objective, vegetation height was estimated using different number of multi-temporal L-band SAR backscatter scenes acquired between 2014 and 2018 (24 scenes in total). Statistical models based on 4, 8, 12, 16, 20 and 24 L-band backscatter intensities were developed and their predictive performance was

assessed. Furthermore, the impact of spatial autocorrelation in the reference data and the importance of sampling size (i.e., number of training data) on modelling predictive performance was investigated.

# Chapter 2

## **Improved Multi-Sensor Satellite-Based Aboveground Biomass Estimation by Selecting Temporally Stable Forest Inventory Plots Using NDVI Time Series**

M. Urbazaev<sup>1</sup>, C. Thiel<sup>1</sup>, M. Migliavacca<sup>2</sup>, M. Reichstein<sup>2,3</sup>, P. Rodriguez- Veiga<sup>4,5</sup> & C. Schmullius<sup>1</sup>

<sup>1</sup>Friedrich-Schiller-University Jena, Department for Earth Observation

<sup>2</sup>Max Planck Institute for Biogeochemistry, Biogeochemical Model-Data Integration Group

<sup>3</sup>Michael-Stifel-Center Jena

<sup>4</sup>University of Leicester, Centre of Landscape and Climate Research

<sup>5</sup>University of Leicester, National Centre for Earth Observation

Published in:

**Forests** (2016), 7, 169

(Received 20 May 2016; Accepted 27 July 2016)

**DOI:** 10.3390/f7080169

## Abstract

Accurate estimates of aboveground biomass (AGB) are crucial to assess terrestrial C-stocks and C-emissions as well as to develop sustainable forest management strategies. In this study we used Synthetic Aperture Radar (SAR) data acquired at L-band and the Landsat tree cover product together with Moderate Resolution Image Spectroradiometer (MODIS) normalized difference vegetation index (NDVI) time series data to improve AGB estimations over two study areas in southern Mexico. We used Mexican National Forest Inventory (INFyS) data collected between 2005 and 2011 to calibrate AGB models as well as to validate the derived AGB products. We applied MODIS NDVI time series data analysis to exclude field plots in which abrupt changes were detected. For this, we used Breaks For Additive Seasonal and Trend analysis (BFAST). We modelled AGB using an original field dataset and BFAST-filtered data. The results show higher accuracies of AGB estimations using BFAST-filtered data than using original field data in terms of  $R^2$  and root mean square error (RMSE) for both dry and humid tropical forests of southern Mexico. The best results were found in areas with high deforestation rates where the AGB models based on the BFAST-filtered data substantially outperformed those based on original field data ( $R^2_{\text{BFAST}} = 0.62$  vs.  $R^2_{\text{orig}} = 0.45$ ;  $\text{RMSE}_{\text{BFAST}} = 28.4$  t/ha vs.  $\text{RMSE}_{\text{orig}} = 33.8$  t/ha). We conclude that the presented method shows great potential to improve AGB estimations and can be easily and automatically implemented over large areas.

**Keywords:** aboveground biomass; Mexico; remote sensing; time series; BFAST; MODIS; NDVI; ALOS PALSAR; Landsat tree cover



## **2.1 Introduction**

Through the process of photosynthesis, vegetation absorbs CO<sub>2</sub> from the atmosphere and stores carbon in the biomass of leaves, branches and stems. This can be summarized as aboveground biomass (AGB), defined as the total amount of aboveground living organic matter in vegetation and expressed as oven-dry tons per unit area (Brown 1997). Around 50% of dry aboveground biomass is carbon. Therefore, AGB is one of the crucial parameters to assess terrestrial aboveground C-stocks and C-emissions caused by deforestation and forest degradation. Since vegetation biomass affects a range of ecosystem processes such as carbon and water cycling, as well as energy fluxes, accurate AGB information is required for the development of sustainable forest management strategies (FAO 2015). Sustainable forest management can contribute to the reduction of carbon in the atmosphere by the decrease of emissions and the increase of carbon storage (carbon sequestration in vegetation). Field measurements of vegetation parameters (e.g., tree height, tree diameter, crown density) that can be further related with AGB are associated with high costs (e.g., labour-intensive and time-consuming) and are limited to point measurements, which may not adequately describe patterns at different spatial scales. Fortunately, rapid advances in information technology have enabled woody vegetation parameters to be estimated from remote sensing. In particular in tropical forests, remote sensing data provides spatially consistent information for areas that are difficult to access.

Synthetic Aperture Radar (SAR) data have been shown to be useful for AGB estimation across the landscape, e.g., (Cartus et al. 2012b; Mitchard et al. 2009b; Saatchi et al. 2011b; Stelmaszczuk-Górska et al. 2016; Tanase et al. 2014a). Microwave signals have the capability to penetrate the vegetation profile, reflecting the three-dimensional vegetation structure, and are useful for weather-independent applications, as long wavelengths penetrate clouds. The interactions of the radar waves with vegetation elements are determined by their size, shape, and dielectric properties. Long wavelengths (e.g., at P-band and L-band) are more suitable for the retrieval of woody vegetation structure parameters (e.g., stem volume, AGB) because of their ability to penetrate deeper in forest canopies as compared to short wavelengths (e.g., at X-band and C-band) (Le Toan et al. 1992; Lucas et al. 2004; Saatchi et al. 2011b), and thus to interact with large branches (in order of the wavelength) and trunks. A key parameter obtained from SAR data, backscatter intensity, measures the return of energy from a ground object and is determined by

the physical (geometry of the object) and electrical (dielectric constant, which is mostly determined by the water content) properties of the target, as well as by the signal properties (e.g., frequency, polarization and angle of incidence of the emitted wave) (Raney 1996). A further SAR parameter, interferometric coherence, can be calculated using interferometry techniques (InSAR). Interferometric coherence represents a degree of correlation between two acquisitions. In general, non-forest areas (e.g., urban areas, bare soil), typically stable over time, have high coherence value. Since coherence is typically lower over forests (through an increase of volume and corresponding temporal decorrelation), interferometric coherence can be used for the mapping of forest/non-forest areas (Luckman et al. 2000) as well as for AGB assessment (Cartus et al. 2011; Wagner et al. 2003). Limitations of radar data for AGB estimation are saturation as well as strong dependence on environmental conditions (e.g., rain fall, and soil moisture conditions). The saturation level of the SAR signal for AGB estimation depends on forest types and wavelengths and varies between 40–150 t/ha for L-band data (Imhoff 1995; Lucas et al. 2004; Mermoz et al. 2014; Mitchard et al. 2011; Saatchi et al. 2007; Yu and Saatchi 2016).

Remote sensing data from optical sensors (e.g., Landsat, Moderate Resolution Image Spectroradiometer (MODIS)) are partly appropriate for AGB estimation. Optical data are sensitive to vegetation density (Avitabile et al. 2012), which relates to AGB and saturates at high biomass values, e.g., (Huete et al. 1997; Huete et al. 2002). Optical data from Landsat and MODIS are attractive as they are freely available and possess long time series. Disadvantages in the use of optical data for AGB estimation are high cloud cover rates over tropics, and strong dependence on environmental, seasonal and acquisition conditions (e.g., solar zenith angle) (Steininger 2000).

The estimation of vegetation parameters (e.g., AGB, vegetation height, growing stock volume) can be improved by the fusing of SAR imagery with optical data (e.g., from Landsat) and complementary information such as altitude (Basuki et al. 2013; Cartus et al. 2012a; Cartus et al. 2014; Montesano et al. 2013; Rodríguez-Veiga et al. 2016).

For the most commonly used parametric and non-parametric AGB models, calibration data are needed. However, the reference data used for model calibration and product validation can contain inaccurate measurements as well as outdated information (Chowdhury et al. 2014). For instance, if field plots were sampled a few years earlier than the remote sensing data acquisition, changes (caused, e.g., by fire or deforestation) within the field plots are likely to occur. Accordingly, these

outdated calibration/validation data can lead to a reduction of model prediction performance and thus decrease product accuracy. Time series analysis of remotely sensed data is recognized as a powerful tool to monitor temporal dynamics in vegetation at different scales (from local to global) (De Jong et al. 2013) and can be used to identify, in an automatic way, reference data within which abrupt changes have occurred. The normalized difference vegetation index (NDVI) (Tucker 1979) is a vegetation index based on a combination of red and near-infrared reflectance; it is sensitive to photosynthetically active vegetation and thus often has been used for vegetation monitoring, e.g., (De Jong et al. 2011; Ichii et al. 2013). Therefore, NDVI time series are one of the important tools to monitor inter-annual and intra-annual variations over a vegetated area (Forkel et al. 2013; Horion et al. 2014). There exist a number of long-term NDVI products, which are mostly based on a combination of different sensors. However, due to temporal inconsistency between the sensors, e.g., caused by orbital shift (Pinzón et al. 2005), these NDVI products may possess sensor artefacts, which can cause misinterpretations using time series analysis. By a comparison of three NDVI products derived from SPOT-VEGETATION, MODIS, and Advanced Very High Resolution Radiometer (AVHRR), Horion et al. (2014) concluded that the MODIS-based NDVI product is more consistent over time than other two products and showed a better potential to detect changes in tree cover in Sahel. Furthermore, MODIS NDVI data do not include platform orbital shift, and possess higher spatial resolution compared to AVHRR- and SPOT-VGT NDVI products.

In this study we investigated whether filtering of calibration data using change detection information obtained from remotely sensed data can improve AGB model performance. This was done by applying Breaks For Additive Seasonal and Trend (BFAST) analysis (Verbesselt et al. 2010a; Verbesselt et al. 2010b) on MODIS NDVI time series data in order to exclude field inventory plots within which abrupt changes were detected. We compared AGB estimates based on original reference data with results based on filtered reference data from the time series analysis. Moreover, due to the fact that canopy density correlates with aboveground biomass, we used the Landsat tree cover (TC) product (Sexton et al. 2013) as an additional predictor layer for SAR-based AGB models. Furthermore, we included altitude from the Shuttle Radar Topography Mission (SRTM) Digital Elevation Model (DEM) in the AGB modelling. We modelled AGB using a different number of input layers, e.g., using SAR backscatter intensities and interferometric coherences separately and together with Landsat TC and SRTM DEM products, and assessed the modelling

performance. Our approach was tested over two study sites located in dry and humid tropical forests in southern Mexico.

## **2.2 Materials and Methods**

### **2.2.1 Study area**

The two study areas are located in the United Mexican States (hereafter Mexico) and are shown in Figure 2-1 together with the Advanced Land Observing Satellite's Phased Array type L-band Synthetic Aperture Radar (ALOS PALSAR) footprints (red and blue polygons). The first study area (Figure 2-1, blue polygon, hereafter Campeche) is partly located in the National Park "Los Petenes-Ría Celestún" in the Campeche and Yucatan federal states. The western part represents a mosaic of mudflats, mixed with mangroves, while the eastern part of the study area is characterized by dry deciduous forests. The climate in the region is tropical sub-humid, with yearly precipitation near 1000 mm, mostly occurring during the summer; the average annual temperature is 26 °C (Flores and Carvajal 1994). The surface consists of a coastal plain with some hills with an average elevation of 37.2 m and a standard deviation of 36.8 m. The mean slope is 1.5° with a standard deviation of 1.8°.

The second study area is located in the Lacandon rain forest region in the north-western part of the state of Chiapas (Figure 2-1, red polygon, hereafter Comillas), and extends over the Montes Azules Biosphere Reserve and the communal lands of Marques de Comillas. The predominant vegetation type in the region is tropical evergreen and semi-evergreen rainforests (De Jong et al. 2000). The climate is humid tropical with the average annual temperature of 25 °C for the areas below 800 m (Mendoza and Dirzo 1999). Average annual precipitation ranges from 2000 mm to 3500 mm, while the period between June and September is characterized by pronounced rainfall, and the relatively dry period extends between February and April (De Jong et al. 2000; Mendoza and Dirzo 1999). An average elevation in the study area is about 280 m with a standard deviation of 195 m. The mean slope is 5.5° with a standard deviation of 6.4°. Since the region has been treated as a main source for timber (De Jong et al. 2000), it was massively deforested since 1960s (Mendoza and Dirzo 1999). The mean deforestation rates for the Lacandon rain forests (except Marques de Comillas) estimated for the periods 1974–1981 and 1981–1991 were 2.1% and 1.6% per year (Mendoza and Dirzo 1999), and 2.1% per year from 1990 to 2010 for the Marques de Comillas region (Couturier et al. 2012).

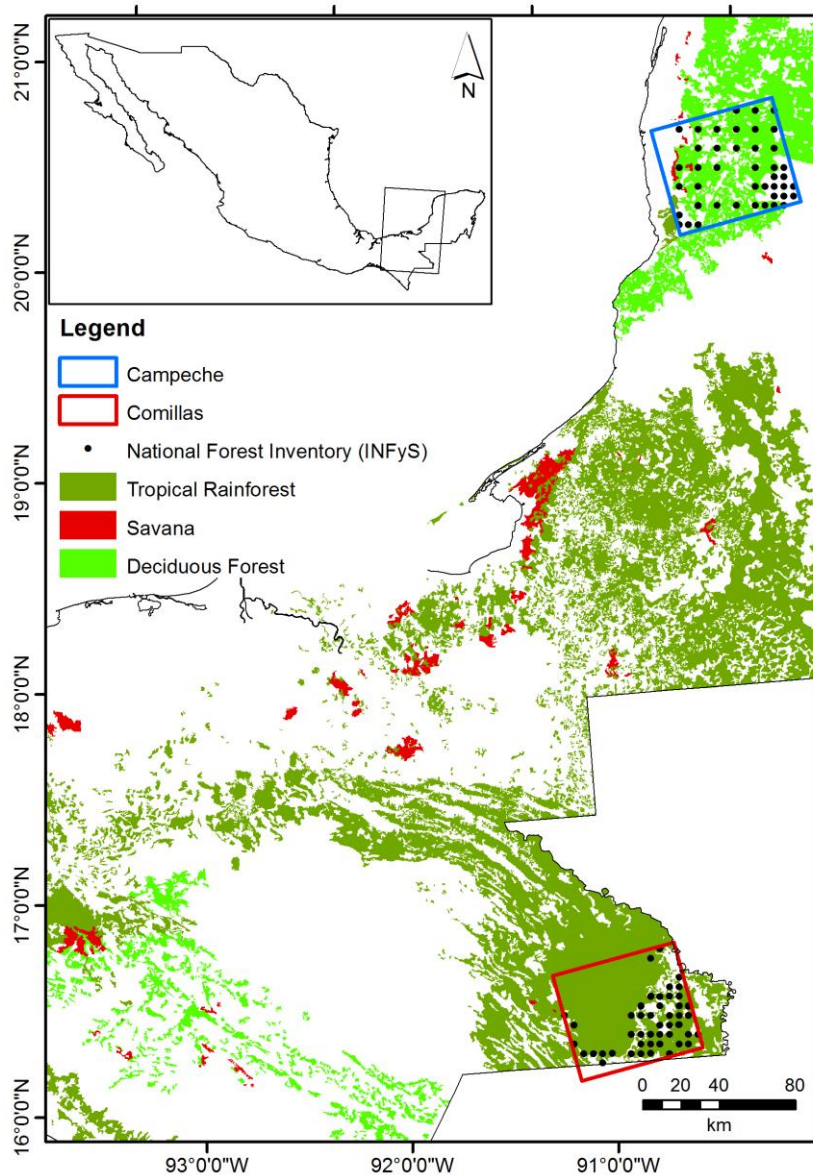


**Figure 2-1:** Study areas. Forest type information provided by the Instituto Nacional de Estadística y Geografía (INEGI) landcover map series IV.

## 2.2.2 Earth Observation Data

### 2.2.2.1 SAR Data

ALOS PALSAR data with a wavelength of 23.6 cm were used in this study. The SAR data were available in Single Look Complex (SLC) format acquired in the Fine Beam Single Polarization (FBS) (i.e., single HH (horizontal send-horizontal receive) polarization) and Fine Beam Double Polarization (FBD) (i.e., dual HH and HV (horizontal send-vertical receive) polarizations) modes with an incidence angle of

34.3°. FBS data were collected from December to April between 2007 and 2011 and FBD data were acquired from May to September between 2007 and 2010. Table 2-1 gives an overview of the number of datasets used in this study. Both FBS and FBD data cover an area of approximately 70 km × 70 km. From the PALSAR SLC data backscatter intensities were calculated (Section 2.2.4.1). Since some PALSAR data were acquired with a repetition of 46 days, interferometric coherences were calculated from the FBS/FBD data, and used as predictors for AGB modelling.

Furthermore, slope-corrected and orthorectified PALSAR mosaics backscatter data (Shimada and Ohtaki 2010) were used as predictor variables in the AGB modelling (Table 2-1). PALSAR mosaics were available in dual-polarization modes in HH/HV polarizations. The mosaics were built by Japan Aerospace Exploration Agency (JAXA) using PALSAR backscatter data and partly consist of backscatters that differ from the FBS and FBD data described above. The data were downloaded from the JAXA server (JAXA 2016) at 50 m spatial resolution.

**Table 2-1:** Earth observation data used in this study

<b>Data sets</b>	<b>Campeche</b>	<b>Comillas</b>
	<b>L-band backscatter:</b>	<b>L-band backscatter:</b>
	8 FBS (HH polarization)	12 FBS (HH polarization)
	5 FBD (HH/HV polarizations)	9 FBD (HH/HV polarizations)
SAR data	4 PALSAR mosaics (HH/HV polarizations)	4 PALSAR mosaics (HH/HV polarizations)
	<b>L-band coherence:</b>	<b>L-band coherence:</b>
	3 FBS pairs (HH polarization)	6 FBS pairs (HH polarization)
	2 FBD pairs (HH/HV polarizations)	4 FBD pairs (HH/HV polarizations)
Optical data	Landsat tree cover 2005 MODIS NDVI from 2005 to 2011	
Ancillary data	SRTM DEM altitude 2000 (1 arc-sec)	

### 2.2.2.2 Optical Data

As canopy density correlates with AGB, Landsat Tree Cover product (TC) for 2005 Version 3 (Sexton et al. 2013) was used in AGB modelling as an additional explanatory variable (Table 2-1). Sexton et al. (2013) rescaled MODIS Vegetation Continuous Fields (VCF) Tree Cover (Dimiceli et al. 2011) using circa 2005 Landsat imagery. Landsat TC product exhibits consistency with MODIS VCF product with improvements in discrimination of forest patches in fragmented landscapes (Sexton et al. 2013). The generated Landsat TC product for 2005 was validated with

independent LiDAR measurements collected over Costa Rica, Utah, California and Wisconsin and possessed an average RMSE of 17.4% (Sexton et al. 2013).

For the time series data analysis, MODIS NDVI 16-daily product at 250 m spatial resolution (MOD13Q1) product (NASA 2016) was used (Table 2-1). The time series data from January 2005 to December 2011 with the quality flags of 0 (i.e., “good data: use with confidence”) were selected. To gap-fill NDVI time series a linear interpolation between neighbouring values was applied (Verbesselt et al. 2006). MODIS NDVI time series data analysis for change detection is further described in Section 2.2.4.2.

### 2.2.3 INFyS Data

The reference INFyS data were collected between 2005 and 2011 by Comisión Nacional Forestal (CONAFOR) of Mexico (CONAFOR 2012). The sampling plot consisted of a single circular plot with a radius of 56.42 m covering an area of 1 ha and comprising four sub-plots with an area of 400 m<sup>2</sup> (0.04 ha). The plot design of INFyS data is similar to the United States Forest Service Forest Inventory and Analysis program (FIA) (Bechtold and Patterson 2005). From the central sub-plot three further sub-plots at an azimuth of 0°, 120° and 240° were defined. The plots are sampled over the whole country using rectangular grid with a distance between single plots varying from 5 km (in tropical and temperate forests) to 20 km (in arid regions). Within each sub-plot different biophysical parameters (e.g., diameter at breast height, tree height, etc.) were measured. AGB was calculated for each sub-plot using 339 species- and genus-specific allometric models and wood densities (CONAFOR 2016) and then extrapolated to 1 ha. If more than one model was available, the one with highest R<sup>2</sup> or with the closest regional relevance was used. Due to the lack of allometries, especially in the tropical areas, also pan-tropical generalized models (Brown 1997; Chave et al. 2005) were used.

Over the first study area (Campeche) 28 plots were measured twice, i.e., in 2005 and 2011, and 13 plots were sampled once either in 2005 or in 2011. For the field plots which were measured twice a mean value for two AGB estimates was calculated in order to reduce variations in the data, which can be caused for instance by wrong measurements. We used data from 41 field plots (hereafter original reference data) for AGB modelling (Section 2.2.4.3) and validation (Section 2.2.4.4) in Campeche study area. In the Marques de Comillas region three plots have less than four sub-plots and three plots were located on the steep slopes (greater than 15°) and were excluded from the calibration/validation procedure. Twenty-five field



plots were sampled twice either in 2005 or in 2011 and 16 once, resulting in 41 plots which were used as original data. Field-based AGB estimates range from 0 to 130 t/ha and from 0 to 170 t/ha in Campeche and Comillas study areas, respectively (Figure 2-2).

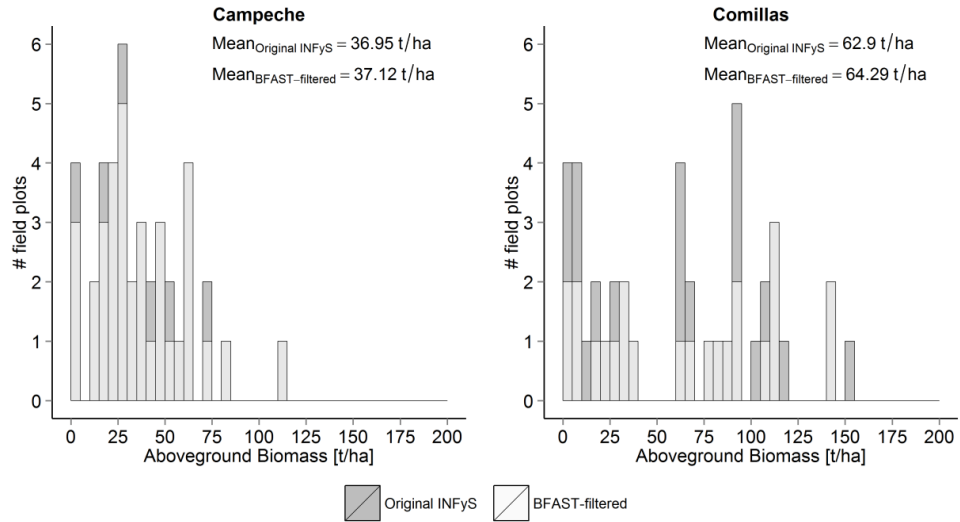


**Figure 2-2:** AGB distribution over Campeche (**left**) and Comillas (**right**) study areas before (dark grey bars) and after BFAST-filtering (light grey).

#### 2.2.4 Processing steps

This study is based on two main steps. Firstly, we identified forest inventory plots within which abrupt changes were detected using MODIS NDVI time series and BFAST (Verbesselt et al. 2010a; Verbesselt et al. 2010b). In the next step we used multi-sensor remote sensing data and temporally stable inventory plots to model AGB. In the following subsections a detailed description of each steps is presented (Figure 2-3).

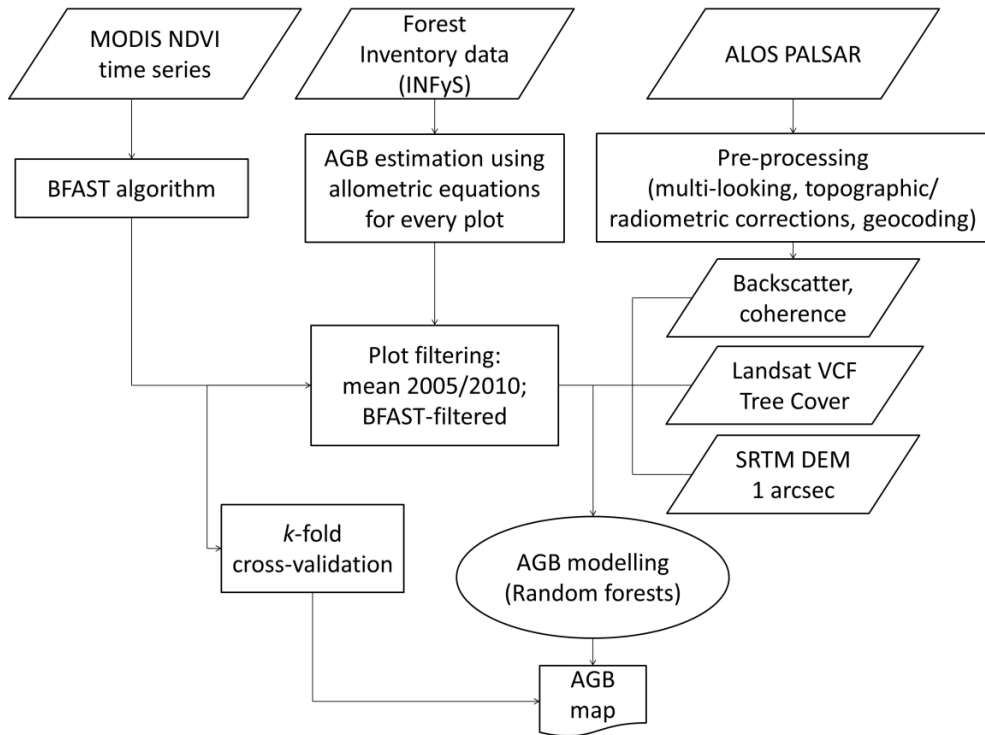


Figure 2-3: Flow chart of the data processing and analysis steps

### 2.2.4.1 SAR Data Processing

On the SLC level 1.1 datasets, a multi-look technique was firstly applied. The original spatial resolution of FBS data in radar geometry was  $4.68 \text{ m} \times 3.23 \text{ m}$  in the range and azimuth directions, respectively. The FBS data were therefore multi-looked by factors 1 and 2 in range and azimuth, resulting in a multi-looked ground resolution of  $8.3 \text{ m} \times 6.46 \text{ m}$ . Using bilinear interpolation the FBS data were oversampled to a pixel size of  $6.25 \text{ m} \times 6.25 \text{ m}$ . For FBD data, which original spatial resolution in radar geometry was  $9.37 \text{ m} \times 3.23 \text{ m}$  in the range and azimuth directions, respectively, multi-looking factors of 1 and 5 in range and azimuth were applied, resulting in a multi-looked ground resolution of  $16.63 \text{ m} \times 16.15 \text{ m}$ . The FBD data were then oversampled to a pixel size of  $12.5 \text{ m} \times 12.5 \text{ m}$  using bilinear interpolation. The multi-look images were radiometrically calibrated using a sensor-specific calibration factor ( $-115 \text{ dB}$ ). Using SLC scene pairs, interferometric coherences were calculated with similar multi-looking factors described above for FBS and FBD data. The SAR parameters were terrain corrected and geocoded using SRTM DEM. The geocoded SAR parameters were then normalized for topographic effects after Castel et al. (2001). The geocoded and terrain-corrected SAR parameters with different pixel sizes were aggregated to a pixel size of  $50 \text{ m}$  using a

block averaging technique. The aggregation of pixels reduces the influence of speckle noise in the SAR data and the co-registration uncertainty between reference and SAR data (Saatchi et al. 2011b).

#### **2.2.4.2 Change Detection Method of NDVI Time Series**

To update calibration data and to exclude outdated field plots, we applied BFAST (Verbesselt et al. 2010a; Verbesselt et al. 2010b) to detect plots within which abrupt changes in the remote data have been occurred, indicating potential disturbance or land use change occurring in that particular plot. BFAST is a generic statistically based change detection method developed for time series data, successfully validated for forest change (Verbesselt et al. 2010a) as well as for the detection of phenological events (Verbesselt et al. 2010b). The algorithm decomposes time series data into trend, seasonal and noise components and detects changes within them. To test whether one or more changes (i.e., breakpoints) in the trend component of time series are occurring, the ordinary least squares (OLS) residual-based MOving SUM (MOSUM) test is applied (Zeileis 2005). By an indication of significant change in the trend component, the breakpoints are estimated using the Bayesian Information Criterion (Verbesselt et al. 2010a). Verbesselt et al. (2010a) tested this approach using simulated NDVI time series data with varying magnitude of seasonality and noise as well as using 16 day MODIS NDVI imagery over a forested area in southern Australia. The both tests verified that the algorithm is able to detect and characterize abrupt changes in trend component with robustness against noise and seasonal changes. Furthermore, Dutrieux et al. (2015) successfully applied this algorithm on MODIS NDVI data to monitor forest cover loss in a tropical dry forest of Bolivia (overall accuracy of 87%).

We applied BFAST algorithm on MODIS NDVI 16-daily product at 250 m spatial resolution over the field plot areas for a time frame between January 2005 and December 2011. We increased a parameter  $h$  (i.e., “the minimal number of observations in each segment divided by the total length of the time series” (BFAST 2016)) in the algorithm to 0.5 (default value 0.1) to reduce the number of breakpoints, i.e., only main big and confident changes were detected. Other parameters have been kept at the default values. In the case of detecting a change (i.e., breakpoint) over a field plot from 2005 to 2011, the field plot was excluded from the AGB model calibration/validation procedure.

### 2.2.4.3 AGB Modelling

AGB was modelled for two study areas using a non-parametric model, random forests algorithm (RF) (Breiman 2001). This machine learning method generates many regression trees with a random selection of predictors at each node as well as with a random subset of samples for each tree with the aim of avoiding overfitting. In order to calculate a single estimate, the predictions of each regression tree are averaged (Breiman 2001). The RF is a computational efficient and robust non-parametric model and was successfully applied to map vegetation structure metrics (e.g., AGB, tree height) with high retrieval accuracy at large spatial scales, e.g., (Avitabile et al. 2012; Baccini et al. 2008; Cartus et al. 2012a). Our random forests were generated with 500 regression trees.

We modelled AGB using three scenarios: (1) a scenario based on original reference data; (2) a scenario based on BFAST-filtered reference data; and (3) a scenario based on random sampling of the same number of observations from the unfiltered data as was used for the BFAST-filtered data. The last scenario was conducted in order to show that the improvements in AGB estimations are due to BFAST-filtering and not due to a reduced number of observations. The random sampling was run 10 times. Furthermore, to investigate the impact of single predictor layers, we modelled AGB using different input variables, e.g., based on PALSAR backscatter intensities, PALSAR interferometric coherences only or in combination with Landsat TC and altitude from SRTM DEM.

### 2.2.4.4 *k*-Fold Cross-Validation

In order to estimate the accuracy of generated products, we applied the *k*-fold cross-validation technique. Using this technique the dataset is randomly divided in a number of folds (in our case we used 10 folds). One single fold is kept for model validation, while *k*-1 folds are used for model calibration. This procedure is then repeated *k* times until all folds have been used as calibration and validation data. All *k* estimates are finally summarized and a linear regression with the coefficient of determination ( $R^2$ ), root mean square error (RMSE) and bias between predicted and observed data is calculated. The benefit of this validation technique is that each observation will be used once for calibration and validation, so that the dataset is completely validated.

### 2.3 Results

The primary objective of this study was to determine whether AGB estimations can be improved by combining multi-sensor remote sensing data and MODIS NDVI time series data. To address this question, we applied the BFAST algorithm on MODIS NDVI time series. The field plots, where abrupt changes were detected, were excluded from the model calibration and products validation. In Figure 2-4 an example of such a field plot is illustrated, showing Google Earth imagery from 2005 and 2011 over a sample plot in the Campeche region where abrupt changes caused by deforestation have occurred. A corresponding BFAST graph for this field plot, consisting of NDVI values ( $Y_t$ ), and seasonal ( $S_t$ ), trend ( $T_t$ ) and noise ( $et$ ) components, presents the detection of abrupt changes in the trend component (Figure 2-4, below).

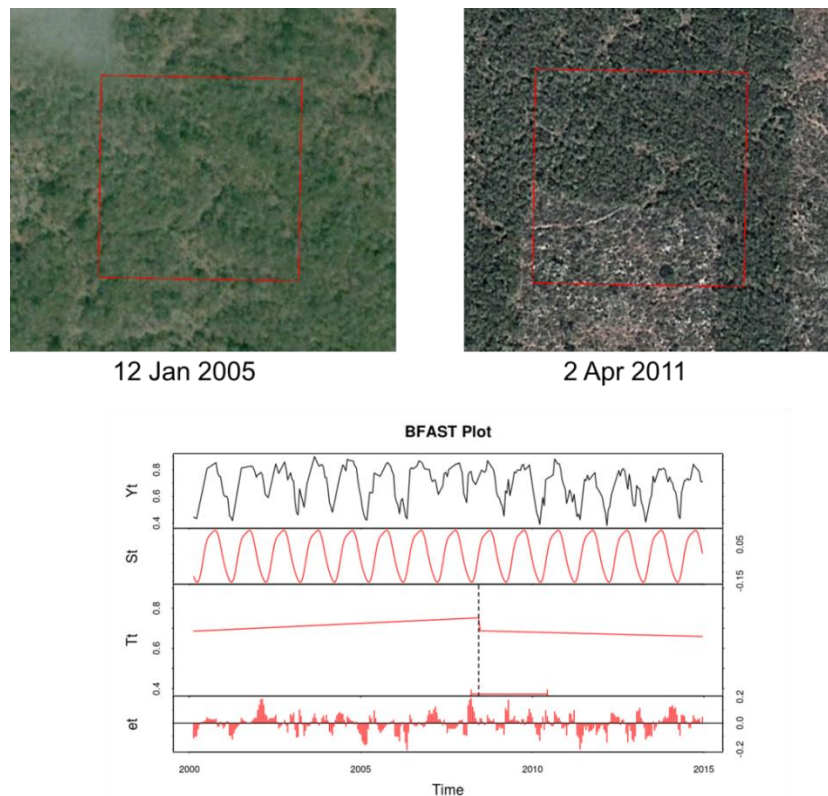


**Figure 2-4:** Google Earth imagery from 2005 and 2011 over a field plot (**red polygon**) showing an example of abrupt changes (**above**) and corresponding BFAST plot (**below**) with NDVI values ( $Y_t$ ), and seasonal ( $S_t$ ), trend ( $T_t$ ) and noise ( $et$ ) components.

We modelled AGB using original, BFAST-filtered and randomly filtered reference data as well as using different predictor variables (Section 2.2.4.3). Using the BFAST algorithm, six and 18 plots were excluded in the Campeche and Comillas study areas, respectively. Accordingly, 35 and 23 BFAST-filtered field plots for Campeche and Comillas were used for AGB modelling. In order to ensure that improvements in AGB estimations are not due to a reduced number of calibration data but due to BFAST, we modelled AGB with 35 and 23 randomly sampled calibration data plots for the Campeche and Comillas study sites, respectively. This random sampling was applied 10 times. The statistics computed using modelled and reference AGB estimates are shown in Figure 2-5 for the Campeche and Comillas study areas, respectively. The bars by randomly filtered data indicate mean values with the standard deviation shown as error bars. Compared to the results based on the original reference data, AGB estimates based on BFAST-filtered reference data exhibit 8% and 38% higher  $R^2$  values for the Campeche ( $R^2_{\text{orig}} = 0.65$  vs.  $R^2_{\text{BFAST}} = 0.7$ ) and Comillas ( $R^2_{\text{orig}} = 0.45$  vs.  $R^2_{\text{BFAST}} = 0.62$ ) study regions, respectively, when using all predictor variables. For the Campeche study area the AGB estimates based on BFAST-filtered data show a slightly lower RMSE compared to the results based on the original reference data. For the Comillas study area the RMSE decreases substantially by around 16% ( $\text{RMSE}_{\text{orig}} = 33.78$  t/ha vs.  $\text{RMSE}_{\text{BFAST}} = 28.4$  t/ha). AGB estimates based on randomly filtered data showed in most cases the lowest mean  $R^2$  as well as the highest mean RMSE for both study areas compared to two other scenarios (Figure 2-5). This indicates that the improvements in AGB estimations are caused not by the reduction of the sample size in the unfiltered data, but by the application of BFAST-filtering. In terms of bias, the results based on BFAST-filtered data showed generally higher bias values than those based on original INFyS data for both test sites. The reason for this can be that the original data contains lower AGB values (Figure 2-2), which can introduce a low bias in the training set.

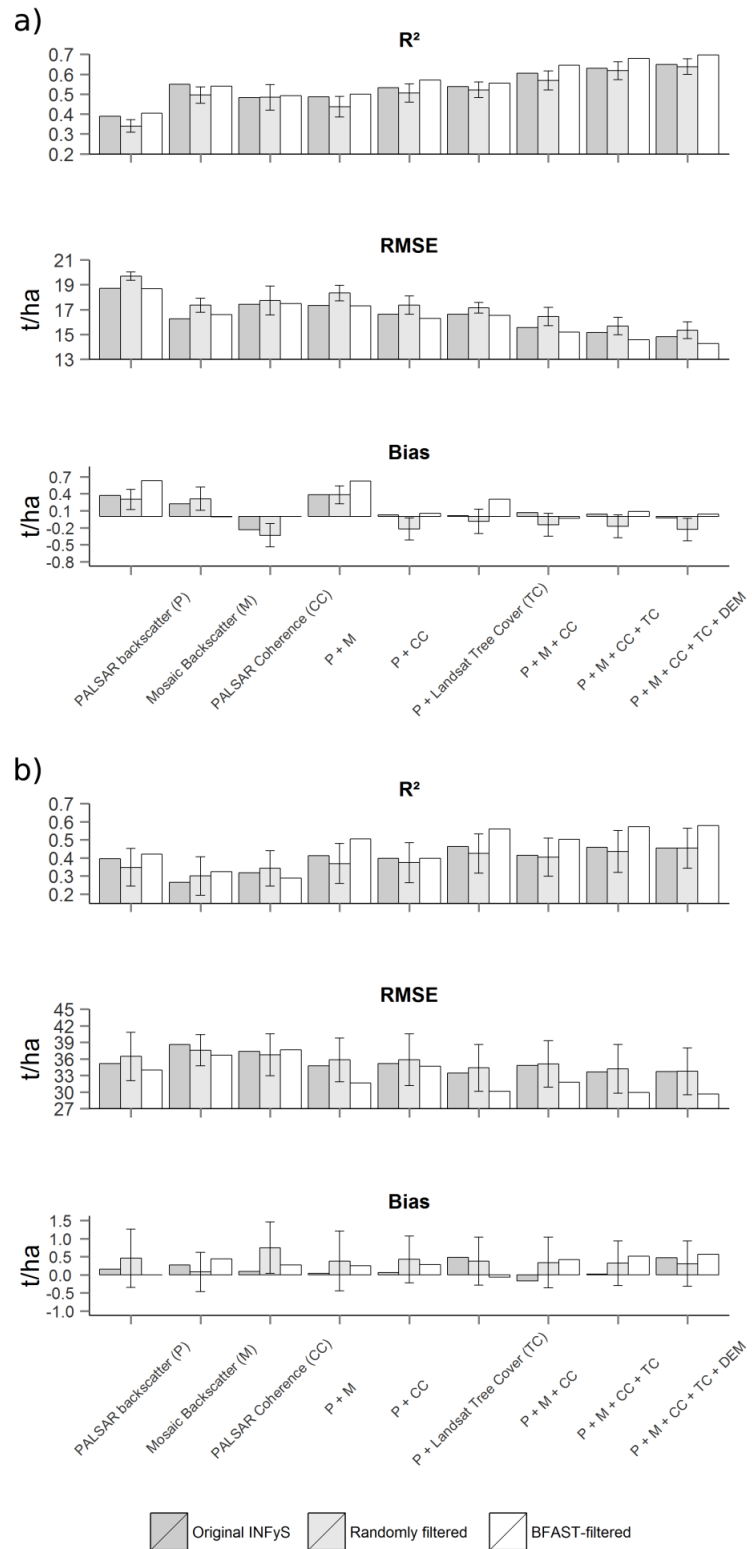


**Figure 2-5:**  $R^2$ , RMSE and bias between estimated and observed AGB using different reference data and predictor variables over Campeche (a) and Comillas (b) study areas. P: FBD and FBD PALSAR backscatter; M: PALSAR mosaic backscatter; CC: PALSAR interferometric coherence; TC: Landsat Tree Cover

Direct comparisons of the performance of AGB models based on original and BFAST-filtered data and all available predictor layers for the Campeche and Comillas study areas are shown in Figure 2-6 and Figure 2-7 (note: 1 ha field inventory plot was covered by four satellite imagery pixels with a spatial resolution of 50 m). In the Campeche study area, only within six field plots abrupt changes were detected and the corresponding number of plots was screened out. This results in a similar distribution of points in the scatterplots with similar statistical metrics (Figure 2-6). In this region BFAST excluded primarily outlier and mixed pixels in the low AGB range, which have changed over time. In contrast, in the Comillas region, where the deforestation activities have been observed since the 1960s (Couturier et al. 2012; Mendoza and Dirzo 1999), 18 field plots were excluded from the calibration data. In Comillas BFAST removed outlier and mixed pixels at low biomass range as well as plots with high biomass ( $>100$  t/ha), indicating deforestation/forest degradation within those field plots (Figure 2-7). Accordingly the model performance is improved significantly in terms of  $R^2$  and RMSE. The point distributions along the 1:1 line in Figure 2-6 and Figure 2-7 showed typical under-/over-estimation patterns for tree-based regression models, as the predictions of such tree-based models are computed as the average values of the regression trees within each node (Baccini et al. 2008; Breiman 2001). Moreover, a lower prediction performance at high biomass ranges (over 100 t/ha) for both study sites can be additionally caused by reaching the saturation level of the SAR signal.

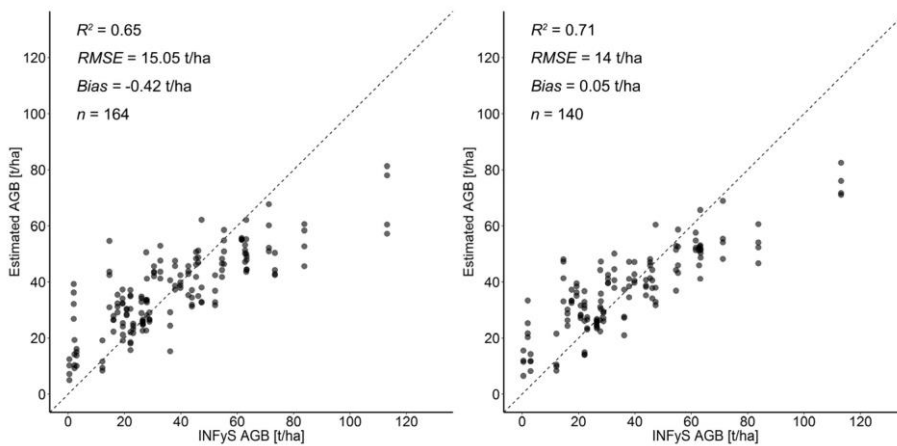


**Figure 2-6:** Comparisons of observed and predicted AGB estimates based on original (left) and BFAST-filtered (right) NFI data in Campeche study area. Dotted line is the 1:1 line.



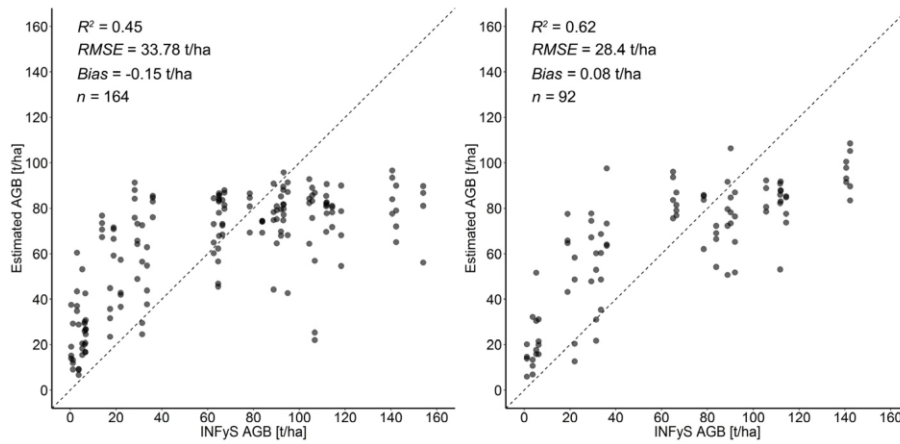


**Figure 2-7:** Comparisons of observed and predicted AGB estimates based on original (left) and BFAST-filtered (right) NFI data in Comillas study area. Dotted line is the 1:1 line.

To investigate the impact of a single predictor on AGB modelling, we estimated AGB using, e.g., PALSAR backscatter intensities or interferometric coherences separately as well as in combination with further parameters. The inclusion of additional predictor layers (e.g., Landsat TC, SRTM DEM) with SAR products improves AGB estimations and they achieve the highest accuracy (in terms of  $R^2$  and RMSE) when all predictors are used for all three scenarios: i.e., using original INFyS, BFAST-filtered and randomly filtered data (Figure 2-5). These results based on the multi-sensor combination are in agreement with previous studies, e.g., (Cartus et al. 2012a; Cartus et al. 2014; Rodríguez-Veiga et al. 2016).

## 2.4 Discussion

The accuracy of AGB estimates based on original data is consistent with the results produced by the authors of (Cartus et al. 2014) in terms of statistical metrics ( $R^2 = 0.52$  (Cartus et al. 2014) vs.  $R^2 = 0.55$  (mean for Campeche and Comillas);  $RMSE = 28.2$  t/ha (Cartus et al. 2014) vs.  $RMSE = 23.8$  t/ha (mean for Campeche and Comillas)), while AGB estimates based on BFAST-filtered plots produce more accurate estimates.

The use of MODIS NDVI time series data to detect areas with abrupt changes has the advantage of being fully automated and so can be applied over large areas. Nevertheless, we cannot exclude the confounding influence of the false detection of abrupt changes over field plots, bearing in mind a lower spatial resolution of a MODIS NDVI pixel compared to the plot area (250 m vs. 100 m), and the possible influence of clouds and cloud shadows. Earth observation data at higher spatial resolution (e.g., Landsat) are limited for the calculation of seasonal trends over large areas taking into account cloud cover, SLC-off gaps, as well as restricted access to the whole Landsat archive. However, the launch of the ESA Sentinel-1/Sentinel-2 satellites with free-of-charge imagery opens new perspectives for time series analysis at high spatial resolution. A multi-sensor combination of Landsat and Sentinel-2 time series data as well as fusion with SAR imagery (Reiche et al. 2015) has great potential to enhance time series analysis both in spatial detail and in temporal coverage, potentially leading to a near-real-time forest monitoring system. The inclusion of additional predictor layers (e.g., interferometric coherence, Landsat TC) leads to an improvement of AGB modelling, and the highest prediction performance was achieved when all available predictor variables were used for both test sites. In the Campeche study site, FBS and FBD PALSAR backscatters showed a lower prediction performance compared to four yearly PALSAR mosaic backscatters and interferometric coherences (Figure 2-5a). The most likely reason is that only five dual-polarized (FBD) backscatter images were available, while one annual PALSAR mosaic consists of different FBD data and may contain additional information. Furthermore, as was shown in Siberia (Stelmaszczuk-Górska et al. 2016), PALSAR coherence was a more important predictor variable than PALSAR backscatter for AGB assessment at a low biomass range (up to 60 t/ha). In the Campeche region, mean field-estimated AGB is around 35–40 t/ha, so L-band interferometric coherences could better explain the AGB distribution than backscatter intensities. However, in the Comillas study site, where a dense stack of L-band backscatters

(nine dual-polarized (FBD) together with 12 single-polarized (FBS) backscatters) were available, the backscatter-based AGB model outperformed the models based on PALSAR mosaic backscatters and coherence data (Figure 2-5b). Moreover, this region exhibits higher AGB distribution (up to 150 t/ha) than Campeche, which can further restrict the use of interferometric coherence in this area. However, SAR-based AGB estimates (i.e., based on PALSAR backscatter, coherence and PALSAR mosaic backscatter) exhibit only slightly lower  $R^2$  ( $R^2_{\text{SAR}} = 0.65$  vs.  $R^2_{\text{all}} = 0.7$  for Campeche and  $R^2_{\text{SAR}} = 0.54$  vs.  $R^2_{\text{all}} = 0.62$  for Comillas), suggesting that L-band SAR data alone would be appropriate for AGB modelling in these tropical dry and humid forests.

The results in the Comillas region are less accurate than in Campeche in terms of statistical metrics due to the several reasons. Firstly, in the Comillas study area tropical rain forests with a higher AGB distribution have occurred, which restricts the use of L-band data in these dense forests. Furthermore, the average annual precipitation in Comillas is more than twice that in Campeche (2000–3500 mm vs. 1000 mm). This leads not only to an increased water content in tree crowns but also to an increased soil moisture, which further limits SAR data for AGB modelling. Finally, the Campeche region is located on a coastal plain with a flat terrain, while in Comillas site hills with partly steep slopes ( $>15^\circ$ ) are present, which not only restricts SAR data but also can increase geolocation and measurement errors of field data. Collectively, these factors (e.g., denser, moister forests in complex terrain) lead to a decrease of AGB modelling performance in the region.

Moreover, we observed in both study sites an underestimation of AGB modelling for the range higher than 100 t/ha (Figure 2-6 and Figure 2-7). From one side it is caused by the L-band signal saturation that occurs in this range. From the other side it is caused by the tree-based regression model itself, as the predictions of the random forest model are computed as the average values of the regression trees within each node (Baccini et al. 2008; Breiman 2001). Finally, due to the global acquisition strategy implemented by JAXA (Rosenqvist et al. 2004), the L-band cross-pol data (HH/HV polarizations) were acquired between May and September during the rainy season in Mexico. During this season, the water content in vegetation and soil moisture is increased and accordingly limits the use of HV SAR backscatter, which correlates stronger with the vegetation structure than HH SAR backscatter (Rauste et al. 1994; Watanabe et al. 2006). In general, AGB estimations are restricted by possible geolocation inaccuracies of the field data as well as by the fact that the total sampled area of 0.16 ha was extrapolated to 1 ha. However, these sources of errors have an impact on general AGB estimations (i.e., using three

scenarios) and not on BFAST-filtering, since the same reference datasets were used for filtering.

## **2.5 Conclusions**

In this study we showed the improvements in AGB estimations by the filtering of calibration data using change detection information derived from time series analysis of remote sensing data. Our results indicate that MODIS NDVI time series data can be used to identify temporally stable field inventory data, which improves the performance of AGB estimations. The method was evaluated in two study areas in the tropical dry and humid forests of Mexico. Especially the performance of time series analysis was noticeable better in the Comillas region, which possesses high deforestation rates (Couturier et al. 2012). Moreover, we showed that the improvements in AGB estimations are caused by the application of BFAST-filtering and not by the reduction of the calibration data as shown for randomly selected data. Furthermore, results based on the combination of different predictor layers (i.e., SAR backscatter, interferometric coherence, Landsat TC, SRTM DEM) showed more accurate AGB estimations than those based on a single variable, providing additional explanatory information.

We showed that the filtering of reference data is an important step to improve AGB estimations using remotely sensed imagery. We argue that the presented method shows great potential to enhance AGB estimations and can be easily and automatically implemented over large areas (at national or biome scales).

**Acknowledgments:** The study was supported by the European Space Agency (ESA) within the Data User Element (DUE) project GlobBiomass (ESA Contract No.4000113100/14/I-NB) and has been undertaken within the framework of the JAXA Kyoto & Carbon Initiative. ALOS PALSAR data have been provided by JAXA EORC. ALOS PALSAR mosaic data were available from ©JAXA PALSAR MOSAIC 2014. The authors would like to thank the following organizations for providing remote sensing data: JAXA (ALOS PALSAR), University of Maryland (Landsat Tree Cover), NASA (MODIS and SRTM data). The authors would like to thank CONAFOR for providing INFyS field plot data. M.U. conducted this work under the International Max Planck Research School for Global Biogeochemical Cycles and acknowledges its funding and support. The authors also thank two anonymous reviewers for their valuable comments and suggestions to improve the quality of the paper.

**Author Contributions:** M.U. and C.T. conceived and designed the experiments; M.U. performed the experiments; M.U., C.T., and M.M. analyzed the data; M.M. contributed analysis tools; M.U. wrote the paper; All co-authors assisted the lead author in writing and revising the manuscript.

**Conflicts of Interest:** The authors declare no conflict of interest.

# Chapter 3

**Estimation of forest aboveground biomass and uncertainties by integration of field measurements, airborne LiDAR, and SAR and optical satellite data in Mexico**

M. Urbazaev<sup>1,2</sup>, C. Thiel<sup>1</sup>, F. Cremer<sup>1</sup>, R. Dubayah<sup>3</sup>, M. Migliavacca<sup>4</sup>, M. Reichstein<sup>4</sup>  
& C. Schmullius<sup>1</sup>

<sup>1</sup>Friedrich-Schiller-University Jena, Department for Earth Observation

<sup>2</sup>Max Planck Institute for Biogeochemistry, International Max Planck Research School

<sup>3</sup>University of Maryland, Department of Geographical Sciences

<sup>4</sup>Max Planck Institute for Biogeochemistry, Biogeochemical Model-Data Integration Group

Published in:

**Carbon Balance and Management** (2018), 13:5  
(Received 11 October 2017; Accepted 21 February 2018)

**DOI:** 10.1186/s13021-018-0093-5

## Abstract

Information on the spatial distribution of aboveground biomass (AGB) over large areas is needed for understanding and managing processes involved in the carbon cycle and supporting international policies for climate change mitigation and adaptation. Furthermore, these products provide important baseline data for the development of sustainable management strategies to local stakeholders. The use of remote sensing data can provide spatially explicit information of AGB from local to global scales. In this study, we mapped national Mexican forest AGB using satellite remote sensing data and a machine learning approach. We modelled AGB using two scenarios: (1) extensive national forest inventory (NFI), and (2) airborne Light Detection and Ranging (LiDAR) as reference data. Finally, we propagated uncertainties from field measurements to LiDAR-derived AGB and to the national wall-to-wall forest AGB map.

The estimated AGB maps (NFI- and LiDAR-calibrated) showed similar goodness-of-fit statistics ( $R^2$ , Root Mean Square Error (RMSE)) at three different scales compared to the independent validation data set. We observed different spatial patterns of AGB in tropical dense forests, where no or limited number of NFI data were available, with higher AGB values in the LiDAR-calibrated map. We estimated much higher uncertainties in the AGB maps based on two-stage up-scaling method (i.e., from field measurements to LiDAR and from LiDAR-based estimates to satellite imagery) compared to the traditional field to satellite up-scaling. By removing LiDAR-based AGB pixels with high uncertainties, it was possible to estimate national forest AGB with similar uncertainties as calibrated with NFI data only.

Since LiDAR data can be acquired much faster and for much larger areas compared to field inventory data, LiDAR is attractive for repetitive large scale AGB mapping. In this study, we showed that two-stage up-scaling methods for AGB estimation over large areas need to be analyzed and validated with great care. The uncertainties in the LiDAR-estimated AGB propagate further in the wall-to-wall map and can be up to 150%. Thus, when a two-stage up-scaling method is applied, it is crucial to characterize the uncertainties at all stages in order to generate robust results. Considering the findings mentioned above LiDAR can be used as an extension to NFI for example for areas that are difficult or not possible to access.



### **3.1 Background**

Tropical intact and regrowth forests have the highest carbon (C) uptake of the world's forests. They account for around 70% of global gross forest sink (Pan et al. 2011). At the same time tropical forests are nearly carbon-neutral taking into account C-emissions from tropical deforestation with the highest uncertainties in C-stocks and -fluxes compared to other biomes (Pan et al. 2011). The status of tropical forests and their temporal dynamics can be assessed by measuring different structural tree parameters (e.g., vegetation height, canopy cover, stem volume and AGB). AGB, defined as the total amount of aboveground living organic matter in vegetation and expressed as oven-dry tons per unit area (Brown 1997), is one of the crucial parameter to assess terrestrial aboveground C-stocks and -fluxes. Since vegetation biomass affects a range of ecosystem processes such as carbon and water cycling, energy fluxes, and thus affects local and regional climate, accurate AGB information is required for developing sustainable forest management strategies.

Traditionally, vegetation structural parameters are assessed using forest inventory data. These measurements are demanding in terms of costs and resources, and thus are limited in space and time. With rapid advances in information technology vegetation parameters can be estimated using remote sensing methods. In particular, in tropical forests remote sensing data provide spatially consistent information for areas that are difficult to access. Moreover, in contrast to point measurements spatial continuous AGB maps can improve estimates of carbon flux (Houghton 2005).

In the past 20 years a number of studies aiming at AGB estimation using remote sensing data have been published. These studies reach from local (e.g., Dubayah et al. 2010) over national (Avitabile et al. 2012; Cartus et al. 2014; Rodríguez-Veiga et al. 2016) to continental (Baccini et al. 2008) and intercontinental scales (Avitabile et al. 2016; Baccini et al. 2012; Saatchi et al. 2011a; Santoro et al. 2013). In general, remote sensing data from optical, Synthetic Aperture Radar (SAR), and LiDAR sensors or a combination of these sensors are used to estimate AGB. Optical remote sensing data (e.g., Landsat, Sentinel-2, MODIS) are sensitive to vegetation density (Avitabile et al. 2012), which relates to AGB but saturates at high biomass (e.g., Huete et al. 1997; Huete et al. 2002). Disadvantages in using optical data for AGB estimation are frequent cloud cover over the tropics, and strong dependence on environmental, seasonal and acquisition conditions (e.g., solar zenith angle) (Steininger 2000). Alternatively, SAR sensors can be used for the estimation of woody vegetation parameters (Antropov et al. 2017; Cartus et al. 2012b; Hame et al.

2013b; Mitchard et al. 2009b; Saatchi et al. 2011b; Santoro et al. 2015; Tanase et al. 2014a; Thiel and Schmillius 2016; Urbazaev et al. 2015). For instance, Hame et al. (2013b) showed that with L-band SAR data estimation of biomass in tropical forests was nearly as good as with optical imagery. Microwave signals (with a spectral range between 1 cm and 1 m) have the capability to penetrate into vegetation, and thus to probe the three-dimensional vegetation structure. Additionally, microwaves are particularly useful for weather independent applications, as long wavelengths penetrate clouds. Limitations of radar data for AGB estimation are saturation at middle-high biomass levels (depending on wavelength) as well as strong dependence on environmental conditions (e.g., rainfall, freezing, different moisture conditions). A way to delineate precise 3D information about the objects on the earth's surface (trees, buildings) and the topography is the usage of LiDAR. Laser pulses sent from a LiDAR sensor are capable to penetrate forest canopy, and to provide information on the vertical structure (e.g., height, canopy volume). LiDAR data can be used to delineate very accurate estimates of AGB without signal saturation. Accordingly, LiDAR is a key information source for assessing carbon stocks including tropical forests (Asner et al. 2012). Zolkos et al. (2013) compared more than 70 studies for AGB estimation and concluded that airborne LiDAR methods provide a higher accuracy compared to SAR or optical data. However, airborne LiDAR data is limited to a small spatial coverage.

The signals from optical, SAR, or LiDAR sensors are commonly compared to the field-estimated AGB using semi-empirical regression models or machine learning algorithms to extrapolate over the entire remote sensing imagery. As mentioned above the plot estimates of AGB are limited in time and space, and might thus not represent the full spectrum of vegetation types or AGB (Marvin et al. 2014). Alternatively, very high resolution (VHR) (<2m) remote sensing data from airborne LiDAR or optical sensors can be used as reference data for up-scaling to larger area. Currently, many large scale mapping efforts both for AGB estimation and forest cover delineation have been applied a two-stage up-scaling method (i.e., from field measurements to LiDAR strips or VHR optical imagery and from LiDAR-, VHR-based estimates to satellite imagery) (Baccini et al. 2012; Englhart et al. 2011; Hame et al. 2013a; Saatchi et al. 2011a; Su et al. 2016). One important step in the two-stage up-scaling method is error propagation analysis. As showed in (Holm et al. 2017; Saarela et al. 2016), ignoring the field to LiDAR error can underestimate the uncertainty in the final satellite-based AGB map by a factor of three or more.

Therefore, an uncertainty map at pixel level is important for the interpretation of the AGB map.

In this study, we estimated forest AGB in Mexico at national scale, where both extensive NFI (~15,000 plots) (Spanish acronym INFyS) and country-wide airborne LiDAR data were available. As spatial predictors to estimate AGB over Mexico we used satellite imagery from the Advanced Land Observing Satellite Phased Array type L-band Synthetic Aperture Radar (ALOS PALSAR), Landsat and the Shuttle Radar Topography Mission (SRTM), since a fusion of optical and SAR imagery provides more accurate estimates of AGB compared to single sensor type data (Cartus et al. 2014; Rodríguez-Veiga et al. 2016; Urbazaev et al. 2016; Xu et al. 2016). We estimated AGB at national scale using two modelling scenarios: 1) using INFyS data collected over the country with systematic sampling as calibration data for satellite imagery, 2) using airborne LiDAR-based AGB as calibration data for satellite imagery. Both national AGB products were validated with INFyS data that were not used for model calibration. Furthermore, we conducted an error propagation analysis for both scenarios and estimated uncertainties at pixel level using Monte Carlo simulations. This kind of comprehensive comparison between NFI and LiDAR data as reference for a large scale AGB mapping with satellite imagery including an error propagation analysis have not been conducted before. This gap needs to be addressed, especially in the context of the upcoming missions designed for global vegetation monitoring (e.g., NISAR, GEDI, BIOMASS, Tandem-L).

## 3.2 Methods

### 3.2.1 Study area and field data

Approximately one-third of Mexico is covered by forests resulting in 65 million ha (FAO 2015) with a variety of forest types (deciduous and coniferous forests, mangroves, cloud forests, and tropical dry and rain forests) (Figure 3-1). These forests are located at different topographies (from coastal plain in the Yucatan peninsula to mountainous regions in central part of the country).

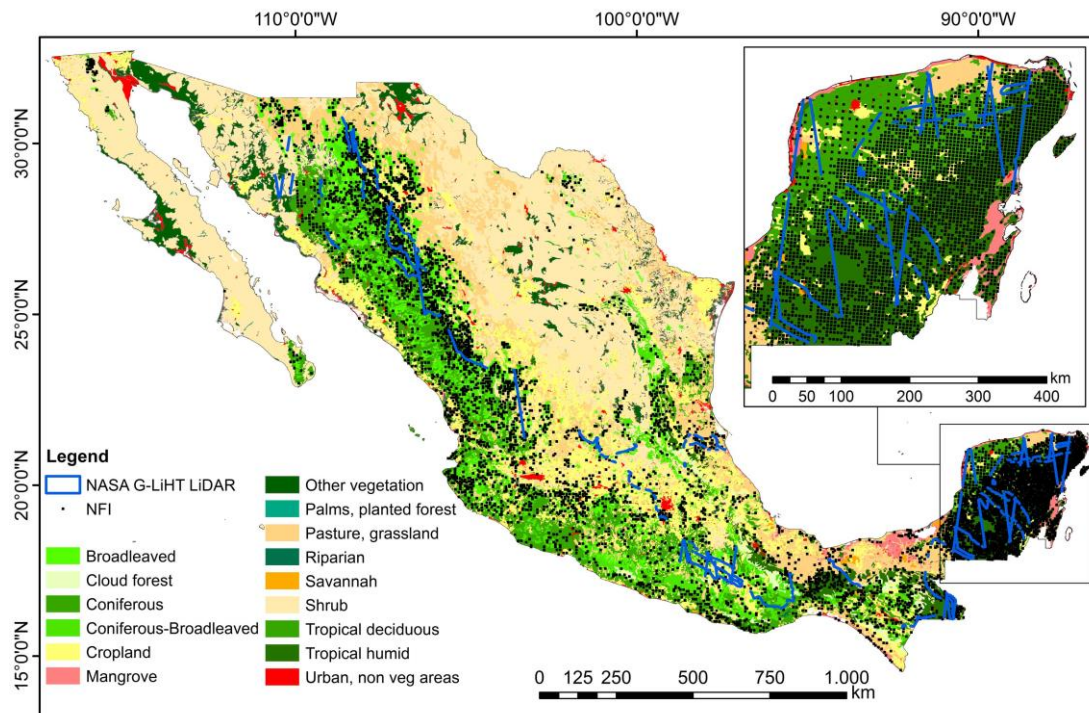


**Figure 3-1:** Land use and vegetation map of Mexico from the Mexican National Institute for Statistics and Geography (INEGI) Series IV (INEGI 2010)

The National Forestry Commission of Mexico (CONAFOR) has established a systematic nationwide network of forest inventory plots (Figure 3-1). In this study, NFI data collected between 2004 and 2011 were used. One sampling plot represents a single circular plot with a radius of 56.42 m covering an area of 1 ha and comprising four sub-plots with an area of 400 m<sup>2</sup> each (0.04 ha). For temperate and tropical forests different sampling designs were used (Figure 3-2). Each circular plot was sampled using rectangular grid with a distance between single plots varying from 5 km (tropical/temperate forests) to 20 km (arid regions) resulting in 28,869 plots, while most of the plots were sampled twice during the mentioned 7 year

period. Within each sub-plot different structural tree parameters (e.g., diameter at breast height, mean tree height etc.) were measured. AGB was calculated for each sub-plot (total sampled area of 0.16 ha) using 339 species- and genus-specific allometric models and wood densities (CONAFOR 2012) and then extrapolated to 1 ha. From all available INFyS data, plots with less than four sub-plots measurements were discarded (1786 plots). Further, for the plots comprising two temporal measurements (either 2004–2007 or 2008–2011) the temporal average was calculated. This step was conducted in order to reduce imprecision due to geolocation errors or inaccurate measurements resulting in 15,982 plots. Finally, inventory plots located on steep slopes ( $> 15^\circ$ ) were also excluded from the analysis (8441 plots), as they can be located in SAR layover and shadow areas and often show high geolocation errors. In total 7541 forest inventory plots were used for AGB mapping and product validation. From 7541 plots, 332 plots were used for AGB estimation along the LiDAR strips. The remaining 7209 field plots were divided into calibration (67%) and validation (33%) data sets based on biomass intervals. For this, the NFI data set were split into ten biomass classes with an interval of 30 t/ha, 67% from each class were selected randomly for calibration and the remaining plots were used for validation. An overview of the whole procedure can be found in Figure 3-4.

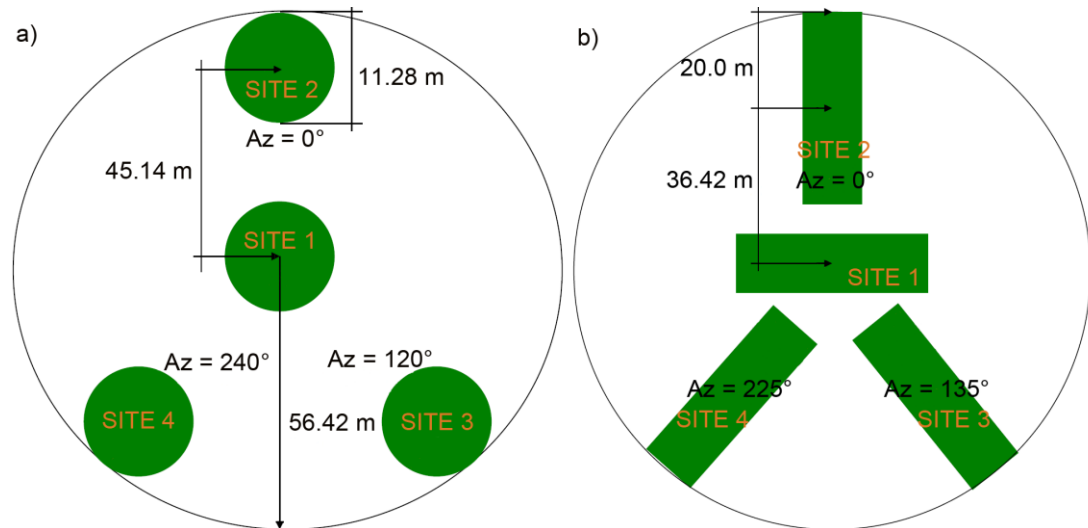


Figure 3-2: INFyS sampling plot design for a) temperate and b) tropical forests

### 3.2.2 Remote sensing data

#### 3.2.2.1 Airborne LiDAR data

Small footprint discrete-return airborne LiDAR data were collected by NASA's G-LiHT imager (Cook et al. 2013) in April–May 2013 over the entire country

resulting in 1123 strips (Figure 3-1). The average pulse density was approximately 6 returns/m<sup>2</sup>. The data were acquired during leaf-off conditions. From the topography-normalized point clouds 88 plot-aggregated LiDAR metrics as described in (Evans et al. 2009; Goetz et al. 2007; Naesset and Okland 2002) were calculated at 1 ha scale. These LiDAR metrics correspond to the vertical structure of a target and were used as predictor variables to estimate AGB along the LiDAR strips (Section 3.2.3.2).

### 3.2.2.2 Satellite imagery

In our study, we used ALOS PALSAR L-band SAR and Landsat optical data. The L-band SAR data were collected and processed by Japan Aerospace Exploration Agency (JAXA) in dual-polarization mode (i.e., HH/HV polarizations). The JAXA pre-processed ALOS PALSAR backscatter (gamma nought) mosaics were slope-corrected and orthorectified using a digital elevation model (DEM) (Shimada and Ohtaki 2010; Shimada et al. 2014). The mosaics feature a pixel spacing of 25 m x 25 m and are provided for free (JAXA 2016). In the next step, ALOS PALSAR backscatter images were speckle filtered using the multi-temporal filter after Quegan et al. (Quegan et al. 2000; Quegan and Yu 2001) with a window size of 7x7 pixels. In order to evaluate the amplitude of speckle, the equivalent number of looks (ENL) was calculated over homogeneous areas for original and filtered images using an empirical approach after (Oliver and Quegan 2004) (i.e.,  $ENL = \text{mean}^2 / \text{variance}$ ). The ENL was increased by factor 2 both for HH and HV polarizations indicating a reduction of speckle.

Optical data was used in form of spectral reflectance (SR) mosaic based on Landsat 5 and 7 ETM+ data for the year 2012. This Landsat SR mosaic was published by Hansen et al. (Hansen et al. 2013) and is freely accessible (University of Maryland 2016). From the Landsat SR the Normalized Differenced Vegetation Index (NDVI) was calculated and used as a predictor layer. A further predictor layer was the Landsat tree cover product by Hansen et al. (Hansen et al. 2013) for the year 2010. First independent product validations suggest that this tree cover product features high accuracy. For instance, a validation study conducted over South America based on VHR commercial optical imagery showed a strong agreement with an  $R^2$  of 0.82 (Pengra et al. 2015). Finally, altitude and slope information obtained from the Shuttle Radar Topography Mission (SRTM) DEM data version 4.1 (CGIAR 2016) were utilized in AGB modelling. All spatial data sets were aggregated to 100 m pixel size using block averaging and nearest neighbour

resampling. In total, 16 predictor layers were used for AGB estimation (Section 3.2.3) (Table 3-1).

**Table 3-1:** Remote sensing products used for AGB estimation at national scale

Remote sensing product	Spatial resolution	Acquisition Date	Layers
ALOS PALSAR	25 m	2007-2010	SAR backscatter: HH and HV polarization for 2007-2010
Landsat	30 m	2010-2012	Normalized Top-of-atmosphere (TOA) Reflectance: Band 3 (red), Band 4 (NIR), Band 5 (SWIR), Band 7 (SWIR); NDVI; Tree cover
SRTM DEM	30 m	2000	Altitude; Slope

### 3.2.3 AGB modelling and uncertainty analysis

As mentioned above, two modelling scenarios were applied. As NFI data were collected over the whole country, we developed a model that was calibrated with NFI data only (scenario 1, Section 3.2.3.3). In the other scenario, we applied a two-stage up-scaling method (i.e., from field measurements to LiDAR strips and from LiDAR-based estimates to satellite imagery) (Figure 3-3) (scenario 2, Sections 3.2.3.2, 3.2.3.4). Since NFI data were collected over forested areas only, we applied a forest mask to the wall-to-wall AGB maps. For this task, the Landsat tree cover product for 2010 (Hansen et al. 2013) was used (forest = tree cover > 10% according to FAO definition of forest (FRA 2012)).

We estimated uncertainties at pixel level for both scenarios using Monte Carlo simulations. For this, we introduced an error term in field-estimated AGB (Section 3.2.3.1) and propagated it to satellite-estimated AGB (Section 3.2.3.3). In the two-stage up-scaling method, first we propagated errors of field-estimated AGB to LiDAR-estimated AGB (Section 3.2.3.2) and the latter to satellite-estimated AGB (Section 3.2.3.4).

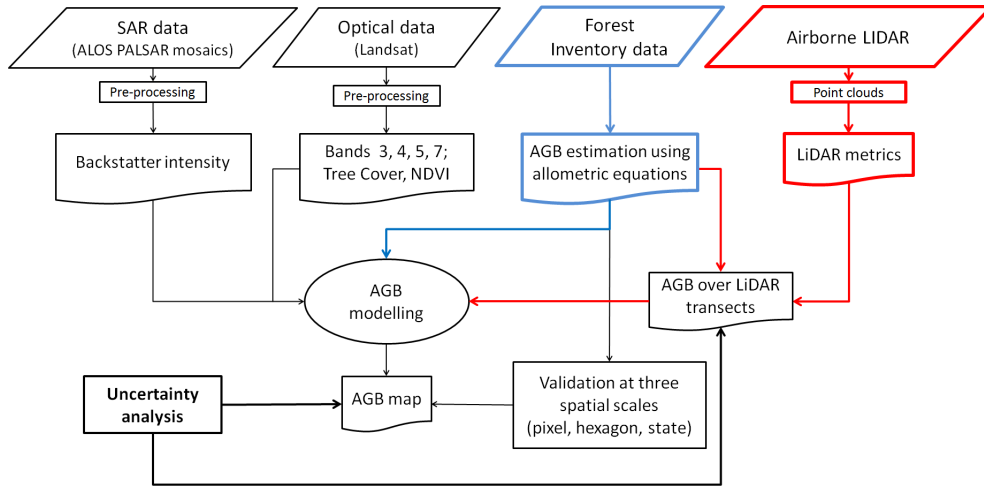


**Figure 3-3:** Flow chart of the data processing and analysis steps. Blue: first modelling scenario based on NFI data; red: second modelling scenario based on two-stage up-scaling method

### 3.2.3.1 Estimation of errors in the field-estimated AGB

The total error of the field-estimated AGB ( $\epsilon_{field}$ ) was composed of three components which were assumed to be independent and random and were calculated as follows:

$$\epsilon_{field} = (\epsilon_{measurement}^2 + \epsilon_{allometry}^2 + \epsilon_{sampling}^2)^{1/2} \quad (1)$$

where  $\epsilon_{measurement}$ ,  $\epsilon_{allometry}$ , and  $\epsilon_{sampling}$  are the measurement error of tree parameters (e.g., diameter at breast height (dbh) and tree height), allometric model error, and sampling error, respectively. Chave et al. (2004) estimated the measurement error of individual trees in central Panama to be 16%. As it averages out at stand level (Chave et al. 2004), it was assumed to be 10% in this study (Mitchard et al. 2011). For species-specific allometric models, we assumed an error of 11% (Chave et al. 2004). To estimate the sampling error, we approximated the errors using the study from (Chave et al. 2003). In the study in central Panama, the authors concluded that in order to estimate AGB for a 50 ha plot with  $\pm 10\%$  uncertainty at least 160 of 0.04 ha plots are needed (Chave et al. 2003). This requires a sampling intensity of 12.8%. By assuming similar variability in 1 ha pixel, and thus similar sampling intensity, the number of 0.04 ha plots required to estimate AGB with  $\pm 10\%$  uncertainty will be 3.2. Therefore, the sampling error in our study was 8.9% ( $10 \times \sqrt{3.2/4}$ ). By summing up each single error term, we suggest that our field-estimated AGB have an error of around 17%.



Under the assumption that our field-estimated AGB ( $Field_{AGB}$ ) have an error of 17%, we generated 100 realizations of field-estimated AGB ( $\widehat{Field}_{AGB}$ ) using normally distributed random values:

$$\widehat{Field}_{AGB\ i,j}^n = Field_{AGB\ i,j} \times (1 + \varepsilon_{field} \times X_{i,j}^n) \quad (2)$$

where the symbol “^” denotes a variable that includes the estimated error,  $n$  is number of Monte Carlo realizations,  $i, j$  is a single pixel,  $X$  is a random number from a normal distribution with mean = 0 and standard deviation = 1.

### 3.2.3.2 Estimation of AGB and uncertainties along the LiDAR strips

To estimate AGB along the LiDAR strips, all NFI data that were located completely within the LiDAR data were selected (332 plots). Since the difference in acquisition time between NFI and LiDAR data is between two to nine years, significant changes (caused, e.g., by fire or deforestation) within the field plots might have occurred (Urbazaev et al. 2016). Consequently, plots for which the residuals exceeded a range of two times the residual standard deviation (20 plots) were excluded from the analysis. For these 312 field plots 100 Monte Carlo realizations of field-estimated AGB ( $\widehat{Field}_{AGB}$ ) were generated and used as response variable. As spatial predictors 88 plot-aggregated LiDAR metrics ( $LiDAR_{metrics}$ ) were used. We estimated 100 different LiDAR-AGB calibrated with  $\widehat{Field}_{AGB}$  using a machine learning approach *Cubist*. *Cubist* is a hybrid tree-based approach that combines rule-based regression with linear multivariate models. Based on the training data a collection of rules is defined. A rule represents a path through a decision tree, for each rule a multivariate linear regression is used to calculate a predicted value. The final prediction is calculated by combining linear models at each node of the trees; therefore, it is smoothed compared to a single linear model. The approach is described in Quinlan (Quinlan 1992, 1993). *Cubist* is computational efficient and robust non-parametric model and was successfully applied to map vegetation structure metrics (e.g., AGB, tree height) with high retrieval accuracy at large spatial scales (Blackard et al. 2008; Gleason and Im 2012; Moisen et al. 2006; Walker et al. 2007).

The 100 LiDAR-AGB estimations for each pixel ( $LiDAR_{AGB\ i,j}$ ) were calculated:

$$LiDAR_{AGB\ i,j}^n = cubist(\widehat{Field}_{AGB\ i,j}^n, LiDAR_{metrics}) \quad (3)$$

From these 100 LiDAR-AGB realizations, 95% Confidence Interval (CI 95) was calculated:

$$CI95 (\widehat{LiDAR}_{AGB_{i,j}}^n) = \frac{CI_{97.5} - CI_{2.5}}{2} \quad (4)$$

The uncertainty for each LiDAR-AGB pixel was calculated:

$$\varepsilon_{LiDAR} = \frac{CI\ 95 (\widehat{LiDAR}_{AGB_{i,j}}^n)}{\overline{mean(LiDAR_{AGB_{i,j}}^n)}} \times 100 \quad (5)$$

### 3.2.3.3 Estimation of AGB and uncertainties at national scale with NFI-AGB as calibration data

For the first modelling scenario at national scale (i.e., based on NFI data only), we proceed similar as for the estimation of AGB along the LiDAR strips. The estimation of AGB at national scale was performed using a machine learning algorithm *Cubist* (Quinlan 1992, 1993). As response variable we used 100 Monte Carlo realizations of NFI-estimated AGB ( $\widehat{Field}_{AGB}$ ), while satellite data ( $Sat_{layers}$ ) (Section 3.2.2.2, Table 3-1) were used as spatial predictors. 100 AGB maps at national scale based on the first modelling scenario ( $\widehat{Sat\_NFI}_{AGB}$ ) were estimated as:

$$\widehat{Sat\_NFI}_{AGB_{i,j}}^n = cubist \left( \widehat{Field}_{AGB_{i,j}}^n, Sat_{layers} \right) \quad (6)$$

Based on the 100 NFI-calibrated national AGB estimates ( $\widehat{Sat\_NFI}_{AGB}$ ) the 95% confidence interval ( $CI\ 95 (\widehat{Sat\_NFI}_{AGB_{i,j}}^n)$ ) was calculated (Equation 4), and the uncertainty for each pixel was determined:

$$\varepsilon_{Sat\_NFI} = \frac{CI\ 95 (\widehat{Sat\_NFI}_{AGB_{i,j}}^n)}{\overline{mean(\widehat{Sat\_NFI}_{AGB_{i,j}}^n)}} \times 100 \quad (7)$$

Finally, we applied the Landsat tree cover product from 2010 (Hansen et al. 2013) to mask areas covered by forests.

### 3.2.3.4 Estimation of AGB and uncertainties at national scale with LiDAR-AGB as calibration data

In the second modelling scenario at national scale, a two-stage up-scaling method was applied. Similar to the first modelling scenario, we applied the machine learning algorithm *Cubist* (Quinlan 1992, 1993) and used the same satellite imagery ( $Sat_{layers}$ ) as spatial predictors (Table 3-1). As model calibration data we used 100 LiDAR-AGB estimations ( $\widehat{LiDAR}_{AGB}$ ) that already include the estimated error of field data and the model prediction error for the LiDAR strips. Accordingly, 100 AGB maps at national scale based on second modelling scenario ( $Sat\_LiDAR_{AGB}$ ) were estimated as:

$$Sat\_LiDAR_{AGB_{i,j}}^n = cubist \left( \widehat{LiDAR}_{AGB_{i,j}}^n, Sat_{layers} \right) \quad (8)$$

Again, based on the 100 LiDAR-calibrated national AGB estimates ( $Sat\_LiDAR_{AGB}$ ) the 95% confidence interval ( $CI\ 95(Sat\_LiDAR_{AGB_{i,j}}^n)$ ) was calculated (Equation 4) and the uncertainty for each pixel was determined:

$$\mathcal{E}_{Sat\_LiDAR} = \frac{CI\ 95(Sat\_LiDAR_{AGB_{i,j}}^n)}{mean(Sat\_LiDAR_{AGB_{i,j}}^n)} \times 100 \quad (9)$$

Additionally to the modelling scenario based on all LiDAR-AGB estimates, we estimated AGB at national scale using LiDAR-AGB samples with uncertainties below 50% ( $Sat\_LiDAR_{AGB_{uncert50}}$ ). This modelling scenario was conducted in order to prevent the propagation of high uncertainties of the LiDAR-AGB to the final AGB map. The threshold of 50% is a trade-off between retaining LiDAR samples for training and keeping the uncertainties of the wall-to-wall map at a low level (i.e., a lower threshold will lead to a lower number of training data; a higher threshold will lead to higher uncertainties in the wall-to-wall map). The number of remaining LiDAR-AGB samples can be found in Figure 3-4. In the next step, we estimated the uncertainties for AGB map calibrated with LiDAR-AGB pixels with uncertainties below 50% ( $\mathcal{E}_{Sat\_LiDAR_{uncert50}}$ ) (Equation 9).

Eventually, all non-forest areas were discarded again using the Landsat tree cover product from 2010 (Hansen et al. 2013).

### 3.2.4 Validation of mean forest AGB maps at different scales

Both national AGB maps (based on NFI and LiDAR training data) were validated at pixel level. For each modelling scenario (i.e., NFI- and LiDAR-calibrated AGB models), we calculated a mean AGB value from 100 Monte Carlo realizations. Goodness-of-fit statistics ( $R^2$ , RMSE, bias) were calculated between NFI- and LiDAR-calibrated mean AGB and the validation data set (Section 3.2.1) (Figure 3-4).

The validation was also performed at hexagon and state levels. Accordingly, we built a mesh of hexagons over the country with an area of 650 km<sup>2</sup> per hexagon. For each hexagon the modelled AGB (i.e., average of 100 Monte Carlo realizations) and the AGB based on forest inventory were extracted. The percentage of the forest cover per hexagon was considered using as a weighting factor. The forest areas were obtained from the Mexican National Institute for Statistics and Geography (INEGI) Land use map (INEGI 2010), since this map was used to establish the field plots. The national INEGI Land use map was generated using visually interpretation of SPOT optical imagery and field verification at a scale of 1:250,000.

For the validation at state level a similar procedure was applied. For each federal state, AGB values from the modelled maps and NFI plots were extracted and weighted by the forest area delineated from the INEGI Land use map (INEGI 2010). Finally, linear regressions and statistics ( $R^2$ , RMSE, bias) comparing modelled and field-estimated AGB were calculated at hexagon and state levels.

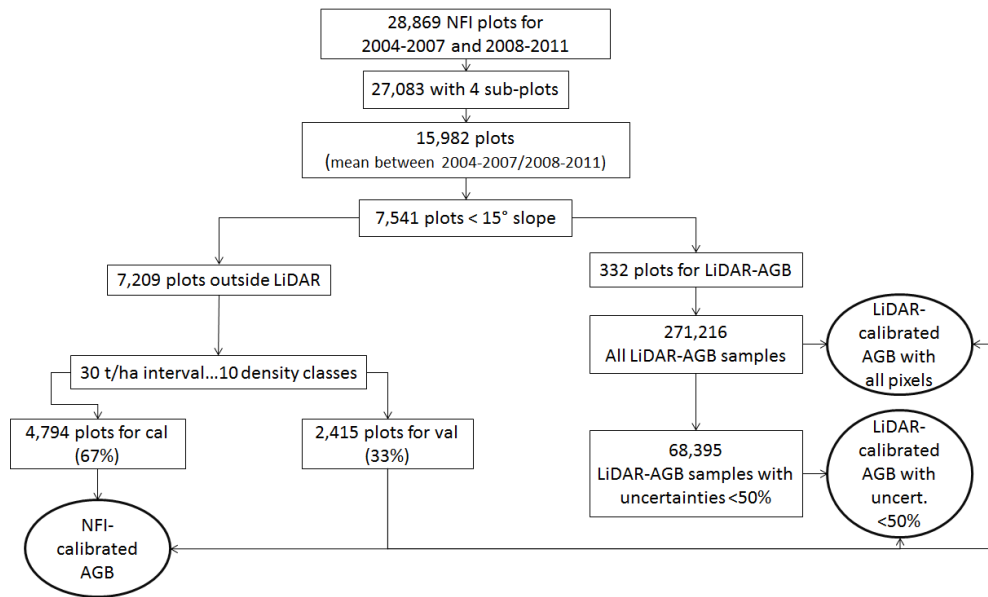


**Figure 3-4:** Filtering steps of reference data (both NFI and LiDAR) for calibration of satellite imagery and validation of the AGB maps.

### 3.3 Results

#### 3.3.1 Estimation of AGB and uncertainties along the LiDAR strips

In order to apply a two-stage up-scaling method (Section 3.2.3.4), we first estimated AGB along the LiDAR strips with the *Cubist* machine learning algorithm. We propagated the estimated field error (17%) to the AGB modelling running 100 Monte Carlo simulations (Equation 3). From the 100 AGB estimations, we calculated the mean AGB, CI 95, and the uncertainty for each single LiDAR pixel and plotted the simulation results against field-estimated AGB (Figure 3-5).

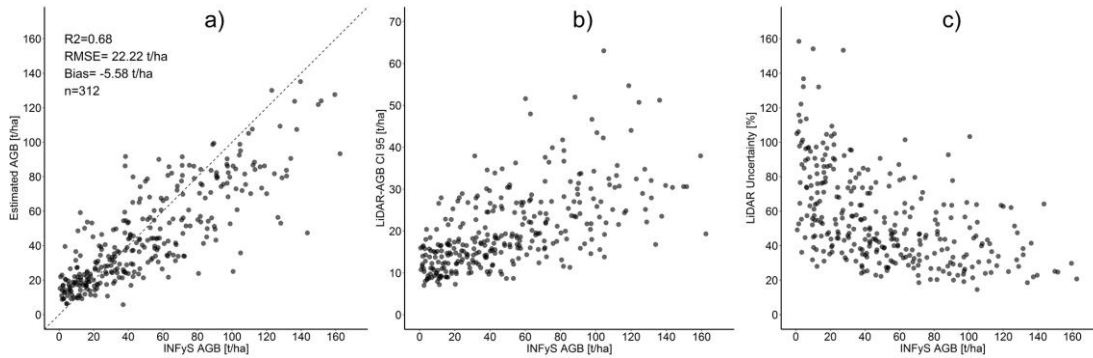


**Figure 3-5:** a) Linear regression between reference (INFyS) and predicted (LiDAR) AGB. The dotted line is the 1:1 line. b) CI 95 of LiDAR-estimated AGB increases with increasing reference AGB. c) The highest uncertainties of LiDAR-estimated AGB at low AGB range decreases with higher reference AGB.

Although the correlation between the mean estimated AGB (from Monte Carlo) and field-estimated AGB was strong (Figure 3-5a), the uncertainties in the LiDAR-AGB were very high and went up to 200% (Figure 3-5c, Figure 3-6c). The absolute AGB uncertainties (in our case CI 95) increased with increasing AGB (Figure 3-5b). However, the highest relative uncertainties were found in areas with low biomass (Figure 3-5c), as in these areas small absolute deviations easily result in large relative uncertainties (Equation 5).

Discrepancies between modelled and reference data are caused by different factors. First, the high variations in 100 LiDAR-AGB estimates (expressed in CI 95 and uncertainties) can be caused by a low amount of training data (i.e., 312 field plots were used to extrapolate AGB for more than 270,000 LiDAR samples), so that each model run produced diverse results. Second, the time lag between the acquisitions of LiDAR and NFI data was between 2 to 9 years, which introduces the

## Results

potential for changes between both data acquisitions. Third, the sampled area of NFI data of 0.16 ha was extrapolated to 1 ha, i.e., for some plots an area of 0.16 ha may be not representative for the 1 ha plot. Fourth, small inventory plots (4 subplots with 0.04 ha size) are more affected by geolocation errors, since they may not reflect the spatial variability in the surrounding area. As reported in (Zolkos et al. 2013), the errors in LiDAR-estimated AGB decrease exponentially with a decreasing plot size, due to spatial averaging of errors (Goetz and Dubayah 2011). Finally, a universal AGB model developed for different forest types can produce additional errors in the prediction results.

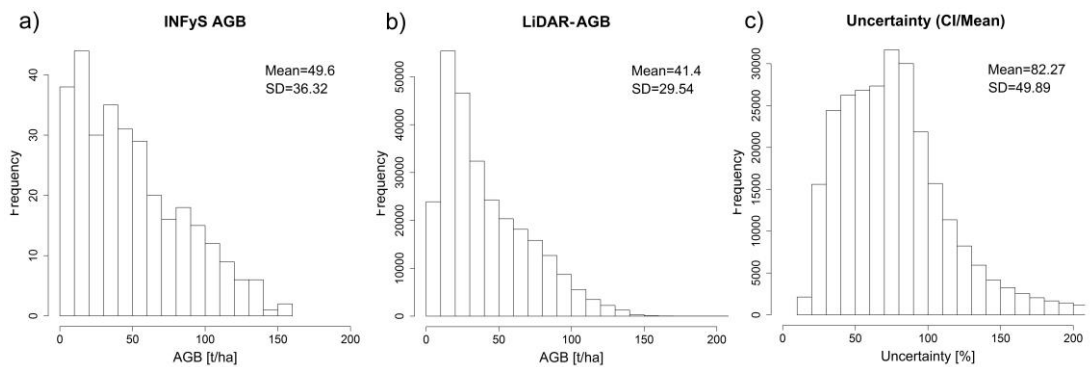


**Figure 3-6:** a) Histogram of field-estimated AGB used for calibration of LiDAR metrics; b) histogram of LiDAR-estimated AGB; c) histogram of uncertainties in LiDAR-estimated AGB

Field-estimated AGB (used for calibration of LiDAR metrics) and the modelled mean LiDAR-AGB showed similar distribution with a mean AGB around 40-50 t/ha, a standard deviation (SD) of 30-40 t/ha, and a maximum AGB up to 150-160 t/ha (Figure 3-6a, 6b). In the mean LiDAR-AGB, however, there were fewer pixels featuring a low AGB (e.g., less than 10 t/ha) compared to the field-estimated AGB. This is caused by the ensemble model of decision trees (Baccini et al. 2008; Hooker and Mentch 2018; Xu et al. 2016), where single predictions of each tree are averaged. These models in general tend to shift the lowest and highest values towards the mean.

As mentioned above (Section 3.2.3.4), we used LiDAR-AGB samples as calibration data for satellite imagery. For this, we used all LiDAR-AGB samples (271,216 1ha LiDAR samples) as well as LiDAR-AGB pixels with uncertainties below 50% (68,395 1 ha LiDAR samples).

### 3.3.2 Estimation of AGB and uncertainties at national scale with NFI-AGB as calibration data

Based on the satellite imagery, the 4,794 NFI-estimated AGB samples, and the *Cubist* machine learning algorithm around 65 Mio. ha of forest land was mapped at 1 ha scale. We propagated the estimated field error (17%) in the AGB modelling with 100 Monte Carlo simulations (Equation 6).

From the 100 AGB estimations, we calculated mean AGB (Figure 3-7), CI 95, and uncertainties (Figure 3-8) for each single 1 ha pixel. We attributed the last class as  $AGB > 120$  t/ha, since a signal saturation of SAR and optical data for a high AGB range occurred (Avitabile et al. 2012; Lucas et al. 2004; Mermoz et al. 2014; Mitchard et al. 2011), and a relatively small country area possess AGB values higher than 120 t/ha (Figure 3-9a). In accordance to (Cartus et al. 2014; Rodríguez-Veiga et al. 2016), the highest forest AGB were located in the tropical forests of the Yucatan Peninsula (Figure 3-7b) and Chiapas (Figure 3-7a) as well as in the mountain forests of Trans-Mexican Volcanic Belt (close to Mexico City). Since we applied a forest mask with 10% tree cover, the AGB in north-central parts of Mexico can be underestimated. The total forest aboveground carbon (AGC) was found to be 1.602 PgC (conversion factor of 0.48). This value is close to the Mexican forest carbon stock according to FAO's Forest Resource Assessment 2010 (1.688 PgC) (FAO 2010). The validation of the map at different scales is presented in Section 3.3.5.



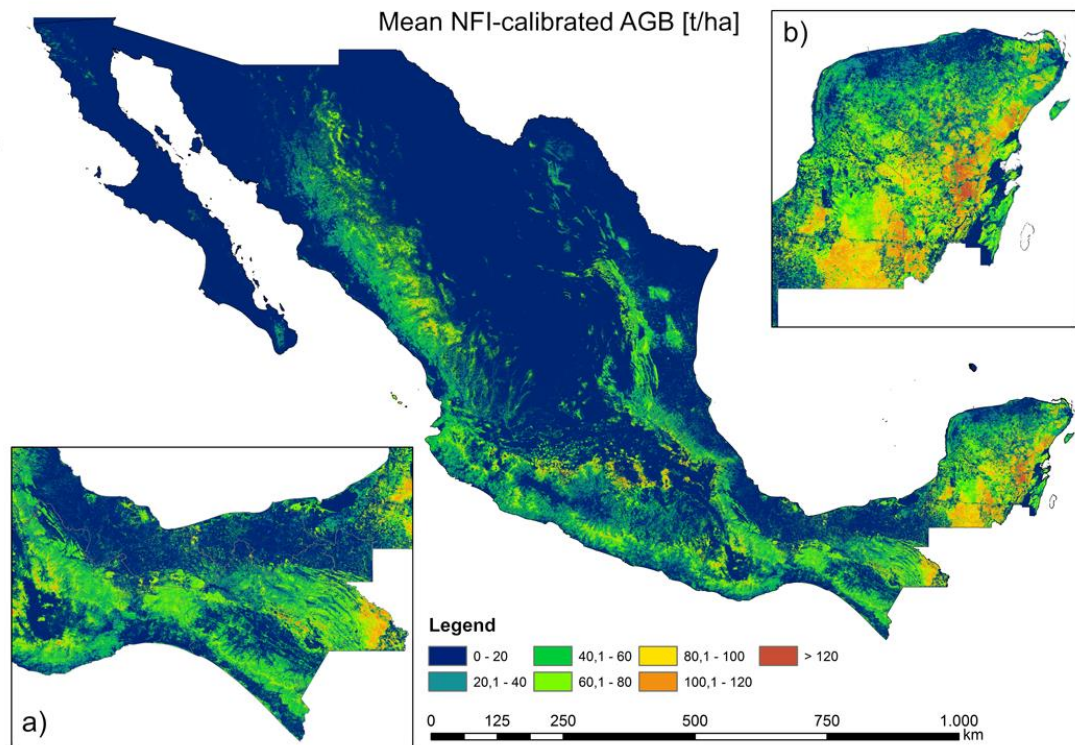


**Figure 3-7:** National forest AGB map based on NFI-estimated AGB, satellite imagery, Cubist machine learning algorithm, and Monte Carlo analyses

Most forest areas in Mexico possessed AGB uncertainties lower than 20-30% with a mean of 29.11% (Figures 3-8, 3-9c). The areas with the highest AGB uncertainties were found in the states of Oaxaca, Chiapas, and Tabasco (Figure 3-8a). For instance, in the state of Tabasco the highest uncertainties (higher than 90%) were estimated for mangrove forests in *Pantanos de Centla* (Figure 3-8a). In the states of Oaxaca and Chiapas the highest uncertainties (up to 90%) occurred in the dense cloud forests of *Sierra Madre del Sur* and *Chimalapas* tropical forests, respectively. In contrast, the dense tropical forests of the Yucatan peninsula featuring high forest AGB (Figure 3-7b)) showed relatively low uncertainties (Figure 3-8b) ranging between 20 and 40%. One reason for the low uncertainties is related to the dense NFI network covering the entire peninsula.

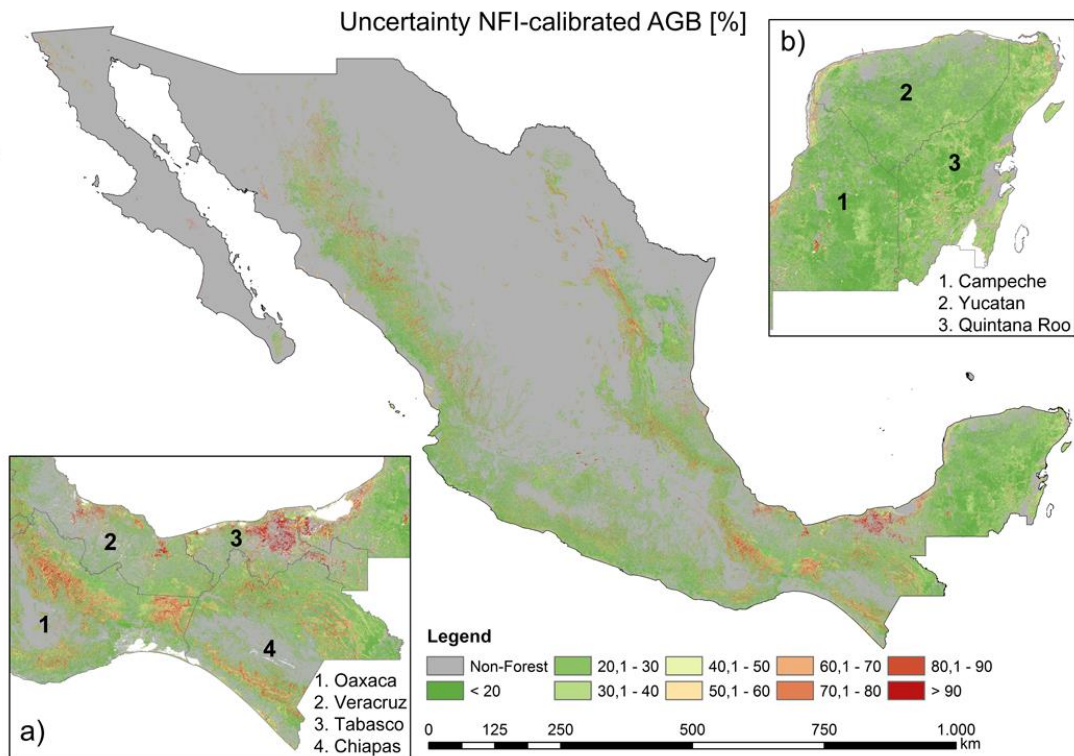


**Figure 3-8:** Estimated uncertainties (incl. error in field data and model prediction error) based on NFI-estimated AGB, satellite imagery, Cubist machine learning algorithm, and Monte Carlo analyses

Similar to the AGB estimation along the LiDAR strips, the AGB distribution in the national NFI-calibrated map was different at low and high AGB ranges compared to the field-estimated AGB (Figures 3-9a, 3-9b). This is again partly caused by the characteristics of the ensemble model of decision trees (Baccini et al. 2008; Hooker and Mentch 2018; Xu et al. 2016) (see above). Also, SAR and optical imagery reached saturation level at high AGB ( $> 100$  t/ha) (Avitabile et al. 2012; Lucas et al. 2004; Mermoz et al. 2014; Mitchard et al. 2011). The uncertainties in the national NFI-calibrated AGB map were smaller compared to the LiDAR-AGB (Figures 3-6c, 3-9c). These lower variations can be caused by the fact that for the mapping at national scale a much larger reference data set were available compared to the AGB mapping along the LiDAR strips (4,794 plots vs. 312 plots). Accordingly, the regression models become more robust.

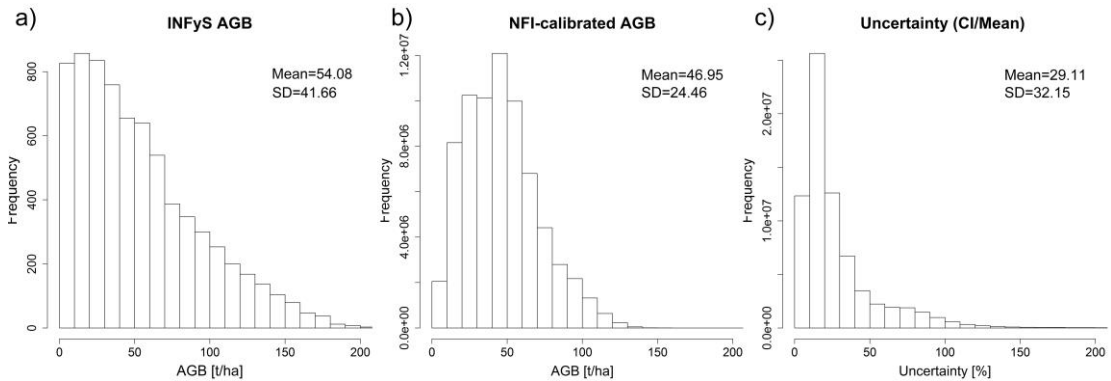


**Figure 3-9:** a) Histogram of field-estimated AGB used for calibration of satellite imagery; b) histogram of estimated national forest AGB calibrated with field-AGB; c) histogram of uncertainties in AGB map calibrated with field-AGB

### 3.3.3 Estimation of AGB and uncertainties at national scale with LiDAR-AGB as calibration data

Using the same satellite imagery as for the first modelling scenario (Section 3.2.3.3, Section 3.3.3) and 271,216 LiDAR-estimated AGB values as calibration data, we applied the *Cubist* machine learning algorithm to map forest AGB in Mexico at 1 ha scale (Figure 3-10). Similar to the NFI-calibrated AGB map, the highest AGB in the LiDAR-calibrated map occurred in the Yucatan Peninsula, Chiapas and Trans-Mexican Volcanic Belt. However, in contrast to the NFI-calibrated map, one of the areas featuring the highest AGB was located in the *Chimalapas* and *Lacandon* tropical forests (Figures 3-8a and 3-10a). Furthermore, the spatial AGB pattern in the Yucatan peninsula shows clear differences between both maps (Figures 3-8b, 3-10b and 3-18). Since we applied a forest mask with 10% tree cover, the AGB in north-central parts of Mexico can be underestimated. The total forest aboveground carbon (AGC) was estimated to be 1,374 PgC (conversion factor of 0.48), and thus lower compared to the NFI-calibrated AGB map (1,602 PgC) as well as compared to the Mexican forest carbon stock according to FAO's Forest Resource Assessment 2010 (1.688 PgC) (FAO 2010). The validation of the map at different scales is presented in Section 3.3.4.

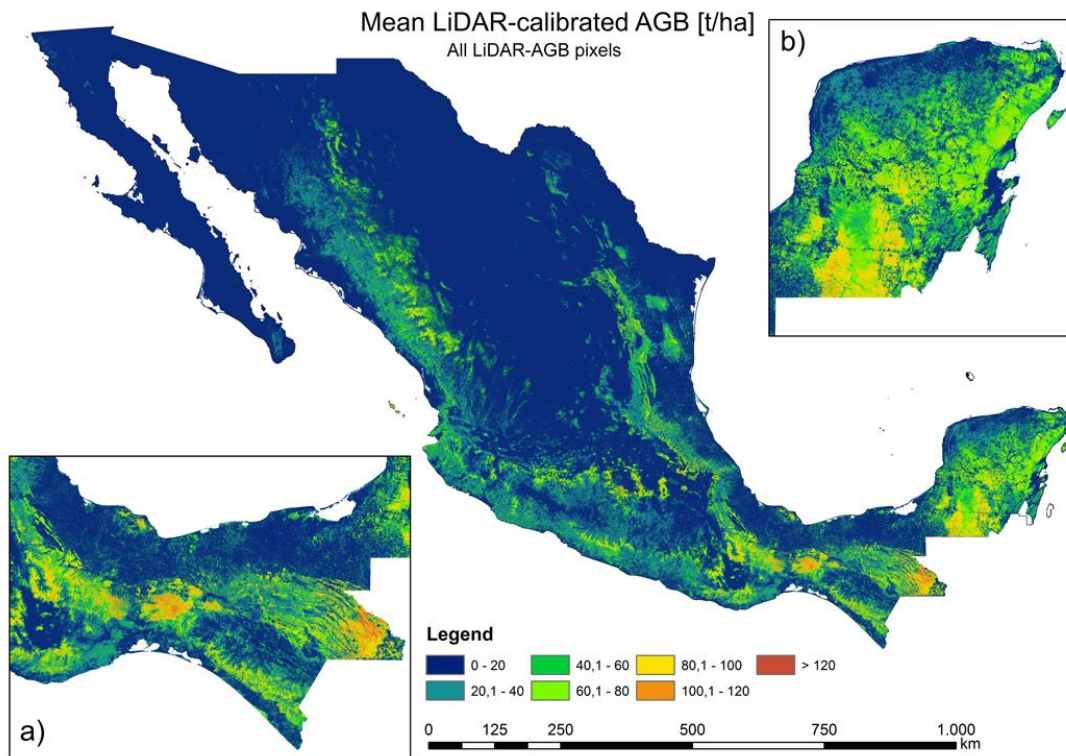


**Figure 3-10:** National forest AGB map based on LiDAR-estimated AGB, satellite imagery, Cubist machine learning algorithm, and Monte Carlo analyses

When using all LiDAR-AGB values (i.e., with uncertainties up to 200%), the uncertainties in LiDAR-AGB propagated to the final AGB map. Accordingly, the national forest AGB map based on all LiDAR-AGB featured high uncertainties (Figure 3-11). Most forest areas in Mexico showed uncertainties between 60 and 90% with a mean of 65.86% (Figure 3-12c). High uncertainties (>60%) occurred in areas with low forest AGB (<60-80 t/ha), while in areas with high forest AGB (>80 t/ha) the AGB uncertainties were lower (20-40%) (Figures 3-10, 3-11).

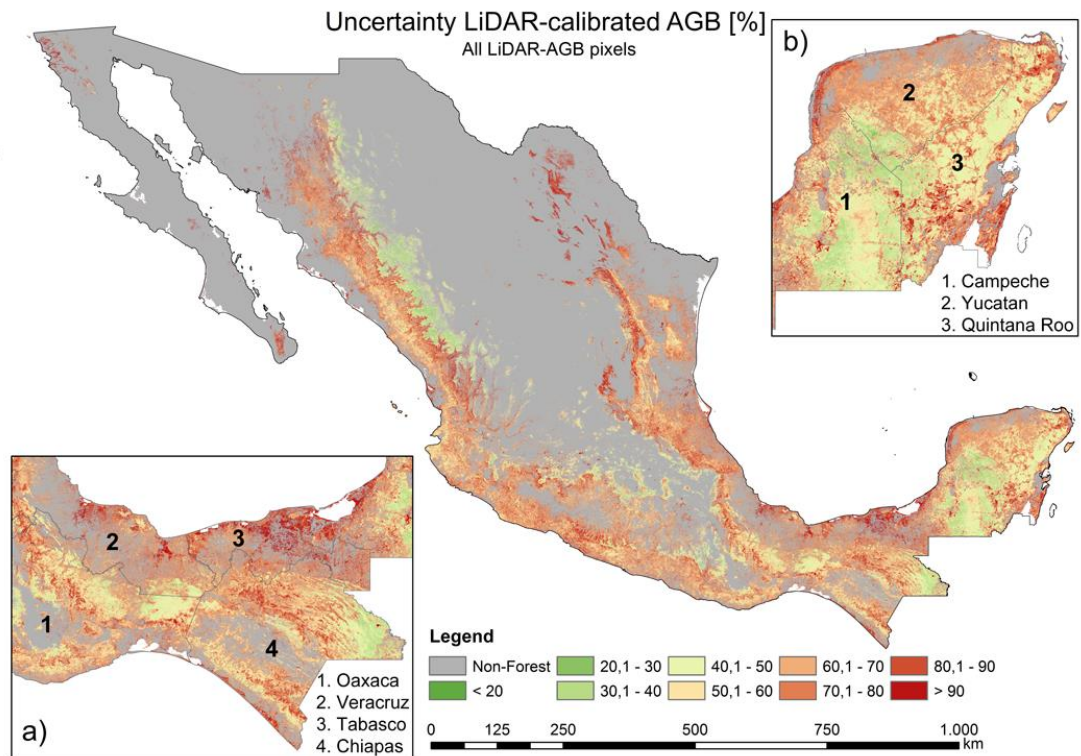


**Figure 3-11:** Estimated uncertainties (incl. error in field data, model prediction errors: NFI to LiDAR and LiDAR to satellite imagery) based on all LiDAR estimated AGB, satellite imagery, Cubist machine learning algorithm, and Monte Carlo analyses

In the next modelling scenario we used only LiDAR-AGB pixels with uncertainties below 50% (henceforth LiDAR-AGB\_50%). The majority of the pixel with uncertainties >50% were located in areas with low forest AGB (Section 3.3.1). For this reason, the forest AGB map calibrated with LiDAR-AGB\_50% possessed higher AGB values than the map calibrated with all LiDAR-AGB pixels (Figures 3-10, 3-12, 3-14). The highest AGB occurred in the Yucatan Peninsula, Chiapas and Trans-Mexican Volcanic Belt. The total forest aboveground carbon (AGC) was 1,966 PgC (conversion factor of 0.48), and thus higher than the NFI-calibrated AGB map (1,602 PgC), the LiDAR-calibrated AGB with all LiDAR-AGB pixels (1,374 PgC) as well as Mexican forest carbon stock according to FAO’s Forest Resource Assessment 2010 (1.688 PgC) (FAO 2010). The validation of the map at different scales is presented in Section 3.3.4.

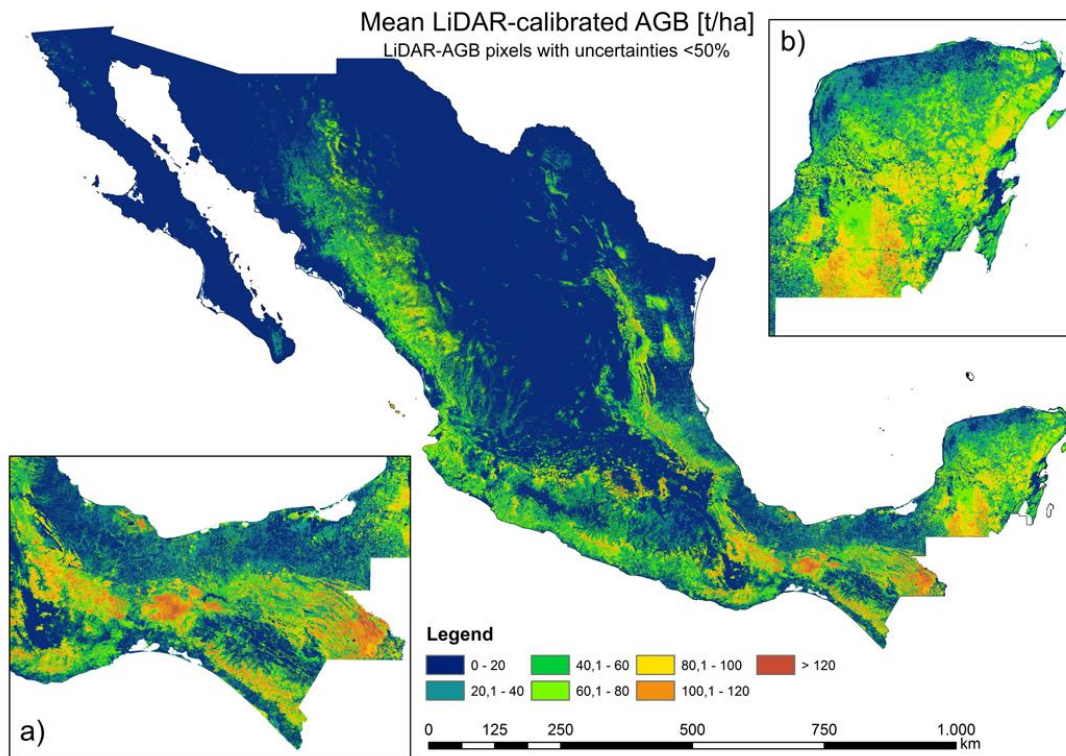


**Figure 3-12:** National forest AGB map based on LiDAR-estimated AGB (with uncertainties <50%), satellite imagery, Cubist machine learning algorithm, and Monte Carlo analyses

When LiDAR-AGB\_50% were used, the uncertainties in the national forest AGB map were reduced by 20-40% compared to the map calibrated with all LiDAR-AGB (Figures 3-11, 3-13, 3-14c, 3-14d). In contrast to the AGB map calibrated with all LiDAR-AGB pixels, here the areas with low forest AGB showed similar uncertainties as the areas with high AGB ranging between 20 and 40%. The highest uncertainty (>80%) in the forest AGB map calibrated with LiDAR-AGB\_50% were found in the mangrove forests of Tabasco in *Pantanos de Centla*, which is similar to the NFI-calibrated AGB map (Figures 3-8a, 3-13a). Furthermore, similar high AGB uncertainties were estimated in the north-eastern part of Mexico (state Coahuila). Possible reasons for this could be a combination of factors: 1) no LiDAR strips and only few NFI plots were available for this region, 2) and steep topography that effected radar backscatter.

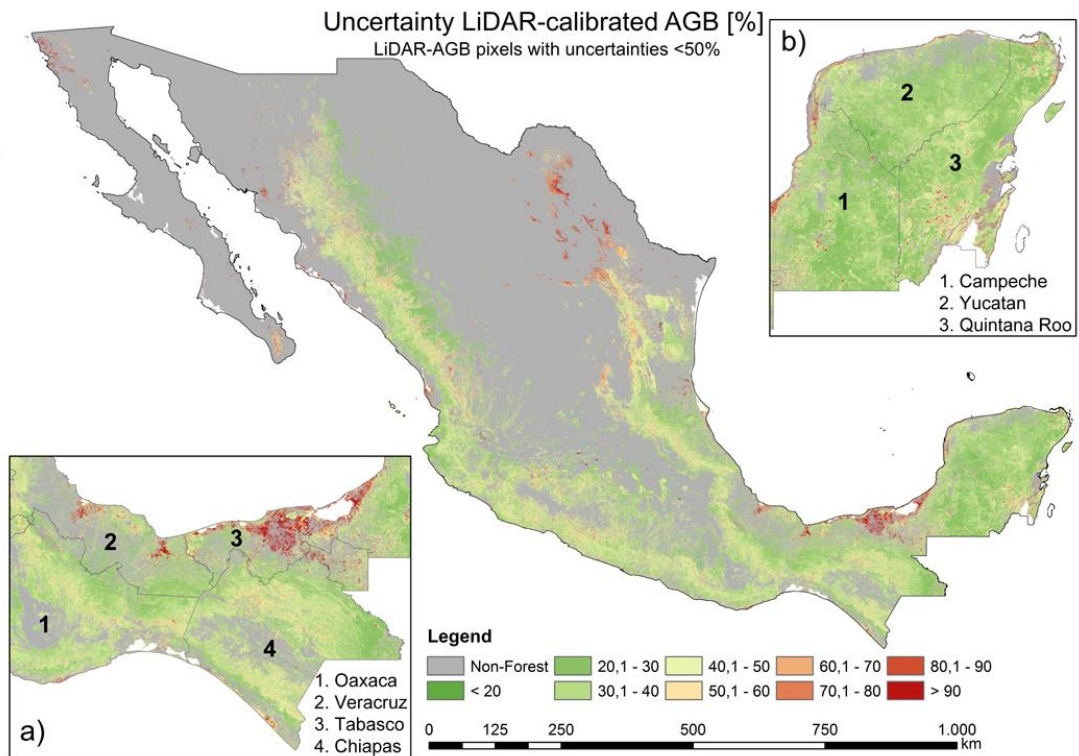


**Figure 3-13:** Estimated uncertainties (incl. error in field data, model prediction errors: NFI to LiDAR and LiDAR to satellite imagery) based on LiDAR-estimated AGB (with uncertainties <50%), satellite imagery, Cubist machine learning algorithm, and Monte Carlo analyses

As mentioned previously, the forest AGB map calibrated with all LiDAR-AGB pixels showed lower AGB values as the map calibrated with LiDAR-AGB\_50%. Figures 3-14a and 3-14b showed that the histogram of the map calibrated with LiDAR-AGB\_50% was shifted towards higher AGB values. The opposite shift towards lower uncertainties was observed in the national forest AGB map that was calibrated with LiDAR-AGB\_50% (Figures 3-14c, 3-14d).

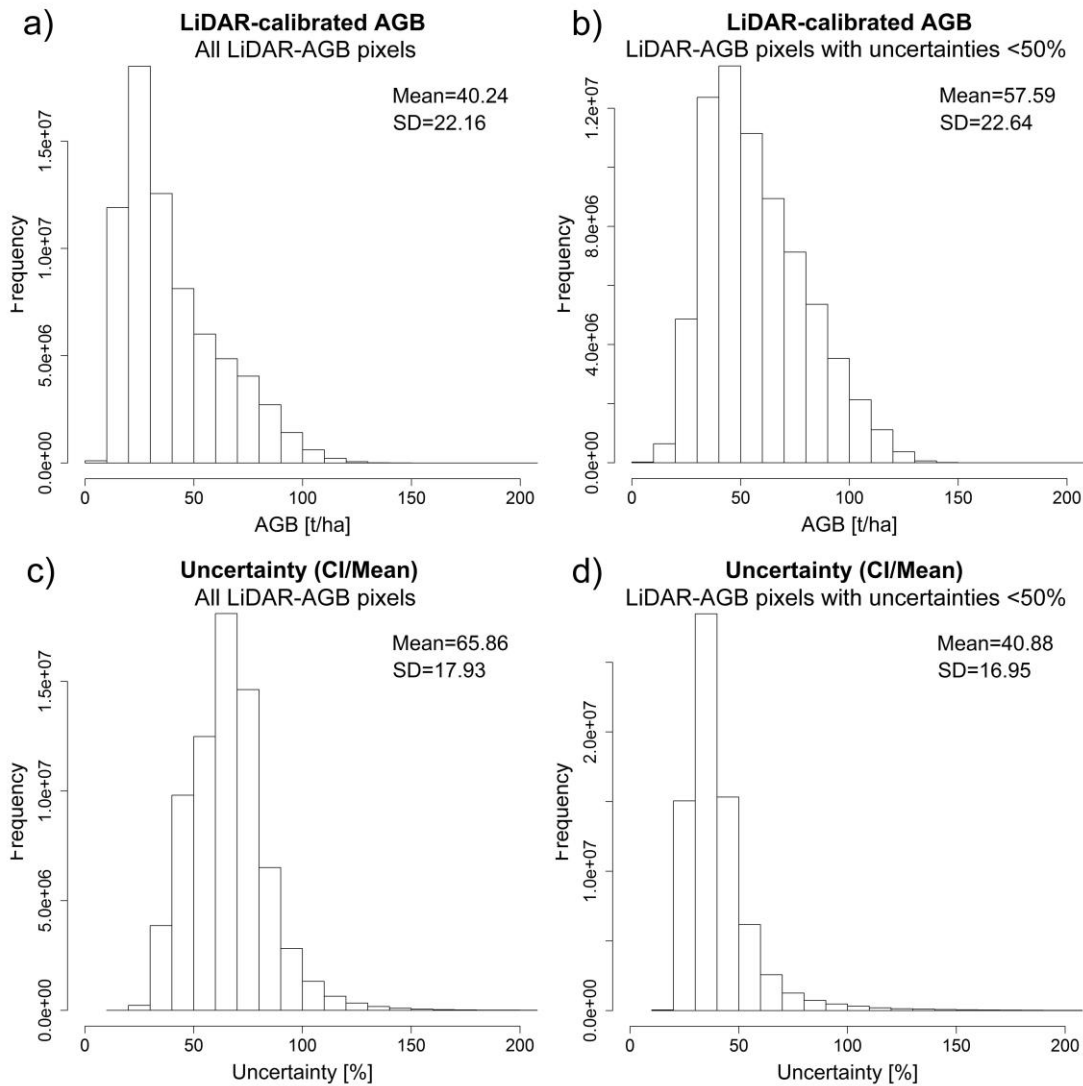


**Figure 3-14:** a) Histogram of estimated national forest AGB calibrated with all LiDAR-AGB pixels; b) histogram of estimated national forest AGB calibrated with LiDAR-AGB pixels with uncertainties <50%; c) histogram of uncertainties in AGB map calibrated with all LiDAR-AGB pixels; d) histogram of uncertainties in AGB map calibrated with LiDAR-AGB pixels with uncertainties <50%.

### 3.3.4 Validation of forest AGB maps at different scales

The first validation was conducted at pixel level. Three maps were validated independently using forest inventory plots that were not used for model calibration (Figure 3-15). The goodness-of-fit statistics were similar for all three AGB maps with similar values for  $R^2$  and RMSE, but a lower bias for the AGB map calibrated with LiDAR-AGB\_50% (Figures 3-15b, 3-15c). Obviously, all three maps underestimated the AGB in the upper range (i.e., 100-120 t/ha). This can be caused



by the fact that SAR and optical imagery saturated at high AGB level, and thus became less sensitive for AGB. Furthermore, only a small amount of training data for areas with high AGB was available. This fact caused an underrepresentation of high AGB during the training process. Also, as already mentioned above, tree-based models tend to underestimate in the high range and to overestimate in the low range (Baccini et al. 2008; Xu et al. 2016). Finally, temporal mismatch between the reference and satellite data could degrade the model performance (e.g., potential change within the field plots, as was shown in (Urbazaev et al. 2016)).

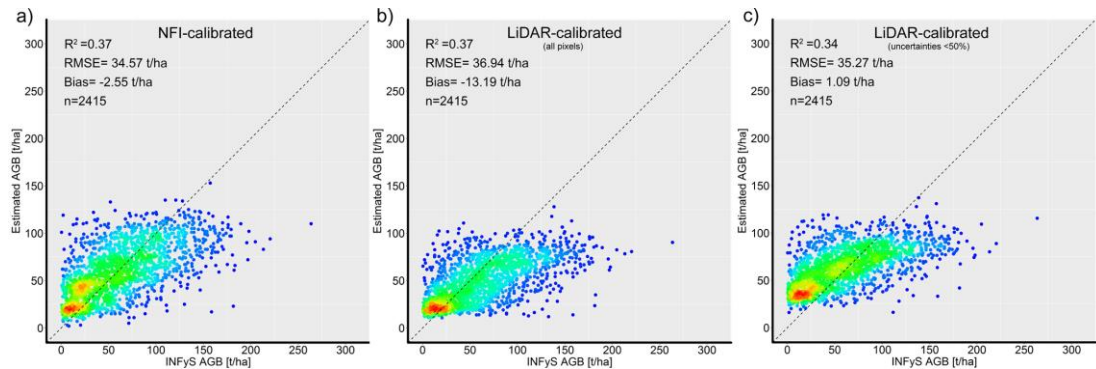


**Figure 3-15:** Validation at pixel scale: field-estimated AGB plotted against a) NFI-calibrated AGB map, b) AGB map calibrated with all LiDAR-AGB pixels, c) AGB map calibrated with LiDAR-AGB\_50%. Dotted line is the 1:1 line. Blue to red colours indicate low to high point density, respectively.

The second validation scale was the hexagon level. Due to spatial aggregation improved correlations were observed. All maps showed similar goodness-of-fit statistics (Figure 3-16). At hexagon level a slight underestimation of AGB is visible, as the most of the dots in the scatterplots were located below the 1:1 line.

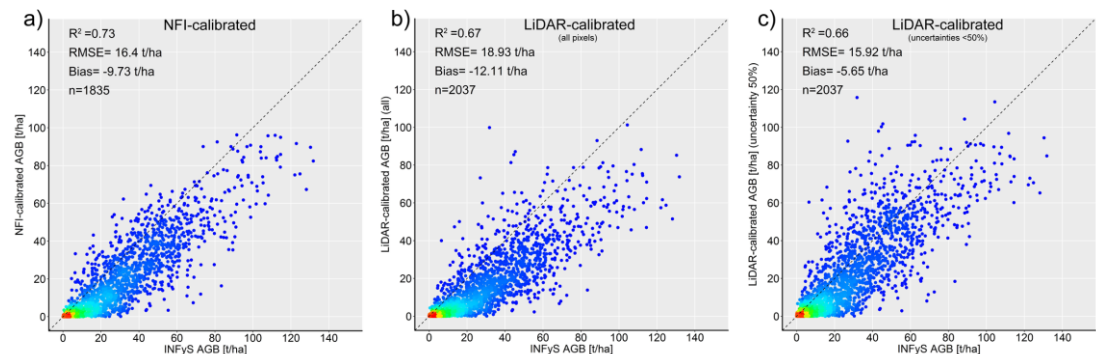


**Figure 3-16:** Validation at hexagon scale: field-estimated forest area weighted AGB plotted against a) NFI calibrated AGB map, b) AGB map calibrated with all LiDAR-AGB pixels, c) AGB map calibrated with LiDAR AGB\_50%. Dotted line is the 1:1 line.

At the state scale the NFI- and LiDAR-calibrated AGB maps correlated clearly with field-estimated forest area weighted AGB (Figure 3-17). However, all three AGB maps showed underestimation of the forest AGB for all federal states. The smallest deviation from the 1:1 line (and the smallest RMSE) was found for the AGB map calibrated with LiDAR-AGB\_50%.

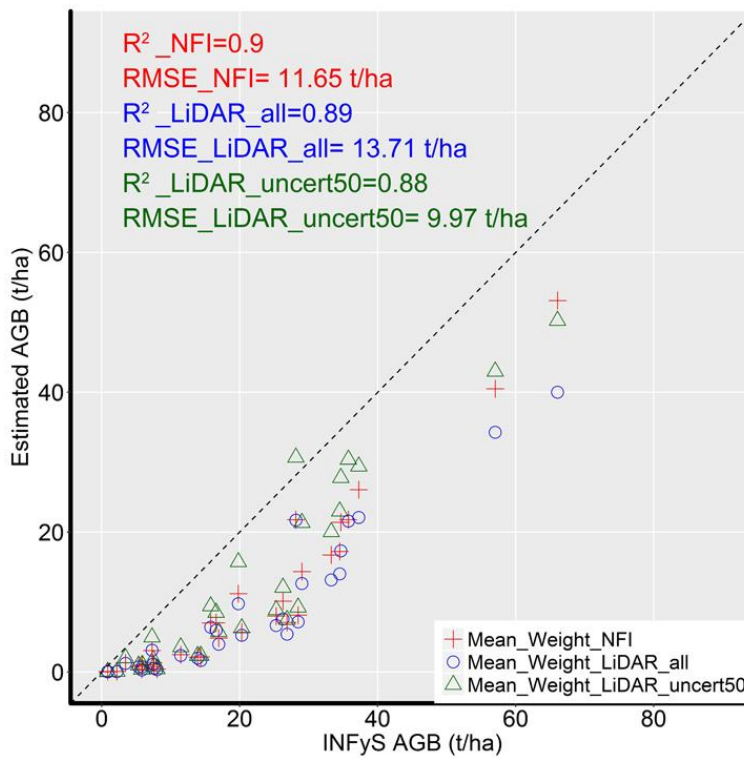


**Figure 3-17:** Validation at state scale: NFI- and LiDAR-calibrated AGB maps plotted against field-estimated forest area weighted AGB. Every point represents mean forest area weighted AGB for each federal state. Dotted line is the 1:1 line.

### 3.4 Discussion

Since NFI data are labor intensive and time consuming, and thus limited in time and space (i.e., point measurements), many remote sensing based applications use very high resolution data as reference to assess AGB. For instance, airborne LiDAR can drastically increase the number of reference data (Asner 2009; Marvin and Asner 2016). In this study, we showed that LiDAR-based AGB should be used with great care for further up-scaling to satellite imagery. Although the NFI-calibrated and LiDAR-calibrated AGB maps showed similar validation results at three spatial scales, the LiDAR-calibrated AGB maps contain much larger uncertainties compared to the NFI-calibrated map. In this study, the uncertainties in the LiDAR-based AGB were much higher than the errors in the field data. These errors were propagated further to the wall-to-wall map. This resulted in very high variation of the national LiDAR-calibrated AGB. To reduce uncertainties and variations in the LiDAR-calibrated AGB map, we removed reference LiDAR-AGB pixels with high uncertainties. Consequently, the national forest AGB map calibrated with LiDAR-AGB\_50% showed similar uncertainties (20-40%) as the forest AGB map calibrated with NFI data only. For further exploitation of an AGB map (e.g., decision making, modelling of C-fluxes) as well as to identify variance of the estimated AGB, a proper characterization of uncertainties and its analysis is a crucial step.

Furthermore, both AGB maps (NFI- and LiDAR-calibrated) showed different spatial patterns of AGB. For instance, the AGB estimates of dense tropical forests in Oaxaca and Chiapas (*Chimalapas* and *Lacandon* forests) showed a difference of 50-100 t/ha (Figure 3-18a). The underestimation of AGB of the NFI-calibrated map can be caused by the fact that no or a limited number of NFI plots were available for these areas. However, we could not independently validate both AGB maps for *Chimalapas* and *Lacandon* forests due to the lack of independent reference data. Different AGB distributions were observed in the Yucatan peninsula as well (Figure 3-18b), although a dense NFI network and LiDAR strips were available here.

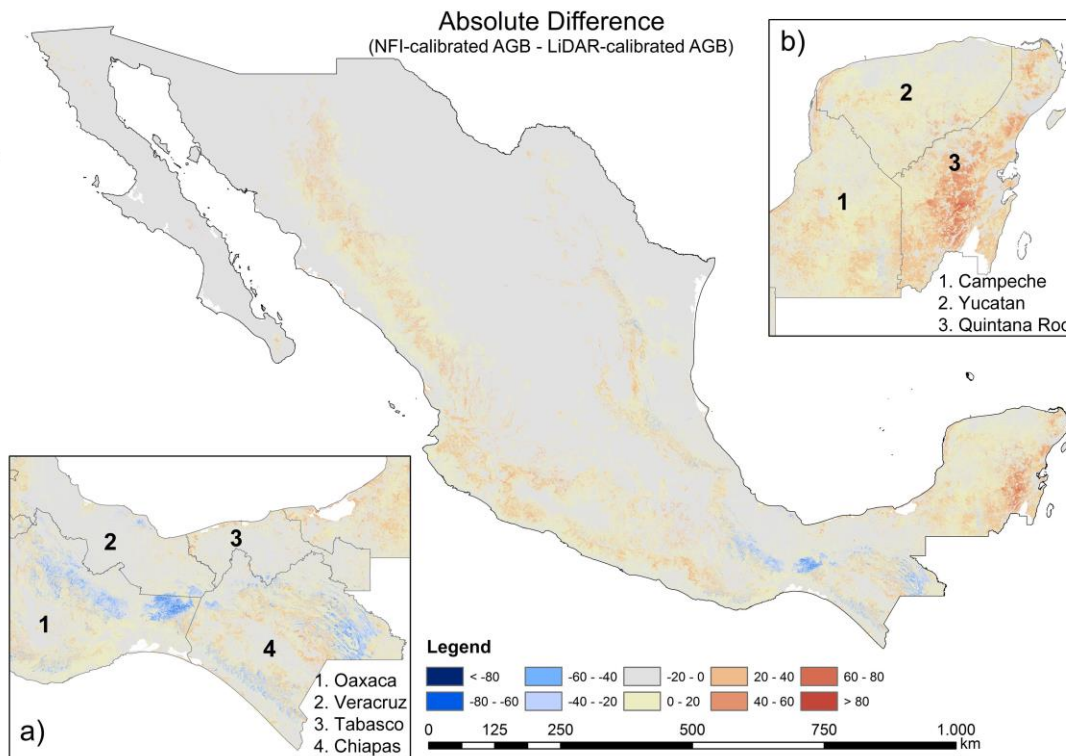


**Figure 3-18:** Absolute difference between the NFI- and LiDAR-calibrated AGB map (based on all LiDAR-pixels). Zoom sections a) and b) illustrate different spatial patterns for dense tropical forests.

Both AGB maps showed an underestimation at high AGB level compared with field-plot estimates (Figure 3-15). The reasons as already discussed above are related to the model characteristics and the insufficient sensitivity of the satellite data for AGB at high levels (Figure 3-15). These shortcomings can be partly solved through bias-correction approaches (Hooker and Mentch 2018; Xu et al. 2016) as well as through a greater amount of high quality reference data for high AGB intervals. Regarding satellite data the use of multi- or hyper-temporal imagery can potentially help to mitigate the signal saturation issue (Cartus et al. 2012b; Santoro et al. 2011). Furthermore, the future P-band SAR mission BIOMASS (Le Toan et al. 2011) will provide data with a higher saturation level in forest covered areas. Eventually, considerable deviations between the AGB maps were observed in areas with steep slopes (beside the Yucatan peninsula) (Figure 3-18). Accordingly, advanced terrain-correction methods for SAR imagery (e.g., Hoekman and Reiche 2015; Small 2011) and new accurate DEM products (e.g., TanDEM-X DEM) should be analyzed and included to further improve AGB estimations for mountainous regions.

Since there are several studies aiming at national AGB mapping for Mexico (Avitabile et al. 2016; Cartus et al. 2014; Rodríguez-Veiga et al. 2016), a comprehensive comparison of the different products available is desirable. There is a clear need to support Mexico's local authorities (e.g., CONAFOR, CONABIO) to identify and understand similarities and discrepancies of the different AGB maps as well as the source of errors.

An important issue in forest AGB mapping in Mexico is the agreement on a forest definition or a forest covered area of interest, respectively. For instance, in (Cartus et al. 2014) the total AGC varied by 44% (2.21 PgC vs. 1.53 PgC), depending on whether a forest mask was applied. Rodríguez-Veiga et al. (Rodríguez-Veiga et al. 2016) applied different forest mask to calculate national forest AGC and concluded that total national forest AGC varied by 31% (lowest forest AGC of 1.47 PgC vs. highest forest AGC of 1.92 PgC). Therefore, a consistent and accurate national forest mask is crucial to assess national forest carbon stocks.

### 3.5 Conclusion

The results of this study indicated that ignoring errors in the LiDAR-estimated AGB can lead to much higher uncertainties in the final wall-to-wall AGB map compared to the field to satellite up-scaling. Although the delineated forest AGB products showed similar goodness-of-fit statistics at different scales compared to the validation NFI data set (Figures 3-15, 3-16, 3-17), we computed clearly higher uncertainties in the LiDAR-calibrated AGB map compared to the NFI-calibrated map. When we removed LiDAR-estimated pixel with high uncertainties, we could estimate national forest AGB with similar uncertainties as with NFI data.

Furthermore, we observed different spatial patterns of AGB in regions where no or only a limited number of NFI data were available (conservation areas in tropical forests (e.g., *Chimalapas* and *Lacandon* forests). A set of independent field plots for these regions would help to analyze and validate the presented results. Moreover, AGB at high level ( $>100$  t/ha) was underestimated in both modelling scenarios. We suggest that a greater number of high quality field data in dense tropical forest can mitigate this issue. Furthermore, the implementation of dense time series of satellite data will help to improve the model results. Thus, the forthcoming L-band missions (NISAR and SAOCOM) and in particular ESA's P-band mission BIOMASS are of great interest.

Since LiDAR data can be acquired for much larger areas than field inventory data, LiDAR is an extremely important tool for repetitive reference data acquisitions over large areas, in particular in areas where the amount of NFI data are limited (e.g., restricted or inaccessible areas). Furthermore, in contrast to point measurements of field data, LiDAR captures spatial variability, which is beneficial at heterogeneous tropical forests. Nevertheless, we showed here that a two-stage up-scaling method needs to be analyzed and validated with great care. Field inventory is an essential tool to measure and observe ecological processes at local scale as it can provide a higher level of data richness when compared to LiDAR. We believe though that LiDAR can be used as an extension to NFI, for example, for areas that are difficult or not possible to access. Therefore, future research can investigate an integration of airborne LiDAR data into field inventory for forests carbon stock assessments (e.g., a trade-off between map accuracy (i.e., user requirements) and resulting costs (i.e., number of NFI and LiDAR data)).

### **Authors' contributions**

MU, CT and FC conceived and designed the experiments; MU performed the experiments; MU and FC analyzed the data; RD and MM contributed analysis tools; MU wrote the paper; all co-authors assisted the lead author in writing and revising the manuscript. All authors read and approved the final manuscript.

### **Acknowledgements**

MU conducted this work under the International Max Planck Research School for Global Biogeochemical Cycles and acknowledges its funding and support. This work was supported by the German Aerospace Center (DLR) in the Sentinel4REDD project (FKZ:50EE1540) and has been undertaken within the framework of the JAXA Kyoto & Carbon Initiative. ALOS PALSAR mosaic data were available from ©JAXA PALSAR MOSAIC 2014. The authors would like to thank the following organizations for providing remote sensing data: JAXA (ALOS PALSAR), University of Maryland (Landsat Tree Cover), NASA (airborne LiDAR data). The authors would like to thank CONAFOR for providing INFyS field plot data.

### **Competing interests**

The authors declare that they have no competing interests.

### **Availability of data and materials**

Remote sensing data for this study are available in (CGIAR 2016; JAXA 2016; University of Maryland 2016). Airborne G-LiHT LiDAR data are available at [https://gliht.gsfc.nasa.gov/data\\_section/](https://gliht.gsfc.nasa.gov/data_section/). Mexican Forest Inventory data (INFyS) can not be shared.

### **Consent for publication**

All authors consent to the publication of this manuscript.

### **Ethics approval and consent to participate**

Not applicable.

### **Funding**

This study was funded through a Ph.D. scholarship from the International Max Planck Research School for Global Biogeochemical Cycles, with additional support from the German Aerospace Center (DLR) within the Sentinel4REDD project (FKZ:50EE1540).

### **Publisher's Note**

Springer Nature remains neutral with regard to jurisdictional claims in published maps and institutional affiliations.





# Chapter 4

## Potential of Multi-Temporal ALOS-2 PALSAR-2 ScanSAR Data for Vegetation Height Estimation in Tropical Forests of Mexico

M. Urbazaev<sup>1,2</sup>, F. Cremer<sup>2</sup>, M. Migliavacca<sup>3</sup>, M. Reichstein<sup>3,4</sup>, C. Schmullius<sup>2</sup> &  
C. Thiel<sup>2</sup>

<sup>1</sup>Max Planck Institute for Biogeochemistry, International Max Planck Research School

<sup>2</sup>Friedrich-Schiller-University Jena, Department for Earth Observation

<sup>3</sup>Max Planck Institute for Biogeochemistry, Biogeochemical Model-Data Integration Group

<sup>4</sup>Michael-Stifel-Center Jena

Published in:

**Remote Sensing** (2018), 10, 1277

(Received 28 June 2018; Accepted 12 August 2018)

**DOI:** 10.3390/rs10081277

## Abstract

Information on the spatial distribution of forest structure parameters (e.g., aboveground biomass, vegetation height) are crucial for assessing terrestrial carbon stocks and emissions. In this study, we sought to assess the potential and merit of multi-temporal dual-polarised L-band observations for vegetation height estimation in tropical deciduous and evergreen forests of Mexico. We estimated vegetation height using dual-polarised L-band observations and a machine learning approach. We used airborne LiDAR-based vegetation height for model training and for result validation. We split LiDAR-based vegetation height into training and test data using two different approaches, i.e., considering and ignoring spatial autocorrelation between training and test data. Our results indicate that ignoring spatial autocorrelation leads to an overoptimistic model's predictive performance. Accordingly, a spatial splitting of the reference data should be preferred in order to provide realistic retrieval accuracies. Moreover, the model's predictive performance increases with an increasing number of spatial predictors and training samples, but saturates at a specific level (i.e., at 12 dual-polarised L-band backscatter measurements and at around 20% of all training samples). In consideration of spatial autocorrelation between training and test data, we determined an optimal number of L-band observations and training samples as a trade-off between retrieval accuracy and data collection effort. In summary, our study demonstrates the merit of multi-temporal ScanSAR L-band observations for estimation of vegetation height at a larger scale and provides a workflow for robust predictions of this parameter.

**Keywords:** L-band; SAR backscatter; vegetation height; forest structure parameters; spatial autocorrelation; Yucatan; Mexico

## **4.1 Introduction**

The status of tropical forests and their temporal dynamics can be assessed and monitored by measuring different forest biophysical parameters (e.g., vegetation height, canopy cover, stem volume and aboveground biomass (AGB)). Accurate spatial estimates of these parameters are crucial to assess terrestrial carbon (C) stocks and C-emissions, as well as to develop sustainable forest management strategies. Furthermore, these products can help provide a better understanding of the ecosystem dynamics and the effects of environmental drivers through modelling. Field measurements of forest biophysical parameters are, however, associated with high costs (e.g., they are labour intensive and time consuming) and are limited to point measurements, which may not adequately describe patterns at different spatial scales. Spatially explicit information on three-dimensional vegetation structure can be provided by Light Detection and Ranging (LiDAR) sensors (Asner et al. 2008; Clark et al. 2004; Lefsky et al. 2002a)). Laser pulses sent from a sensor are capable to penetrate the forest canopy and to directly measure vertical vegetation structure. LiDAR is usually operated from an airborne platform and thus limited to small spatial coverage. Both spaceborne as well as airborne LiDAR may provide samples of forest structure parameters over large areas (e.g., regional, national, continental scales) and need to be integrated with satellite imagery to derive wall-to-wall estimates of forest biophysical parameters.

Satellite imagery collected by Radio Detection and Ranging (RADAR) sensors are sensitive to forest structure parameters (e.g., Berninger et al. 2018; Cartus et al. 2012b; Lucas et al. 2010; Mitchard et al. 2011; Saatchi et al. 2011b; Santoro et al. 2011; Santos et al. 2003; Tanase et al. 2014b)), as microwave signals have the capability to penetrate the vegetation profile, and thus to probe the three-dimensional vegetation structure. Furthermore, RADAR data are particularly useful for weather independent applications, as long wavelengths (with a spectral range between 1 cm and 1 m) penetrate clouds. A key parameter obtained from Synthetic Aperture Radar (SAR) data, backscatter intensity, measures the return energy from a target and is determined by the geometric and dielectric properties (which is mostly determined by the water content) of the reflective material, as well as by the frequency, polarisation and angle of incidence of the emitted wave (Raney 1996). Long wavelengths (e.g., at P-band and L-band) are more suitable for the retrieval of forest structure parameters (e.g., growing stock volume, AGB) because of their ability to penetrate deeper in forest canopies as compared to short wavelengths (e.g., at X-band and C-band) (Le Toan et al. 1992; Lucas et al. 2004; Saatchi et al.

2011b), and thus to interact with large branches (in order of the wavelength) and trunks. In general, the cross-polarised (HV, VH) waves are induced by volume scattering (Lee and Pottier 2009) (e.g., as occurring within woody canopies) and are thus more sensitive to volume and possess a stronger correlation with forest structure parameters compared to co-polarised (HH, VV) waves (Rauste et al. 1994; Watanabe et al. 2006). Advanced SAR techniques (e.g., interferometry (InSAR), polarimetry (PolSAR), polarimetric interferometry (PolInSAR), tomography (TomoSAR)) show promising results for estimating vegetation structure parameters (Antropov et al. 2017; Askne et al. 2013; Dinh Ho Tong et al. 2014; Hajnsek et al. 2009; Papathanassiou and Cloude 2001; Solberg et al. 2013). For instance, studies based on TanDEM-X single-pass interferometer (e.g., Askne et al. 2013; Schlund et al. 2016; Solberg et al. 2013; Solberg et al. 2017)) reported promising sensitivity of the InSAR height to canopy height and thus to stem volume and AGB in boreal and tropical forests. Since the temporal baseline of the TanDEM-X mission is quasi zero, temporal decorrelation of the interferometric coherence can be excluded, and the InSAR coherence is primarily impacted by volume decorrelation. Furthermore, due to the short wavelength of TanDEM-X data (i.e., X-band), most of the incoming electromagnetic energy is scattered from the top of vegetation and the TanDEM-X InSAR height exhibits a strong correlation with vegetation height. For PolInSAR analysis, at least two full polarimetric (i.e., all polarisations are available) SAR datasets acquired from two slightly different positions are needed to determine the volume phase scattering centre, which is located close to the top of a canopy. Accordingly, this measurement is useful to estimate tree height. For TomoSAR methods, a stack of multi-baseline SAR data is required to delineate SAR Tomograms. From the Tomogram, the 3D position and scattering amplitude of each relevant scatterer can be derived, i.e., individual tomographic layers can be classified as surface layers, topmost layers and volume layers (e.g., middle heights). However, currently only one of these methods can be applied for large-scale mapping (i.e., single-pass InSAR), due to the lack of PolInSAR and TomoSAR data at this scale. Moreover, single-pass interferometry based on TanDEM-X data is also somehow limited due to data policy, including restricted data access for scientific use. Because of the data availability and technically less complex analysis compared to InSAR, PolInSAR and TomoSAR, most studies on the estimation of forest structure parameters are based on SAR backscatter analysis (e.g., for AGB estimation (Santoro and Cartus 2018)). For instance, L-band backscatter was successfully applied to map fractional woody cover (Bucini et al. 2010; Li et al. 2012; Musick et

al. 1998; Naidoo et al. 2016; Urbazaev et al. 2015) as well as regional or global forests (Dong et al. 2014; Shimada et al. 2014; Thiel et al. 2006; Thiel et al. 2009). Moreover, L-band backscatter was used to predict vegetation height in various biomes from boreal (Suzuki et al. 2013) and temperate (Cartus et al. 2012a; García et al. 2018) to tropical forests (Xu et al. 2016).

In this study, we examine the potential of multi-temporal L-band SAR backscatter acquired by the Advanced Land Observation Satellite 2 Phased Array L-band Synthetic Aperture Radar 2 (ALOS-2 PALSAR-2) in ScanSAR mode to estimate vegetation height over tropical deciduous and evergreen forests in the Yucatan peninsula, Mexico. ScanSAR data exhibit much larger swath width compared to Stripmap data (i.e., 350 km vs. 70 km) and accordingly can cover wider areas at higher repetition rates. For instance, ScanSAR acquisitions cover the entire tropical region approximately every 42 days. Therefore, we analyse the performance of the multi-temporal combination of L-band backscatter for vegetation height mapping. Airborne LiDAR-based vegetation height is used as reference data for model training and validation.

In this paper, we demonstrate the value of multi-temporal PALSAR-2 ScanSAR mosaics compared to open global PALSAR-2 Stripmap Fine Beam Dual Polarisation (FBD) mosaics. Moreover, we apply two different validation approaches to show the effect of spatial autocorrelation on model performance. In previous studies (e.g., García et al. 2018; Xu et al. 2016)) it was reported that statistical models improve by increasing the number of spatial predictors as well as response variables. We examine these findings considering two different validation schemes, which include and minimise the autocorrelation. The results of the study are relevant in the context of the upcoming L-band missions for global vegetation monitoring (e.g., ALOS-4, NISAR, SAOCOM, Tandem-L) and an increasing number of L-band SAR data in the near future. Since vegetation height correlates with other forest parameters (e.g., AGB, tree canopy cover) (Chave et al. 2005; Colgan et al. 2013; Saatchi et al. 2011a), we can assume that similar results can be achieved for the estimation of AGB and tree canopy cover using multi-temporal dual-polarised L-band SAR backscatter.

## 4.2 Material and Methods

### 4.2.1 Study area

The study area is the Yucatan peninsula, Mexico, which is mostly covered by tropical deciduous and evergreen forests (Figure 4-1). According to a land use map for 2010 generated by the Mexican National Institute for Statistics and Geography (INEGI) (INEGI 2010), around 1/3 of the total area (i.e., ~140,000 km<sup>2</sup>) is covered by tropical deciduous forests (i.e., ~42,000 km<sup>2</sup>), whereas around 1/2 of the total area is covered by tropical evergreen forests (~68,000 km<sup>2</sup>). Based on ca. 5000 field plots collected over the entire peninsula during the National Forest Inventory programme between 2004 and 2011 (CONAFOR 2012), mean tree height is 9 m (max. height 27 m), mean diameter at breast height (DBH) is 13 cm (max. DBH 46 cm), mean basal area is 12 m<sup>2</sup> · ha<sup>-1</sup> (max. 36 m<sup>2</sup> · ha<sup>-1</sup>) and mean AGB is 70 t · ha<sup>-1</sup> (max. AGB 227 t · ha<sup>-1</sup>). The area of the peninsula is rather flat. According to the Shuttle Radar Topography Mission (SRTM) Digital Elevation Model (DEM) version 4.1 (CGIAR 2016), average elevation is 62 m with a standard deviation of 70.8 m. The average slope is 1.3° with a standard deviation of 1.5°.

The regional climate is tropical sub-humid with slightly higher air temperatures in summer than in winter (Figure 4-2). The average annual temperature between 2013 and 2017 was ~27 °C (SMN 2018). Average annual precipitation ranges from 1000 to 1500 mm, while the period between May and November is characterised by pronounced rainfall, and the relatively dry period extends between December and April (Figure 4-2) (SMN 2018). Furthermore, the rainfall increases from north (~1100 mm mean annual total precipitation between 2013 and 2017 for the federal state of Yucatan) to south (~1400–1450 mm mean annual total precipitation between 2013 and 2017 for the federal states of Campeche and Quintana Roo, respectively). The forests in the north-western part of the peninsula have experienced slash-and-burn agriculture for 2000 years, resulting in forest patches at different succession stages (Urquiza-Haas et al. 2007). In contrast, the southern and eastern parts of the Yucatan peninsula show one of the lowest annual deforestation rates, with some nearly intact areas of tropical forest in Central America (e.g., Calakmul Biosphere Reserve) (Urquiza-Haas et al. 2007).

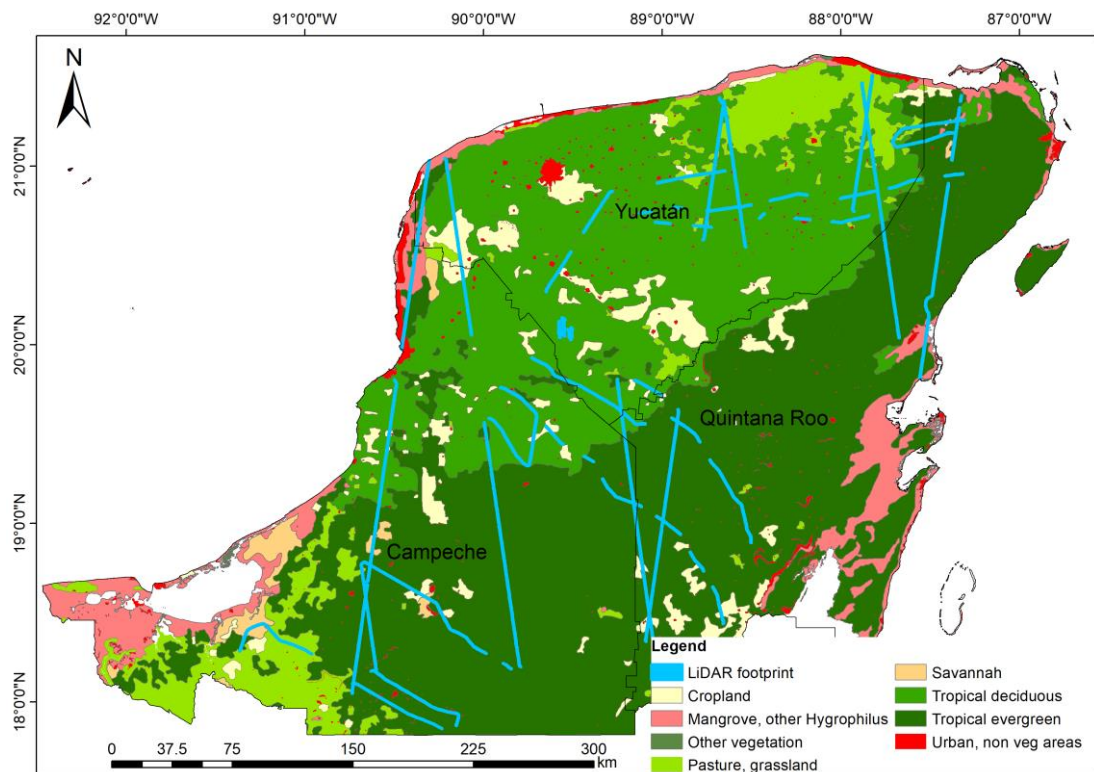


**Figure 4-1:** Study area. Land use and vegetation map of Mexico from the Mexican National Institute for Statistics and Geography (INEGI) Series IV (INEGI 2010) with the available airborne LiDAR strips

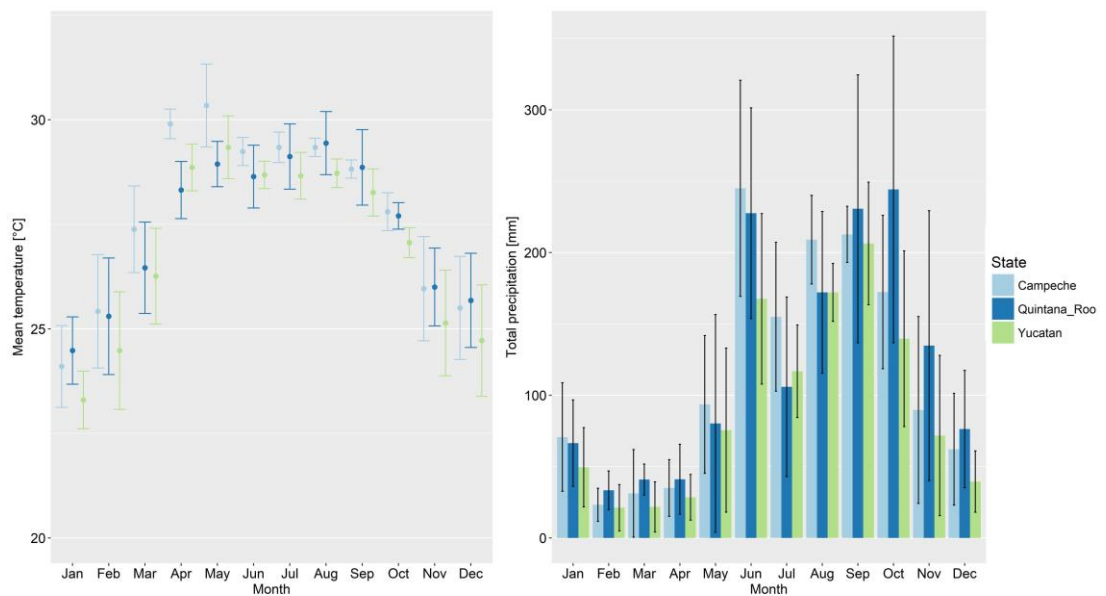


**Figure 4-2:** Mean monthly air temperature (circles on the left-hand side) and total monthly precipitation (bars on the right-hand side) for three Mexican federal states for the years 2013–2017. Error bars represent monthly standard deviations.

## 4.2.2 Remote Sensing Data

### 4.2.2.1 Airborne LiDAR data

Small-footprint discrete-return airborne LiDAR data were collected by the NASA’s G-LiHT imager (Cook et al. 2013) in April–May 2013 over entire Mexico (Figure 4-1). The average pulse density was approximately  $6 \text{ returns} \cdot \text{m}^{-2}$ . The data over the Yucatan peninsula were acquired during leaf-off conditions, which can lead to an underestimation of vegetation height. The LiDAR returns were classified into “ground returns”, “shrub returns” (i.e., non-ground returns below 1.37 m) and “tree returns” (i.e., returns above 1.37 m). From the topography-normalised point clouds, 88 plot-aggregated LiDAR metrics (e.g., percentiles, density metrics for “shrub returns”, “tree returns” and “all returns”) as described in (Evans et al. 2009; Goetz et al. 2007; Næsset 2002) were calculated at 13 m spatial resolution. These LiDAR metrics correspond to the vertical structure of a target. Both LiDAR point cloud, as well as metrics, can be downloaded from the NASA G-LiHT data portal (NASA 2018). In this study, a LiDAR metric, percentile 100% of all returns (hereafter p100) (i.e., top-of-canopy estimate), was used as reference data (i.e., for model training and result validation). In the next step, we aggregated this LiDAR metric from  $13 \text{ m} \times 13 \text{ m}$  to  $100 \text{ m} \times 100 \text{ m}$  using block averaging and nearest neighbour resampling, i.e., a top-of-canopy estimate for a  $13 \text{ m} \times 13 \text{ m}$  pixel was averaged to 100 m. In total, ca.  $150,000 \cdot 1 \text{ ha}$  LiDAR samples (ca. 1% of the total area of the Yucatan peninsula) were used as reference data for wall-to-wall mapping of vegetation height. Although LiDAR provides an estimation of height, its accuracy might be higher than field height measurements, especially in a forest with a closed canopy, where the top of a tree is difficult to detect from the ground.

### 4.2.2.2 SAR Data

The multi-temporal L-band SAR backscatter measurements used in this study were collected by the ALOS-2 PALSAR-2 sensor in dual-polarisation (i.e., HH and HV) ScanSAR mode between October 2014 and February 2018 (resulting in 24 ScanSAR mosaics). ALOS-2 PALSAR-2 ScanSAR data feature a swath width of ca. 350 km and a repetition rate of ca. 42 days (Rosenqvist et al. 2014). The data were distributed by the Japan Aerospace Exploration Agency (JAXA) in the frame of the Kyoto & Carbon Initiative as  $1^\circ \times 1^\circ$  tiles with a pixel spacing of 50 m. Single



ScanSAR tiles were then mosaicked to provide wall-to-wall L-band backscatter mosaics (hereafter ScanSAR mosaics) over the entire peninsula. In addition to the ScanSAR mosaics, three annual global PALSAR-2 mosaics based on Stripmap Fine Beam Dual Polarisation (i.e., HH and HV) data from 2015, 2016 and 2017 (hereafter FBD mosaics) (JAXA 2016) were used in the study to examine the merit of ScanSAR time series data. The FBD mosaics feature a pixel spacing of 25 m. Both ScanSAR and FBD mosaics were pre-processed (slope-corrected and orthorectified) by JAXA. In the next step, ScanSAR and FBD mosaics were speckle-filtered using the multi-temporal filter by Quegan et al. (Quegan et al. 2000; Quegan and Yu 2001). Finally, the speckle-filtered ScanSAR and FBD mosaics were aggregated to a pixel spacing of 100 m using block averaging and nearest neighbour resampling. The SAR data were aggregated to a pixel spacing of 100 m as a trade-off between the efficiency of the model and the spatial details (García et al. 2018). The model’s predictive performance increases with decreasing of spatial scale caused by reduction of speckle in SAR data and local variability in reference data (García et al. 2018; Mathieu et al. 2013; Saatchi et al. 2011b; Urbazaev et al. 2015). 24 ScanSAR mosaics and 3 FBD mosaics were then used separately for vegetation height estimation (Section 4.2.4) (Table 4-1).

**Table 4-1:** Dataset used in the study

Parameter	Dataset	Pixel spacing [m]	Data acquisition
SAR L-band backscatter	24 ScanSAR mosaics (HH/HV polarisations)	50	Oct 2014 - Feb 2018
	3 FBD mosaics (HH/HV polarisations)	25	2015, 2016, 2017
Airborne LiDAR metric	Top-of-Canopy (p100)	13	Apr - May 2013

### 4.2.3 Splitting Methods of Reference Data

For model training and validation of SAR-based estimates, we applied two different splitting methods of the reference data (i.e., LiDAR-based vegetation height). For both approaches, 70% of the reference data were selected for model training (calibration) and the remaining 30% were used for testing (validation). In the first approach, we applied stratified random sampling, i.e., the data were split based on value intervals with ignoring spatial location of the samples. For this, intervals of 3 m were selected, i.e., 70/30 partition for each 3 m height class. We used intervals of 3 m as a trade-off between a sufficient number of samples for each height class and small enough bins to ensure the intra-class similarity. This splitting

approach does not consider spatial autocorrelation between the training and test datasets, which generally results in overoptimistic model prediction statistics (Brenning 2012). Therefore, in the second splitting approach, we divided the reference data based on their spatial location using *k-means* clustering of spatial coordinates (i.e., latitude and longitude) (Figure 4-3) using the R package “sperrorest” (Brenning 2012). The first splitting approach will hereafter be called “stratified random sampling”, while the second splitting approach will be called “spatial sampling”. After data splitting using a “stratified random sampling” approach, the value distribution in training and test dataset is similar (Figure 4-4a). In “spatial sampling” after data splitting based on their geographical location, we fit the histograms of training and test data to each other, to ensure that value distribution in both datasets is similar, and the differences in the model’s predictive performance are from spatial autocorrelation and not from different value distributions. For this, the number of samples for specific 3 m height classes have been reduced until similar height distributions in the training and test datasets are reached (Figure 4-4b).



**Figure 4-3:** Location of training and validation data using the “spatial sampling” approach of the LiDAR metric p100. Black stripes represent model training data; red stripes represent validation data.

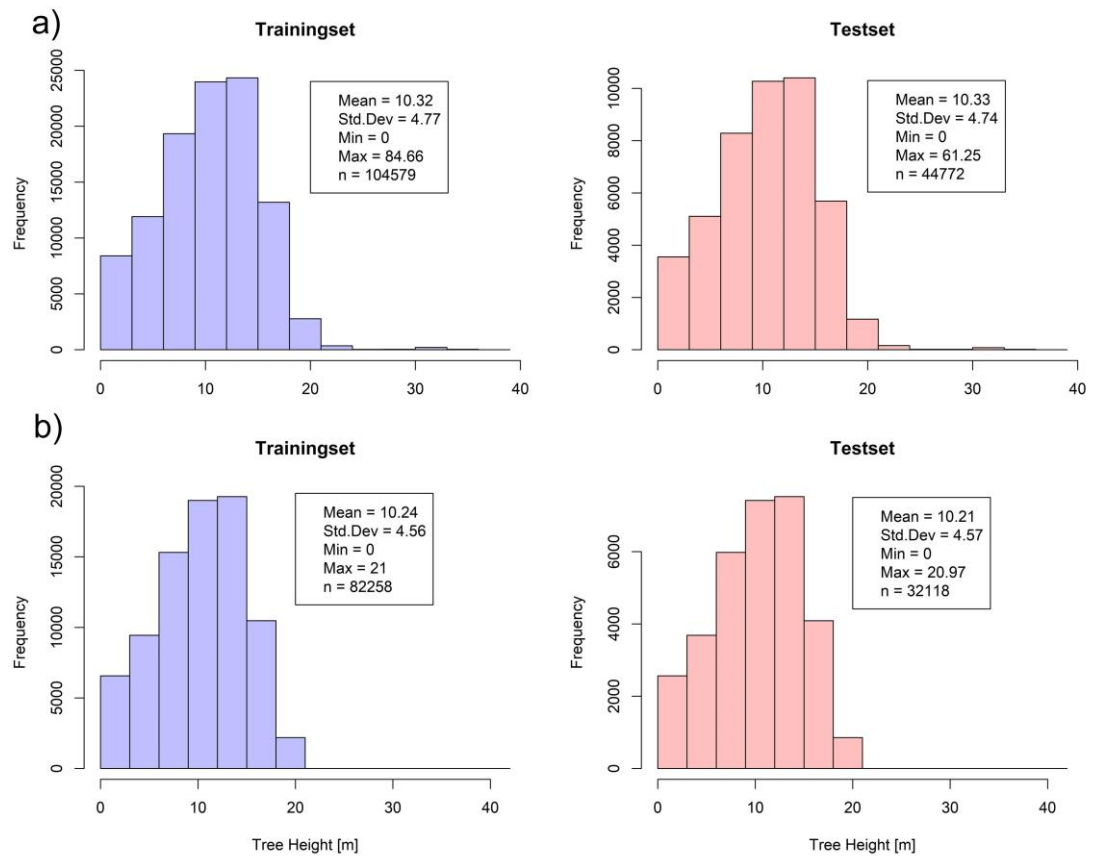


**Figure 4-4:** Histograms of LiDAR-based vegetation height data used for training and test using (a) “stratified random sampling” (i.e., based on value intervals while ignoring spatial location) and (b) “spatial sampling” (i.e., based on spatial location).

#### 4.2.4 Estimation of Vegetation Height from SAR Data

To estimate vegetation height using PALSAR-2 L-band backscatter, we applied different scenarios comprising two splitting approaches of reference data (i.e., “stratified random sampling” and “spatial sampling”) and two sets of input variables (i.e., ScanSAR and FBD mosaics). For all scenarios, the estimation of vegetation height was performed using a machine learning algorithm, namely Random Forests (RF) (Breiman 2001). This machine learning algorithm generates an ensemble of regression trees with a random selection of predictors at each node as well as with a random subset of samples for each tree to prevent overfitting. To calculate a single estimate, the predictions of each regression tree are averaged (Breiman 2001). We selected RF, since it is computationally efficient and has already been successfully applied to map vegetation structure metrics over large areas (e.g., AGB, vegetation height) with high retrieval accuracy (e.g., Avitabile et al. 2012; Baccini et al. 2008;

Baccini et al. 2012; Cartus et al. 2012a)). We generated RF models with 500 regression trees.

We furthermore investigated the impact of multi-temporal combination of ScanSAR data on the model’s predictive performance. Therefore, we modelled vegetation height using a different number of input layers. The acquisition date of a single ScanSAR mosaic can be found in Figure 4-5 (note: a single mosaic can be comprised of different ScanSAR products with slightly different acquisition dates (+/- one week from the reference date in Figure 4-5). We first estimated vegetation height with the first four ScanSAR scenes from 2014–2015 (i.e., mosaics from 13 October 2014 to 16 February 2015 (Figure 4-5)) and added four further scenes at each step, i.e., we estimated vegetation height using 4, 8, 12, 16, 20 and 24 ScanSAR mosaics. The reference data were split using “stratified random sampling” and “spatial sampling” with 100 repetitions, i.e., the training and testing data were selected 100 times using both approaches to get reliable goodness-of-fit statistics (i.e.,  $R^2$  and RMSE). Additionally, we performed the same steps for speckle unfiltered ScanSAR data to show the effect of speckle filtering.

Finally, we examined the impact of the number of training samples on the model prediction performance. Therefore, from the training set, 1%, 5%, and every decile (i.e., 10%, 20% ... 90%) of the data were sampled randomly 100 times and model performance statistics (i.e.,  $R^2$  and RMSE) for each scenario were analysed. The validation dataset from “stratified random sampling” and “spatial sampling” (e.g., red stripes in Figure 4-3) remained unchanged.

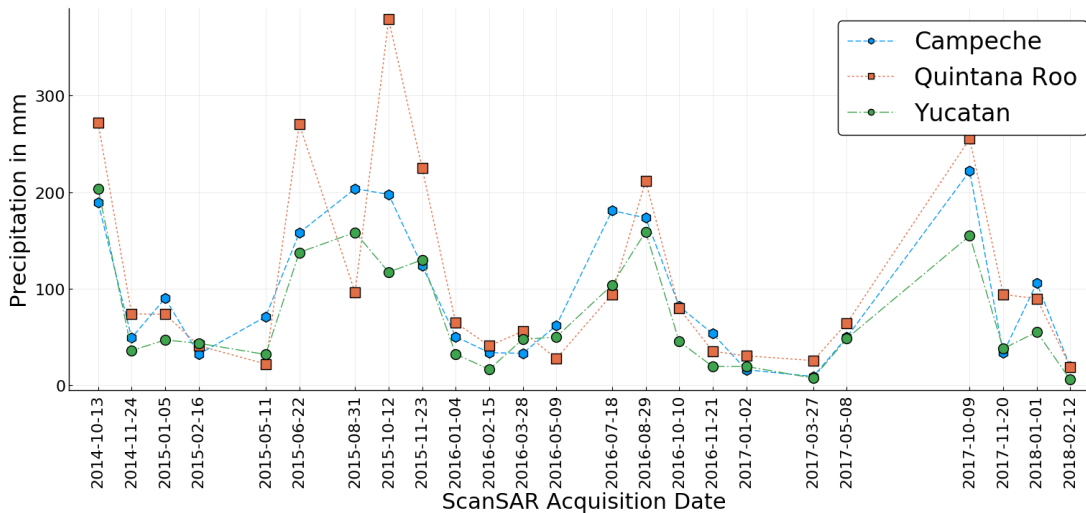


**Figure 4-5:** Acquisition dates of the ScanSAR mosaics with corresponding monthly precipitation for the three federal states from (SMN 2018).

## 4.3 Results

### 4.3.1 Estimation of Vegetation Height from SAR Data

We first sought to determine the merit of multi-temporal ScanSAR mosaics compared to the annual global FBD mosaics to map vegetation height. To examine this, we modelled vegetation height using ScanSAR and FBD mosaics separately. As described above, we applied two validation approaches, i.e., “stratified random sampling” and “spatial sampling” of reference data.

The results based on the “stratified random sampling” approach provide higher goodness-of-fit statistics ( $R^2$  and RMSE) compared to the “spatial sampling” approach for different sets of input variables (i.e., ScanSAR and FBD mosaics) (Figure 4-6). This is caused by the spatial autocorrelation of reference data, which is ignored in the “stratified random sampling” approach. In contrast, the “spatial sampling” validation considers this effect, providing a more realistic estimation of the model’s predictive performance (Brenning 2012), and might contribute to building a more robust predictive model. Furthermore, in the “spatial sampling” validation, the effect of over- and underestimations at low and high ranges, respectively, is more apparent compared to “stratified random sampling”. The effect of over- and underestimations at both ends have been reported in many studies that have applied an ensemble of regression trees (e.g., Random Forests) (Cartus et al. 2014; Urbazaev et al. 2018; Xu et al. 2016).

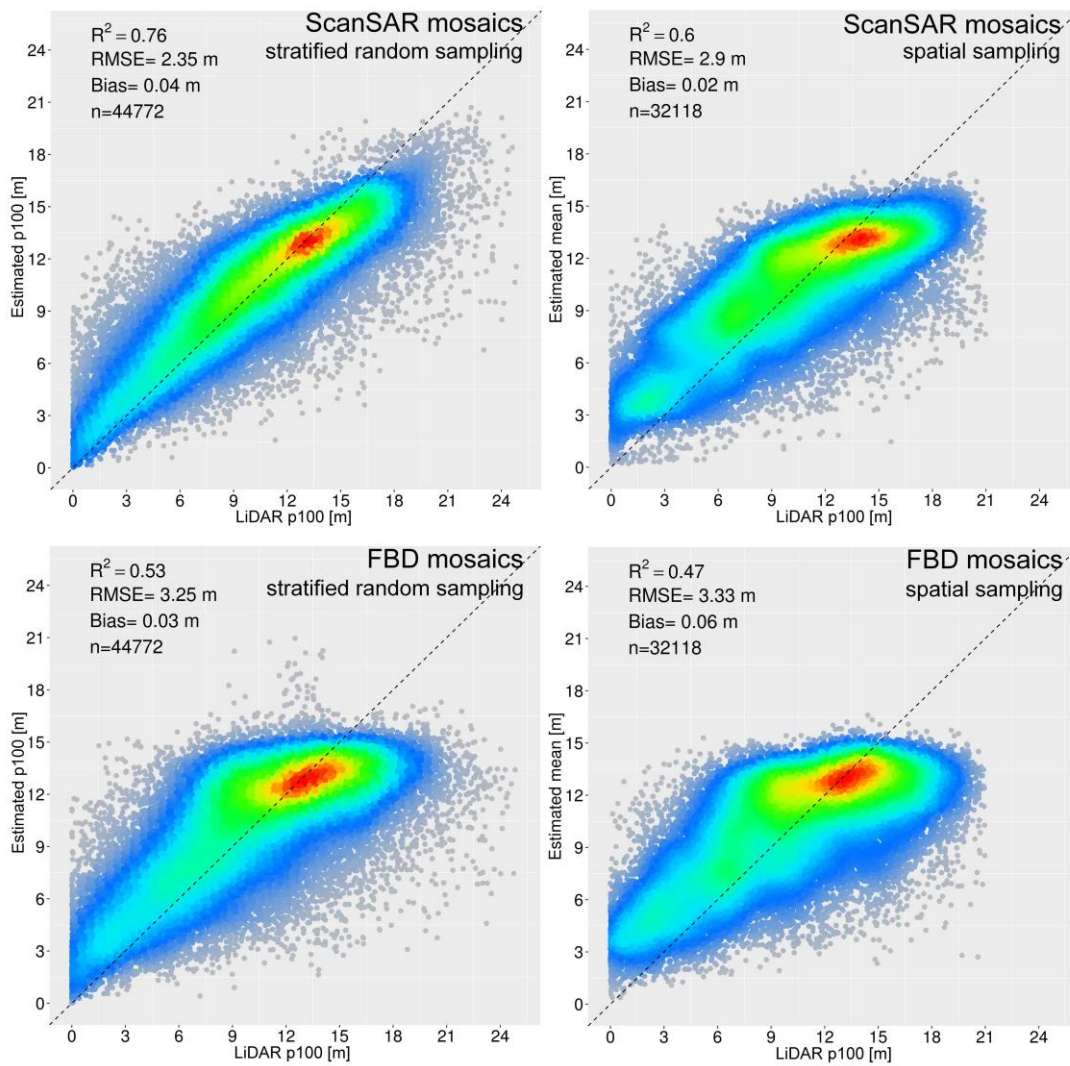


**Figure 4-6:** ScanSAR (above) and FBD (bottom)-based vegetation height estimates plotted against LiDAR p100 metric. The training and test data were split using “stratified random sampling” (left) and “spatial sampling” (right). ScanSAR mosaics (24 scenes) show higher retrieval accuracy compared to FBD mosaics (3 scenes) due to a larger number of SAR images. The “stratified random sampling” approach shows higher goodness-of-fit statistics compared to the “spatial sampling” approach due to spatial autocorrelation between training and test data.

Moreover, the FBD-based vegetation height estimates are more biased at low and high ranges compared to the results based on ScanSAR mosaics for both validation scenarios (Figure 4-6). In other words, FBD-based vegetation height estimates tend to average height values of the training data. In the difference map between the two products (Figure 4-7), the FBD height possesses greater values in the areas with small vegetation (e.g., the northern part of the peninsula) compared to the ScanSAR-based product (i.e., it shows a larger overestimation), while in the intact

## Results

areas (e.g., the Calakmul Biosphere Reserve) the FBD height exhibits lower values than in the ScanSAR height (i.e., it shows a larger underestimation).

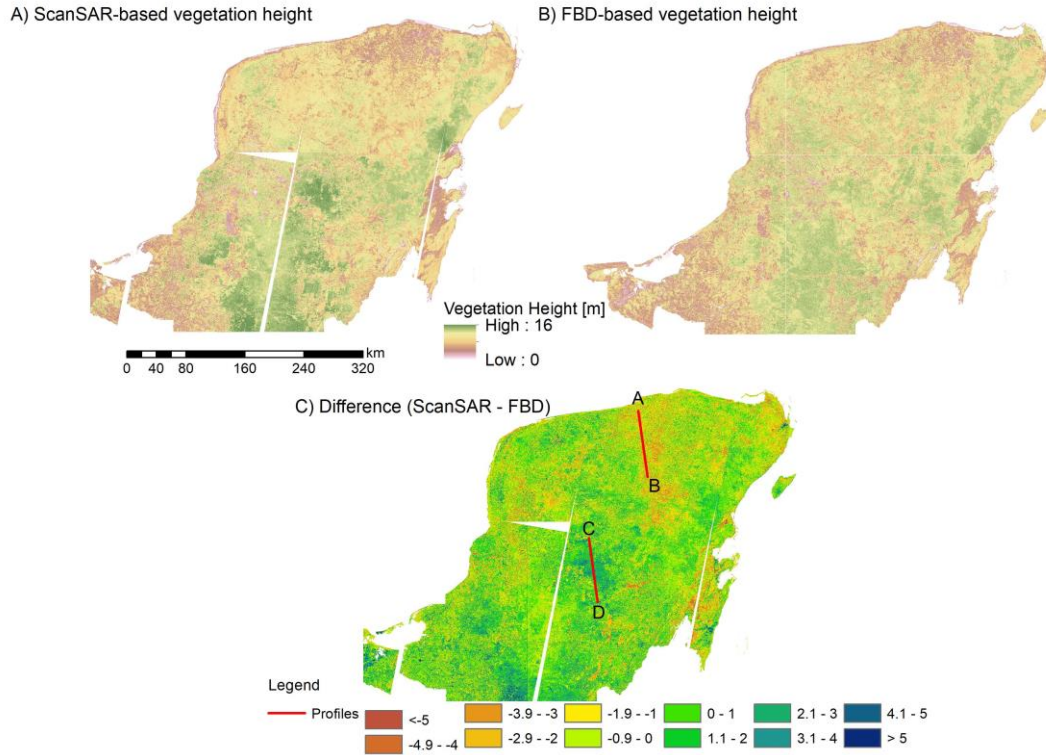


**Figure 4-7:** Vegetation height estimates based on ScanSAR (A) and FBD (B) mosaics using the “spatial sampling” approach. The difference map (C) between the two products depicts disagreements in areas with low (northern part) and tall trees (central and southern parts). The height values over the two red transects (A-B profile and C-D profile) are shown in Figure 4-8. White gaps in the ScanSAR-based vegetation height map resulted from the gaps in the ScanSAR backscatter mosaics.

For areas with obvious disagreements between the two maps and where LiDAR data were available, transects of vegetation height (red stripes at the bottom of Figure 4-7) were generated (Figure 4-8). Compared to the LiDAR measurements, both SAR-based vegetation height maps show an overestimation of small vegetation and an underestimation of tall vegetation. The over- and underestimation at both ends (small and large trees) is partly caused by a tree-based regression (e.g., Random Forests and Cubist), where single predictions of each tree are averaged. Thus, height at low and high range tends to a mean value. Larger bias is observed for the FBD-based estimates (Figure 4-8). Accordingly, the increasing number of spatial predictors results in a reduction of the bias at both ends (i.e., the lowest and highest vegetation heights). Moreover, a lower deviation from LiDAR height for the A-B transect between pixel IDs 80–150 (Figure 4-8) can be observed. This is caused

by the fact that this part of the LiDAR transect was used for model training, while other parts are independent (Figures 4-3 and 4-8).

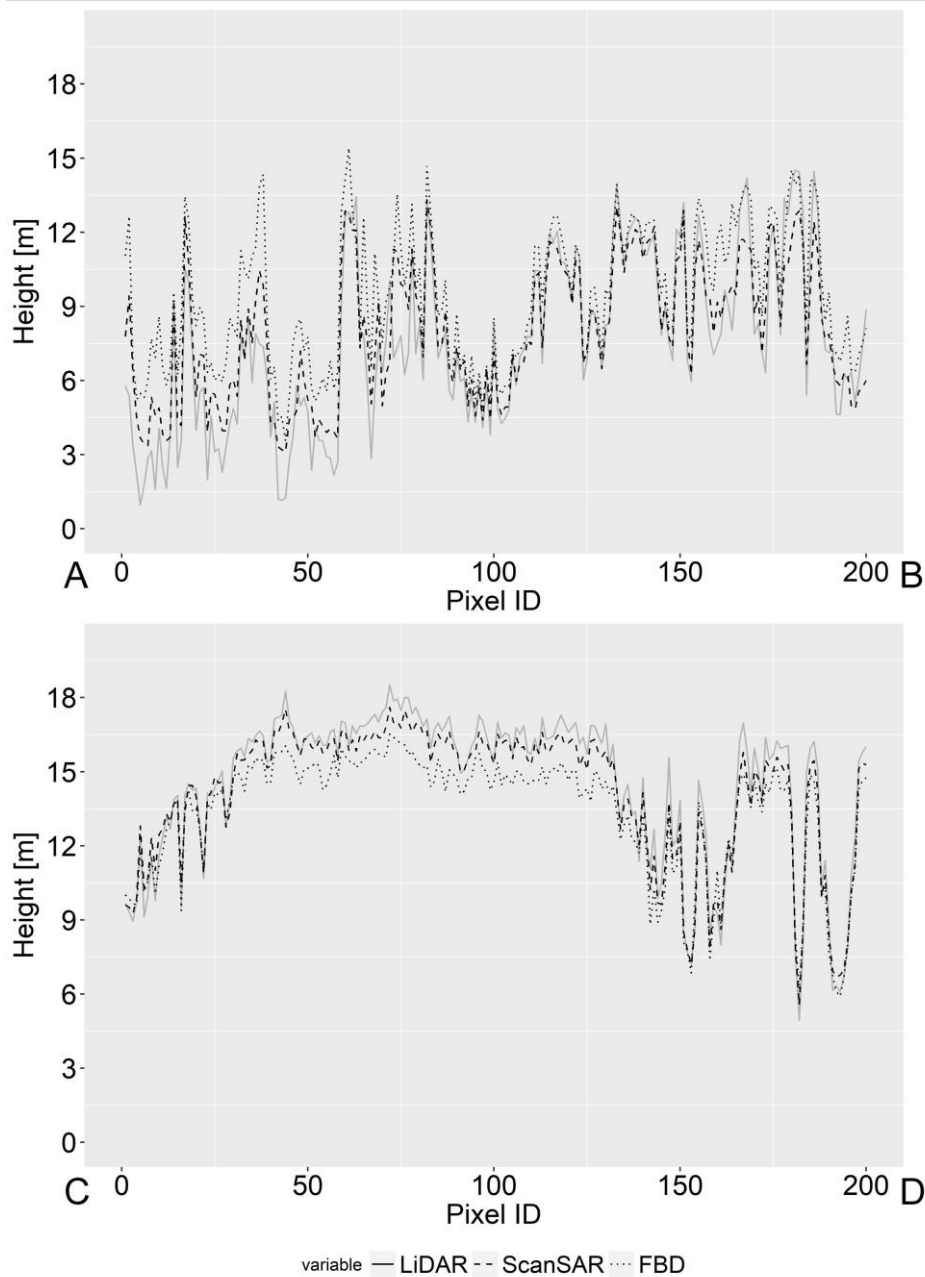


**Figure 4-8:** Transects of the vegetation height of the three products over areas with small (upper profile) and tall trees (bottom profile). The upper image shows vegetation height for the transect A-B in the northern part of the peninsula (Figure 4-7), while the bottom image shows vegetation height for the transect C-D in the central part of the peninsula (Figure 4-7). The FBD-based map overestimated height in areas with small vegetation and underestimated in areas with tall vegetation more noticeably compared to the ScanSAR-based map. For visualisation reasons, every 5 pixels from north to south was averaged.



### **4.3.2 Impact of Number of L-Band Observations on Model’s Predictive Performance**

Here, we analysed the influence of the number of spatial predictors on model prediction performance. For this analysis, we used ScanSAR mosaics only. As mentioned in Section 4.2.3, the reference data were divided into training and test data using “stratified random sampling” and “spatial sampling” with 100 repetitions. Furthermore, to show the effect of a speckle filter on the model’s predictive performance, unfiltered and multi-temporal speckle-filtered SAR data after (Quegan and Yu 2001) were used as predictive variables. The models based on “stratified random sampling” demonstrate a steady increase of  $R^2$  and decrease of RMSE using both unfiltered and filtered SAR data (Figure 4-9 upper and bottom left). Moreover, the results based on the filtered SAR data possess much higher  $R^2$  and lower RMSE compared to the results from unfiltered SAR data. The increase of  $R^2$  and decrease of RMSE from 4 to 8 scenes and further is much stronger in the models based on speckle-filtered SAR data. This is most likely caused by the fact that the applied filter uses a  $7 \times 7$  moving window and thus strengthens the spatial autocorrelation between training and test data.

Another observation is that the variance of the model statistics based on “stratified random sampling” is much lower compared to the model statistics based on “spatial sampling”. Considering the models based on “spatial sampling”, those based on filtered data possess higher  $R^2$  and lower RMSE compared to those based on unfiltered SAR data (Figure 4-9 upper and bottom right). However, the differences in the statistics are not as high as in the “stratified random sampling” models. This confirms that the differences between the results based on filtered and unfiltered SAR data using “stratified random sampling” are caused by the spatial autocorrelation of the reference data. Finally, it can be observed that for more than 12 scenes, further increment of acquisitions does not result in further improvement of  $R^2$  and RMSE.

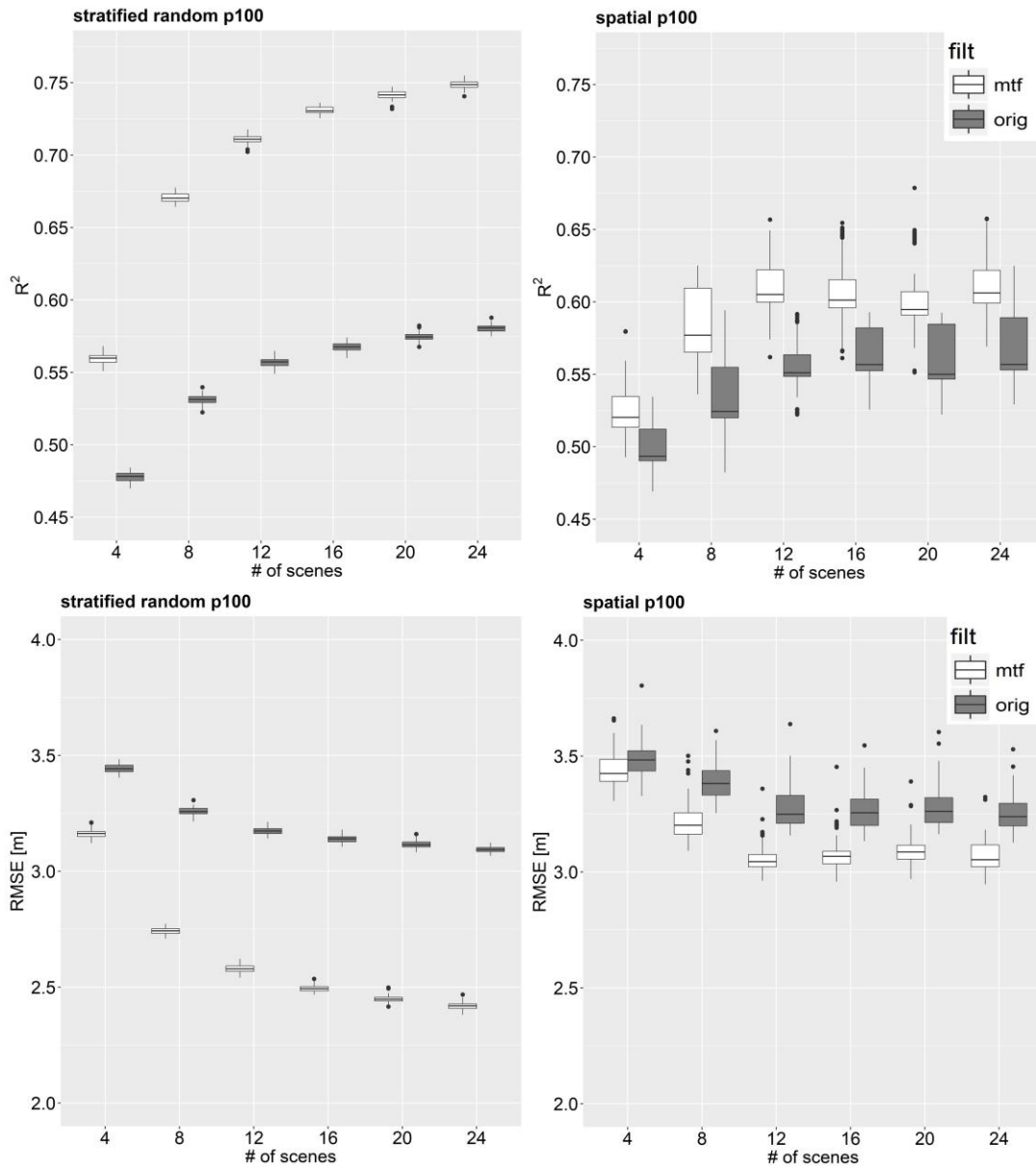


**Figure 4-9:** Impact of number of scenes on model prediction performance using “stratified random sampling” (left) and “spatial sampling” (right) for multi temporal Qegan speckle-filtered data (“mtf”, white boxplots) and unfiltered ScanSAR data (“orig”, dark-grey boxplot).

### 4.3.3 Impact of Number of Samples on Model Prediction Performance

To test the impact of number of training samples on model’s predictive performance, the test data from both sampling strategies remained unchanged, while training set from both sampling strategies were sampled randomly 100 times with 1%, 5%, and every decile of the data. According to Figure 4-10 (dark-grey boxplots), for the “stratified random sampling” scenario, an increasing number of training data

results in a steady improvement of the goodness-of-fit statistics (i.e., increase of  $R^2$  of about 27% and decrease of RMSE of about 22%). This is again caused by the spatial autocorrelation between training and test data, i.e., with an increasing number of training data, the probability to be adjoined with test data increases, resulting in continuous improvement of retrieval accuracies. However, if spatial autocorrelation is considered (i.e., the “spatial sampling” scenario), the model’s predictive performance saturates with an increasing number of training samples (Figure 4-10, white boxplots). With an increasing number of training data in the “spatial sampling” scenario, the model performance is enhanced up to a threshold of 20% of the training data, and very slightly afterwards. Additionally, the variance in the model statistics decreases with an increasing number of training samples. Based on the results, a threshold of around 20% of training data represents a plausible trade-off between model efficiency and data collection effort. 20% of training data corresponds here to 20,000 1-ha samples.

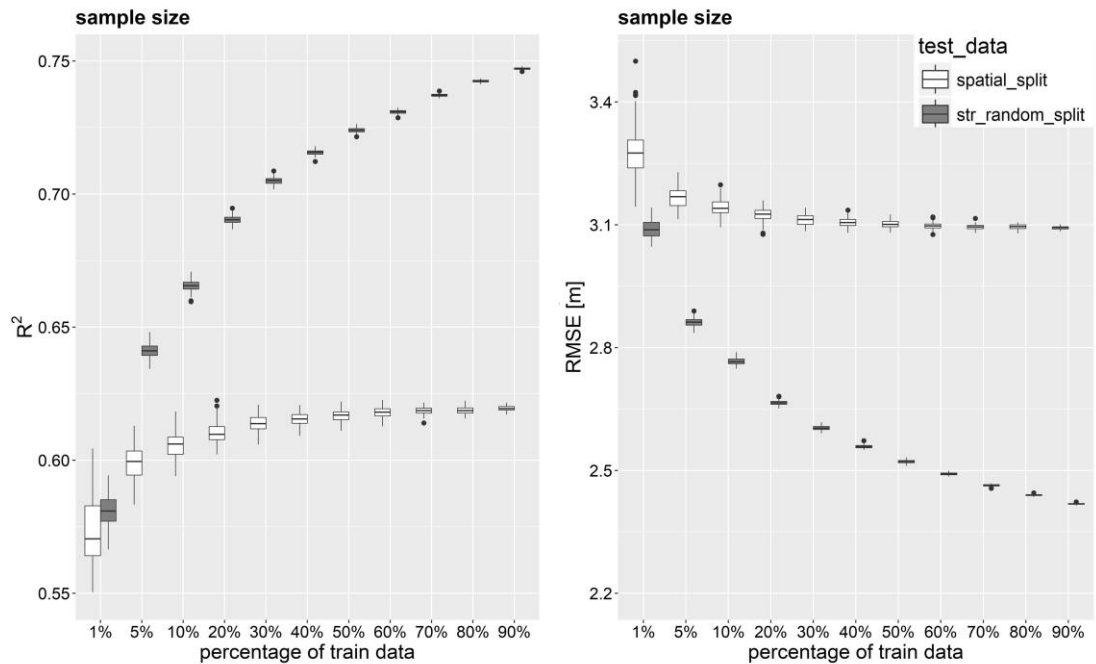


**Figure 4-10:** Impact of sample quantity on model prediction performance using “stratified random sampling” (dark-grey boxplot) and “spatial sampling” (white boxplot).

With an increasing number of training samples, the model performance increases continuously for “stratified random sampling” and saturates for “spatial sampling”. 1% of training data corresponds to 1000 1-ha samples.

## 4.4 Discussion and Summary

We examined the potential of multi-temporal L-band SAR backscatter to estimate vegetation height. Additionally, we investigated the impact of the number of spatial predictors and training samples on the model’s predictive performance given that the dataset is characterised by spatial autocorrelation.

This study has three main implications. First, we showed the value of multi-temporal L-band SAR backscatter for estimation of vegetation height. It is well known that, depending on forest structure, L-band SAR backscatter saturates in dense forests at biomass levels around 100 t/ha (Mermoz et al. 2014; Mitchard et al. 2009a; Yu and Saatchi 2016). Our results indicate that including more L-band observations in a statistical model can partly help to reduce under- and overestimation at low and high ranges of a forest parameter, respectively (Figure 4-8). These results are in agreement with previous studies reporting that the usage of multi-temporal L- and C-band SAR data improves retrieval accuracies of growing stock volume and AGB (Antropov et al. 2017; Cartus et al. 2012b; Santoro et al. 2006; Santoro et al. 2011; Santoro et al. 2015). We found, however, that after a specific number of observations, the model’s predictive performance is not further enhanced. In our case, using 12 dual-polarised L-band SAR observations, we estimated vegetation height with similar retrieval accuracies as using 24 dual-polarised L-band SAR observations (Figure 4-9). Obviously, 10–12 ScanSAR observations are sufficient to represent the multi-seasonal conditions of the forest vegetation over one year including dry and wet conditions at different phenological stages (i.e., leaf-off/leaf-on). According to our findings, the integration of 12 additional ScanSAR scenes does not lead to further prediction improvements. Hence, no relevant additional information can be gained from these images.

Second, spatial autocorrelation in the training and test dataset must be considered to provide a realistic predictive performance of the model. In the case where spatial autocorrelation in the reference data is ignored, estimation of the model’s performance is overoptimistic, caused by spatial autocorrelation between training and test data (Brenning 2012). Moreover, ignoring spatial autocorrelation between training and test data can lead to incorrect conclusions, e.g., an increasing number of spatial predictors and/or training samples leads to steady improvements of the model’s predictive performance.

Third, an increasing number of training samples leads to improvements in the model’s predictive performance, but it saturates at a specific percentage of training

samples. In contrast, Xu et al. (Xu et al. 2016) reported steady improvements of model performance with an increasing number of training samples in tropical forests. Garcia et al. (García et al. 2018) showed that retrieval accuracies were enhanced and saturated at a different percentage of training samples depending on forest structure (i.e., temperate broadleaf, mixed or coniferous forests). Nonetheless, neither study split the training and test data using geographical location of them, which might result in an overoptimistic model performance due to the likely spatial autocorrelation. In our study, using 20% of the training data was sufficient to get a similar level of accuracy as using 100% of the training data (Figure 4-10). 20% of the training data represents 20,000 1-ha samples, though it is still a large number of training data. In any case, it is crucial that training samples represent the entire range of values (in our case vegetation height) from different forest types (i.e., deciduous and evergreen forests) of the study area.

As expected, speckle filtering of the SAR images resulted in a better retrieval accuracy. However, using a speckle filter based on a moving window approach strengthens the spatial autocorrelation in the reference data. Nowadays, with the increasing availability of SAR time series (e.g., Sentinel-1), novel approaches that rely on temporal patterns only can be applied to suppress speckle and preserve spatial details without spatial blurring (Cremer et al. 2018). Furthermore, since the difference in acquisition time between LiDAR and SAR data is between one to five years, significant changes (caused, e.g., by fire or deforestation) within the LiDAR transects might have occurred, which together with forest growth reduce model's predictive performance (Urbazaev et al. 2016).

As shown in several studies (Cartus et al. 2014; García et al. 2018; Rodríguez-Veiga et al. 2016; Urbazaev et al. 2016; Xu et al. 2016), retrieval accuracies of forest structure parameters can be improved by including additional information from optical remote sensing data, i.e., Landsat or Sentinel-2 surface reflectance, and digital surface model (e.g., SRTM DEM). Nevertheless, in this study, we analysed the performance of multi-temporal L-band backscatter data only for the estimation of vegetation height. Since vegetation height correlates with other forest parameters (e.g., AGB, tree canopy cover) (Chave et al. 2005; Colgan et al. 2013; Saatchi et al. 2011a), we can assume that similar results can be achieved for the estimation of AGB and tree canopy cover using multi-temporal dual-polarised L-band SAR backscatter.

## 4.5 Conclusion

ALOS-2 PALSAR-2 ScanSAR data provide time series of dual-polarised L-band observations (~10 observations per year) over wider areas (i.e., 350 km) at medium spatial resolution (i.e., 50 m), which is crucial for land monitoring at national or continental scales. In this study, we investigated the potential of this dataset to map vegetation height over tropical deciduous and evergreen forests of the Yucatan peninsula, Mexico. For this, we used airborne LiDAR-based vegetation height for the training of L-band backscatter using the Random Forests algorithm. Specifically, we examined the value of multi-temporal L-band data for the estimation of vegetation height taking the spatial autocorrelation between training and test data into account. Our results indicate that ignoring spatial autocorrelation between training and test data lead to an overoptimistic model's predictive performance. Accordingly, a spatial splitting of the reference data into training and test data should be preferred to provide realistic retrieval accuracies. Moreover, based on this analysis, we determined an optimal number of L-band observations and training samples as a trade-off between retrieval accuracies and data collection effort.

Open data policies such as those of the ESA and NASA stimulate development of novel approaches based on these data (e.g., Landsat, Sentinels). Bearing in mind new L-band missions in near future (ALOS-4, NISAR, SAOCOM, Tandem-L) that will provide time series of L-band observations, open L-band PALSAR-2 ScanSAR data for the scientific community would foster further development of innovative algorithms for forest monitoring including mapping of forest structure parameters and detection of deforestation and forest degradation over large areas to support international climate initiatives (e.g., UN Reducing Emissions from Deforestation and Forest Degradation+ programme).

**Author Contributions:** M.U. and C.T. conceived and designed the experiments; M.U. performed the experiments; M.U. and F.C. analysed the data; M.U. wrote the paper; all co-authors assisted the lead author in writing and revising the manuscript. All authors read and approved the final manuscript.

**Funding:** M.U. was funded by the International Max Planck Research School for Global Biogeochemical Cycles. This work was partly funded by the German Aerospace Center (DLR) in the Sentinel4REDD project (FKZ: 50EE1540).

**Acknowledgments:** M.U. conducted this work under the International Max Planck Research School for Global Biogeochemical Cycles and acknowledges its funding and support. This work has been undertaken within the framework of the JAXA Kyoto & Carbon Initiative. ALOS PALSAR mosaic data were available from ©JAXA PALSAR MOSAIC 2014. The authors would like to thank JAXA for providing ALOS-2 PALSAR-2 ScanSAR data and NASA for providing airborne LiDAR data.

**Conflicts of Interest:** The authors declare no conflict of interest. The funders had no role in the design of the study; in the collection, analyses, or interpretation of data; in the writing of the manuscript, and in the decision to publish the results.





# Chapter 5

## **Synthesis**

*Comparison with the existing national AGB maps*

*Summary*

*Outlook*

## 5.1 Comparison with the existing national AGB maps

The NFI- and LiDAR-calibrated forest aboveground biomass maps introduced in the Section 3 were compared with four existing nationwide remote sensing based aboveground biomass maps, i.e., Saatchi et al. (2011a); Cartus et al. (2014); Avitabile et al. (2016); Rodriguez-Veiga et al. (2016). The pan-tropical AGB map of Baccini et al. (2012) was not considered, since this map covers only the southern Mexico. A summary of the data and methods used for AGB estimation is shown in Table 5-1.

**Table 5-1:** Summary of materials and methods used for AGB estimation in Mexico

Study	Input data	Training data	Pixel spacing	Temporal coverage	Forest mask	Model
Saatchi et al. 2011a	MODIS SR (surface reflectance), QuickScat, SRTM DEM	Pan-tropical forest plots and IceSAT GLAS	1 km	2000	no	MaxEnt
Avitabile et al. 2016	Pan-tropical AGB maps of Saatchi et al. 2011 and Baccini et al. 2012	INFyS	1 km	2000-2008	no	Weighted average between Saatchi and Baccini and calibration with local reference data
Cartus et al. 2014	ALOS PALSAR, Landsat Tree Cover, INEGI Land use map, SRTM DEM	INFyS between 2004-2009	30 m	2007	no	Random Forests
Rodriguez-Veiga et al. 2016	MODIS SR, ALOS PALSAR, SRTM DEM	INFyS between 2004-2011	250 m	2008	Forest probability layer based on PALSAR HV backscatter	MaxEnt
Urbazaev et al. 2018	ALOS PALSAR, Landsat SR, Landsat Tree Cover, SRTM	INFyS between 2004-2011	100 m	2008	Landsat Tree Cover > 10%	Cubist
Urbazaev et al. 2018	ALOS PALSAR, Landsat SR, Landsat Tree Cover, SRTM	INFyS between 2004-2011, airborne LiDAR	100 m	2008	Landsat Tree Cover > 10%	Cubist

The AGB maps of Saatchi et al. (2011a) (hereafter Saatchi map) and Avitabile et al. (2016) (hereafter Avitabile map) were produced for the entire tropics at a coarse spatial resolution (1 km). Cartus et al. (2014) (hereafter Cartus map), Rodriguez-Veiga et al. (2016) (hereafter Rodriguez-Veiga map) and a part of the results of this work (Urbazaev et al. 2018) (hereafter Urbazaev map) estimated AGB specifically for Mexico. A crucial difference between the Saatchi map and the three national AGB maps (Cartus map, Rodriguez-Veiga map, and Urbazaev map) is that the pan-tropical map was calibrated with spaceborne LiDAR-based AGB estimates collected over the entire Latin America (incl. Amazon basin). In contrast to the

Saatchi map, the Cartus, Rodriguez-Veiga and Urbazaev maps were calibrated with the national forest inventory (INFyS) data. In addition to the national forest inventory data, Urbazaev et al. (2018) used airborne LiDAR data for model calibration (hereafter Urbazaev-LiDAR map). The Avitabile map is a fused product of the Saatchi map, the Baccini et al. (2012) map and the national forest inventory data. Therefore, the Avitabile map for Mexico can be considered as the fusion of two pan-tropical maps and the Mexican NFI data. A detailed description of the methods can be found in the corresponding publications.

The Saatchi, Avitabile and Cartus maps represent total aboveground biomass (incl. shrub and herbaceous biomass), while the Rodriguez-Veiga and Urbazaev maps estimated AGB in forests. Furthermore, the INFyS data have been collected in forested areas only and represent forest AGB stocks. Therefore, a forest mask was applied for the Saatchi, Avitabile and Cartus maps, in order to compare six national forest AGB maps. Forested areas were defined as areas with tree cover > 10% obtained from the global Landsat Tree Cover product for 2010 (Hansen et al. 2013) similarly as for the Urbazaev maps.

The national Mexican AGB maps that were calibrated with the INFyS data (i.e., all except the Saatchi map) show similar mean and total national AGB values and are in accordance with the INFyS estimates (Figure 5-1). All maps (except the Saatchi map) and the INFyS data indicate that Mexican forest AGB reach values up to 125-150 t ha<sup>-1</sup>. According to these maps, forest AGB with values higher than 150 t ha<sup>-1</sup> represent only a small part of the total forested areas. The Saatchi map show a second AGB peak at around 140 t ha<sup>-1</sup> and the AGB values in this map goes up to 300 t ha<sup>-1</sup>.

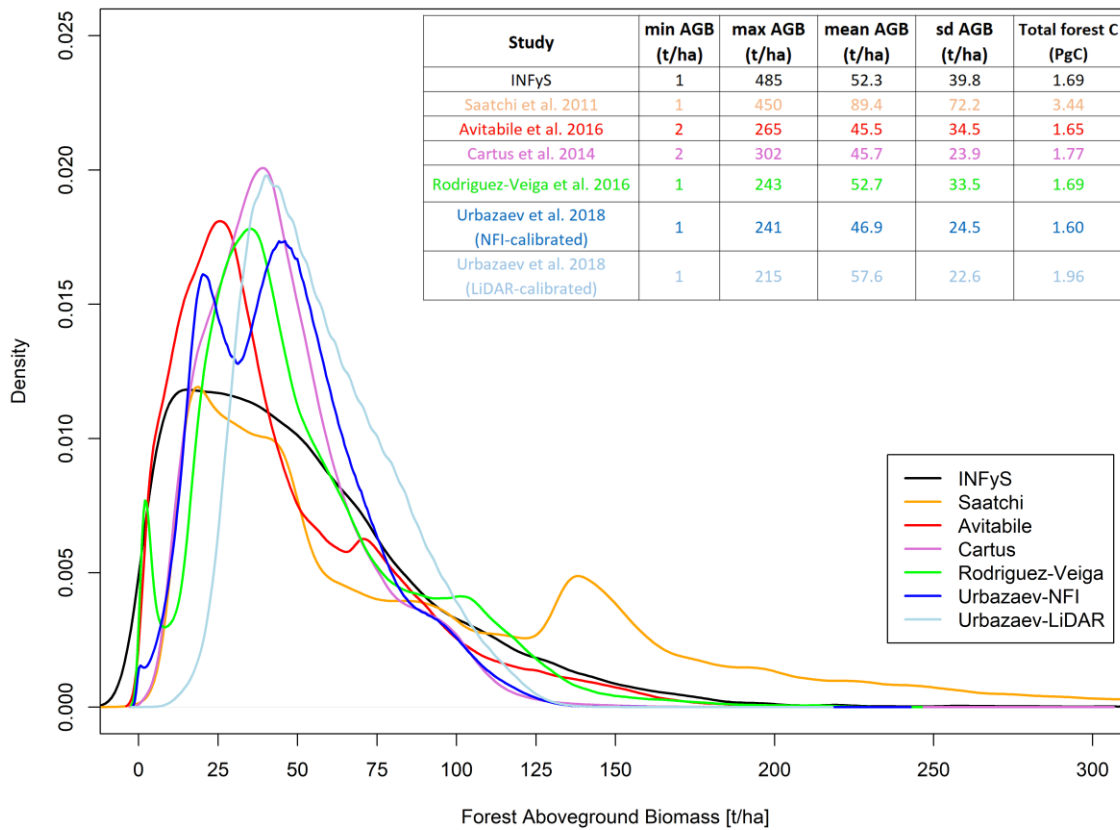


**Figure 5-1:** Distribution of the Mexican national forest AGB according to the six remote sensing based maps (Table 5-1) and the INFyS estimates. Non-forested areas were masked out using Landat Tree Cover product (Hansen et al. 2013) with a threshold of 10%.

Although the forest AGB maps show similar total forest AGB distribution at national scale (with some deviation of the Saatchi map), at pixel scale the individual maps indicate different spatial distribution of forest AGB (Figure 5-2). To compare the maps spatially, all the maps were first aggregated to 1 km (pixel spacing of the Saatchi and Avitabile maps) by averaging of the corresponding pixel within the 1 km pixel. Between all AGB maps the absolute difference as well as scatterplots with coefficient of determination were calculated (Figure 5-2).

### Comparison with the Saatchi map

An AGB map with the greatest difference to the other maps is the Saatchi map. The spatial difference maps between the Saatchi and other maps show similar patterns with much higher AGB values almost everywhere besides the areas in the mid-western part of Mexico (*Sierra-Madre Occidental*) (blue areas in the Figure 5-2: first row and third to sixth columns), where the Cartus, Rodriguez-Veiga and Urbazaev maps depict higher values. The reason for much higher estimates in the

Saatchi map is the model calibration conducted at the continental scale with some training areas located in dense tropical forests of the Amazon basin. In the mid-western part of Mexico (*Sierra-Madre Occidental*), the Cartus, Rodriguez-Veiga and Urbazaev maps were calibrated locally with a large amount of training data over these areas (Figure 1-11) and show higher AGB estimates as in the Saatchi map. The Avitabile map possesses strongest correlation to the Saatchi map, since it is based on the fusion of the Saatchi and Baccini maps. Interestingly to note that the Urbazaev-LiDAR has the second strongest correlation to the Saatchi map. One reason for this can be that the both maps were calibrated with LiDAR data (spaceborne ICESAT GLAS and airborne G-LiHT) and not with NFI data.

### Comparison with the Avitabile map

Since Avitabile et al. (2016) used Mexican inventory data for bias removal between the Saatchi and Baccini maps, this map has stronger correlation with the locally calibrated AGB maps as the Saatchi map. Two areas of disagreements between the Avitabile map and locally calibrated AGB maps can be identified. Similarly as the Saatchi map, Avitabile et al. (2016) estimated lower AGB values in the areas in the mid-western part of Mexico (*Sierra-Madre Occidental*). The second area with greater AGB values in the Avitabile map are the areas in the southern Mexico along the dense cloud forests of *Sierra-Madre del Sur* and *Chimalapas and Lacandon* tropical forests (red areas from west to east in the Figure 5-2: second row and third to fifth columns). In contrast to the NFI-calibrated maps, the Urbazaev-LiDAR map possesses not such high differences with the Avitabile map over these areas.

### Comparison of the NFI-calibrated maps

The strongest correlation ( $R^2 > 0.7$ ) between the single maps indicate the NFI-calibrated AGB maps, i.e., the Cartus, Rodriguez-Veiga and Urbazaev-NFI maps. These three national AGB maps are based on the similar input variables (L-band backscatter together with optical data (Landsat or MODIS) and SRTM DEM), but different machine learning algorithms were applied (Table 5-1). The Cartus and Urbazaev-NFI maps indicate similar spatial distribution of AGB (within  $\pm 20 \text{ t ha}^{-1}$ ) with small areas of larger discrepancies. Rodriguez-Veiga et al. (2016) estimated more forest biomass in the Yucatan peninsula as the Cartus, Urbazaev-NFI and Urbazaev-LiDAR. One of the reason for different spatial distribution of AGB is the statistical approaches used. While Cartus et al. (2014) and Urbazaev et al. (2018) applied tree-based regressions (Random Forests and Cubists), the MaxEnt algorithm used in the Rodriguez-Veiga et al. (2016) is based

on probability distribution of discrete biomass classes with maximum entropy. Urbazaev et al. (2018) and Cartus et al. (2014) reported an underestimation at high AGB ranges, which is partly caused by a tree-based regression (i.e., averaging of single estimates for each prediction tree). Furthermore, Rodriguez-Veiga et al. (2016) used MODIS optical data (at coarse spatial resolution of 250 m) in contrast to Landsat optical data used in Cartus et al. (2014) and Urbazaev et al. (2018). MODIS mid-infrared channels have showed sensitivity to high biomass over pan-tropical regions (e.g., Baccini et al. 2008; Saatchi et al. 2011a; Baccini et al. 2012) and thus, might improve AGB estimation over the Yucatan peninsula in the Rodriguez-Veiga map.

### Comparison with the Urbazaev-LiDAR map

The Urbazaev-NFI and Urbazaev-LiDAR possess strongest correlation as the same input variables and statistical algorithm were applied. The main difference between the Urbazaev-LiDAR map and NFI-calibrated maps (Cartus, Rodriguez-Veiga and Urbazaev-NFI) is the spatial distribution of AGB in the southern Mexico (cloud forests of *Sierra-Madre del Sur* and tropical forests of *Chimalapas and Lacandon*). Since these areas are the conservation areas, a very small amount of forest inventory data have been collected there. There exist, however, airborne LiDAR acquisitions over the *Sierra-Madre del Sur* and *Lacandon* forests, which were used in the Urbazaev-LiDAR map. The Saatchi and Avitabile maps estimated high AGB over these three regions as well.

In general, three main regions with large discrepancies between the maps can be identified. In the pan-tropical maps the mid-western part of Mexico (*Sierra Madre Occidental*) possesses lower AGB estimates as the locally calibrated AGB maps. Furthermore, in the southern Mexico (cloud forests of *Sierra-Madre del Sur* and tropical forests of *Chimalapas and Lacandon*) the pan-tropical maps as well as the Urbazaev-LiDAR map show higher AGB values as the NFI-calibrated maps. Finally, between the locally calibrated AGB maps the main discrepancies are in the Yucatan peninsula with greater AGB estimates in the Rodriguez-Veiga map.

Although the locally calibrated national AGB maps showed similar goodness-of-fit statistics with the NFI data at pixel scale ( $R^2$  between 0.3 and 0.5) as well as good agreement at state and national scales (Cartus et al. 2014; Rodriguez-Veiga et al. 2016; Urbazaev et al. 2018), these four maps illustrated different spatial distribution of forest AGB (Figure 5-2). To further improve AGB estimates and assess the retrieval accuracies of these maps independently, additional field inventory data (for instance, through the Mexican Network of Intensive Carbon

Comparison with the existing national AGB maps

Monitoring Sites (Red Mex-SMIC) (Birdsey et al. 2015)) and/or airborne LiDAR data can be collected over the areas with discrepancies and used for model calibration and validation.

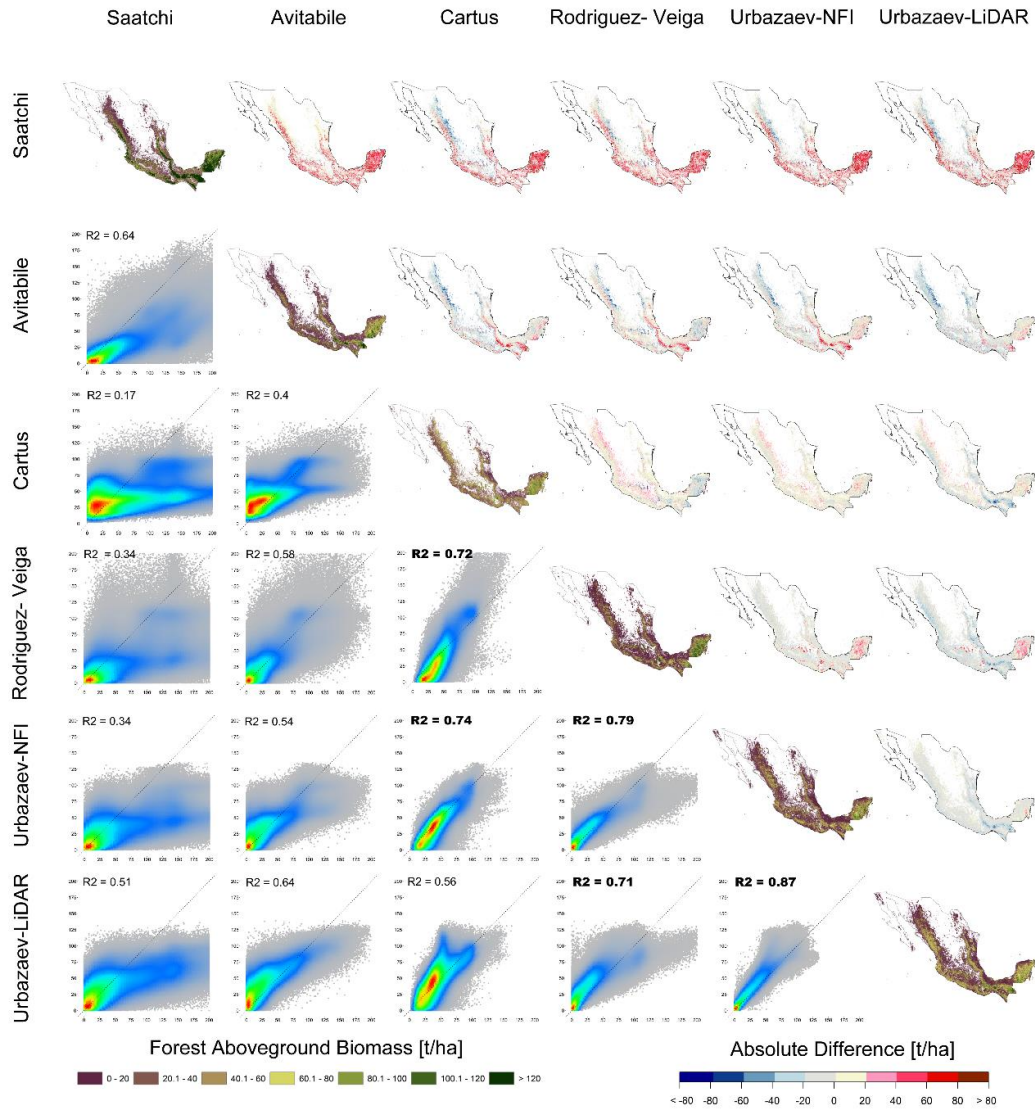


**Figure 5-2:** Comparison between the Mexican national AGB maps. The maps in the diagonals show single AGB maps at pixel spacing of 1 km. The maps outside the diagonal represent absolute AGB difference between the products. To calculate the absolute difference, a map in the row is the minuend and a map in the column is the subtrahend (e.g., Saatchi-Avitabile difference map represents Saatchi AGB minus Avitabile AGB). In the scatterplots between the single AGB maps the columns indicate the X-axes and the rows are the Y-axes. Non-forested areas were masked out using Landat Tree Cover product (Hansen et al. 2013) with a threshold of 10%.

## 5.2 Summary

The main research aim of this work was to determine capabilities and limitations of remote sensing data (SAR, optical and LiDAR) to estimate forest structure parameters in sub-tropical forests of Mexico. For this, various scenarios by integrating multi-temporal SAR-, optical-, LiDAR-based parameters, and field data were applied at local, regional and national scales.

**Research objective #1** - *Improved Multi-Sensor Satellite-Based Aboveground Biomass Estimation by Selecting Temporally Stable Forest Inventory Plots Using NDVI Time Series*

Combination of multi-sensor remote sensing data (SAR and optical) leads to an improvement of AGB modelling compared to the results based on either sensor alone (Figure 2-5). This can be explained by providing additional explanatory information from Landsat-based tree cover product as well as SRTM elevation data. Furthermore, more accurate AGB estimates can be derived by selecting temporally stable forest inventory data, if there exists a time lag between field and satellite data acquisitions. MODIS NDVI time series and the BFAST change detection algorithm have been shown to be efficient tools to detect and isolate forest inventory data, where abrupt land cover changes might occur. We showed that improvements in AGB estimations are due to BFAST-filtering and not due to a reduced number of field observations. For this, the same number of the NFI data were randomly excluded as were selected for the BFAST-filtered data (Figure 2-5). This method can be applied over large areas, where field data are outdated in relation to satellite data acquisition (e.g., >5 years). Nevertheless, it was not possible to exclude the confounding influence of the false detection of abrupt changes over field plots, bearing in mind a lower spatial resolution of a MODIS NDVI pixel compared to the plot area (250 m vs. 100 m), and the possible influence of clouds and cloud shadows.

Both methods (multi-sensor combination and filtering of NFI data) were evaluated in two study areas (each site size ca. 70x70 km) in tropical dry and humid forests of Mexico. The accuracy of AGB estimation based on original (unfiltered) NFI data is consistent with the results produced by Cartus et al. (2014) in terms of statistical metrics ( $R^2 = 0.52$  (Cartus et al. 2014) vs.  $R^2 = 0.55$  (mean for two study sites);  $RMSE = 28.2 \text{ t ha}^{-1}$  (Cartus et al. 2014) vs.  $RMSE = 23.8 \text{ t ha}^{-1}$  (mean for two study sites), while AGB estimates based on BFAST-filtered plots produce more accurate estimates (mean for two study sites  $R^2 = 0.67$  and  $RMSE = 21.2 \text{ t ha}^{-1}$ ).



**Research objective #2** - *Estimation of Forest Aboveground Biomass and Uncertainties by Integration of Field Measurements, Airborne LiDAR, and SAR and Optical Satellite Data in Mexico*

Three national forest aboveground biomass maps for Mexico at a spatial resolution of 100 m based on remote sensing data and two sets of reference data were derived. One AGB map was calibrated with a large number of NFI data collected over the forested areas across the country. Two others AGB maps were produced by applying a two-stage up-scaling method of reference data, i.e., from field-AGB to LiDAR-AGB and from LiDAR-AGB to satellite-based AGB estimates. For one LiDAR-calibrated wall-to-wall AGB map all LiDAR-AGB samples were used, while to generate another wall-to-wall map LiDAR-AGB samples with uncertainties lower than 50% were utilized for model training. A comprehensive comparison of the derived AGB maps with another available satellite-based AGB products as well as with the NFI data can be found in Section 5.1 and Section 3.3.4.

For all AGB maps corresponding uncertainty layers were derived. For this, errors in the field-AGB were estimated and propagated to LiDAR-AGB and satellite-based AGB using Monte Carlo simulations. A two-stage up-scaling approach can be considered as more cost-efficient compared to the traditional field to satellite imagery up-scaling, since a lower amount of field data are required. However, the uncertainty analysis showed that by applying two-stage up-scaling methods an error propagation should be performed. This should be done to prevent propagation of errors in the final wall-to-wall map. We showed that ignoring field to LiDAR error lead to an uncertainty in the wall-to-wall LiDAR-calibrated AGB map of up to 150%, which is much higher compared to the NFI-calibrated AGB map (Figure 3-8, 3-11).

**Research objective #3** - *Potential of Multi-Temporal ALOS-2 PALSAR-2 ScanSAR Data for Vegetation Height Estimation in Tropical Forests of Mexico*

A vegetation height map for the Yucatan peninsula, which is covered by tropical dry and humid forests, was derived. Furthermore, 24 multi-temporal L-band backscatter imagery (collected between 2014 and 2018) and more than 150,000 1 ha LiDAR samples (ca. 1% of the total area of the Yucatan peninsula collected in 2013) were used to investigate: 1) the impact of number of L-band backscatter intensities and training samples on model's predictive performance; 2) the influence of spatial autocorrelation between the calibration and validation data on model's accuracy.

Using 12 dual-polarised L-band SAR observations, we estimated vegetation height with similar retrieval accuracies as using 24 dual-polarised L-band SAR observations (Figure 4-9). Obviously, 12 L-band observations were sufficient to

represent the multi-seasonal conditions of the forest vegetation over one year including dry and wet conditions at different phenological stages (i.e., leaf-off/leaf-on), so that additional 12 acquisitions did not provide extra information. However, we showed the merit of multi-temporal L-band backscatter compared, for instance, to the four annual global L-band mosaics by decreasing over- and underestimation at low and high vegetation height (Figure 4-8).

Furthermore, with an increasing number of training samples model's accuracy was improved, but the prediction performance was saturated already at 20% of all training samples (Figure 4-10). Finally, spatial autocorrelation between training and validation data should be considered, i.e., they should be spatially separated, in order to provide a realistic model's accuracy (Figure 4-9). In general, time series of PALSAR-2 ScanSAR L-band observations, which features a wide swath of 350 km, are crucial for land monitoring at large national or continental scales.

### 5.3 Outlook

Based on the results of this work following limitations for estimation of forest structure parameters with remote sensing methods can be determined:

1. Mono-temporal satellite imagery (either optical or SAR) are less appropriate for forest structure mapping due to the impact of environmental conditions.
2. SAR imagery acquired over hilly terrain might lead to AGB overestimation on slopes facing the sensor (strong return) and to AGB underestimation on the opposite side (low return).
3. Signal from both optical and L-band SAR sensors saturates at high biomass ( $>100 \text{ t ha}^{-1}$ ). The underestimation of dense biomass is further strengthened due to a limited amount of training samples collected at this range, i.e., these biomass levels are less represented in a statistical model.
4. Forest biomass at low range ( $<10\text{-}20 \text{ t ha}^{-1}$ ) is often overestimated. The reason for this is strong impact of surface conditions, such as roughness, moisture as well as photosynthetically active non-woody vegetation that contribute to a higher SAR or optical signal.
5. In tree-based ensemble methods (e.g., Random Forests, Cubist) a final estimate is usually determined by averaging of many estimates from single trees. The averaging of single estimates reduces model variance, i.e., precision is increased. On the other side, however, the averaging introduces bias, e.g., under- and overestimation at low and high biomass, respectively. In contrast, empirical or physically-based models are less biased but possess high variance.
6. Quality, amount and spatial distribution of in situ data are crucial to develop and validate remote sensing based models.
7. Very high resolution (VHR) remote sensing data can be served as reference data, but might introduce large uncertainties to the final estimates.
8. Spatial autocorrelation between the training and validation data might cause overoptimistic prediction statistics.

Bearing in mind the limitations listed above, remote sensing methods offer following capabilities for estimation of forest structure parameters:

1. Remote sensing based products of forest AGB are in line with in situ based statistics on national forest biomass at aggregated scales (hexagon, federal states and national AGB level) (Figure 3-16, 3-17, 5-1).
2. Multi-sensor combination of remote sensing data improves AGB retrieval accuracy (Figure 2-5).

3. Optical imagery are an important tool for providing information on photosynthetically active vegetation and tree density.
4. SRTM DEM correlates with object height and contribute to a more accurate AGB retrieval.
5. MODIS NDVI time series are able to detect outdated forest inventory plots and improves AGB modelling performance by selecting temporally stable inventory plots.
6. Multi-temporal combination of SAR imagery reduces over- and underestimation in sparse and dense forests, respectively (Figure 4-8). For instance, over the entire tropics there exist around 8-10 PALSAR-2 dual-polarised ScanSAR mosaics per year that are much more valuable than single annual mosaics (Figure 4-6).
7. The impact of topography on forest structure mapping with SAR can be reduced e.g., by combining ascending and descending orbits to compensate for radar shadow effects. Furthermore, high quality DEM can be used for a more accurate radiometric terrain correction. Finally, more weight might be given to optical imagery over hilly terrain in statistical models.
8. VHR remote sensing data can be used as reference data, and hence reduce collection effort of field data. It is important to characterize errors contained in the VHR-based reference data in order to prevent propagation of errors in the wall-to-wall map.
9. VHR remote sensing data can be served as an efficient tool for model calibration, bearing in mind repetitive reference data acquisitions as well as sampling from not accessible areas.
10. Although satellite-based maps of forest structure parameters contain errors, they represent the relative distribution of forest parameters over large areas. Therefore, satellite-based products can be used for forest stratification analyses, i.e., to improve sampling strategies of field data by reducing cost and increasing representativeness of them.

Some of the limitations and capabilities listed above are well known and documented phenomena (e.g., saturation at high biomass, impact of environmental conditions). In this work we showed how the quality (e.g., outdated data), quantity (LiDAR as training data) and distribution (spatial autocorrelation) of reference data might impact the estimation of forest structure using satellite imagery.

Considering Mexico as the study area, the main limitation for estimation of forest parameters is the hilly terrain of the country (Figure 1-11). Local topography

complicates both the collection of field data and hence, quality, quantity and distribution, as well as impacts the signal scattered back to the sensors (SAR, optical and LiDAR). The saturation of L-band signal theoretically should not be the main restriction of forest structure mapping in Mexico, since a small part of the total area is covered by forests with biomass higher than 100-120 t ha<sup>-1</sup> (Figure 5-1). However, by comparison of the three national AGB products (Cartus et al. 2014; Rodriguez-Veiga et al. 2016; Urbazaev et al. 2018), forest biomass magnitude varies in the Yucatan peninsula (flat terrain) up to 100 t ha<sup>-1</sup> (Figure 5-2). The main reason for this is rather the statistical models applied (Section 5.1), since similar input and training data were used. A further important issue in biomass mapping in Mexico is the forest definition, since large areas are covered by woodland-to-forest transition (INEGI 2010). For instance, in Cartus et al. (2014) the total aboveground carbon varied by 44% (2.21 PgC vs. 1.53 PgC), depending on whether a forest mask was applied. Rodriguez-Veiga et al. (2016) applied different forest masks (e.g., MODIS Tree Cover >10%, PALSAR-based forest mask, forest class from the INEGI national land cover) to calculate national forest AGC and concluded that the total AGC varied by 31% (lowest forest AGC 1.47 PgC, highest forest AGC 1.92 PgC). Therefore, a consistent and accurate national forest mask is crucial to assess national forest carbon stocks and changes.

We showed the merit of multi-temporal L-band SAR data to reduce over- and underestimation in sparse and dense forests, respectively. Bearing in mind new L-band missions in the near future (SAOCOM, NISAR, ALOS-4, potentially Tandem-L), dense time series of L-band backscatter are of great interest to improve forest structure mapping. LiDAR is an extremely important tool for repetitive reference data acquisitions over large areas. LiDAR captures spatial variability of heterogeneous tropical forests. However, we showed that a two-stage up-scaling method needs to be analysed and validated with great care. Field inventory is an essential tool to measure and observe ecological processes at local scale as it can provide a higher level of data richness when compared to LiDAR. Therefore, LiDAR can be used as an extension to NFI, for example, for areas that are difficult or not possible to access. Future research can investigate an integration of dense time series of L-band backscatter with airborne LiDAR data and field inventory for forest carbon stock assessments as a trade-off between map accuracy (i.e., user requirements) and resulting costs (i.e., number of NFI and LiDAR data).



# References

- Achard, F., Beuchle, R., Mayaux, P., Stibig, H.J., Bodart, C., Brink, A., Carboni, S., Desclée, B., Donnay, F., & Eva, H.D. (2014). Determination of tropical deforestation rates and related carbon losses from 1990 to 2010. *Global Change Biology*, *20*, 2540-2554
- Antropov, O., Rauste, Y., Häme, T., & Praks, J. (2017). Polarimetric ALOS PALSAR Time Series in Mapping Biomass of Boreal Forests. *Remote Sensing*, *9*, 1-24
- Askne, J., & Santoro, M. (2005). Multitemporal repeat pass SAR interferometry of boreal forests. *Ieee Transactions on Geoscience and Remote Sensing*, *43*, 1219-1228
- Askne, J.I., Dammert, P.B., Ulander, L.M., & Smith, G. (1997). C-band repeat-pass interferometric SAR observations of the forest. *Ieee Transactions on Geoscience and Remote Sensing*, *35*, 25-35
- Askne, J.I.H., Fransson, J.E.S., Santoro, M., Soja, M.J., & Ulander, L.M.H. (2013). Model-Based Biomass Estimation of a Hemi-Boreal Forest from Multitemporal TanDEM-X Acquisitions. *Remote Sensing*, *5*, 5574-5597
- Askne, J.I.H., Soja, M.J., & Ulander, L.M. (2017). Biomass estimation in a boreal forest from TanDEM-X data, lidar DTM, and the interferometric water cloud model. *Remote Sensing of Environment*, *196*, 265-278
- Asner, G.P., Hughes, R.F., Vitousek, P.M., Knapp, D.E., Kennedy-Bowdoin, T., Boardman, J., Martin, R.E., Eastwood, M., & Green, R.O. (2008). Invasive plants transform the three-dimensional structure of rain forests. *Proceedings of the National Academy of Sciences*, *105*, 4519-4523
- Asner, G.P. (2009). Tropical forest carbon assessment: integrating satellite and airborne mapping approaches. *Environmental Research Letters*, *4*, 1-11

- Asner, G.P., Mascaro, J., Muller-Landau, H.C., Vieilledent, G., Vaudry, R., Rasamoelina, M., Hall, J.S., & van Breugel, M. (2012). A universal airborne LiDAR approach for tropical forest carbon mapping. *Oecologia*, *168*, 1147-1160
- Attema, E.P.W., & Ulaby, F.T. (1978). Vegetation modeled as a water cloud. *Radio Science*, *13*, 357-364
- Avitabile, V., Baccini, A., Friedl, M.A., & Schullius, C. (2012). Capabilities and limitations of Landsat and land cover data for aboveground woody biomass estimation of Uganda. *Remote Sensing of Environment*, *117*, 366-380
- Avitabile, V., Herold, M., Heuvelink, G.B.M., Lewis, S.L., Phillips, O.L., Asner, G.P., Armston, J., Ashton, P.S., Banin, L., Bayol, N., Berry, N.J., Boeckx, P., de Jong, B.H.J., DeVries, B., Girardin, C.A.J., Kearsley, E., Lindsell, J.A., Lopez-Gonzalez, G., Lucas, R., Malhi, Y., Morel, A., Mitchard, E.T.A., Nagy, L., Qie, L., Quinones, M.J., Ryan, C.M., Ferry, S.J.W., Sunderland, T., Laurin, G.V., Gatti, R.C., Valentini, R., Verbeeck, H., Wijaya, A., & Willcock, S. (2016). An integrated pan-tropical biomass map using multiple reference datasets. *Global Change Biology*, *22*, 1406-1420
- Baccini, A., Laporte, N., Goetz, S.J., Sun, M., & Dong, H. (2008). A first map of tropical Africa's above-ground biomass derived from satellite imagery. *Environmental Research Letters*, *3*, 1-9
- Baccini, A., Goetz, S.J., Walker, W., Laporte, N.T., Sun, M., Sulla-Menashe, D., Hackler, J., Beck, P.S.A., Dubayah, R., Friedl, M.A., Samanta, S., & Houghton, R.A. (2012). Estimated carbon dioxide emissions from tropical deforestation improved by carbon-density maps. *Nature Climate Change Letter*, *2*, 182-185
- Baccini, A., Walker, W., Carvalho, L., Farina, M., Sulla-Menashe, D., & Houghton, R. (2017). Tropical forests are a net carbon source based on aboveground measurements of gain and loss. *Science*, *358*, 230-234
- Basuki, T.M., Skidmore, A.K., Hussin, Y.A., & Van Duren, I. (2013). Estimating tropical forest biomass more accurately by integrating ALOS PALSAR and Landsat-7 ETM+ data. *International Journal of Remote Sensing*, *34*, 4871-4888
- Bechtold, W.A., & Patterson, P.L. (2005). The enhanced forest inventory and analysis program-national sampling design and estimation procedures. *Gen. Tech. Rep. SRS-80*. Asheville, NC: US Department of Agriculture, Forest Service, Southern Research Station., *80*, 1-85
- Beer, C., Reichstein, M., Tomelleri, E., Ciais, P., Jung, M., Carvalhais, N., Rödenbeck, C., Arain, M.A., Baldocchi, D., & Bonan, G.B. (2010). Terrestrial gross carbon dioxide uptake: global distribution and covariation with climate. *Science*, 1184984



## References

- Berninger, A., Lohberger, S., Stängel, M., & Siegert, F. (2018). SAR-Based Estimation of Above-Ground Biomass and Its Changes in Tropical Forests of Kalimantan Using L- and C-Band. *Remote Sensing*, *10*, 1-22
- BFAST. Breaks for Additive Season and Trend Project. <http://bfast.r-forge.r-project.org/>
- Birdsey, R., Wayson, C., Olguín, M., Angeles-Perez, G., Maldonado, V., Lopez, D., Dupuy, J., Arreola, J., Esparza, L., Serrano, E., Caamal, J.P., Mendez, B., Sanchez, G., & Carillo, O. (2015). Network of Intensive Carbon Monitoring Sites in Mexico: Multi-institutional Collaboration to Support Mexico's National MRV/REDD+ Systems and North American Carbon Cycle Research. In, *NASA Carbon*. Pasadena, USA
- Blackard, J., Finco, M., Helmer, E., Holden, G., Hoppus, M., Jacobs, D., Lister, A., Moisen, G., Nelson, M., & Riemann, R. (2008). Mapping U.S. forest biomass using nationwide forest inventory data and moderate resolution information. *Remote Sens Environ*, *112*, 1658-1677
- Bonan, G.B. (2008). Forests and climate change: forcings, feedbacks, and the climate benefits of forests. *Science*, *320*, 1444-1449
- Bouvet, A., Mermoz, S., Le Toan, T., Villard, L., Mathieu, R., Naidoo, L., & Asner, G.P. (2018). An above-ground biomass map of African savannahs and woodlands at 25m resolution derived from ALOS PALSAR. *Remote Sensing of Environment*, *206*, 156-173
- Breiman, L., Friedman, J., Stone, C., & Olshen, R.A. (1984). *Classification and Regression Trees (Wadsworth Statistics/Probability)*. Chapman and Hall/CRC
- Breiman, L. (2001). Random Forests. *Machine Learning*, *45*, 5-32
- Brenning, A. (2012). Spatial cross-validation and bootstrap for the assessment of prediction rules in remote sensing: the R package 'sperrorest'. . In, *2012 IEEE International Geoscience and Remote Sensing Symposium (IGARSS)* (pp. 5372-5375). Munich, Germany: IEEE
- Brown, S. (1997). *Estimating biomass and biomass change of tropical forests: a Primer*. Rome: FAO
- Brownlee, J. (2016). *Master Machine Learning Algorithms. Discover how they work and implement them from scratch*.
- Bucini, G., Hanan, N., P. , Boone, R., B. , Smit, I., P. J. , Saatchi, S., S., Lefsky, M., A., & Asner, G., P. (2010). Woody Fractional Cover in Kruger National Park, South Africa. *Ecosystem Function in Savannas* (pp. 219-237): CRC Press
- Cartus, O., Santoro, M., Schmullius, C., & Li, Z. (2011). Large area forest stem volume mapping in the boreal zone using synergy of ERS-1/2 tandem coherence and MODIS vegetation continuous fields. *Remote Sensing of Environment*, *115*, 931-943

- Cartus, O., Kelldorfer, J., Rombach, M., & Walker, W. (2012a). Mapping Canopy Height and Growing Stock Volume Using Airborne Lidar, ALOS PALSAR and Landsat ETM+. *Remote Sensing*, *4*, 3320-3345
- Cartus, O., Santoro, M., & Kelldorfer, J. (2012b). Mapping forest aboveground biomass in the Northeastern United States with ALOS PALSAR dual-polarization L-band. *Remote Sensing of Environment*, *124*, 466-478
- Cartus, O., Kelldorfer, J., Walker, W., Franco, C., Bishop, J., Santos, L., & Fuentes, J. (2014). A National, Detailed Map of Forest Aboveground Carbon Stocks in Mexico. *Remote Sensing*, *6*, 5559-5588
- Castel, T., Beaudoin, A., Stach, N., Stussi, N., Le Toan, T., & Durand, P. (2001). Sensitivity of space-borne SAR data to forest parameters over sloping terrain. Theory and experiment. *International Journal of Remote Sensing*, *22*, 2351-2376
- Cazcarra-Bes, V., Tello-Alonso, M., Fischer, R., Heym, M., & Papathanassiou, K. (2017). Monitoring of forest structure dynamics by means of L-band SAR tomography. *Remote Sensing*, *9*, 1229
- CGIAR. SRTM 90m Digital Elevation Database v4.1. <https://cgiasi.community/data/srtm-90m-digital-elevation-database-v4-1/> (02.09.2016)
- Chapin III, F.S., Matson, P.A., & Mooney, H.A. (2002). *Principles of terrestrial ecosystem ecology*. New York: Springer
- Chave, J., Condit, R., Lao, S., Caspersen, J.P., Foster, R.B., & Hubbell, S.P. (2003). Spatial and temporal variation of biomass in a tropical forest: results from a large census plot in Panama. *Journal of Ecology*, *91*, 240-252
- Chave, J., Condit, R., Aguilar, S., Hernandez, A., Lao, S., & Perez, R. (2004). Error propagation and scaling for tropical forest biomass estimates. *Philos Trans R Soc Lond B Biol Sci*, *359*, 409-420
- Chave, J., Andalo, C., Brown, S., Cairns, M.A., Chambers, J.Q., Eamus, D., Folster, H., Fromard, F., Higuchi, N., Kira, T., Lescure, J.P., Nelson, B.W., Ogawa, H., Puig, H., Riera, B., & Yamakura, T. (2005). Tree allometry and improved estimation of carbon stocks and balance in tropical forests. *Oecologia*, *145*, 87-99
- Chowdhury, T.A., Thiel, C., & Schmullius, C. (2014). Growing stock volume estimation from L-band ALOS PALSAR polarimetric coherence in Siberian forest. *Remote Sensing of Environment*, *155*, 129-144
- Ciais, P., Sabine, C., Bala, G., Bopp, L., Brovkin, V., Canadell, J., Chhabra, A., DeFries, R., Galloway, J., Heimann, M., Jones, C., Le Quéré, C., Myneni, R.B., Piao, S., & Thornton, P. (2013). Carbon and Other Biogeochemical Cycles. In T.F. Stocker, D.

## References

- Qin, G.-K. Plattner, M. Tignor, S.K. Allen, J. Boschung, A. Nauels, Y. Xia, V. Bex, & P.M. Midgley (Eds.), *Climate Change 2013: The Physical Science Basis. Contribution of Working Group I to the Fifth Assessment Report of the Intergovernmental Panel on Climate Change*. Cambridge University Press
- Clark, D.A., Brown, S., Kicklighter, D.W., Chambers, J.Q., Thomlinson, J.R., Ni, J., & Holland, E.A. (2001). Net primary production in tropical forests: an evaluation and synthesis of existing field data. *Ecological Applications*, *11*, 371-384
- Clark, M.L., Clark, D.B., & Roberts, D.A. (2004). Small-footprint lidar estimation of sub-canopy elevation and tree height in a tropical rain forest landscape. *Remote Sensing of Environment*, *91*, 68-89
- Cloude, S.R., & Pottier, E. (1997). An entropy based classification scheme for land applications of polarimetric SAR. *Geoscience and Remote Sensing, IEEE Transactions on*, *35*, 68-78
- Colgan, M.S., Asner, G.P., & Swemmer, T. (2013). Harvesting tree biomass at the stand level to assess the accuracy of field and airborne biomass estimation in savannas. *Ecological Applications*, *23*, 1170-1184
- CONAFOR (2010). *Vision de Mexico sobre REDD+. Hacia una estrategia nacional*. Zapopan, Mexico: CONAFOR
- CONAFOR (2012). *Inventario Nacional Forestal y de Suelos. Informe 2004-2009*. Zapopan, Mexico: CONAFOR
- CONAFOR. Allometric Modells. <http://www.mrv.mx/index.php/en/mrv-m-3/workareas/allometric-modells.html> (02.06.2016)
- Cook, B., Corp, L., Nelson, R., Middleton, E., Morton, D., McCorkel, J., Masek, J., Ranson, K., Ly, V., & Montesano, P. (2013). NASA Goddard's LiDAR, Hyperspectral and Thermal (G-LiHT) Airborne Imager. *Remote Sensing*, *5*, 4045-4066
- Couturier, S., Núñez, J.M., & Kolb, M. (2012). Measuring tropical deforestation with error margins: A method for REDD monitoring in south-eastern Mexico. *Tropical forests* (pp. 269-296): InTech
- Cremer, F., Urbazaev, M., Berger, C., Mahecha, M.D., Schullius, C., & Thiel, C. (2018). An Image Transform Based on Temporal Decomposition. *IEEE Geoscience and Remote Sensing Letters*, *15*, 537-541
- Curtis, P.G., Slay, C.M., Harris, N.L., Tyukavina, A., & Hansen, M.C. (2018). Classifying drivers of global forest loss. *Science*, *361*, 1108-1111
- De Jong, B.H., Ochoa-Gaona, S., Castillo-Santiago, M.A., Ramírez-Marcial, N., & Cairns, M.A. (2000). Carbon flux and patterns of land-use/land-cover change in the Selva Lacandona, Mexico. *AMBIO: A Journal of the Human Environment*, *29*, 504-511

- De Jong, R., de Bruin, S., de Wit, A., Schaepman, M.E., & Dent, D.L. (2011). Analysis of monotonic greening and browning trends from global NDVI time-series. *Remote Sensing of Environment*, 115, 692-702
- De Jong, R., Verbesselt, J., Zeileis, A., & Schaepman, M. (2013). Shifts in Global Vegetation Activity Trends. *Remote Sensing*, 5, 1117-1133
- Dimiceli, C., Carroll, M., Sohlberg, R.A., Huang, C.Q., Hansen, M.C., & Townshend, J. Annual Global Automated MODIS Vegetation Continuous Fields (MOD44B) at 250 m Spatial Resolution. <http://www.glcf.umd.edu/data/vcf/>
- Dinh Ho Tong, M., Thuy Le, T., Rocca, F., Tebaldini, S., d'Alessandro, M.M., & Villard, L. (2014). Relating P-Band Synthetic Aperture Radar Tomography to Tropical Forest Biomass. *Geoscience and Remote Sensing, IEEE Transactions on*, 52, 967-979
- Dobson, M.C., Ulaby, F.T., Letoan, T., Beaudoin, A., Kasischke, E.S., & Christensen, N. (1992). Dependence of Radar Backscatter on Coniferous Forest Biomass. *Ieee Transactions on Geoscience and Remote Sensing*, 30, 412-415
- Dong, J., Xiao, X., Sheldon, S., Biradar, C., Zhang, G., Dinh Duong, N., Hazarika, M., Wikantika, K., Takeuchi, W., & Moore, B., III (2014). A 50-m Forest Cover Map in Southeast Asia from ALOS/PALSAR and Its Application on Forest Fragmentation Assessment. *PLoS One*, 9, 1-12
- Dubayah, R.O., Sheldon, S.L., Clark, D.B., Hofton, M.A., Blair, J.B., Hurtt, G.C., & Chazdon, R.L. (2010). Estimation of tropical forest height and biomass dynamics using lidar remote sensing at La Selva, Costa Rica. *Journal of Geophysical Research*, 115, 1-17
- Dutrieux, L.P., Verbesselt, J., Kooistra, L., & Herold, M. (2015). Monitoring forest cover loss using multiple data streams, a case study of a tropical dry forest in Bolivia. *ISPRS Journal of Photogrammetry and Remote Sensing*, 107, 112-125
- Englhart, S., Keuck, V., & Siegert, F. (2011). Aboveground biomass retrieval in tropical forests — The potential of combined X- and L-band SAR data use. *Remote Sensing of Environment*, 115, 1260-1271
- Evans, J., Hudak, A., Faux, R., & Smith, A.M. (2009). Discrete Return Lidar in Natural Resources: Recommendations for Project Planning, Data Processing, and Deliverables. *Remote Sensing*, 1, 776-794
- FAO (2010). Evaluación de los Recursos Forestales Mundiales 2010 - Informe Nacional Mexico. In. Rome, Italy: FAO
- FAO (2015). *Global Forest Resources Assessment 2015. Desk reference*. Rome: FAO
- Feldpausch, T.R., Lloyd, J., Lewis, S.L., Brien, R.J.W., Gloor, M., Monteagudo Mendoza, A., Lopez-Gonzalez, G., Banin, L., Abu Salim, K., Affum-Baffoe, K., Alexiades, M.,

## References

- Almeida, S., Amaral, I., Andrade, A., Aragão, L.E.O.C., Araujo Murakami, A., Arets, E.J.M.M., Arroyo, L., Aymard C, G.A., Baker, T.R., Bánki, O.S., Berry, N.J., Cardozo, N., Chave, J., Comiskey, J.A., Alvarez, E., de Oliveira, A., Di Fiore, A., Djangbletey, G., Domingues, T.F., Erwin, T.L., Fearnside, P.M., França, M.B., Freitas, M.A., Higuchi, N., C, E.H., Iida, Y., Jiménez, E., Kassim, A.R., Killeen, T.J., Laurance, W.F., Lovett, J.C., Malhi, Y., Marimon, B.S., Marimon-Junior, B.H., Lenza, E., Marshall, A.R., Mendoza, C., Metcalfe, D.J., Mitchard, E.T.A., Neill, D.A., Nelson, B.W., Nilus, R., Nogueira, E.M., Parada, A., Peh, K.S.H., Pena Cruz, A., Peñuela, M.C., Pitman, N.C.A., Prieto, A., Quesada, C.A., Ramírez, F., Ramírez-Angulo, H., Reitsma, J.M., Rudas, A., Saiz, G., Salomão, R.P., Schwarz, M., Silva, N., Silva-Espejo, J.E., Silveira, M., Sonké, B., Stropp, J., Taedoumg, H.E., Tan, S., ter Steege, H., Terborgh, J., Torello-Raventos, M., van der Heijden, G.M.F., Vásquez, R., Vilanova, E., Vos, V.A., White, L., Willcock, S., Woell, H., & Phillips, O.L. (2012). Tree height integrated into pantropical forest biomass estimates. *Biogeosciences*, *9*, 3381-3403
- Flores, J., & Carvajal, I. (1994). *Etnoflora Yucatanense*. Universidad Autonoma de Yucatan
- Foody, G.M., Cutler, M.E., Mcmorrow, J., Pelz, D., Tangki, H., Boyd, D.S., & Douglas, I. (2001). Mapping the biomass of Bornean tropical rain forest from remotely sensed data. *Global Ecology and Biogeography*, *10*, 379-387
- Forkel, M., Carvalhais, N., Verbesselt, J., Mahecha, M., Neigh, C., & Reichstein, M. (2013). Trend Change Detection in NDVI Time Series: Effects of Inter-Annual Variability and Methodology. *Remote Sensing*, *5*, 2113-2144
- FRA (2012). *Forest Resources Assessment 2015. Terms and Definitions*. Rome: Food and Agriculture Organization of the United Nations
- García, M., Saatchi, S., Ustin, S., & Balzter, H. (2018). Modelling forest canopy height by integrating airborne LiDAR samples with satellite Radar and multispectral imagery. *International Journal of Applied Earth Observation and Geoinformation*, *66*, 159-173
- Gates, D.M., Keegan, H.J., Schleter, J.C., & Weidner, V.R. (1965). Spectral properties of plants. *Applied optics*, *4*, 11-20
- Gleason, C.J., & Im, J. (2012). Forest biomass estimation from airborne LiDAR data using machine learning approaches. *Remote Sensing of Environment*, *125*, 80-91
- Goetz, S., Steinberg, D., Dubayah, R., & Blair, B. (2007). Laser remote sensing of canopy habitat heterogeneity as a predictor of bird species richness in an eastern temperate forest, USA. *Remote Sensing of Environment*, *108*, 254-263
- Goetz, S., Baccini, A., Laporte, N.T., Johns, T., Walker, W., Kellndorfer, J., Houghton, R.A., & Sun, M. (2009). Mapping and monitoring carbon stocks with satellite observations: a comparison of methods. *Carbon Balance Manag*, *4*, 2

- Goetz, S., & Dubayah, R. (2011). Advances in remote sensing technology and implications for measuring and monitoring forest carbon stocks and change. *Carbon Management*, 2, 231-244
- Gregoire, T.G. (1998). Design-based and model-based inference in survey sampling: appreciating the difference. *Canadian Journal of Forest Research*, 28, 1429-1447
- Grey, W., & Luckman, A. (2003). Mapping urban extent using satellite radar interferometry. *Photogrammetric Engineering & Remote Sensing*, 69, 957-961
- Hajnsek, I., Kugler, F., Lee, S.-K., & Papathanassiou, K.P. (2009). Tropical-forest-parameter estimation by means of Pol-InSAR: The INDREX-II campaign. *Geoscience and Remote Sensing, IEEE Transactions on*, 47, 481-493
- Hame, T., Kilpi, J., Ahola, H.A., Rauste, Y., Antropov, O., Rautiainen, M., Sirro, L., & Bounpone, S. (2013a). Improved Mapping of Tropical Forests With Optical and SAR Imagery, Part I: Forest Cover and Accuracy Assessment Using Multi-Resolution Data. *Selected Topics in Applied Earth Observations and Remote Sensing, IEEE Journal of*, 6, 74-91
- Hame, T., Rauste, Y., Antropov, O., Ahola, H.A., & Kilpi, J. (2013b). Improved Mapping of Tropical Forests With Optical and SAR Imagery, Part II: Above Ground Biomass Estimation. *Selected Topics in Applied Earth Observations and Remote Sensing, IEEE Journal of*, 6, 92-101
- Hansen, M., DeFries, R., Townshend, J., Carroll, M., Dimiceli, C., & Sohlberg, R. (2003). Global percent tree cover at a spatial resolution of 500 meters: first results of the MODIS vegetation continuous fields algorithm. *Earth Interactions*, 7
- Hansen, M.C., Potapov, P.V., Moore, R., Hancher, M., Turubanova, S.A., Tyukavina, A., Thau, D., Stehman, S.V., Goetz, S.J., Loveland, T.R., Kommareddy, A., Egorov, A., Chini, L., Justice, C.O., & Townshend, J.R. (2013). High-resolution global maps of 21st-century forest cover change. *Science*, 342, 850-853
- Hermosilla, T., Wulder, M.A., White, J.C., Coops, N.C., & Hobart, G.W. (2015). Regional detection, characterization, and attribution of annual forest change from 1984 to 2012 using Landsat-derived time-series metrics. *Remote Sensing of Environment*, 170, 121-132
- Herold, M., & Skutsch, M. (2011). Monitoring, reporting and verification for national REDD+ programmes: two proposals. *Environmental Research Letters*, 6, 014002
- Hese, S., Lucht, W., Schmullius, C., Barnsley, M., Dubayah, R., Knorr, D., Neumann, K., Riedel, T., & Schröter, K. (2005). Global biomass mapping for an improved understanding of the CO<sub>2</sub> balance—the Earth observation mission Carbon-3D. *Remote Sensing of Environment*, 94, 94-104

## References

- Hoekman, D.H., & Reiche, J. (2015). Multi-model radiometric slope correction of SAR images of complex terrain using a two-stage semi-empirical approach. *Remote Sensing of Environment*, 156, 1-10
- Holm, S., Nelson, R., & Ståhl, G. (2017). Hybrid three-phase estimators for large-area forest inventory using ground plots, airborne lidar, and space lidar. *Remote Sensing of Environment*, 197, 85-97
- Hooijer, A., Page, S., Canadell, J., Silvius, M., Kwadijk, J., Wösten, H., & Jauhiainen, J. (2010). Current and future CO<sub>2</sub> emissions from drained peatlands in Southeast Asia. *Biogeosciences*, 7, 1505-1514
- Hooker, G., & Mentch, L. (2018). Bootstrap bias corrections for ensemble methods. *Statistics and Computing*, 28, 77-86
- Horion, S., Fensholt, R., Tagesson, T., & Ehammer, A. (2014). Using earth observation-based dry season NDVI trends for assessment of changes in tree cover in the Sahel. *International Journal of Remote Sensing*, 35, 2493-2515
- Houghton, R.A. (2005). Aboveground Forest Biomass and the Global Carbon Balance. *Global Change Biology*, 11, 945-958
- Houghton, R.A., Hall, F., & Goetz, S.J. (2009). Importance of biomass in the global carbon cycle. *Journal of Geophysical Research: Biogeosciences*, 114
- Houghton, R.A., Byers, B., & Nassikas, A.A. (2015). A role for tropical forests in stabilizing atmospheric CO<sub>2</sub>. *Nature Climate Change*, 5, 1022
- Huete, A., Liu, H.Q., Batchily, K., & van Leeuwen, W. (1997). A comparison of vegetation indices over a global set of TM images for EOS-MODIS. *Remote Sensing of Environment*, 59, 440-451
- Huete, A., Didan, K., Miura, T., Rodriguez, E.P., Gao, X., & Ferreira, L.G. (2002). Overview of the radiometric and biophysical performance of the MODIS vegetation indices. *Remote Sensing of Environment*, 83, 195-213
- Ichii, K., Kondo, M., Okabe, Y., Ueyama, M., Kobayashi, H., Lee, S.-J., Saigusa, N., Zhu, Z., & Myneni, R. (2013). Recent Changes in Terrestrial Gross Primary Productivity in Asia from 1982 to 2011. *Remote Sensing*, 5, 6043-6062
- Imhoff, M.L. (1995). Radar backscatter and biomass saturation: ramifications for global biomass inventory. *Geoscience and Remote Sensing, IEEE Transactions on*, 33, 511-518
- INEGI (2010). Conjunto Nacional de Uso del Suelo y Vegetación a escala 1:250,000, Serie IV. In INEGI (Ed.). Aguascalientes, Mexico

- James, G., Witten, D., Hastie, T., & Tibshirani, R. (2015). *An Introduction to Statistical Learning with Applications in R*. New York: Springer
- JAXA. New global 25m-resolution PALSAR-2/PALSAR mosaic and Global Forest/Non-forest Map. [http://www.eorc.jaxa.jp/ALOS/en/palsar\\_fnf/data/index.htm](http://www.eorc.jaxa.jp/ALOS/en/palsar_fnf/data/index.htm) (31.07.2016)
- Jensen, J.R. (2007). *Remote Sensing of the Environment. An Earth Resource Perspective*. Upper Saddle River: Pearson Prentice Hall
- Joshi, N., Mitchard, E.T., Broily, M., Schumacher, J., Fernández-Landa, A., Johannsen, V.K., Marchamalo, M., & Fensholt, R. (2017). Understanding ‘saturation’ of radar signals over forests. *Scientific Reports*, 7, 3505
- Kennedy, R.E., Yang, Z., & Cohen, W.B. (2010). Detecting trends in forest disturbance and recovery using yearly Landsat time series: 1. LandTrendr—Temporal segmentation algorithms. *Remote Sensing of Environment*, 114, 2897-2910
- Koch, B. (2010). Status and future of laser scanning, synthetic aperture radar and hyperspectral remote sensing data for forest biomass assessment. *ISPRS Journal of Photogrammetry and Remote Sensing*, 65, 581-590
- Köhler, P., & Huth, A. (1998). The effects of tree species grouping in tropical rainforest modelling: simulations with the individual-based model FORMIND. *Ecological Modelling*, 109, 301-321
- Kurvonen, L., Pulliainen, J., & Hallikainen, M. (1999). Retrieval of biomass in boreal forests from multitemporal ERS-1 and JERS-1 SAR images. *Ieee Transactions on Geoscience and Remote Sensing*, 37, 198-205
- Le Quéré, C., Andrew, R.M., Friedlingstein, P., Sitch, S., Pongratz, J., Manning, A.C., Korsbakken, J.I., Peters, G.P., Canadell, J.G., & Jackson, R.B. (2017). Global carbon budget 2017. *Earth System Science Data Discussions*, 1-79
- Le Toan, T., Beaudoin, A., Riou, J., & Guyon, D. (1992). Relating Forest Biomass to Sar Data. *Ieee Transactions on Geoscience and Remote Sensing*, 30, 403-411
- Le Toan, T., Quegan, S., Davidson, M.W.J., Balzter, H., Paillou, P., Papathanassiou, K., Plummer, S., Rocca, F., Saatchi, S., Shugart, H., & Ulander, L. (2011). The BIOMASS mission: Mapping global forest biomass to better understand the terrestrial carbon cycle. *Remote Sensing of Environment*, 115, 2850-2860
- Lê, T.T., Atto, A.M., Trouvé, E., & Nicolas, J.-M. (2014). Adaptive multitemporal SAR image filtering based on the change detection matrix. *IEEE Geoscience and Remote Sensing Letters*, 11, 1826-1830



## References

- Leckie, D.G., & Ranson, K.J. (1996). Forestry applications using imaging radar. In F.M. Henderson, & A.J. Lewis (Eds.), *Principles & Applications of Imaging Radar. Manual of Remote Sensing* (pp. 435-509)
- Lee, J.-S., & Pottier, E. (2009). *Polarimetric radar imaging: from basics to applications*. CRC press
- Lefsky, M.A., Cohen, W.B., Harding, D.J., Parker, G.G., Acker, S.A., & Gower, S.T. (2002a). LiDAR remote sensing of above-ground biomass in three biomes. *Glob Ecol Biogeogr*, 11, 393-399
- Lefsky, M.A., Cohen, W.B., Parker, G.G., & Harding, D.J. (2002b). Lidar Remote Sensing for Ecosystem Studies. *BioScience*, 52, 19-30
- Lefsky, M.A., Harding, D.J., Keller, M., Cohen, W.B., Carabajal, C.C., Del Bom Espirito-Santo, F., Hunter, M.O., & de Oliveira, R. (2005). Estimates of forest canopy height and aboveground biomass using ICESat. *Geophysical Research Letters*, 32, L22S02
- Li, S., Potter, C., Hiatt, C., & Shupe, J. (2012). Fusion of Hyperspectral and L-Band SAR Data to Estimate Fractional Vegetation Cover in a Coastal California Scrub Community. *Journal of Geophysics and Remote Sensing*, 1-9
- Lillesand, T.M., Kiefer, R.W., & Chipman, J.W. (2008). *Remote Sensing and Image Interpretation*. John Wiley & Sons Inc.
- Lim, K., Treitz, P., Wulder, M., St-Onge, B., & Flood, M. (2003). LiDAR remote sensing of forest structure. *Progress in physical geography*, 27, 88-106
- Lucas, R.M., Moghaddam, M., & Cronin, N. (2004). Microwave scattering from mixed-species forests, Queensland, Australia. *Geoscience and Remote Sensing, IEEE Transactions on*, 42, 2142-2159
- Lucas, R.M., Cronin, N., Lee, A., Moghaddam, M., Witte, C., & Tickle, P. (2006). Empirical relationships between AIRSAR backscatter and LiDAR-derived forest biomass, Queensland, Australia. *Remote Sensing of Environment*, 100, 407-425
- Lucas, R.M., Armston, J., Fairfax, R., Fensham, R., Accad, A., Carreiras, J., Kelley, J., Bunting, P., Clewley, D., Bray, S., Metcalfe, D., Dwyer, J., Bowen, M., Eyre, T., Laidlaw, M., & Shimada, M. (2010). An Evaluation of the ALOS PALSAR L-Band Backscatter & Above Ground Biomass Relationship Queensland, Australia: Impacts of Surface Moisture Condition and Vegetation Structure. *Selected Topics in Applied Earth Observations and Remote Sensing, IEEE Journal of*, 3, 576-593
- Luckman, A., Baker, J., & Wegmüller, U. (2000). Repeat-pass interferometric coherence measurements of disturbed tropical forest from JERS and ERS satellites. *Remote Sensing of Environment*, 73, 350-360

- Marvin, D.C., Asner, G.P., Knapp, D.E., Anderson, C.B., Martin, R.E., Sinca, F., & Tupayachi, R. (2014). Amazonian landscapes and the bias in field studies of forest structure and biomass. *Proc Natl Acad Sci USA*, *111*, 5224-5232
- Marvin, D.C., & Asner, G.P. (2016). Spatially explicit analysis of field inventories for national forest carbon monitoring. *Carbon Balance Manag*, *11*, 1-12
- Matasci, G., Hermosilla, T., Wulder, M.A., White, J.C., Coops, N.C., Hobart, G.W., Bolton, D.K., Tompalski, P., & Bater, C.W. (2018). Three decades of forest structural dynamics over Canada's forested ecosystems using Landsat time-series and lidar plots. *Remote Sensing of Environment*, *216*, 697-714
- Mathieu, R., Naidoo, L., Cho, M.A., Leblon, B., Main, R., Wessels, K., Asner, G.P., Buckley, J., Van Aardt, J., Erasmus, B.F.N., & Smit, I.P.J. (2013). Toward structural assessment of semi-arid African savannahs and woodlands: The potential of multitemporal polarimetric RADARSAT-2 fine beam images. *Remote Sensing of Environment*, *138*, 215-231
- Mendoza, E., & Dirzo, R. (1999). Deforestation in Lacandonia (southeast Mexico): evidence for the declaration of the northernmost tropical hot-spot. *Biodiversity & Conservation*, *8*, 1621-1641
- Mermoz, S., Le Toan, T., Villard, L., Réjou-Méchain, M., & Seifert-Granzin, J. (2014). Biomass assessment in the Cameroon savanna using ALOS PALSAR data. *Remote Sensing of Environment*, *155*, 109-119
- Mermoz, S., Réjou-Méchain, M., Villard, L., Le Toan, T., Rossi, V., & Gourlet-Fleury, S. (2015). Decrease of L-band SAR backscatter with biomass of dense forests. *Remote Sensing of Environment*, *159*, 307-317
- Mitchard, E.T.A., Saatchi, S.S., Gerard, F.F., Lewis, S.L., & Meir, P. (2009a). Measuring Woody Encroachment along a Forest-Savanna Boundary in Central Africa. *Earth Interactions*, *13*, 1-29
- Mitchard, E.T.A., Saatchi, S.S., Woodhouse, I.H., Nangendo, G., Ribeiro, N.S., Williams, M., Ryan, C.M., Lewis, S.L., Feldpausch, T.R., & Meir, P. (2009b). Using satellite radar backscatter to predict above-ground woody biomass: A consistent relationship across four different African landscapes. *Geophysical Research Letters*, *36*, 1-6
- Mitchard, E.T.A., Saatchi, S.S., Lewis, S.L., Feldpausch, T.R., Woodhouse, I.H., Sonké, B., Rowland, C., & Meir, P. (2011). Measuring biomass changes due to woody encroachment and deforestation/degradation in a forest-savanna boundary region of central Africa using multi-temporal L-band radar backscatter. *Remote Sensing of Environment*, *115*, 2861-2873

## References

- Mitchard, E.T.A. (2018). The tropical forest carbon cycle and climate change. *Nature*, *559*, 527-534
- Moisen, G.G., Freeman, E.A., Blackard, J.A., Frescino, T.S., Zimmermann, N.E., & Edwards, T.C. (2006). Predicting tree species presence and basal area in Utah: A comparison of stochastic gradient boosting, generalized additive models, and tree-based methods. *Ecological Modelling*, *199*, 176-187
- Montesano, P.M., Cook, B.D., Sun, G., Simard, M., Nelson, R.F., Ranson, K.J., Zhang, Z., & Luthcke, S. (2013). Achieving accuracy requirements for forest biomass mapping: A spaceborne data fusion method for estimating forest biomass and LiDAR sampling error. *Remote Sensing of Environment*, *130*, 153-170
- Musick, H.B., Schaber, G.S., & Breed, C.S. (1998). AIRSAR studies of woody shrub density in semiarid rangeland: Jornada del Muerto, New Mexico. *Remote Sensing of Environment*, *66*, 29-40
- Næsset, E. (2002). Predicting forest stand characteristics with airborne scanning laser using a practical two-stage procedure and field data. *Remote Sensing of Environment*, *80*, 88-99
- Naesset, E., & Okland, T. (2002). Estimating tree height and tree crown properties using airborne scanning laser in a boreal nature reserve. *Remote Sensing of Environment*, *79*, 105-115
- Naidoo, L., Mathieu, R., Main, R., Kleynhans, W., Wessels, K., Asner, G., & Leblon, B. (2015). Savannah woody structure modelling and mapping using multi-frequency (X-, C-and L-band) Synthetic Aperture Radar data. *ISPRS Journal of Photogrammetry and Remote Sensing*, *105*, 234-250
- Naidoo, L., Mathieu, R., Main, R., Wessels, K., & Asner, G.P. (2016). L-band Synthetic Aperture Radar imagery performs better than optical datasets at retrieving woody fractional cover in deciduous, dry savannahs. *International Journal of Applied Earth Observation and Geoinformation*, *52*, 54-64
- NASA. MOD 13-Gridded Vegetation Indices (NDVI & EVI). [http://modis.gsfc.nasa.gov/data/dataproducts.php?MOD\\_NUMBER=13](http://modis.gsfc.nasa.gov/data/dataproducts.php?MOD_NUMBER=13)
- NASA. Airborne G-LiHT Data. <https://glihtdata.gsfc.nasa.gov/> (05.06.2018)
- Neumann, M., Saatchi, S.S., Ulander, L.M.H., & Fransson, J.E.S. (2012). Assessing Performance of L- and P-Band Polarimetric Interferometric SAR Data in Estimating Boreal Forest Above-Ground Biomass. *Geoscience and Remote Sensing, IEEE Transactions on*, *50*, 714-726
- Oliver, C., & Quegan, S. (2004). *Understanding Synthetic Aperture Radar Images*. SciTech Publ.

- Pagani, M., Arthur, M.A., & Freeman, K.H. (1999). Miocene evolution of atmospheric carbon dioxide. *Paleoceanography*, *14*, 273-292
- Page, S.E., Rieley, J.O., & Banks, C.J. (2011). Global and regional importance of the tropical peatland carbon pool. *Global Change Biology*, *17*, 798-818
- Pan, Y., Birdsey, R.A., Fang, J., Houghton, R., Kauppi, P.E., Kurz, W.A., Phillips, O.L., Shvidenko, A., Lewis, S.L., Canadell, J.G., Ciais, P., Jackson, R.B., Pacala, S.W., McGuire, A.D., Piao, S., Rautiainen, A., Sitch, S., & Hayes, D. (2011). A large and persistent carbon sink in the world's forests. *Science*, *333*, 988-993
- Papathanassiou, K.P., & Cloude, S.R. (2001). Single-baseline polarimetric SAR interferometry. *Geoscience and Remote Sensing, IEEE Transactions on*, *39*, 2352-2363
- Pearson, P.N., & Palmer, M.R. (2000). Atmospheric carbon dioxide concentrations over the past 60 million years. *Nature*, *406*, 695
- Pearson, T.R., Brown, S., Murray, L., & Sidman, G. (2017). Greenhouse gas emissions from tropical forest degradation: an underestimated source. *Carbon Balance Manag*, *12*, 3
- Pengra, B., Long, J., Dahal, D., Stehman, S.V., & Loveland, T.R. (2015). A global reference database from very high resolution commercial satellite data and methodology for application to Landsat derived 30m continuous field tree cover data. *Remote Sensing of Environment*, *165*, 234-248
- Petit, J.-R., Jouzel, J., Raynaud, D., Barkov, N.I., Barnola, J.-M., Basile, I., Bender, M., Chappellaz, J., Davis, M., & Delaygue, G. (1999). Climate and atmospheric history of the past 420,000 years from the Vostok ice core, Antarctica. *Nature*, *399*, 429
- Pflugmacher, D., Cohen, W.B., & Kennedy, R.E. (2012). Using Landsat-derived disturbance history (1972–2010) to predict current forest structure. *Remote Sensing of Environment*, *122*, 146-165
- Pinzón, J.E., Brown, M.E., & Tucker, C.J. (2005). EMD correction of orbital drift artifacts in satellite data stream. *Hilbert–Huang Transform and Its Applications* (pp. 241-260)
- Qi, W., & Dubayah, R.O. (2016). Combining Tandem-X InSAR and simulated GEDI lidar observations for forest structure mapping. *Remote Sensing of Environment*, *187*, 253-266
- Quegan, S., Le Toan, T., Jiong Jiong, Y., Ribbes, F., & Floury, N. (2000). Multitemporal ERS SAR analysis applied to forest mapping. *Geoscience and Remote Sensing, IEEE Transactions on*, *38*, 741-753
- Quegan, S., & Yu, J.J. (2001). Filtering of multichannel SAR images. *Ieee Transactions on Geoscience and Remote Sensing*, *39*, 2373-2379

## References

- Quinlan, J.R. (1992). Learning with continuous classes. In, *5th Australian joint conference on artificial intelligence* (pp. 343-348): Singapore
- Quinlan, J.R. (1993). Combining instance-based and model-based learning. In
- Raney, R.K. (1996). Radar fundamentals: technical perspective. In F.M. Henderson, & A.J. Lewis (Eds.), *Principles & Applications of Imaging Radar. Manual of Remote Sensing* (pp. 9-130)
- Rauste, Y., Hame, T., Pulliainen, J., Heiska, K., & Hallikainen, M. (1994). Radar-based forest biomass estimation. *International Journal of Remote Sensing*, *15*, 2797-2808
- Rauste, Y. (2005). Multi-temporal JERS SAR data in boreal forest biomass mapping. *Remote Sensing of Environment*, *97*, 263-275
- Reiche, J., Verbesselt, J., Hoekman, D., & Herold, M. (2015). Fusing Landsat and SAR time series to detect deforestation in the tropics. *Remote Sensing of Environment*, *156*, 276-293
- Reichstein, M., Bahn, M., Ciais, P., Frank, D., Mahecha, M.D., Seneviratne, S.I., Zscheischler, J., Beer, C., Buchmann, N., & Frank, D.C. (2013). Climate extremes and the carbon cycle. *Nature*, *500*, 287
- Rodríguez-Veiga, P., Saatchi, S., Tansey, K., & Balzter, H. (2016). Magnitude, spatial distribution and uncertainty of forest biomass stocks in Mexico. *Remote Sensing of Environment*, *183*, 265-281
- Rosenqvist, A., Shimada, M., & Watanabe, M. (2004). ALOS PALSAR: Technical outline and mission concepts. In, *4th International Symposium on Retrieval of Bio- and Geophysical Parameters from SAR Data for Land Applications*. Innsbruck, Austria
- Rosenqvist, A., Shimada, M., Suzuki, S., Ohgushi, F., Tadono, T., Watanabe, M., Tsuzuku, K., Watanabe, T., Kamijo, S., & Aoki, E. (2014). Operational performance of the ALOS global systematic acquisition strategy and observation plans for ALOS-2 PALSAR-2. *Remote Sensing of Environment*, *155*, 3-12
- Saarela, S., Holm, S., Grafström, A., Schnell, S., Næsset, E., Gregoire, T.G., Nelson, R.F., & Ståhl, G. (2016). Hierarchical model-based inference for forest inventory utilizing three sources of information. *Annals of Forest Science*, *73*, 895-910
- Saatchi, S.S., & Moghaddam, M. (2000). Estimation of crown and stem water content and biomass of boreal forest using polarimetric SAR imagery. *Geoscience and Remote Sensing, IEEE Transactions on*, *38*, 697-709
- Saatchi, S.S., Houghton, R.A., Dos Santos Alvalá, R.C., Soares, J.V., & Yu, Y. (2007). Distribution of aboveground live biomass in the Amazon basin. *Global Change Biology*, *13*, 816-837

- Saatchi, S.S., Harris, N.L., Brown, S., Lefsky, M., Mitchard, E.T., Salas, W., Zutta, B.R., Buermann, W., Lewis, S.L., Hagen, S., Petrova, S., White, L., Silman, M., & Morel, A. (2011a). Benchmark map of forest carbon stocks in tropical regions across three continents. *Proc Natl Acad Sci U S A*, *108*, 9899-9904
- Saatchi, S.S., Marlier, M., Chazdon, R.L., Clark, D.B., & Russell, A.E. (2011b). Impact of spatial variability of tropical forest structure on radar estimation of aboveground biomass. *Remote Sensing of Environment*, *115*, 2836-2849
- Santoro, M., Eriksson, L., Askne, J., & Schmullius, C. (2006). Assessment of stand-wise stem volume retrieval in boreal forest from JERS-1 L-band SAR backscatter. *International Journal of Remote Sensing*, *27*, 3425-3454
- Santoro, M., Beer, C., Cartus, O., Schmullius, C., Shvidenko, A., McCallum, I., Wegmüller, U., & Wiesmann, A. (2011). Retrieval of growing stock volume in boreal forest using hyper-temporal series of Envisat ASAR ScanSAR backscatter measurements. *Remote Sensing of Environment*, *115*, 490-507
- Santoro, M., Schmullius, C., Pathe, C., Schwilk, J., Beer, C., Thurner, M., Fransson, J.E.S., Shvidenko, A., Schepaschenko, D., McCallum, I., Hall, R.J., & Beaudoin, A. (2013). Estimates Of Forest Growing Stock Volume Of The Northern Hemisphere From Envisat ASAR. In ESA (Ed.), *ESA Living Planet Symposium*. Edinburgh,
- Santoro, M., Beaudoin, A., Beer, C., Cartus, O., Fransson, J.E.S., Hall, R.J., Pathe, C., Schmullius, C., Schepaschenko, D., Shvidenko, A., Thurner, M., & Wegmüller, U. (2015). Forest growing stock volume of the northern hemisphere: Spatially explicit estimates for 2010 derived from Envisat ASAR. *Remote Sensing of Environment*, *168*, 316-334
- Santoro, M., & Cartus, O. (2018). Research Pathways of Forest Above-Ground Biomass Estimation Based on SAR Backscatter and Interferometric SAR Observations. *Remote Sensing*, *10*, 1-23
- Santos, J.R., Freitas, C.C., Araujo, L.S., Dutra, L.V., Mura, J.C., Gama, F.F., Soler, L.S., & Sant'Anna, S.J.S. (2003). Airborne P-band SAR applied to the aboveground biomass studies in the Brazilian tropical rainforest. *Remote Sensing of Environment*, *87*, 482-493
- Schlund, M., von Poncet, F., Kuntz, S., Boehm, H.-D.V., Hoekman, D.H., & Schmullius, C. (2016). TanDEM-X elevation model data for canopy height and aboveground biomass retrieval in a tropical peat swamp forest. *International Journal of Remote Sensing*, *37*, 5021-5044
- Sexton, J.O., Song, X.P., Feng, M., Noojipady, P., Anand, A., Huang, C.Q., Kim, D.H., Collins, K.M., Channan, S., DiMiceli, C., & Townshend, J.R. (2013). Global, 30-m resolution continuous fields of tree cover: Landsat-based rescaling of MODIS

## References

- vegetation continuous fields with lidar-based estimates of error. *International Journal of Digital Earth*, 6, 427-448
- Shimada, M., & Ohtaki, T. (2010). Generating large-scale high-quality SAR mosaic datasets: Application to PALSAR data for global monitoring. *Selected Topics in Applied Earth Observations and Remote Sensing, IEEE Journal of*, 3, 637-656
- Shimada, M., Itoh, T., Motooka, T., Watanabe, M., Shiraishi, T., Thapa, R., & Lucas, R. (2014). New global forest/non-forest maps from ALOS PALSAR data (2007–2010). *Remote Sensing of Environment*, 155, 13-31
- Simard, M., Pinto, N., Fisher, J.B., & Baccini, A. (2011). Mapping forest canopy height globally with spaceborne lidar. *Journal of Geophysical Research: Biogeosciences*, 116, G04021
- Sitch, S., Huntingford, C., Gedney, N., Levy, P., Lomas, M., Piao, S., Betts, R., Ciais, P., Cox, P., & Friedlingstein, P. (2008). Evaluation of the terrestrial carbon cycle, future plant geography and climate-carbon cycle feedbacks using five Dynamic Global Vegetation Models (DGVMS). *Global Change Biology*, 14, 2015-2039
- Small, D. (2011). Flattening Gamma: Radiometric Terrain Correction for SAR Imagery. *Geoscience and Remote Sensing, IEEE Transactions on*, 49, 3081-3093
- SMN. Resúmenes Mensuales de Temperaturas y Lluvia. <https://smn.cna.gob.mx/es/climatologia/temperaturas-y-lluvias/resumenes-mensuales-de-temperaturas-y-lluvias> (05.06.2018)
- Solberg, S., Astrup, R., Breidenbach, J., Nilsen, B., & Weydahl, D. (2013). Monitoring spruce volume and biomass with InSAR data from TanDEM-X. *Remote Sensing of Environment*, 139, 60-67
- Solberg, S., Hansen, E.H., Gobakken, T., Næssset, E., & Zahabu, E. (2017). Biomass and InSAR height relationship in a dense tropical forest. *Remote Sensing of Environment*, 192, 166-175
- Ståhl, G., Saarela, S., Schnell, S., Holm, S., Breidenbach, J., Healey, S.P., Patterson, P.L., Magnussen, S., Næssset, E., & McRoberts, R.E. (2016). Use of models in large-area forest surveys: comparing model-assisted, model-based and hybrid estimation. *Forest Ecosystems*, 3, 5
- Steininger, M. (2000). Satellite estimation of tropical secondary forest above-ground biomass: data from Brazil and Bolivia. *International Journal of Remote Sensing*, 21, 1139-1157
- Stelmaszczuk-Górska, M., Rodriguez-Veiga, P., Ackermann, N., Thiel, C., Balzter, H., & Schmullius, C. (2016). Non-Parametric Retrieval of Aboveground Biomass in Siberian Boreal Forests with ALOS PALSAR Interferometric Coherence and Backscatter Intensity. *Journal of Imaging*, 2, 1-24

- Su, Y., Guo, Q., Xue, B., Hu, T., Alvarez, O., Tao, S., & Fang, J. (2016). Spatial distribution of forest aboveground biomass in China: Estimation through combination of spaceborne lidar, optical imagery, and forest inventory data. *Remote Sensing of Environment*, *173*, 187-199
- Suzuki, R., Kim, Y., & Ishii, R. (2013). Sensitivity of the backscatter intensity of ALOS/PALSAR to the above-ground biomass and other biophysical parameters of boreal forest in Alaska. *Polar Science*, *7*, 100-112
- Tanase, M.A., Panciera, R., Lowell, K., Siyuan, T., Garcia-Martin, A., & Walker, J.P. (2014a). Sensitivity of L-Band Radar Backscatter to Forest Biomass in Semiarid Environments: A Comparative Analysis of Parametric and Nonparametric Models. *Geoscience and Remote Sensing, IEEE Transactions on*, *52*, 4671-4685
- Tanase, M.A., Panciera, R., Lowell, K., Tian, S., Hacker, J.M., & Walker, J.P. (2014b). Airborne multi-temporal L-band polarimetric SAR data for biomass estimation in semi-arid forests. *Remote Sensing of Environment*, *145*, 93-104
- Thiel, C.J., Drezet, P., Weise, C., Quegan, S., & Schmullius, C. (2006). Radar remote sensing for the delineation of forest cover maps and the detection of deforestation. *Forestry: An International Journal of Forest Research*, *79*, 589-597
- Thiel, C.J., Thiel, C., & Schmullius, C.C. (2009). Operational Large-Area Forest Monitoring in Siberia Using ALOS PALSAR Summer Intensities and Winter Coherence. *Ieee Transactions on Geoscience and Remote Sensing*, *47*, 3993-4000
- Thiel, C.J., & Schmullius, C.C. (2016). The potential of ALOS PALSAR backscatter and InSAR coherence for forest growing stock volume estimation in Central Siberia. *Remote Sensing of Environment*, *173*, 258-273
- Tucker, C.J. (1979). Red and photographic infrared linear combinations for monitoring vegetation. *Remote Sensing of Environment*, *8*, 127-150
- University of Maryland. Global Forest Change 2000–2012 Data. [https://earthenginepartners.appspot.com/science-2013-global-forest/download\\_v1.0.html](https://earthenginepartners.appspot.com/science-2013-global-forest/download_v1.0.html) (02.09.2016)
- Urbazaev, M., Thiel, C., Mathieu, R., Naidoo, L., Levick, S.R., Smit, I.P.J., Asner, G.P., & Schmullius, C. (2015). Assessment of the mapping of fractional woody cover in southern African savannas using multi-temporal and polarimetric ALOS PALSAR L-band images. *Remote Sensing of Environment*, *166*, 138-153
- Urbazaev, M., Thiel, C., Migliavacca, M., Reichstein, M., Rodriguez-Veiga, P., & Schmullius, C. (2016). Improved Multi-Sensor Satellite-Based Aboveground Biomass Estimation by Selecting Temporally Stable Forest Inventory Plots Using NDVI Time Series. *Forests*, *7*, 1-16



## References

- Urbazaev, M., Thiel, C., Cremer, F., Dubayah, R., Migliavacca, M., Reichstein, M., & Schmullius, C. (2018). Estimation of forest aboveground biomass and uncertainties by integration of field measurements, airborne LiDAR, and SAR and optical satellite data in Mexico. *Carbon Balance Manag*, *13*, 1-20
- Urquiza-Haas, T., Dolman, P.M., & Peres, C.A. (2007). Regional scale variation in forest structure and biomass in the Yucatan Peninsula, Mexico: Effects of forest disturbance. *Forest Ecology and Management*, *247*, 80-90
- Van der Werf, G.R., Morton, D.C., DeFries, R.S., Olivier, J.G.J., Kasibhatla, P.S., Jackson, R.B., Collatz, G.J., & Randerson, J.T. (2009). CO2 emissions from forest loss. *Nature Geoscience*, *2*, 737-738
- Verbesselt, J., Jonsson, P., Lhermitte, S., Aardt, J.v., & Coppin, P. (2006). Evaluating satellite and climate data-derived indices as fire risk indicators in savanna ecosystems. *Ieee Transactions on Geoscience and Remote Sensing*, *44*, 1622-1632
- Verbesselt, J., Hyndman, R., Newnham, G., & Culvenor, D. (2010a). Detecting trend and seasonal changes in satellite image time series. *Remote Sensing of Environment*, *114*, 106-115
- Verbesselt, J., Hyndman, R., Zeileis, A., & Culvenor, D. (2010b). Phenological change detection while accounting for abrupt and gradual trends in satellite image time series. *Remote Sensing of Environment*, *114*, 2970-2980
- Wagner, W., Luckman, A., Vietmeier, J., Tansey, K., Balzter, H., Schmullius, C., Davidson, M., Gaveau, D., Gluck, M., & Le Toan, T. (2003). Large-scale mapping of boreal forest in SIBERIA using ERS tandem coherence and JERS backscatter data. *Remote Sensing of Environment*, *85*, 125-144
- Walker, W.S., Kelldorfer, J.M., LaPoint, E., Hoppus, M., & Westfall, J. (2007). An empirical InSAR-optical fusion approach to mapping vegetation canopy height. *Remote Sensing of Environment*, *109*, 482-499
- Watanabe, M., Shimada, M., Rosenqvist, A., Tadono, T., Matsuoka, M., Shakil Ahmad, R., Ohta, K., Furuta, R., Nakamura, K., & Moriyama, T. (2006). Forest Structure Dependency of the Relation Between L-Band  $\sigma_0$  and Biophysical Parameters. *Geoscience and Remote Sensing, IEEE Transactions on*, *44*, 3154-3165
- Wulder, M.A., & Franklin, S.E. (2003). *Remote sensing of forest environments: concepts and case studies*. New York: Springer Science & Business Media
- Wulder, M.A., Masek, J.G., Cohen, W.B., Loveland, T.R., & Woodcock, C.E. (2012). Opening the archive: How free data has enabled the science and monitoring promise of Landsat. *Remote Sensing of Environment*, *122*, 2-10

- Xu, L., Saatchi, S.S., Yang, Y., Yu, Y., & White, L. (2016). Performance of non-parametric algorithms for spatial mapping of tropical forest structure. *Carbon Balance Manag*, 11, 1-14
- Yu, Y., & Saatchi, S. (2016). Sensitivity of L-Band SAR Backscatter to Aboveground Biomass of Global Forests. *Remote Sensing*, 8, 1-18
- Zeileis, A. (2005). A unified approach to structural change tests based on ML scores, F statistics, and OLS residuals. *Econometric Reviews*, 24, 445-466
- Zolkos, S.G., Goetz, S.J., & Dubayah, R. (2013). A meta-analysis of terrestrial aboveground biomass estimation using lidar remote sensing. *Remote Sensing of Environment*, 128, 289-298

# Manuscript Overview

Erklärung zu den Eigenanteilen des Promovenden/der Promovendin sowie der weiteren Doktoranden/Doktorandinnen als Koautoren an den Publikationen und Zweitpublikationsrechten bei einer kumulativen Dissertation.

**Manuscript #1**

**Urbazaev, M.<sup>1</sup>, Thiel, C.<sup>1</sup>, Migliavacca, M.<sup>2</sup>, Reichstein, M.<sup>2,3</sup>, Rodriguez-Veiga, P.<sup>4,5</sup> & C. Schmullius<sup>1</sup> (2016).** Improved Multi-Sensor Satellite-Based Aboveground Biomass Estimation by Selecting Temporally Stable Forest Inventory Plots Using NDVI Time Series. *Forests*, 7(8), 169

<sup>1</sup>Department of Earth Observation, Friedrich-Schiller University Jena

<sup>2</sup>Max Planck Institute for Biogeochemistry

<sup>3</sup>Michael-Stifel-Center Jena

<sup>4</sup>Centre for Landscape and Climate Research, University of Leicester

<sup>5</sup>National Center for Earth Observation (NCEO), University of Leicester

<b>Beteiligt an</b>	M. Urbazaev	C. Thiel	M. Migliavacca	M. Reichstein	P. Rodriguez-Veiga	C. Schmullius
Konzeption des Forschungsansatzes	X	X				X
Planung der Untersuchungen	X	X				
Datenerhebung und -vorbereitung	X					
Datenanalyse und -interpretation	X		X		X	
Schreiben des Manuskripts	X	X	X	X	X	
<b>Vorschlag Anrechnung Publikations-äquivalente</b>	1	n.a.	n.a.	n.a.	n.a.	n.a.

**Manuscript #2**

**Urbazaev, M.<sup>1,2</sup>, Thiel, C.<sup>1</sup>, Cremer, F.<sup>1</sup>, Dubayah, R.<sup>3</sup>, Migliavacca, M.<sup>4</sup>, Reichstein, M.<sup>4</sup> & C. Schmullius<sup>1</sup> (2018).** Estimation of forest aboveground biomass and uncertainties by integration of field measurements, airborne LiDAR, and SAR and optical satellite data in Mexico. *Carbon Balance and Management*, 13(1):5

<sup>1</sup>Department of Earth Observation, Friedrich-Schiller-University Jena

<sup>2</sup>International Max Planck Research School (IMPRS), Max Planck Institute for Biogeochemistry

<sup>3</sup>Department of Geographical Sciences, University of Maryland

<sup>4</sup>Department of Biogeochemical Integration, Max Planck Institute for Biogeochemistry

<b>Beteiligt an</b>	M. Urbazaev	C. Thiel	F. Cremer	R. Dubayah	M. Migliavacca	M. Reichstein	C. Schmullius
Konzeption des Forschungsansatzes	X	X			X	X	X
Planung der Untersuchungen	X		X	X			
Datenerhebung und -vorbereitung	X						
Datenanalyse und -interpretation	X	X	X	X	X		
Schreiben des Manuskripts	X	X	X		X		
<b>Vorschlag Anrechnung Publikations-äquivalente</b>	1	n.a.	n.a.	n.a.	n.a.	n.a.	n.a.

**Manuscript #3**

Urbazaev, M.<sup>1,2</sup>, Cremer, F.<sup>2</sup>, Migliavacca, M.<sup>3</sup>, Reichstein, M.<sup>3,4</sup>, Schmulius, C.<sup>2</sup> & C. Thiel<sup>2</sup> (2018). Potential of Multitemporal ALOS-2 PALSAR-2 ScanSAR Data for Vegetation Height Estimation in Tropical Forests of Mexico. *Remote Sensing*, 10(8), 1277.

<sup>1</sup>International Max Planck Research School for Global Biogeochemical Cycles,  
Max Planck Institute for Biogeochemistry

<sup>2</sup>Department of Earth Observation, Friedrich-Schiller University Jena

<sup>3</sup>Department of Biogeochemical Integration, Max Planck Institute for  
Biogeochemistry

<sup>4</sup>Michael-Stifel-Center Jena

<b>Beteiligt an</b>	M. Urbazaev	F. Cremer	M. Migliavacca	M. Reichstein	C. Schmulius	C. Thiel
Konzeption des Forschungsansatzes	X			X	X	X
Planung der Untersuchungen	X	X				X
Datenerhebung und -vorbereitung	X					
Datenanalyse und -interpretation	X	X	X			X
Schreiben des Manuskripts	X	X	X			X
<b>Vorschlag Anrechnung Publikationsäquivalente</b>	<b>1</b>	n.a.	n.a.	n.a.	n.a.	n.a.

Die Koautoren der in dieser kumulativen Dissertation verwendeten Manuskripte sind sowohl über die Nutzung als auch über die oben angegebenen Eigenanteile informiert und stimmen dem zu.

Ich bin mit der Abfassung der Dissertation als publikationsbasiert, d.h. kumulativ, einverstanden und bestätige die vorstehenden Angaben. Eine entsprechende begründete Befürwortung mit Angabe des wissenschaftlichen Anteils des Doktoranden / der Doktorandin an den verwendeten Publikationen werde ich parallel an den Rat der Fakultät der Chemisch-Geowissenschaftlichen Fakultät richten.

_____	_____	_____
Name Promovend	Ort Datum	Unterschrift

_____	_____	_____
Name Erstbetreuer(in)	Ort Datum	Unterschrift





# Statement of Authorship

Selbstständigkeitserklärung:

Ich erkläre, dass ich die vorliegende Arbeit selbstständig und unter Verwendung der angegebenen Hilfsmittel, persönlichen Mitteilungen und Quellen angefertigt habe.

Jena, 07.12.2018

---

Ort, Datum

---

Mikhail Urbazaev